AD NUMBER
AD889039
LIMITATION CHANGES

TO:

Approved for public release; distribution is unlimited.

FROM:

Distribution authorized to U.S. Gov't. agencies only; Test and Evaluation; 12 AUG 1971. Other requests shall be referred to Air Force Flight Dynamics Laboratory, Attn: FY, Wright-Patterson AFB, OH 45433.

AUTHORITY

AFFDC ltr, 29 Nov 1973

AFFDL-TR-71-7
Volume I

AD 889039

A STUDY OF FOLDING PROPROTOR VTOL AIRCRAFT DYNAMICS

VOLUME I. ANALYTICAL METHODS

DR. JING G. YEN

GOTTFRIED E. WEBER

TROY M. GAFFEY

BELL HELICOPTER COMPANY

TECHNICAL REPORT AFFDL-TR-71-7, VOLUME I

SEPTEMBER 1971

D D C

RECEIVED

NOV 15 1971

AIR FORCE FLIGHT DYNAMICS LABORATORY
AIR FORCE SYSTEMS COMMAND
WRIGHT-PATTERSON AIR FORCE BASE, OHIO

NOTICE

When Government drawings, specifications, or other data are used
for any purpose other than in connection with a definitely related
Government procurement operation, the United States Government thereby
incurs no responsibility nor any obligation whatsoever; and the fact
that the Government may have formulated, furnished, or in any way supplied
the said drawings, specifications, or other data, is not to be regarded
by implication or otherwise as in any manner licensing the holder or any
other person or corporation, or conveying any rights or permission to
manufacture, use, or sell any patented invention that may in any way be
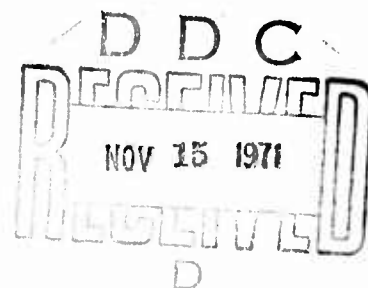related thereto.

Copies of this report should not be returned unless return is
required by security considerations, contractual obligations, or notice
on a specific document.

A STUDY OF FOLDING PROPROTOR VTOL AIRCRAFT DYNAMICS

VOLUME I. ANALYTICAL METHODS

DR. JING G. YEN

GOTTFRIED E. WEBER

TROY M. GAFFEY

BELL HELICOPTER COMPANY

D D C

NOV 15 1971

ABSTRACT

This report describes the results of a study of the dynamic
stability and response during the feathering and folding
of the blades of a folding-proprotor VTOL. This study involved
the development of analytical methods of predicting the
dynamic characteristics during feathering and folding, corre-
lation of the theoretical methods with experimental data, a
dynamic analysis of a representative folding-proprotor VTOL
design, and a parametric study to identify design factors
which can be used to control dynamic characteristics during
feathering and folding. Correlation of the theory with
measured dynamic stability and response characteristics
during feathering and folding is good, and indicates the
analytical methods can be used with confidence. The results
of the dynamic analysis indicate satisfactory stability and
response characteristics can be achieved in a 66,000-pound
gross-weight class, folding-proprotor VTOL. The results of
the parametric study are summarized in terms of design guide-
lines. This volume contains the development of the theory,
correlation of theory with experimental data, and the dynamic
analysis and parametric study. Volume II is a guide to the
computer programs and contains FORTRAN listings.

TABLE OF CONTENTS

VOLUME I

TABLE OF CONTENTS (Continued)

VOLUME I

LIST OF ILLUSTRATIONS

LIST OF ILLUSTRATIONS (Cont'd)

LIST OF ILLUSTRATIONS (Cont'd)

LIST OF ILLUSTRATIONS (Cont'd)

LIST OF ILLUSTRATIONS (Cont'd)

LIST OF ILLUSTRATIONS (Cont'd)

LIST OF TABLES

VOLUME I

LIST OF TABLES (Continued)

VOLUME I

LIST OF SYMBOLS FOR FEATHER-STOP ANALYSIS

A_1 blade lateral cyclic

A_{1c}, A_{1s} coefficients of time dependent swashplate lateral excitation as defined in equation 145

AC   aerodynamic center

$\vec{a}_i$ acceleration of a blade discrete mass

a_{ix}, a_{iy}, a_{iz} components of $\vec{a}_i$ in xyz coordinate system

a_o rotor precone angle

a' master blade flapping

B_1 blade longitudinal cyclic

B_{1c}, B_{1s} coefficients of time dependent swashplate longitudinal excitation as defined in equation 146

BS   total number of blade discrete masses per rotor

b' tip-path-plane flapping 90 degrees to master blade

bl   number of blades

C   flap-damping coefficient

C_L, C_D, C_M lift, drag, and pitching-moment coefficients for a blade strip

$\bar{C}_L$, $\bar{C}_D$ lift and drag coefficients for a wing strip

$C_{\dot{\alpha}i}$ blade pitch-damping coefficient

CA   pylon conversion axis

c   chord length of a flat plate

c_i blade chord

c_{wi} wing chord

D   dissipation function

D_{wi} wing strip drag force

Symbol	Description
dD_i	blade local drag
$\vec{d}_i$	position vector from a wing leading-edge to CA
dL_i	blade local lift
dM_i	blade pitching-moment
dM_i'	blade pitch-damping moment
$d\vec{Q}_i$	blade aerodynamic pitching moment
dr_i	blade segment length
e_f	blade flapping hinge offset
e_L	blade lead-lag hinge offset
$\vec{F}_{Ai}$	proprotor aerodynamic force
$\vec{F}_H$	external force at pylon tip
F_i	blade thrust
$\vec{F}_i$	external force at a blade element
$\vec{F}_p$	external force at pylon center of gravity
$F_x,\ F_y,\ F_z$	components of rotor inertial force in rotating coordinate system
$\vec{F}_{wi}$	external force at a wing segment
$FF_X,\ FF_Y,\ FF_Z$	components of total airloads per rotor in pylon coordinate system
$\vec{f}$	inertia loads at rotor hub
f_i	blade aerodynamic radial force
g_Y	gravitational acceleration component along Y_F axis in $X_F Y_F Z_F$ coordinate system
g_Z	gravitational acceleration component along Z_F axis in $X_F Y_F Z_F$ coordinate system
H	rotor hub center
H_i	blade aerodynamic inplane force
H_{wi}	wing drag force

I_{ci}	blade pitching mass moment-of-inertia about its feathering axis
I_p	pylon pitching mass moment-of-inertia about its center of gravity
I_{wi}	wing torsional mass moment-of-inertia about its elastic axis
i	used as subscripts to denote the ith blade discrete mass
K_a	longitudinal hub restraint spring rate
K_b	lateral hub restraint spring rate
K_i	reduced velocity
K_{stop}	simulated hub restraint spring rate for flapping-stops
L	parameter defined by Figure 17
$\vec{L}_i$	angular momentum vector of a blade discrete mass
L_{wi}	wing strip lift force
M_X, M_Y	hub-spring moments
M_{ej}	wing/pylon effective mass
M_i	Mach number
M_x, M_y, M_z	components of rotor inertial moment
m_{ej}, m_{en}	flexible blade effective mass of the jth or n^{th} normal mode
m_H	hub mass
m_i	blade discrete mass
m_p	pylon mass
m_{wi}	wing discrete mass
m_x, m_y	hub spring moments
$\vec{N}$	total external moment acting on a proprotor
N	number of blade normal modes

xvi

$\vec{N}_A$	component of $\vec{N}$ from aerodynamic forces
$\vec{N}_G$	component of $\vec{N}$ from gravitational forces
$\vec{N}_I$	component of $\vec{N}$ from inertia loads at rotor hub
$\vec{N}_M$	component of $\vec{N}$ from aerodynamic pitching moment
N_x, N_y, N_z	Cartesian components of $\vec{N}$
NS	number of blade discrete masses
O	a fixed point
$\vec{P}_i$	linear momentum vector of a blade discrete mass
Q_i	blade aerodynamic pitching moment
Q_{Ej}	part of flexible blade forcing function as a result of external loads
$Q_{Ek1}, Q_{Ek2}, Q_{Ek3}$	external loads as part of flexible blade forcing functions for the master blade, the second blade, and the third blade, respectively
Q_{Ij}	part of flexible blade forcing function as a result of hub and blade rigid-body motion
$Q_{Ik1}, Q_{Ik2}, Q_{Ik3}$	inertial loads as a part of flexible blade forcing functions for the master blade, the second blade, and the third blade, respectively
Q_j	j^{th} generalized force
Q_{wi}	wing pitching moment
q_n	wing normal coordinates
R	total blade radius
$\bar{R}$	75 percent of R
R_1	a parameter defined by equation 112
R_2	a parameter defined by equation 113
$\vec{R}_H$	vector to define the rotor hub center with respect to a fixed point in space

$\vec{R}_i$	vector to define a blade mass point with respect to a fixed point in space
R_{ix}, R_{iy}, R_{iz}	components of $\vec{R}_i$ in xyz coordinate system
$\vec{R}_p$	position vector for the pylon
$\vec{R}_{wi}$	position vector for a wing segment
r_i	radial distance of a blade discrete mass along blade feathering axis
$\vec{r}_i$	vector to define a blade discrete mass referring to hub center
$\vec{r}_{i\varepsilon}$	displacement vector of blade aerodynamic center from rotor hub
rpm	proprotor angular velocity in revolutions per minute
r_{wi}	distance from wing root to a wing discrete mass
S	speed of sound
T	kinetic energy
T_{wi}	wing lift force
TFF_X, TFF_Y, TFF_Z	components of net rotor force at the hub in pylon coordinate system
TFM_X, TFM_Y, TFM_Z	components of net rotor moment at the hub in pylon coordinate system
t	time
t_e	time when aerodynamic vane excitation begins
t_τ	time when swashplate excitation initiated
U	free stream velocity
$U_{\zeta e}$	velocity field around an ellipse
$U_{\zeta p}$	velocity field around a flat plate
u_∞	free stream velocity along wing-chord direction
V	potential energy

xviii

V_{Pi}	normal component of a wing strip velocity
V_{Ti}	tangential component of a wing strip velocity
$\vec{V}_g$	gust velocity
V_{g_h}	head-on gust component
V_{g_v}	vertical gust component
V_i	blade strip total velocity
V_{wi}	wing strip total velocity
V_∞	component of free stream velocity perpendicular to wing chord
$\vec{v}_i$	velocity vector of a blade discrete mass
v_{ix}, v_{iy}, v_{iz}	components of $\vec{v}_i$ in xyz coordinate system
v_{Pi}	normal component of a blade strip velocity
v_{Pv}	vertical velocity component on the aerodynamic vane
v_{Ti}	tangential component of a blade strip velocity
v_{Tv}	tangential velocity component on the aerodynamic vane
W_X, W_Y, W_Z	force components of rotor gravitational force
X_F, Y_F, Z_F	Cartesian coordinates used as inertial system
XYZ	pylon coordinate system
X_0, Y_0, Z_0	linear displacements of CA
X_P	component of eccentricity of pylon center of gravity
x, y, z	proprotor rotating coordinate system
x', y', z'	blade local coordinate system differing from xyz by blade rigid-body flapping
Y_{CA}	distance defined in Figure 17

xix

Y_p	component of eccentricity of pylon center of gravity
y_i	mass unbalance of a blade mass point from feathering axis
$\bar{y}_i$	mass unbalance of a blade segment from feathering axis. Therefore, $\bar{y}_i$ is the result of integrating y_i in the chordwise direction
Y_{wi}	distance from wing elastic axis to a wing discrete mass
Z-plane	math plane defined by Figure 16
Z_p	distance from CA to pylon center of gravity
z_H	pylon length (from CA to H)
α_e	angle-of-attack of the aerodynamic vane
α_i	blade strip angle-of-attack
α_{oe}	steady angle-of-attack of the aerodynamic vane
α_{os}	oscillatory angle-of-attack of the aerodynamic vane
α_w	wing steady angle-of-attack
β	blade rigid-body flapping angle
β_2	second blade rigid-body flapping angle
β_{if}	flapping angle due to blade flexibility
β_j	the jth blade rigid-body flapping angle
β_{lat}	lateral tip-path-plane flapping
β_{long}	longitudinal tip-path-plane flapping
β_{stop}	maximum flapping before flapping-stops apply
Γ	circulation
γ	blade lock number
ΔL_i	wing segment length

δ	wing thickness ratio
δ_1	blade out-of-plane foreshortening component as blade bends elastically
δ_3	blade negative pitch-flap coupling
ε_{ci}	distance from blade quarter chord to its center of gravity
ε_{ei}	distance from blade quarter chord to its elastic axis
ε_{fi}	distance from blade feathering axis to its quarter chord
ε_i	blade inplane foreshortening component as blade bends elastically
ε_{wi}	distance from wing elastic axis to its AC
ζ-plane	physical plane defined by Figure 16
$\vec{\zeta}_i$	position vector of a blade mass element from wing leading-edge
ζ_{iX_F}, ζ_{iY_F}, ζ_{iZ_F}	parameters defined by equation 129, 130, and 131, respectively
ζ_j	normal coordinate for flexible blades
ζ_1, ζ_2, ζ_3	normal coordinate of the master blade, the second blade, and the third blade, respectively
ζ_{ka}, ζ_{kb}	normal coordinate components of the kth cyclic mode
ζ_{k1}, ζ_{k2}, ζ_{k3}	normal coordinate of the kth cyclic mode for the master blade, the second blade, and the third blade, respectively
η_i	blade out-of-plane deflection
η_{wi}	wing beamwise displacement
θ_c	blade root collective
$\bar{\theta}_i$	blade element total pitch (root collective, built-in twist, cyclics, pitch-flap coupling as well as blade flexible pitching deflections)

$\overline{\overline{\theta}}_i$	blade element pitch considering root collective and built-in twist only
θ_{if}	blade flexible pitching deflection
θ_p	total pylon pitching angle
θ_{pc}	steady pylon pitching angle
θ_{pp}	pylon pitch from wing torsional deflections
θ_{Ti}	blade built-in twist
θ_t	blade twist at the 73 percent radius
θ_{wi}	wing torsional deflection
Λ	wing sweep angle
ξ_i	blade inplane deflection
ξ_{wi}	wing chordwise displacement
π	ratio of the circumference of a circle to its diameter
ρ	mass density of air
σ_i	induced velocity
τ	viscous damping ratio
ϕ	complex velocity potential
ϕ_i	inflow angle of a blade strip
$\phi_{i\eta n}$	flexible blade out-of-plane mode shape
$\phi_{i\theta n}$	flexible blade pitching mode shape
$\phi_{i\xi n}$	flexible blade in-plane mode shape
$\phi_{\psi An}$	yawing component of the nth normal mode at CA
$\phi_{\theta An}$	pitching component of the nth normal mode at CA
$\phi_{\theta in}$	pitching component of the nth normal mode at a wing segment
$\phi_{3/4}$	inflow angle at blade 3/4 radius

ϕ_{wi}	wing inflow angle
ϕ_{XAn}, ϕ_{YAn}, ϕ_{ZAn}	linear component of nth normal mode at CA
ϕ_{Xin}, ϕ_{Zin}	components of nth normal mode at a wing segment
ψ	blade azimuth position
$\dot{\psi}$	rotor instantaneous rotating velocity
ψ_p	pylon yawing angle
Ω	proprotor angular velocity
$\vec{\omega}$	total rotation vector of blade rotating coordinates
ω_{ac}, ω_{as}, ω_{bc}, ω_{bs}	swashplate excitation frequencies as defined by equations 147, 148, 149, and 150, respectively
ω_{aco}, ω_{aso}, ω_{bco}, ω_{bso}	steady components of ω_{ac}, ω_{as}, ω_{bc}, ω_{bs}, respectively
ω_{eo}	steady component of ω_e
ω_n	flexible blade natural frequency of the nth mode
ω_x, ω_y, ω_z	components of $\vec{\omega}$ in xyz coordinate system
ω_θ	blade torsional frequency
$(\dot{\ })$	time rate
$\dfrac{D}{Dt}$	time derivative referred to an inertial coordinate system
$\dfrac{\partial}{\partial t}$	time derivative referred to a body coordinate system
Σ	summation
$(\vec{\ })$	vector notation

LIST OF SYMBOLS FOR BLADE FOLDING DYNAMICS ANALYSIS

A	area
AE	segment axial stiffness
B	$K^{-1}m + iD \dfrac{K^{-1}}{\omega} - K^{-1} F_e$
b	semichord
b_1	first eigenvalue
b_i	remainder of eigenvalues
b_r	reference semichord
C	mean aerodynamic chord
C_h	aerodynamic influence coefficient
C_{h_1}, C_{h_1}	partition of C_h
C_{h_s}	steady-state aerodynamic influence coefficient
C_{L_α}	lift curve slope
CA	pylon conversion axis
CG	center of gravity
c_i	strip semichord
D	aerodynamic damping
d	distance between dumbbells
E	$\dfrac{d}{dt} F(t)$
EA	elastic axis
EI_c	segment chord bending stiffness
EI_β	segment beam bending stiffness
e_1, e_2	constant coefficients
F, F_1, F_2	forces on dumbbells
F'	$\dfrac{K^{-1}}{\omega^2} F(t)$

$\overline{F}$ complex forcing function

F_e external aerodynamic force resulting from wing motion

$F(t)$ externally applied force

GJ   segment torsional stiffness

g   complex structural damping parameter

h, h_1, h_2 displacements defined in Figure 20

I   identity matrix

I_e inertia about elastic axis

i   imaginary unit

K   complete stiffness matrix

K_1 a parameter defined by equation 198

K_e elemental stiffness matrix in main coordinate system

k_e elemental stiffness matrix in elemental coordinate system

k   reduced frequency $\dfrac{b_r * \omega}{V}$

L   lift

L^{-1} inverse Laplace transform

L_h unsteady aerodynamic functions

L_i gust induced lift on an aerodynamic section

ℓ, ℓ_i segment length

L_α unsteady aerodynamic functions

M   aerodynamic moment

$\overline{M}$ total internal moment

M_h, M_α unsteady aerodynamic functions

m   mass matrix

N_0, D_0, D_1	linear coefficients in response
NP	total number of eigenvalues
$p(Z)$	zeroes of the system
q	generalized coordinate
$q(Z)$	poles of the system
R_i	contribution of ith mode to total response
S	weight unbalance of section
SH	shear force
SIC	structural influence coefficient matrix
s	reference semispan
T	kinetic energy
U	transformation matrix
V	forward velocity
V_g	gust velocity
W	weight of section
X	basic coordinate system
$\overline{X}$	distance from elastic axis to forward dumbbell
Y	basic coordinate system
$\overline{Y}$	distance from elastic axis to aft dumbbell
Z	basic coordinate system
$\overline{Z}$	differential operator $\dfrac{d}{dt}$
α, β	stiffness transformation angles
Δt	time increment
ΔY	segment width
ΔY_i	width of strip i
δ	deflection

θ	element rotation
θ_X, θ_Y, θ_Z	basic coordinate system
Λ	sweep angle
λ	complex eigenvalue
π	ratio of the circumference of a circle to its diameter
ρ	air density
τ	distance traveled in semichord
Φ	Jones function
ψ	stiffness transformation angle
ω	frequency
ω_1	frequency of the first mode
$(\ )_R$	real part
$(\ )_I$	imaginary part
$(\dot{\ })$	first derivative with respect to time
$(\ddot{\ })$	second derivative with respect to time
$[\ ]$	square matrix
$[\ ]^T$	transpose
$\{\ \}$	column matrix
$\lfloor\ \rfloor$	row matrix
$\dfrac{d}{dt}$	derivative with respect to time
subscript i, j	denotes i^{th} row and j^{th} column
subscript L	to denote associated variables at the left end of a segment
subscript $\overline{R}$	to denote associated variables at the right end of a segment

SECTION I

INTRODUCTION

The folding-proprotor VTOL concept combines the low-speed flight characteristics of the helicopter with the high subsonic cruise characteristics of the conventional turbojet airplane. Because of this highly desirable combination of flight characteristics, the folding-proprotor concept is currently being investigated for both military and commercial applications.

The folding-proprotor VTOL (hereafter referred to as FPR) principle of operation is illustrated in Figure 1. Takeoff is accomplished in helicopter mode with the nacelles vertical. After takeoff, the FPR is accelerated to an airspeed at which wing lift can support the aircraft. The nacelles are then mechanically tilted 90-degrees so that the proprotors act as propellers. During vertical and low-speed flight, control of the aircraft is by use of the usual helicopter collective and cyclic pitch controls. These controls are washed-out as the nacelles are tilted forward, and at 90 degrees nacelle tilt, control is by conventional fixed-wing control. The nacelle-tilting process is operationally flexible; it can be accomplished over a wide range of airspeeds and maneuver conditions, and with or without power.

After the nacelles are tilted, flight can be continued with the proprotors acting as propellers or the proprotors can be feathered and folded, and fan engine thrust used for propulsion. Proprotor feathering and folding is accomplished by transferring power from the proprotors to high bypass ratio fans (compound engines capable of delivering shaft power or fan thrust are employed) until the proprotors are windmilling. The proprotors are then declutched from the engines and the blades feathered. When stopped, the proprotors are indexed and the blades folded. With the blades folded, the FPR is operated as a conventional jet aircraft. For landing, the tilt/feather/fold sequence described above is reversed.

Preliminary investigations were made in 1967-68 to determine feasibility of the FPR concept.[1,2] These concentrated on the feather/fold process since helicopter, nacelle-tilting, and propeller modes of flight were found to be feasible during the XV-3 flight tests,[3] and since technical considerations after the blades are folded are expected to be similar to those of conventional fixed wing aircraft.

The preliminary investigations included small-scale model tests as well as analytical studies and showed the feather/fold procedure to be relatively simple and straightforward. However,

1
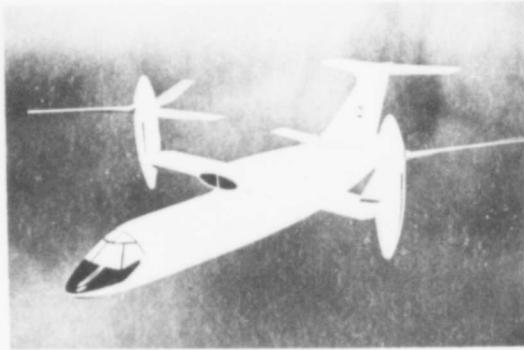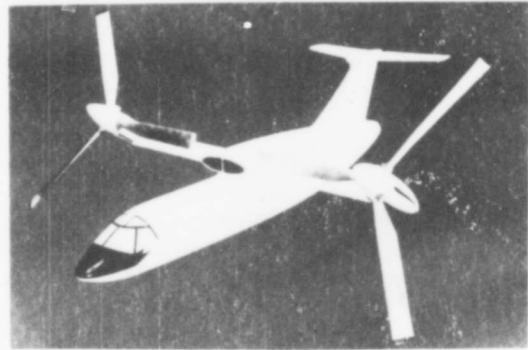
HELICOPTER FLIGHT   FORWARD TILT CONVERSION
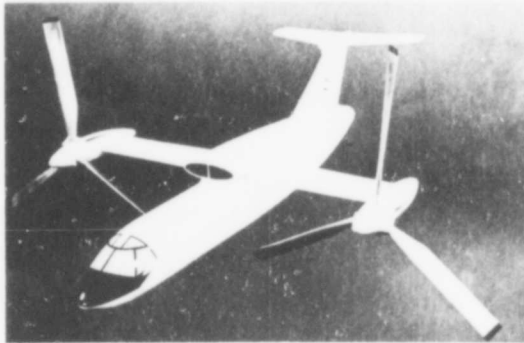
PROPROTOR FLIGHT
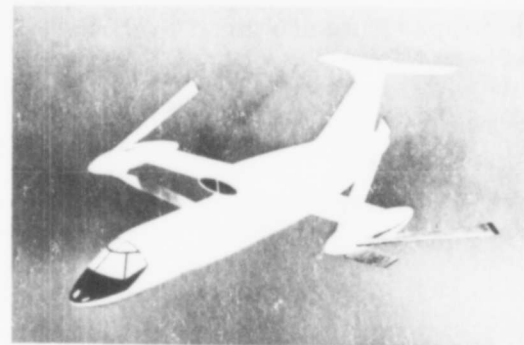
FAN PROPULSION –
ROTORS STOPPED AND
FOLDING
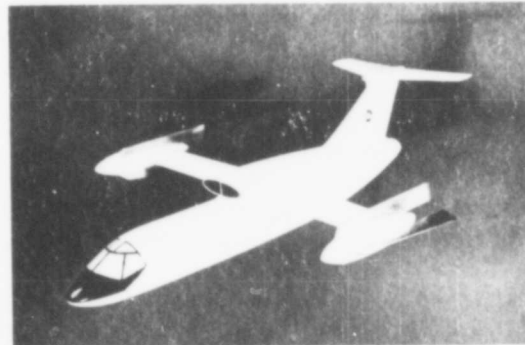
HIGH-SPEED CRUISE MODE
ROTORS FOLDED

NOT REPRODUCIBLE

FIGURE 1. Folding-Proprotor Principle of Operation

2

they also identified several areas requiring further investigation. Among these were the dynamic and aeroelastic characteristics during proprotor feathering and folding.

A. FOLDING PROPROTOR DYNAMIC CONSIDERATIONS

The analytical and experimental investigations of the dynamics of the tilting-proprotor VTOL[4,5,6] and the results of the preliminary investigations of folding-proprotor dynamics, have provided a good background for an understanding of FPR dynamic considerations. Some of these considerations are discussed below.

1. Dynamic Stability

Proprotor instability, similar in nature to propeller whirl flutter, was encountered during tests of the XV-3 convertiplane. Subsequent investigations have led to an understanding of proprotor instability and have provided design approaches which can provide an adequate margin of stability for tilting-proprotor VTOLs.

The airloads generated by precession are the cause of proprotor instability. However, the proprotor's flapping freedom causes a basic difference in the manner in which the precession generated aerodynamic forces act on the pylon.

In the case of the propeller the rigid attachment to the hub precesses the propeller in response to nacelle pitching (or yawing). If the nacelle pitches up the angle of attack generated airloads cause a yawing moment at the hub. This yawing moment acts as negative damping on the nacelle backward whirl mode and at some airspeed will exceed the combined nacelle structural damping and aerodynamic damping caused by transverse velocities over the propeller disc. Flutter in the backward whirl mode results.

In the case of the proprotor airloads are required to precess the proprotor because of the blade flapping freedom. (In a vacuum the proprotor would not precess in response to pylon pitching or yawing.) In order to generate the precessional airloads a change in blade angle of attack is required. This means the rotor must develop a flapping angle with respect to its control plane (swashplate). Consequently, a proprotor must lag the pylon motion. This leads to frequency dependent aerodynamic flapping moments and hub inplane shear forces. In contrast, a propeller's aerodynamics forces and moments are essentially independent of the frequency of the nacelle motions.

From the standpoint of proprotor stability, the normal shear force is the most significant. It can be conveniently expressed

3

as H_α, the component of the normal force in-phase with pylon pitch and H_q, the component in-phase with pylon pitch rate. H_α acts as a negative spring reducing the pylon natural frequency. Depending on the pylon pitching frequency H_q can act as either positive or nagative damping and thus be stabilizing or destabilizing. Small side forces are also generated but are not of consequence in proprotor instability.

In the case of the FPR aircraft, the proprotor stability requirements are somewhat relaxed since the blades are folded for operation at high speed. Based on tilt-proprotor design experience, the wing stiffnesses resulting from strength requirements should provide an adequate proprotor stability margin. However, the provision of feather/fold capability may require design features which have a destabilizing influence on proprotor stability. For example, a longer mast may be required to accommodate blade folding. Another consideration is that during feathering and unfeathering proprotor natural frequencies can become coincident with wing/pylon natural frequencies. Any resulting adverse dynamic or aerodynamic coupling could then cause instability. An example of this was encountered during the dynamic model test conducted under this program when coincidence of the blade flapping and wing-beam bending mode was found to cause the blade flapping mode to become unstable thereby requiring a flapping lockout to insure stability.

Wing and blade flutter and divergence become considerations when the proprotor is stopped. Wing divergence is of concern since the proprotor is located well ahead of the wing torsional axis. Wing flutter does not appear to be a serious problem because of the forward location of the pylon center of gravity. However, coupled blade/wing flutter could be a problem. As the blades are folded, the blade natural frequencies change and can become coincident with wing/pylon frequencies. Also, at large fold angles, when the blades are in close proximity to the nacelle, aerodynamic buffetting could occur. Blade divergence does not appear to be a problem since the blades are not sub-ject to large forward sweep angles or reversed flow, in contrast to the case of the edgewise stoppable-rotor concept.

2. Blade Flapping and Loads

The XV-3 flight tests showed that provision of adequate flapping clearance between the proprotor blades and the wing leading edge in the airplane mode is required for tilting-proprotor aircraft. In general, the required clearance is proportional to the square of the proprotor advance ratio, $V/\Omega R$, and can be reduced if the blade flapping natural frequency is detuned from one-per-rev by using flapping restraint and/or pitch-flap coupling.[7]

For the FPR, the large advance ratios occurring during blade feathering will cause excessive flapping unless flapping is restrained. An important result of this study is the finding that rapid rates of feathering of the blades increases the flapping caused by shaft angle of attack.

However, restraining flapping or the use of very stiff hingeless blades, increases one-per-rev loads in the rotor, since flapping acts to alleviate one-per-rev airloads. While only a limited number of cycles is incurred during a stop/start cycle, these one-per-rev loads may limit the maneuver capability in helicopter and conversion modes.

Another blade load consideration is maneuvers and gust encounters when the proprotor is at low rpm or is stopped but not folded. Blade stresses under these conditions could be greater than those at normal operating rpm at the same forward speed.

Blade load build-up due to traversing blade natural frequency resonances during feathering were not a problem during preliminary model tests. However, the model proprotors had the lowest inplane natural frequency of the blades designed above operating rpm. In rotor types where the lowest inplane natural frequency is below operating rpm, high blade loads might occur when the blades are feathered and the mode transits one-per-rev resonance.

3. Dynamic Response

Initially it was thought that the dynamic response during proprotor feathering would be negligible. This was based on the assumption that the axial flow condition of the proprotor would not induce significant oscillatory excitation.

However, during wind tunnel tests of small-scale dynamic models, relatively high vibrations of the wing and pylon were recorded. These occurred at the blade passage frequency with peak vibrations occurring when the proprotor angular velocity was one-third of the wing/pylon natural frequency (a three-bladed proprotor was employed on the model). The source of this vibration was determined to be wing-blade aerodynamic interference, principally the change in the blade airloads as it passed immediately in front of the wing.

The principal risk, insofar as this blade passage frequency vibration is concerned, appears to be the acceptability of the level of crew station and cabin vibrations during feathering or unfeathering. Of course, the design of the nacelle must take into account these vibrations.

In the preliminary tests, only very slow rates of feathering were possible because of mechanical limitations. A fast rate

5

of feathering appears to be desirable since it will reduce resonance buildup. This was investigated in this study and is discussed in Sections III and V.

B. PROGRAM APPROACH

As stated earlier, the objective of this program of study was to develop analytical methods of predicting dynamic behavior during proprotor feathering and folding. To accomplish this, the study was conducted in three phases.

In Phase I, three digital computer programs were developed; one treating the feathering and stopping of the proprotor, and the other two blade folding. The programs are based on existing computer programs, which were extensively modified to simulate the FPR configuration.

Phase II involved the testing of a small-scale, aeroelastically-scaled model. Data were obtained on dynamic stability at low rpm and on the dynamic response during feathering. The effect of feathering rate was investigated. The accuracy of the computer programs developed in Phase I was then evaluated by comparing predicted dynamic characteristics with those recorded during the model test and with the results of other related tests.

The dynamic characteristics of a 66,000-pound gross weight FPR design was investigated in Phase III. This investigation provided the basis for a parametric study to identify design parameters having significant influence on dynamic characteristics during blade feathering and folding.

This Volume contains a description of the analytical methods employed, the results of the model test and program correlation, and the parametric study. Volume II contains the information required for utilization of the computer programs and FORTRAN listings.

SECTION II

DEVELOPMENT OF THEORY

In order to simplify the development of a dynamic theory the
transition mode was considered to be separated into two distinct
phases: (1) a blade feathering or unfeathering phase, in
which the proprotor is stopped or started and, (2) a blade
folding or unfolding phase. These overlap only at the con-
dition of zero rpm and zero fold angle. By developing
separate analyses for each phase, the most applicable dynamic
and aerodynamic theory was used.

The theory treating the blade feathering/unfeathering phase
is based on a Bell Helicopter Company tilt-proprotor aero-
elastic analysis, called DYN5. The folding-proprotor version
of that analysis is referred to in this report as the Feather-
Stop Analysis and its digital computer mechanization is named
program ARAP06. The theory treating the blade folding and
unfolding phase is based on a fixed wing flutter analysis
developed for the U.S. Air Force by the Aerospace Corporation.[8]
It is referred to in this report as the Folding Dynamics
Analysis and its digital computer mechanizations are named
DFAL17 and DFAL18 (two separate programs).

This section is intended to provide the reader with an under-
standing of the theory and assumptions used in the analyses.
No attempt is made to give the complete equations of motion
as they are rather extensive. However, the equations which
define the math model are given to provide the reader with
insight into the details of the analysis. The FORTRAN listings
for each of the computer programs are included in Volume II
and serve as the documentation of the equations of motion.
A brief discussion of the computer programs is also given in
this section.

A. FEATHER-STOP ANALYSIS

The requirement to predict proprotor stability and whirl
flutter characteristics, and the blade and pylon response
during feathering or unfeathering dictate a fully coupled
wing-pylon-proprotor math model in which certain dynamic and
aerodynamic characteristics are rigorously accounted for.
The feather/unfeather simulation poses unusual requirements
for rotor aeroelastic analysis; (1) that the rotor angular
velocity be an independent variable, and (2) that the blades
be treated as individual blades rather than assuming identical
response for each blade. The second requirement is the result
of wing-rotor aerodynamic interference considerations.

1. Description of the Math Model

An overview of the math model for the feather-stop analysis is shown in Figure 2. The degrees of freedom include: (1) rigid-body blade flapping, feathering, and rotation, (2) blade beam and chord bending and torsion, (3) pylon pitching and yawing with respect to the wing-tip, and (4) wing beam and chord bending and torsion.

The development of the equations of motion are greatly simplified by treating as separate systems the wing, pylon, and hub, the proprotor rigid-body flapping, feathering and rotation, and the blade elastic motions as illustrated in Figure 3. The equations of motion for the proprotor rigid-body motion are obtained using the moment of momentum theorem and those of the wing-pylon-hub and blade elastic deformation using the normal mode method. The equations are joined through generalized force coupling.

Four Cartesian coordinate systems are employed in the feather-stop analysis. The right hand rule is used in all cases. These are illustrated in Figure 4. The wing coordinate system,

$$X_F Y_F Z_F$$

serves as the reference inertial system and has the following sign convention:

$$X_F$$ is positive forward
$$Y_F$$ is positive outboard
$$Z_F$$ is positive downward

The pylon coordinate system, XYZ, is located at the intersection of the shaft axis and the pylon conversion axis and rotates as the pylon converts. The sign convention of the XYZ system is such that in helicopter mode (shaft axis vertical), X is positive aft, Y outboard and Z upward, i.e. the Z axis lies along the shaft. In airplane mode (shaft axis horizontal) X is positive upward, Y outboard, and Z forward. Rotating the XYZ coordinate system with the shaft generates the proprotor rotating coordinate system, xyz. In this third coordinate system the x axis is parallel to the feathering axis and the negative y axis parallel to the flapping axis of the designated master blade. The z axis lies on the rotor shaft. Flapping the xyz system about the negative y axis yields a fourth coordinate system x'y'z' which is used primarily for blade airload calculations.

2. Proprotor Equations of Motion

a. Rigid-Body Motion

The equations of motion for the rigid-body motions are derived in a general form by first writing down the position vector

WING/PYLON FLEXIBILITY
IS REPRESENTED BY FOUR
NORMAL MODES (STEADY
WING AERODYNAMICS)

PYLON YAW
HINGE

PYLON
PITCH
HINGE
(CONVERSION
HINGE)

PYLON MASS

GIMBALLED HUB
WITH FLAPPING
RESTRAINT AND
PITCH-FLAP
COUPLING,
COLLECTIVE AND
CYCLIC PITCH

BLADE HAS RIGID BODY
FLAPPING, FEATHERING, AND
ROTATIONAL DEGREES OF
FREEDOM. BLADE FLEXIBILITY
IS REPRESENTED BY FOUR
NORMAL MODES (QUASI-STEADY
PROPROTOR AERODYNAMICS)

Figure 2.   Overview of Math Model for Feather-Stop
Analysis.

9

(1) Wing-Pylon
     Dynamics

— NORMAL MODE APPROACH
  USED TO REPRESENT WING-
  PYLON SYSTEM

— FORCES AND MOMENTS FROM
  PROPROTOR TREATED AS
  GENERALIZED FORCES
  (COUPLING WITH PROPROTOR)

— COUPLED EQUATIONS FOR
  TPP PITCH AND YAW AND
  ROTATION USED TO
  REPRESENT GIMBAL FREEDOM

(2) Proprotor
     Rigid Body
     Flapping and
     Rotational
     Freedom

— WING-PYLON SYSTEM
  COUPLING REPRE-
  SENTED BY HUB
  MOTION

— NORMAL MODES USED TO
  REPRESENT BLADE
  ELASTIC MODES

(3) Blade
     Elastic Modes

— COUPLING WITH WING-
  PYLON SYSTEM AND
  PROPROTOR RIGID BODY
  MOTIONS THROUGH
  GENERALIZED FORCE
  (AERODYNAMIC AND
  INERTIAL)

Figure 3. Variable Groupings for Feather-Stop Analysis.

10
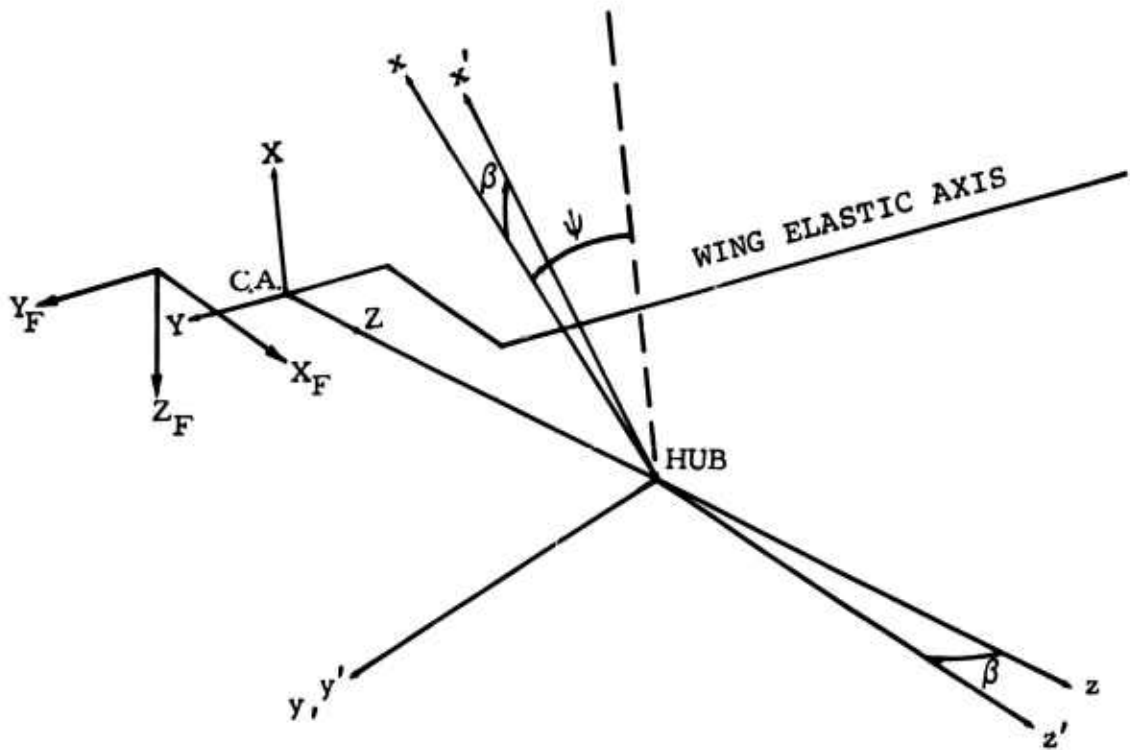
Figure 4. Coordinate Systems

of a discrete mass point on a designated master blade. The mass
point velocity and acceleration are determined by successive
differentiation of the position vector. The equations of
motion are then formulated by applying the moment of momentum
theorem, which states that the time derivative of the total
angular momentum of the system is equal to the moment of the
external forces about a given point. The equations of motion
for the remaining blades are obtained from those for the master
blade by coordinate transformation.

Figure 5 shows the relationship between a discrete mass point
on a designated master blade and the fixed coordinate system,
$X_F Y_F Z_F$. The position of the pylon conversion axis-shaft inter-
section (point CA) is denoted by $X_o Y_o Z_o$, which are linear dis-
placements referred to the $X_F Y_F Z_F$ coordinate system. θ_p and
ψ_p are the pylon pitching and yawing respectively; point H is
the hub centerline (zero flapping hinge offset is assumed).
The discrete mass, m_i, is located relative to point H by the
following rigid-body coordinates: r_i, the radial distance
along the feathering axis, and β, the rigid-body flapping, y_i,
the chordwise position from the feathering axis, and $\bar{\theta}_i$, the
blade element pitch. The elastic displacements further define
the location of m_i: η_i and ξ_i are the blade out-of-plane and
inplane deflections, respectively, and θ_{if} is the pitching
deflection. δ_i and ε_i account for the radial motion of the
mass point as the blade bends elastically. Since η_i and ξ_i are
both perpendicular to the undeflected blade, fictious spanwise
motion is introduced, i.e., terms indicating "stretching" of the
blade are generated when the blade deflects. In nonrotating
beam analysis these fictious terms are not important. But, for
a rotating beam, fictious Coriolis forces are generated. To
correctly represent the blade bending deflections δ_i and ε_i are
used to cancel the fictious spanwise motion, i.e., to represent
the "arcing" when the blade bends.

The elastic deflections are dropped out of the rigid-body
equations when the normal mode approach for the elastic
deflection is applied (orthogonality condition). They are
included in this development for generality.

To define the position vector of the point mass, m_i, the five
coordinate rotations illustrated in Figure 6 are required:

(1) Pylon pitch - rotating inertia axis system by
θ_p about $\hat{E}_2$ at the point CA gives an axis system
defined by unit vectors $\hat{e}_1$, $\hat{E}_2$, and $\hat{e}_2$.

(2) Pylon yaw - rotating by ψ_p about $\hat{e}_2$ at the point CA
gives the axis system defined by unit vectors $\hat{e}_3$, $\hat{e}_4$,
and $\hat{e}_2$.

(3) Rotor rotation - rotating by ψ about $\hat{e}_3$ at the point H
(rotor hub) gives the axis system defined by unit
vectors $\hat{e}_5$, $\hat{e}_6$, and $\hat{e}_3$.
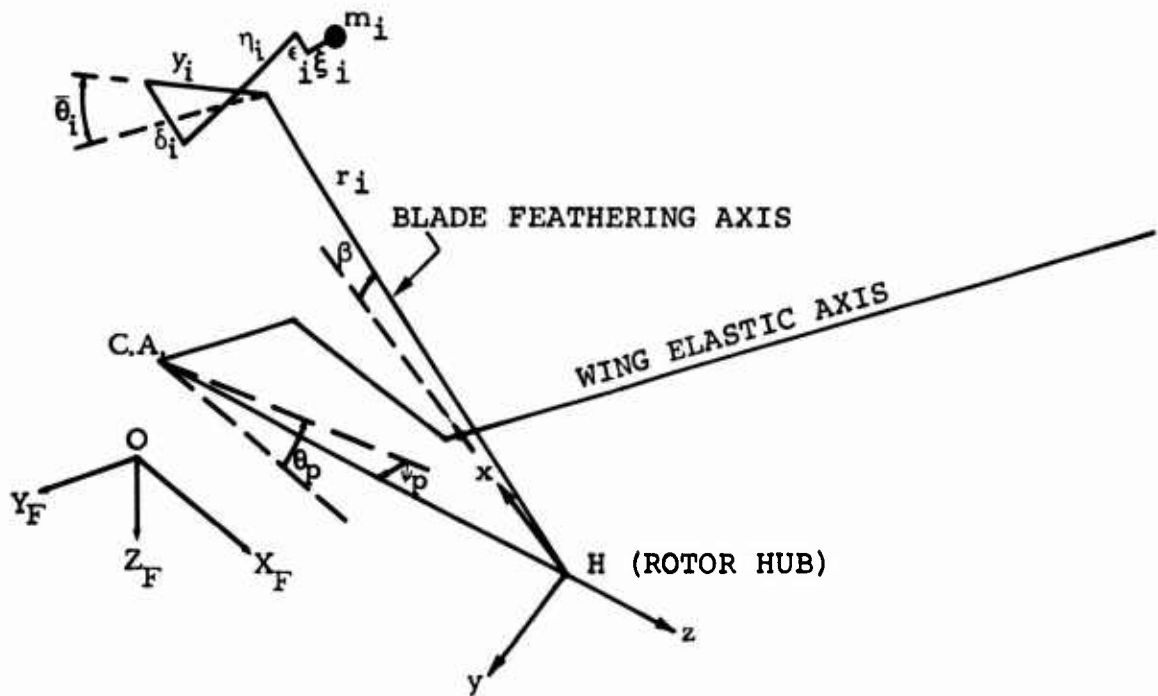
Figure 5. Relationship of Discrete Mass Point,
m_i, With Fixed Coordinate System $X_F Y_F Z_F$.
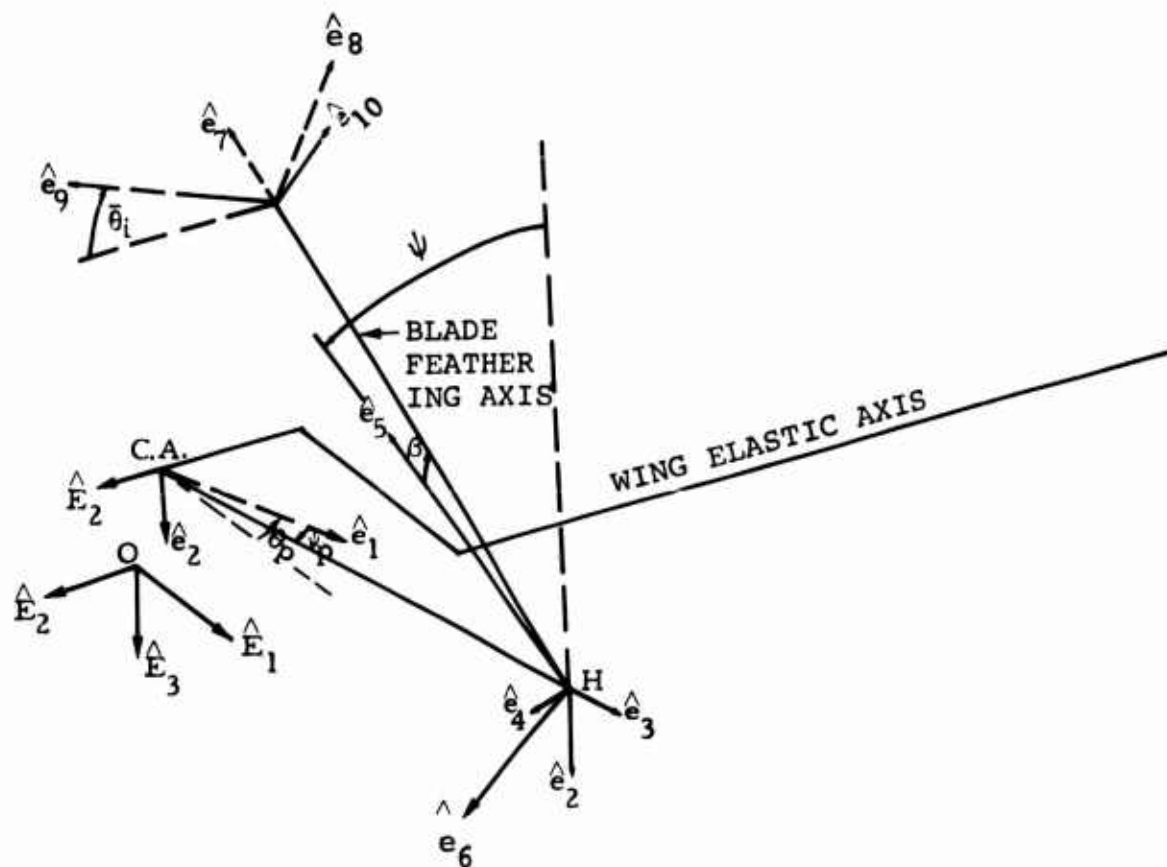
Figure 6. Coordinate Rotations.

(4) Blade flap - rotating by β about $-\hat{e}_6$ at the point
    H gives the axis system defined by unit vectors $-\hat{e}_6$,
    $\hat{e}_7$, and $\hat{e}_8$. This is the blade local coordinate
    system which blade airloads calculation is referred to.

(5) Blade pitch - rotating by $\bar{\theta}_i$ about $\hat{e}_7$ at the point H
    gives the axis system defined by unit vectors $\hat{e}_7$, $\hat{e}_9$,
    and $\hat{e}_{10}$. $\bar{\theta}_i$ is the blade total pitch.

The vector defining the mass point position is given by

$$\vec{R}_i = \vec{R}_H + \vec{r}_b \qquad (1)$$

in which

$$\vec{R}_H = X_o\hat{E}_1 + Y_o\hat{E}_2 + Z_o\hat{E}_3 + z_H\hat{e}_3 \qquad (2)$$

and

$$\vec{r}_b = r_i\hat{e}_7 + y_i\hat{e}_9 - \delta_i\hat{e}_7{}' + \eta_i\hat{e}_8{}' - \epsilon_i\hat{e}_7{}' - \xi_i\hat{e}_6 \qquad (3)$$

where $\hat{e}_7{}'$ and $\hat{e}_8{}'$ are referred to preconed blade position.

To work consistently in the rotating system the coordinate
rotations shown above (and in Figure 6) are employed. From
inspection,

$$\hat{e}_7 = \cos\beta \; \hat{e}_5 + \sin\beta \; \hat{e}_3 \qquad (4)$$

$$\hat{e}_8 = - \sin\beta \; \hat{e}_5 + \cos\beta \; \hat{e}_3 \qquad (5)$$

$$\hat{e}_9 = - \sin\bar{\theta}_i \sin\beta \; \hat{e}_5 + \cos\bar{\theta}_i \; \hat{e}_6 + \sin\bar{\theta}_i \cos\beta \; \hat{e}_3 \qquad (6)$$

$$\hat{E}_1 = - \left(\sin\theta_p \cos\psi + \cos\theta_p \sin\psi_p \sin\psi\right)\hat{e}_5$$
$$+ \left(\sin\theta_p \sin\psi - \cos\theta_p \sin\psi_p \cos\psi\right)\hat{e}_6 + \cos\theta_p \cos\psi_p \; \hat{e}_3 \qquad (7)$$

$$\hat{E}_2 = \cos\psi_p \sin\psi \; \hat{e}_5 + \cos\psi_p \cos\psi \; \hat{e}_6 + \sin\psi_p \; \hat{e}_3 \qquad (8)$$

$$\hat{E}_3 = \left(\sin\theta_p \sin\psi_p \sin\psi - \cos\theta_p \cos\psi\right)\hat{e}_5$$
$$+ \left(\sin\theta_p \sin\psi_p \cos\psi + \cos\theta_p \sin\psi\right)\hat{e}_6 - \sin\theta_p \cos\psi_p \; \hat{e}_3 \qquad (9)$$

15

When equations 4 through 9 are substituted into 1 through 3, the mass position vector can be written as

$$\vec{R}_i = R_{ix} \hat{e}_5 + R_{iy} \hat{e}_6 + R_{iz} \hat{e}_3 \tag{10}$$

in which

$$R_{ix} = - X_o \left(\sin\theta_p \cos\psi + \cos\theta_p \sin\psi_p \sin\psi \right) + Y_o \cos\psi_p \sin\psi$$

$$+ Z_o \left(\sin\theta_p \sin\psi_p \sin\psi - \cos\theta_p \cos\psi \right) + r_i \cos\beta - \left(\delta_i + \epsilon_i \right) \cos a_o$$

$$- \eta_i \sin a_o - y_i \sin\bar{\theta}_i \sin\beta \tag{11}$$

$$R_{iy} = X_o \left(\sin\theta_p \sin\psi - \cos\theta_p \sin\psi_p \cos\psi \right) + Y_o \cos\psi_p \cos\psi$$

$$+ Z_o \left(\sin\theta_p \sin\psi_p \cos\psi + \cos\theta_p \sin\psi \right) + \left(y_i \cos\bar{\theta}_i - \xi_i \right) \tag{12}$$

$$R_{iz} = X_o \cos\theta_p \cos\psi_p + Y_o \sin\psi_p - Z_o \sin\theta_p \cos\psi_p + z_H + r_i \sin\beta$$

$$- \left(\delta_i + \epsilon_i \right) \sin a_o + \eta_i \cos a_o + y_i \sin\bar{\theta}_i \cos\beta \tag{13}$$

At this point an approximation for the shortening displacements, δ_i and ϵ_i, must be made. If the flapping angle due to blade flexibility, β_{if}, is assumed to be small and the difference between the deflected and undeflected radial position to be negligible, one can write (see Figure 7)

$$\beta_{if} \cong \sin\beta_{if} = \frac{\eta_i}{r_i} \tag{14}$$

and

$$\delta_i = \eta_i \tan\frac{\beta_{if}}{2} = \frac{1}{2}\eta_i \beta_{if} = \frac{\eta_i^2}{2r_i} \tag{15}$$

Similarly

$$\epsilon_i = \frac{\xi_i^2}{2r_i} \tag{16}$$

16

The velocity of the mass point, m_i, is obtained by differentiating equation 10 with respect to time. Thus

$$\vec{v}_i = \frac{D\vec{R}_i}{Dt} = \frac{\partial \vec{R}_i}{\partial t} + \vec{\omega} \times \vec{R}_i \qquad (17)$$

where

$$\vec{\omega} = \dot{\theta}_p \hat{E}_2 + \dot{\psi}_p \hat{e}_2 + \dot{\psi} \hat{e}_3 \qquad (18)$$

or

$$\vec{\omega} = \left(\dot{\theta}_p \cos\psi_p \sin\psi - \dot{\psi}_p \cos\psi \right) \hat{e}_5 + \left(\dot{\theta}_p \cos\psi_p \cos\psi + \dot{\psi}_p \sin\psi \right) \hat{e}_6$$

$$+ \left(\dot{\theta}_p \sin\psi_p + \dot{\psi} \right) \hat{e}_3 \qquad (19)$$

or

$$\vec{\omega} = \omega_x \hat{e}_5 + \omega_y \hat{e}_6 + \omega_z \hat{e}_3 \qquad (20)$$

in which $\frac{D}{Dt}$ and $\frac{\partial}{\partial t}$ denote the time rate of change of a vector referred to an inertial and a body coordinate system respectively.
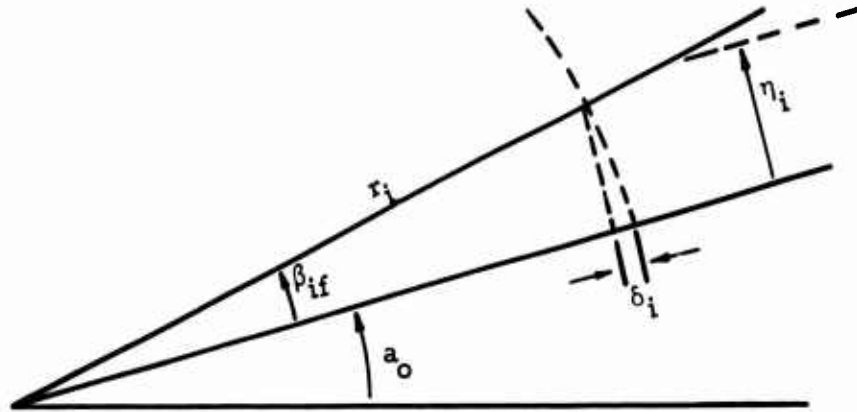
Figure 7. Geometrical Relation Between Foreshortening and Generalized Coordinate.

17

Performing the mathematical manipulation indicated in equation 17, the result is

$$\vec{v}_i = v_{ix}\,\hat{e}_5 + v_{iy}\,\hat{e}_6 + v_{iz}\,\hat{e}_3 \tag{21}$$

where

$$
\begin{aligned}
v_{ix} = &-r_i\,\sin\beta\left[\dot{\beta}-\left(\dot{\theta}_p\,\cos\psi_p\,\cos\psi + \dot{\psi}_p\,\sin\psi\right)\right] \\
&- y_i\left\{\sin\bar{\theta}_i\,\cos\beta\left[\dot{\beta}-\left(\dot{\theta}_p\,\cos\psi_p\,\cos\psi + \dot{\psi}_p\,\sin\psi\right)\right]\right. \\
&\left.+ \cos\bar{\theta}_i\left[\dot{\bar{\theta}}_i\,\sin\beta + \left(\dot{\theta}_p\,\sin\psi_p + \dot{\psi}\right)\right]\right\} \\
&- \dot{X}_0\left(\cos\theta_p\,\sin\psi_p\,\sin\psi + \sin\theta_p\,\cos\psi\right) + \dot{Y}_0\,\cos\psi_p\,\sin\psi \\
&+ \dot{Z}_0\left(\sin\theta_p\,\sin\psi_p\,\sin\psi - \cos\theta_p\,\cos\psi\right) \\
&+ z_H\left(\dot{\theta}_p\,\cos\psi_p\,\cos\psi + \dot{\psi}_p\,\sin\psi\right) \\
&+ \eta_i\,\cos a_0\left(\dot{\theta}_p\,\cos\psi_p\,\cos\psi + \dot{\psi}_p\,\sin\psi\right) \\
&+ \xi_i\left(\dot{\theta}_p\,\sin\psi_p + \dot{\psi}\right) - \dot{\eta}_i\,\sin a_0 \\
&- \frac{1}{2r_i}\left(\eta_i^{\,2} + \xi_i^{\,2}\right)\sin a_0\left(\dot{\theta}_p\,\cos\psi_p\,\cos\psi + \dot{\psi}_p\,\sin\psi\right) \\
&- \frac{1}{r_i}\left(\eta_i\dot{\eta}_i + \xi_i\dot{\xi}_i\right)\cos a_0 \tag{22}
\end{aligned}
$$

$$
\begin{aligned}
v_{iy} = &\ r_i\left[\cos\beta\left(\dot{\theta}_p\,\sin\psi_p + \dot{\psi}\right) - \sin\beta\left(\dot{\theta}_p\,\cos\psi_p\,\sin\psi - \dot{\psi}_p\,\cos\psi\right)\right] \\
&- y_i\,\sin\bar{\theta}_i\left[\dot{\bar{\theta}}_i + \sin\beta\left(\dot{\theta}_p\,\sin\psi_p + \dot{\psi}\right) + \cos\beta\left(\dot{\theta}_p\,\cos\psi_p\,\sin\psi - \dot{\psi}_p\,\cos\psi\right)\right] \\
&- \dot{X}_0\left(\cos\theta_p\,\sin\psi_p\,\cos\psi - \sin\theta_p\,\sin\psi\right) + \dot{Y}_0\,\cos\psi_p\,\cos\psi \\
&+ \dot{Z}_0\left(\sin\theta_p\,\sin\psi_p\,\cos\psi + \cos\theta_p\,\sin\psi\right) \\
&- z_H\left(\dot{\theta}_p\,\cos\psi_p\,\sin\psi - \dot{\psi}_p\,\cos\psi\right) \\
&- \eta_i\left[\sin a_0\left(\dot{\theta}_p\,\sin\psi_p + \dot{\psi}\right) + \cos a_0\left(\dot{\theta}_p\,\cos\psi_p\,\sin\psi - \dot{\psi}_p\,\cos\psi\right)\right] - \dot{\xi}_i
\end{aligned}
$$

18

$$+ \frac{1}{2r_i}\left(\eta_i{}^2 + \xi_i{}^2\right)\left[\sin a_o\left(\dot{\theta}_p \cos\psi_p \sin\psi - \dot{\psi}_p \cos\psi\right)\right.$$

$$\left. - \cos a_o\left(\ddot{\psi} + \dot{\theta}_p \sin\psi_p\right)\right] \tag{23}$$

$$v_{iz} = \dot{X}_o \cos\theta_p \cos\psi_p + \dot{Y}_o \sin\psi_p - \dot{Z}_o \sin\theta_p \cos\psi_p$$

$$+ r_i \cos\beta\left[\dot{\beta} - \left(\dot{\theta}_p \cos\psi_p \cos\psi + \dot{\psi}_p \sin\psi\right)\right]$$

$$+ y_i\left\{\cos\bar{\theta}_i\left[\dot{\bar{\theta}}_i \cos\beta + \left(\dot{\theta}_p \cos\psi_p \sin\psi - \dot{\psi}_p \cos\psi\right)\right]\right.$$

$$\left. - \sin\bar{\theta}_i \sin\beta\left[\dot{\beta} - \left(\dot{\theta}_p \cos\psi_p \cos\psi + \dot{\psi}_p \sin\psi\right)\right]\right\}$$

$$+ \eta_i \sin a_o\left(\dot{\theta}_p \cos\psi_p \cos\psi + \dot{\psi}_p \sin\psi\right)$$

$$- \xi_i\left(\dot{\theta}_p \cos\psi_p \sin\psi - \dot{\psi}_p \cos\psi\right) + \dot{\eta}_i \cos a_o$$

$$+ \frac{1}{2r_i}\left(\eta_i{}^2 + \xi_i{}^2\right)\cos a_o\left(\dot{\theta}_p \cos\psi_p \cos\psi + \dot{\psi}_p \sin\psi\right)$$

$$- \frac{1}{r_i}\left(\eta_i \dot{\eta}_i + \xi_i \dot{\xi}_i\right)\sin a_o \tag{24}$$

The moment of momentum theorem is now applied. If $\vec{p}_i$ denotes the linear momentum and $\vec{v}_i$ the velocity, $\vec{L}_i$, the angular momentum of a mass particle m_i on the master blade, by definition is

$$\vec{p}_i = m_i \vec{v}_i \tag{25}$$

$$\vec{L}_i = \vec{R}_i \times \vec{p}_i \tag{26}$$

where $\vec{R}_i$ has been defined by equation 10. Then

$$\frac{D\vec{L}_i}{Dt} = \vec{R}_i \times \frac{D}{Dt}(m_i \vec{v}_i) \tag{27}$$

or

$$\frac{D\vec{L}_i}{Dt} = m_i \vec{R}_i \times \frac{D\vec{v}_i}{Dt} \tag{28}$$

19

For a system of particles,

$$\sum_i^{BS} \frac{D\vec{L_i}}{Dt} = \vec{N} \tag{29}$$

where $\sum_i^{BS}$ denotes summation over all blades and $\vec{N}$ is the total

moment about the fixed point of the external forces acting on the system. Differentiating equation 21 with respect to time gives

$$\frac{D\vec{v_i}}{Dt} = \frac{\partial\vec{v_i}}{\partial t} + \vec{\omega} \times \vec{v_i} \tag{30}$$

or

$$\frac{D\vec{v_i}}{Dt} = \left(\frac{\partial v_{ix}}{\partial t} + \omega_y v_{iz} - v_{iy} \omega_z\right)\hat{e}_5 + \left(\frac{\partial v_{iy}}{\partial t} + \omega_z v_{ix} - v_{iz} \omega_x\right)\hat{e}_6$$

$$+ \left(\frac{\partial v_{iz}}{\partial t} + \omega_x v_{iy} - v_{ix} \omega_y\right)\hat{e}_3 \tag{31}$$

or

$$\vec{a_i} = \frac{D\vec{v_i}}{Dt} = a_{ix}\hat{e}_5 + a_{iy}\hat{e}_6 + a_{iz}\hat{e}_3 \tag{32}$$

in which a_{ix}, a_{iy}, and a_{iz} are the components of the acceleration of a blade particle.

Substituting equation 32 into 28 and using equation 29, the results are

$$\sum_i^{BS} \left(R_{iy} a_{iz} - a_{iy} R_{iz}\right) = N_x \tag{33}$$

$$\sum_i^{BS} \left(R_{iz} a_{ix} - a_{iz} R_{ix}\right) = N_y \tag{34}$$

$$\sum_i^{BS} \left(R_{ix} a_{iy} - a_{ix} R_{iy}\right) = N_z \tag{35}$$

20

The components of the total external torque about the fixed origin, O, consist of aerodynamic forces and moments, gravitational torque and moments generated by inertial loads at the rotor hub. Thus

$$\vec{N} = \vec{N_A} + \vec{N_M} + \vec{N_G} + \vec{N_I} \qquad (36)$$

where

$$\vec{N_A} = \sum_i^{BS} \vec{r_{i\epsilon}} \times \vec{F_{Ai}} \qquad (37)$$

$$\vec{N_M} = \sum_i^{BS} d\vec{Q_i} \qquad (38)$$

$$\vec{N_G} = \sum_i^{BS} \vec{r_i} \times \left(m_i g_Z \hat{E}_3 - m_i g_Y \hat{E}_2 \right) \qquad (39)$$

$$\vec{N_I} = \vec{R_H} \times (-\vec{f}) \qquad (40)$$

in which

$\vec{r_{i\epsilon}}$ is the displacement vector of the ith blade segment aerodynamic center from the rotor hub

$\vec{F_{Ai}}$ is the aerodynamic force

$d\vec{Q_i}$ is the aerodynamic pitching moment

g_Y and g_Z are gravitational acceleration components

$\vec{f}$ is the inertia load of all blades

Two assumptions are now made. First, it is assumed that the rigid-body flapping degrees of freedom are used to simulate the flapping motion of a gimballed semirigid proprotor. (The blade elastic degrees of freedom are used to simulate hingeless and fully articulated rotor types.) When this assumption is made, the individual blade flapping can be related to tip-path plane motion. For example, the flapping of the blades of a

21

four-bladed rotor can be expressed in terms of the flapping of opposite pairs of blades. Thus the number of flapping degrees of freedom can be reduced to two.

For a three-bladed gimballed rotor the individual blade flapping relationships with the tip-path-plane motion are more complex. If a_0 represents the blade precone and a' and b' orthonormal tip-path-plane flapping in the rotating system, the individual blade flapping is

$$\beta_1 = a_0 + a' \tag{41}$$

$$\beta_2 = a_0 - \frac{1}{2}a' + \frac{\sqrt{3}}{2}b' \tag{42}$$

and

$$\beta_3 = a_0 - \frac{1}{2}a' - \frac{\sqrt{3}}{2}b' \tag{43}$$

where a' is the flapping of the master blade and b' is the tip-path-plane flapping 90 degrees to the master blade.

This assumption results in the number of rigid-body equations being reduced to three: tip-path-plane flapping 90 degrees to the master blade, master blade flapping a', and proprotor rotation ψ. These correspond to equations 33, 34, and 35.

The second assumption is that the blade elastic motion will be represented using normal modes obtained from a vibration analysis which includes the rigid-body flapping and rotational freedoms. This assumption will be discussed in more detail below. Here, the implication is that the coupling terms involving blade elastic motion, η_i, ξ_i, and θ_{if} may be neglected in the rigid-body equations of motion.

The form of the resulting rigid-body equations of motion is given at the end of this section.

b. <u>Blade Elastic Equations of Motion</u>

(1) <u>General Formulation</u> - The use of the normal mode approach to represent the blade elastic motion consists of employing Lagrange's equation plus the normal mode orthogonality condition. Lagrange's equation for normal coordinates, ζ_j, is

$$\frac{D}{Dt}\left(\frac{\partial T}{\partial \dot{\zeta}_j}\right) - \frac{\partial T}{\partial \zeta_j} + \frac{\partial V}{\partial \zeta_j} + \frac{\partial D}{\partial \dot{\zeta}_j} = Q_j \tag{44}$$

22

where

T,V,D   are kinetic energy, potential energy,
             and dissipation function, respectively

Q_j is the generalized force, defined as

$$Q_j = \sum_i \vec{F_i} \cdot \frac{\partial \vec{R_i}}{\partial \zeta_j} \qquad (45)$$

where

$\vec{R_i}$ is the displacement vector of the ith
             element

$\vec{F_i}$ is the external force acting at the
             element ($\vec{F}$ in this case consists of
             aerodynamic forces and moments as well
             as gravitational and inertial forces)

The kinetic energy for a blade has the following form,

$$T = \frac{1}{2}\sum_i^{NS} m_i \left(v_{ix}^2 + v_{iy}^2 + v_{iz}^2 \right) \qquad (46)$$

in which

v_{ix}, v_{iy},   are defined by equations 22, 23, and 24,
and v_{iz} respectively

NS   is the number of discrete mass stations
            on the blade

The potential energy may be written as

$$V = \frac{1}{2}\sum_n^{N} m_{en} \, \omega_n^2 \, \zeta_n^2 \qquad (47)$$

in which

m_{en} and   are effective mass and natural frequency
ω_n of the nth mode, respectively

N   is the total number of natural modes
                under consideration

23

The energy dissipation arising from the structural damping of the blade is

$$D = \sum_{n}^{N} \tau \, m_{en} \, \omega_n \, \dot{\zeta}_n^{\,2} \tag{48}$$

where τ is the equivalent viscous damping ratio.

The kinetic energy expression given by equation 46 contains the generalized coordinates η_i, ζ_i, and θ_{if} representing the element out-of-plane, in-plane, and pitching deflection, respectively, and their time derivatives. In terms of normal coordinates, the following relationships apply.

$$\eta_i = \sum_{n}^{N} \phi_{i\eta n} \, \zeta_n \qquad \xi_i = \sum_{n}^{N} \phi_{i\xi n} \, \zeta_n \qquad \theta_{if} = \sum_{n}^{N} \phi_{i\theta n} \, \zeta_n \tag{49}$$

Successive differentiating with respect to time gives

$$\dot{\eta}_i = \sum_{n}^{N} \phi_{i\eta n} \, \dot{\zeta}_n \qquad \dot{\xi}_i = \sum_{n}^{N} \phi_{i\xi n} \, \dot{\zeta}_n \qquad \dot{\theta}_{if} = \sum_{n}^{N} \phi_{i\theta n} \, \dot{\zeta}_n \tag{50}$$

and

$$\ddot{\eta}_i = \sum_{n}^{N} \phi_{i\eta n} \, \ddot{\zeta}_n \qquad \ddot{\xi}_i = \sum_{n}^{N} \phi_{i\xi n} \, \ddot{\zeta}_n \qquad \ddot{\theta}_{if} = \sum_{n}^{N} \phi_{i\theta n} \, \ddot{\zeta}_n \tag{51}$$

Substituting equations 45, 46, 47, and 48 into equation 44, using expressions 49, 50, and 51, and the orthogonality conditions among normal modes, the following equation of motion for a normal mode is obtained

$$m_{ej}\left(\ddot{\zeta}_j + 2\tau\omega_j\dot{\zeta}_j + \omega_j^2\zeta_j\right) - Q_{Ij} = Q_{Ej} \tag{52}$$

The effective mass, m_{ej}, of the jth mode has the form

$$\begin{aligned} m_{ej} = \sum_{i}^{NS} \Big[& m_i\left(\phi_{i\eta j}^{\,2} + \phi_{i\xi j}^{\,2}\right) + \left(I_{ci} + m_i \bar{y}_i^{\,2}\right)\phi_{i\theta j}^{\,2} \\ & + 2m_i\bar{y}_i\left(\cos\bar{\bar{\theta}}_i \, \phi_{i\eta j} \, \phi_{i\theta j} + \sin\bar{\bar{\theta}}_i \, \phi_{i\xi j} \, \phi_{i\theta j}\right)\Big] \end{aligned} \tag{53}$$

24

in which $\bar{y}_i$ is the distance of a blade segment mass to the feathering axis, $\bar{\theta}_i$ is measured with respect to the feathering axis. Only blade root collective pitch and blade built-in twist are considered in $\bar{\theta}_i$.

The Q_{Ij} term in equation 52 represents the inertial forces acting on the blade due to hub and rigid-body blade motion. The expression for Q_{Ij} is extremely long, but to illustrate the coupling terms included, equation 54 is provided.

$$
\begin{aligned}
Q_{Ij}(x) = \sum_i^{NS} &\left[\phi_{i\eta j} \sin a_o + \frac{1}{r_i}\left(\eta_i \phi_{i\eta j} + \xi_i \phi_{i\xi j}\right)\cos a_o \right] \\
&\left\{ \left(r_i \sin\beta + \eta_i \cos a_o\right)\cdot\left(\ddot{\theta}_p \cos\psi_p \cos\psi + \dot{\theta}_p \dot{\psi}_p \sin\psi_p \cos\psi \right.\right. \\
&\qquad\qquad \left. - \dot{\theta}_p \dot{\psi} \cos\psi_p \sin\psi + \ddot{\psi}_p \sin\psi + \dot{\psi}_p \dot{\psi} \cos\psi \right) \\
&+ r_i \dot{\beta}\cos\beta\left[\dot{\beta} - \left(\dot{\theta}_p \cos\psi_p \cos\psi + \dot{\psi}_p \sin\psi\right)\right] \\
&- \dot{\eta}_i \cos a_o \left(\dot{\theta}_p \cos\psi_p \cos\psi + \dot{\psi}_p \sin\psi \right) \\
&+ \ddot{X}_o \left(\cos\theta_p \sin\psi_p \sin\psi + \sin\theta_p \cos\psi \right) \\
&+ \dot{X}_o \left(\dot{\theta}_p \sin\theta_p \sin\psi_p \sin\psi - \dot{\psi}_p \cos\theta_p \cos\psi_p \sin\psi \right. \\
&\qquad\qquad - \dot{\psi} \cos\theta_p \sin\psi_p \cos\psi - \dot{\theta}_p \cos\theta_p \cos\psi \\
&\qquad\qquad \left. + \dot{\psi}_p \sin\theta_p \sin\psi \right) \\
&+ \ddot{Y}_o \cos\psi_p \sin\psi + \dot{Y}_o \left(\dot{\psi}_p \sin\psi_p \sin\psi + \dot{\psi} \cos\psi_p \cos\psi \right) \\
&+ \ddot{Z}_o \left(\cos\theta_p \cos\psi - \sin\theta_p \sin\psi_p \sin\psi \right) \\
&- \dot{Z}_o \left(\dot{\psi}_p \sin\theta_p \cos\psi_p \sin\psi + \dot{\theta}_p \cos\theta_p \sin\psi_p \sin\psi \right. \\
&\qquad\qquad + \dot{\psi} \sin\theta_p \sin\psi_p \cos\psi + \dot{\theta}_p \sin\theta_p \cos\psi \\
&\qquad\qquad \left. + \dot{\psi} \cos\theta_p \sin\psi \right)
\end{aligned}
$$

25

$$+ z_H \left(\ddot{\theta}_p \cos\psi_p \cos\psi - \dot{\theta}_p \dot{\psi}_p \sin\psi_p \cos\psi - \dot{\theta}_p \dot{\psi} \cos\psi_p \sin\psi \right.$$
$$\left. + \ddot{\psi}_p \sin\psi + \dot{\psi}_p \dot{\psi} \cos\psi \right)$$

$$+ \dot{\xi}_i \left(\dot{\theta}_p \sin\psi_p + \dot{\psi} \right) + \xi_i \left(\ddot{\theta}_p \sin\psi_p + \dot{\theta}_p \dot{\psi}_p \cos\psi_p \right)$$

$$- \ddot{\eta}_i \sin a_o$$

$$- \frac{1}{2r_i} \left(\eta_i^2 + \xi_i^2 \right) \sin a_o \left(\ddot{\theta}_p \cos\psi_p \cos\psi - \dot{\theta}_p \dot{\psi}_p \sin\psi_p \cos\psi \right.$$
$$- \dot{\theta}_p \dot{\psi} \cos\psi_p \sin\psi + \ddot{\psi}_p \sin\psi$$
$$\left. + \dot{\psi}_p \dot{\psi} \cos\psi \right)$$

$$- \frac{1}{r_i} \left(\eta_i \dot{\eta}_i + \xi_i \dot{\xi}_i \right) \sin a_o \left(\dot{\theta}_p \cos\psi_p \cos\psi + \dot{\psi}_p \sin\psi \right)$$

$$- \frac{1}{r_i} \left(\dot{\eta}_i^2 + \dot{\xi}_i^2 \right) \cos a_o$$

$$+ v_{iz} \left(\dot{\theta}_p \cos\psi_p \cos\psi - \dot{\psi}_p \sin\psi \right)$$

$$\left. - v_{iy} \left(\dot{\psi} + \dot{\theta}_p \sin\psi_p \right) \right\} \tag{54}$$

Equation 54 is the x component of Q_{Ij}, with blade mass un-
balance and blade torsional mass moment of inertia, assumed to
be zero. The hub motion coupling terms are those involving
X_0, Y_0, Z_0, θ_p, and ψ_p and their derivatives. The blade Coriolis
terms are those containing a_o and $\dot{\beta}$. (The blade flapping
acceleration terms, $\ddot{\beta}$, have been dropped because of the
orthogonality condition. In this formulation the rigid-body
flapping is considered to be the first normal mode.)

26

Q_{Ej}, the external force, has the following form:

$$
Q_{Ej} = \sum_i^{NS} \left\{ \left[\left(\phi_{i\eta j} + \bar{y}_i \cos\bar{\theta}_i \, \phi_{iej} \right) \cos a_o \right. \right.
$$

$$
- \frac{1}{r_i} \left(\phi_{i\eta j} \, \eta_i + \phi_{i\xi j} \, \xi_i \right) \sin a_o \left] \left[F_i - m_i g_Z \sin\theta_p \cos\psi_p \right. \right.
$$

$$
\left. - m_i g_Y \sin\psi_p \right] + \left[\left(\phi_{i\eta j} + \bar{y}_i \cos\bar{\theta}_i \, \phi_{i\theta j} \right) \sin a_o + \frac{1}{r_i} \left(\phi_{i\eta j} \, \eta_i \right. \right.
$$

$$
\left. + \phi_{i\xi j} \, \xi_i \right) \cos a_o \left] \left[f_i + m_i g_Z \left(\cos\theta_p \cos\psi - \sin\theta_p \sin\psi_p \sin\psi \right) \right] \right.
$$

$$
+ \left[\phi_{i\xi j} + \bar{y}_i \sin\bar{\theta}_i \, \phi_{i\theta j} \right] \left[H_i - m_i g_Z \left(\sin\theta_p \sin\psi_p \cos\psi \right. \right.
$$

$$
\left. \left. \left. + \cos\theta_p \sin\psi \right) \right] + Q_i \, \phi_{i\theta j} \right\} \qquad (55)
$$

in which

F_i, f_i and H_i	are components of the aerodynamic force in shaft coordinate system
Q_i	is aerodynamic pitching moments acting at the blade elements
g_Z and g_Y	are components of gravitational acceleration along coordinates of Z_F and $-Y_F$ respectively

(2) <u>Rigid-Body Coupling Considerations</u> - Application of the normal mode approach is complicated by the fact that the blade root boundary condition is variable, depending upon the loading of the blades. For example, the blade reaction to forces acting in the plane of the rotor depends upon whether the forces produce a net torque about the shaft. If a torque is produced, the shaft will rotate and the blade root constraint must be considered as being pinned. On the other hand, if the net torque is zero, then the blade root condition must be considered as being cantilevered. Similar reasoning can be applied to the out-of-plane response.

In this program the blade root boundary consideration is resolved by considering the blade response as being either polar symmetric or polar asymmetric about the shaft. This is essentially equivalent to the usual symmetric-asymmetric assumption applied to beams symmetrical about a center axis, e.g. elastic wing response about the longitudinal axis.

27

The polar symmetric motion is commonly referred to as collective motion of the blades; the polar asymmetric as cyclic motion. Figure 8 illustrates this definition of collective and cyclic modes. These names arise from the blade elastic response to collective and cyclic pitch respectively. It can be shown that any rotor type, rigid (hingeless) gimballed or teetering semi-rigid, or fully articulated will respond to external excitation in a combination of collective and cyclic motion, depending upon the nature of the excitation.

For the collective modes the normal mode representation is simple. One normal mode is used to represent each collective mode. For a three bladed rotor the collective mode normal mode equation is written as

$$\ddot{\zeta}_j + 2\tau\omega_j\dot{\zeta}_j + \omega_j^2\zeta_j = \frac{1}{3m_{ej}}\left\{\sum_{bl=1}^{3}\left(Q_{Ej} + Q_{Ij}\right)\right\} \tag{56}$$

The normal coordinate for each individual blade is then given as

$$\zeta_1 = \zeta_2 = \zeta_3 = \zeta_{j_{collective}} \tag{57}$$

A more complex relationship exists for the cyclic modes. In that case, the two normal modes, having the same natural frequency and mode shape, must be used to represent the cyclic response of the three blades. This follows the same reasoning as employed for the rigid-body flapping and is illustrated in Figure 9.

If the modes are designated mode a and mode b, the normal mode equation for a cyclic mode becomes

$$\frac{3}{2}\left(\ddot{\zeta}_{ka} + 2\tau\,\omega_k\,\dot{\zeta}_{ka} + \omega_k^2\,\zeta_{ka}\right)$$

$$= \frac{1}{m_{ek}}\left[Q_{Ik1} + Q_{Ek1} - \frac{1}{2}\left(Q_{Ik2} + Q_{Ek2}\right) - \frac{1}{2}\left(Q_{Ik3} + Q_{Ek3}\right)\right] \tag{58}$$

and

$$\frac{3}{2}\left(\ddot{\zeta}_{kb} + 2\tau\,\omega_k\,\dot{\zeta}_{kb} + \omega_k^2\,\zeta_{kb}\right)$$

$$= \frac{1}{m_{ek}}\left[\frac{\sqrt{3}}{2}\left(Q_{Ik2} + Q_{Ek2}\right) - \frac{\sqrt{3}}{2}\left(Q_{Ik3} + Q_{Ek3}\right)\right] \tag{59}$$

28
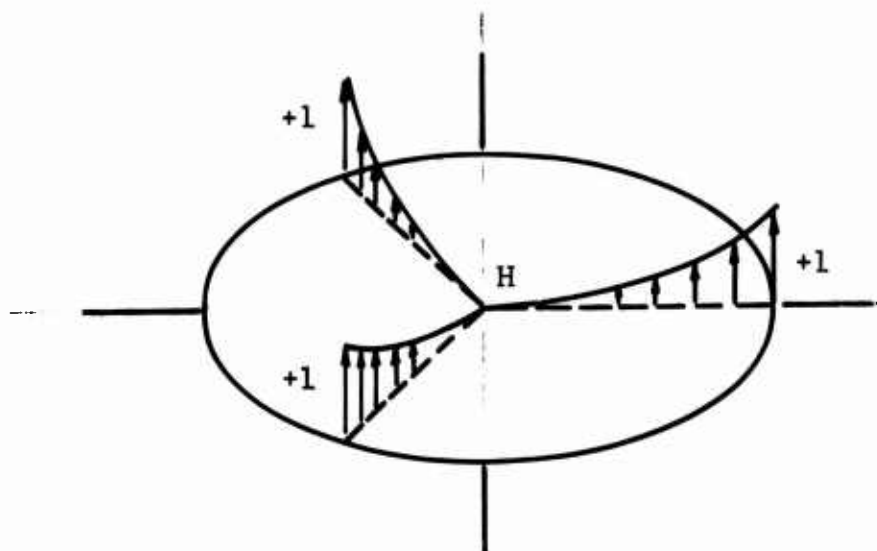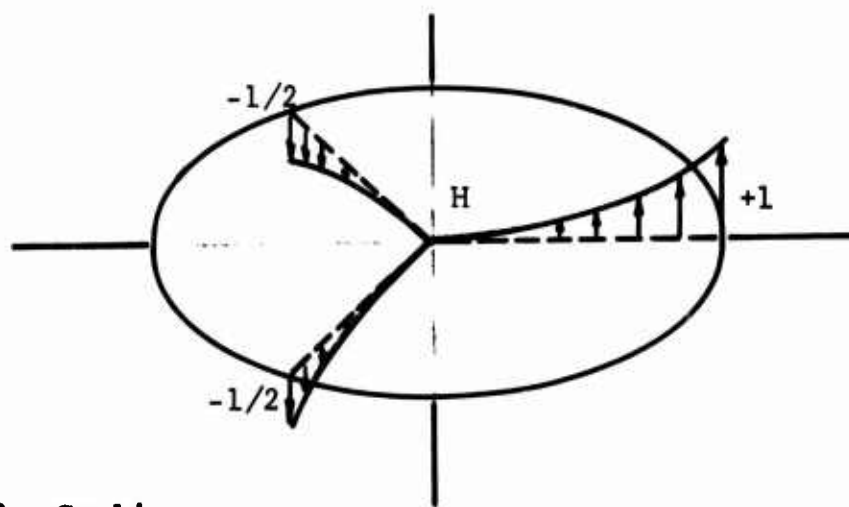
(a) Collective

(b) Cyclic

Figure 8. Collective and Cyclic Modes.
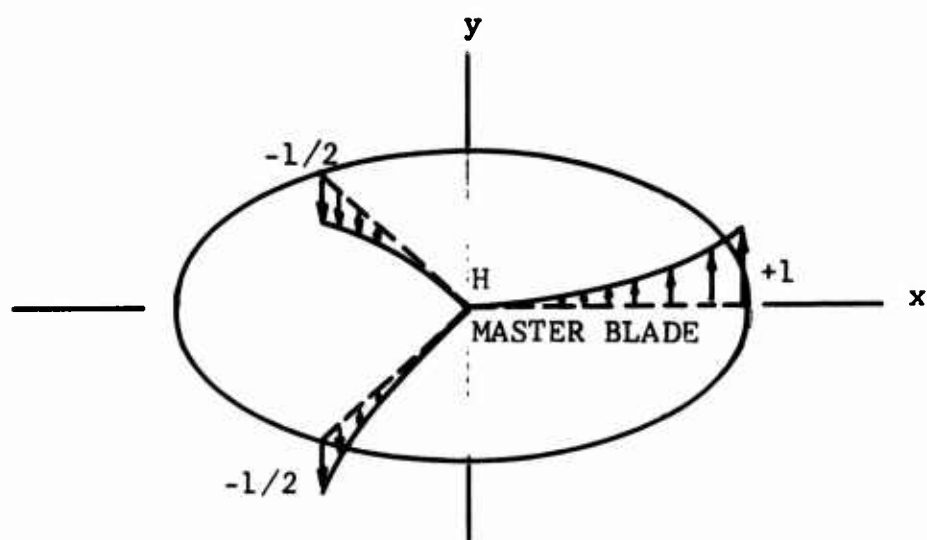
(a) About y Axis
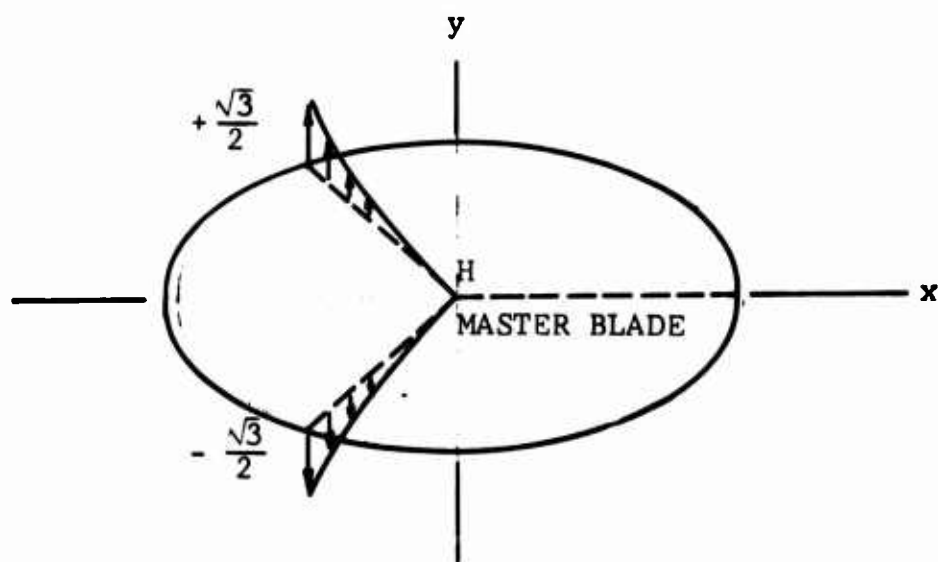
(b) About x Axis

Figure 9. Components of Cyclic Mode for a Three-
Bladed Rotor.

The normal coordinates for each blade are then given as

$$\zeta_{k1} = \zeta_{ka} \tag{60}$$

$$\zeta_{k2} = -\frac{1}{2}\zeta_{ka} + \frac{\sqrt{3}}{2}\zeta_{kb} \tag{61}$$

$$\zeta_{k3} = -\frac{1}{2}\zeta_{ka} - \frac{\sqrt{3}}{2}\zeta_{kb} \tag{62}$$

Table I gives the boundary conditions which must be used to determine the collective and cyclic modes for the Feather-Stop Analysis. Note that if the analysis is being used to simulate blade folding individual blade modes are employed.

TABLE I. BLADE BOUNDARY CONDITION REQUIREMENTS				
	Collective		Cyclic	
Rotor Type	Vertical	Inplane	Vertical	Inplane
Fully Articulated[*],[+]	P	P	P	P
Offset Flapping Hinge[*]	P	P	P	C
Gimballed	C	P	P	C
Hingeless	C	P	C	C
Blade Folding	C	C	C	C
P - Pinned C - Cantilevered				
[*] - The first normal mode is rigid-body flapping.				
[+] - The blade lead-lag motion must be represented using a normal mode.				

c. Proprotor Aerodynamics

Two dimensional, quasi-steady strip theory is used to calculate the airloads acting on the blades.[10] Each blade is divided into strips centered on a mass point, as illustrated in Figure 10. Up to ten strips may be used. The width, chord, chordwise location of the aerodynamic center, and the built-in twist is specified for each individual strip.

The local velocities at a blade element, i, are first determined by adding the free-stream and induced velocity to the mass point velocity vector, $-\vec{v}_i$ (equation 21). If σ_i represents the induced velocity perpendicular to the tip path plane, and $\vec{U}$ the free stream velocity, the total velocity at a mass point on a blade can be written as

31
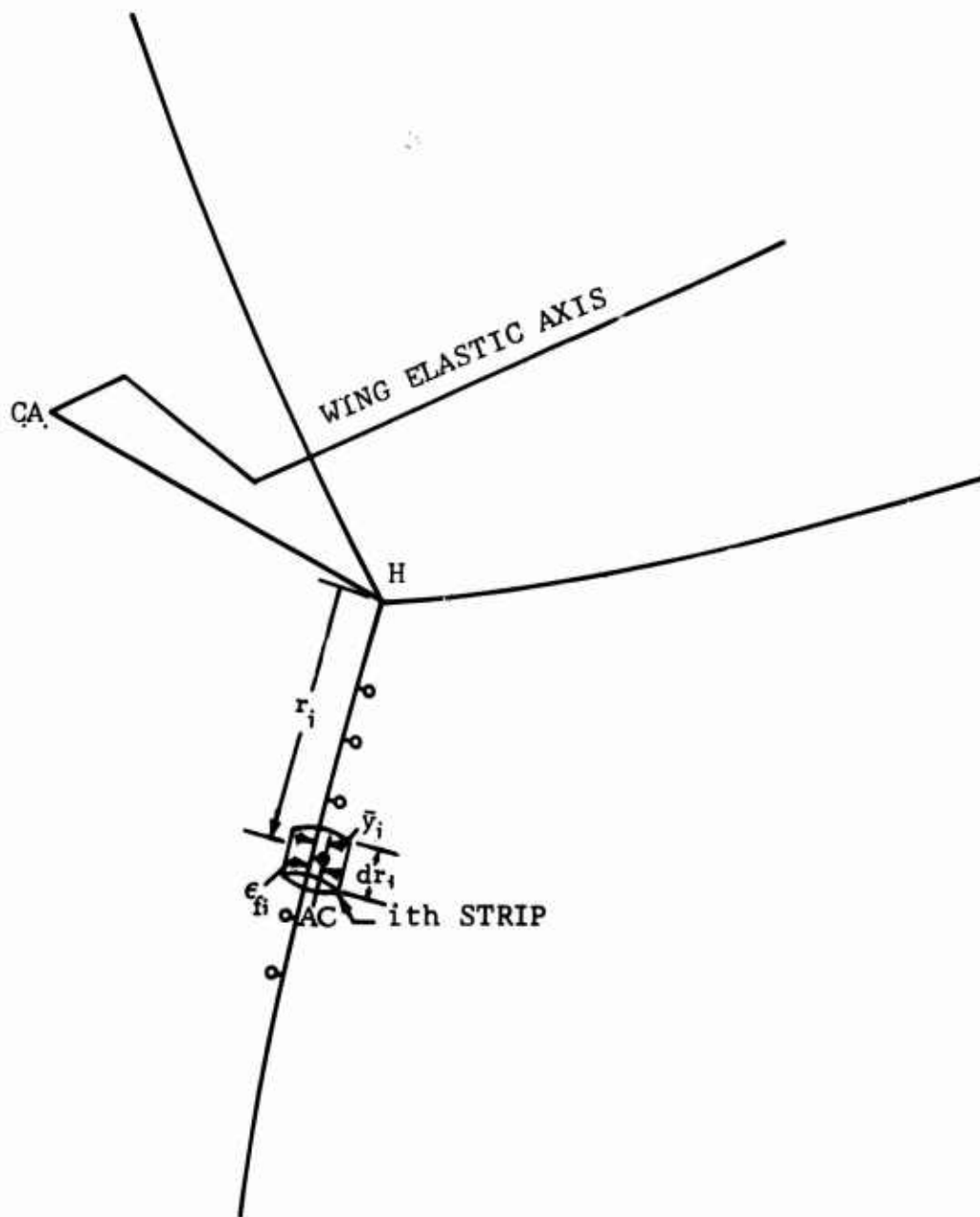
Figure 10.   Blade Aerodynamic Strip Relationships.

$$\vec{v}_i = - v_{ix}\,\hat{e}_5 - v_{iy}\,\hat{e}_6 - v_{iz}\,\hat{e}_3 - U\,\hat{E}_1$$

$$- \sigma_i \cos a_o\,\hat{e}_8 - v_i \sin a_o\,\hat{e}_7 \tag{63}$$

where a_o is the rotor precone.

The radial tangential and vertical components of the total velocity can then be obtained by forming dot products of $\vec{v}_i$ with unit vectors $\hat{e}_7$, $-\hat{e}_6$, and $\hat{e}_8$, respectively. However, the radial flow will be neglected. The other two components take the following forms:

$$
\begin{aligned}
v_{Ti} =\ & \dot{X}_o\left(\sin\theta_p\,\sin\psi - \cos\theta_p\,\sin\psi_p\,\cos\psi\right) + \dot{Y}_o\,\cos\psi_p\,\cos\psi \\[4pt]
& + \dot{Z}_o\left(\sin\theta_p\,\sin\psi_p\,\cos\psi + \cos\theta_p\,\sin\psi\right) \\[4pt]
& - z_H\left(\dot{\theta}_p\,\cos\psi_p\,\sin\psi - \dot{\psi}_p\,\cos\psi\right) \\[4pt]
& + r_i\left[\left(\dot{\theta}_p\,\sin\psi_p + \dot{\psi}\right)\cos\beta - \left(\dot{\theta}_p\,\cos\psi_p\,\sin\psi - \dot{\psi}_p\,\cos\psi\right)\sin\beta\right] \\[4pt]
& - \bar{y}_i\left[\dot{\bar{\theta}}_i + \left(\dot{\theta}_p\,\sin\psi_p + \dot{\psi}\right)\sin\beta + \left(\dot{\theta}_p\,\cos\psi_p\,\sin\psi - \dot{\psi}_p\,\cos\psi\right)\cos\beta\right]\sin\bar{\theta}_i \\[4pt]
& + \varepsilon_{ci}\,\dot{\bar{\theta}}_i\,\sin\bar{\theta}_i + U\left(\sin\theta_p\,\sin\psi - \cos\theta_p\,\sin\psi_p\,\cos\psi\right) \\[4pt]
& - \eta_i\left[\left(\dot{\theta}_p\,\sin\psi_p + \dot{\psi}\right)\sin a_o + \left(\dot{\theta}_p\,\cos\psi_p\,\sin\psi - \dot{\psi}_p\,\cos\psi\right)\cos a_o\right] - \dot{\xi}_i \\[4pt]
& + \frac{1}{2r_i}\left(\eta_i{}^2 + \xi_i{}^2\right)\left[\left(\dot{\theta}_p\,\cos\psi_p\,\sin\psi - \dot{\psi}_p\,\cos\psi\right)\sin a_o\right. \\[4pt]
& \left. - \left(\dot{\theta}_p\,\sin\psi_p + \dot{\psi}\right)\cos a_o\right] \tag{64}
\end{aligned}
$$

$$v_{Pi} = -\dot{X}_0\left[\sin\theta_p \cos\psi \sin\beta + \cos\theta_p\left(\cos\psi_p \cos\beta + \sin\psi_p \sin\psi \sin\beta\right)\right.$$

$$+ \dot{Y}_0\left(\cos\psi_p \sin\psi \sin\beta - \sin\psi_p \cos\beta\right)$$

$$- \dot{Z}_0\left[\cos\theta_p \cos\psi \sin\beta - \sin\theta_p\left(\cos\psi_p \cos\beta + \sin\psi_p \sin\psi \sin\beta\right)\right]$$

$$+ z_H\left(\dot{\theta}_p \cos\psi_p \cos\psi \sin\beta + \dot{\psi}_p \sin\psi \sin\beta\right)$$

$$- r_i\left(\dot{\beta} - \dot{\theta}_p \cos\psi_p \cos\psi - \dot{\psi}_p \sin\psi\right)$$

$$- \bar{y}_i \,\theta_p \cos\bar{\theta}_i\left(\sin\psi_p \sin\beta + \cos\psi_p \sin\psi \cos\beta\right)$$

$$- \bar{y}_i \cos\bar{\theta}_i\left(\dot{\bar{\theta}}_i - \dot{\psi}_p \cos\psi \cos\beta + \dot{\psi} \sin\beta\right) + \varepsilon_{ci}\,\dot{\bar{\theta}}_i \cos\bar{\theta}_i$$

$$- U\left[\sin\theta_p \cos\psi \sin\beta + \cos\theta_p\left(\cos\psi_p \cos\beta + \sin\psi_p \sin\psi \sin\beta\right)\right]$$

$$- \sigma_i \cos a_0 + \left[\xi_i \cos a_0\left(\dot{\theta}_p \cos\psi_p \sin\psi - \dot{\psi}_p \cos\psi\right)\right.$$

$$+ \xi_i \sin a_0\left(\dot{\theta}_p \sin\psi_p + \dot{\psi}\right) - \dot{\eta}_i$$

$$\left. - \frac{1}{2r_i}\left(\eta_i^2 + \xi_i^2\right)\left(\dot{\theta}_p \cos\psi_p \cos\psi + \dot{\psi}_p \sin\psi \cos\beta - a_0\right)\right] \tag{65}$$

in which ε_{ci} is the distance from the blade quarter chord to its center of gravity, positive if center of gravity is on the leading edge side. The terms containing ε_{ci} are the components of the relative velocity between the center of gravity and the quarter chord.

The strip total velocity, inflow angle, and Mach number are then obtained from the following relationships:

$$V_i = \left(v_{Ti}^2 + v_{Pi}^2\right)^{1/2} \tag{66}$$

$$\phi_i = \tan^{-1}\frac{v_{Pi}}{v_{Ti}} \tag{67}$$

$$M_i = \frac{V_i}{S} \tag{68}$$

where S is the speed of sound.

34

The strip angle of attack is then calculated as

$$\alpha_i = \bar{\theta}_i + \phi_i \qquad (69)$$

where

$$\bar{\theta}_i = \theta_c - A_1 \cos\psi - B_1 \sin\psi + \theta_{Ti} + \theta_{if} - \left(\beta - a_o\right)\tan\delta_3 \qquad (70)$$

in which

θ_c	is blade root collective pitch angle
A_1	is the lateral cyclic
B_1	is the longitudinal cyclic
θ_{Ti}	is the blade built-in twist
θ_{if}	is the blade flexible pitching deflection
δ_3	is the negative pitch-flap coupling

The aerodynamic lift, drag, and pitching moment at the quarter chord of the strip are then given by

$$dL_i = \frac{1}{2} C_L \rho c_i V_i^2 \left(dr_i\right) \qquad (71)$$

$$dD_i = \frac{1}{2} C_D \rho c_i V_i^2 \left(dr_i\right) \qquad (72)$$

$$dM_i = \frac{1}{2} C_M \rho c_i^2 V_i^2 \left(dr_i\right) \qquad (73)$$

where

c_i	is the blade chord
dr_i	is the segment length
C_L	is the lift coefficient for the strip
C_D	is the drag coefficient for the strip
C_M	is the pitching moment coefficient for the strip

The lift, drag, and pitching moment coefficients for the strip are obtained from tabular forms, where the coefficients are given versus angle of attack and Mach number. Figure 11 is an example of the tabular form employed in the computer program. Note that reverse flow and stall are accounted for in the tables.

LIFT TABLE

MACH NUMBERS 11, ANGLES OF ATTACK 33

ANGLES OF ATTACK	MACH NUMBERS										
	0.0	0.30000	0.40000	0.50000	0.60000	0.66300	0.71000	0.76000	0.82000	0.85000	1.30000
-180.0	0.0	0.0	0.0	0.0	0.0	0.0	0.0	0.0	0.0	0.0	0.0
-10.0	-0.76700	-0.76700	-0.74100	-0.70600	-0.49500	-0.99000	-0.87000	0.0	0.0	0.0	0.0
-9.0	-0.75000	-0.75000	-0.72000	-0.70500	-0.64000	-0.86500	-0.85000	-0.80000	0.0	0.0	0.0
-8.0	-0.70800	-0.70800	-0.70800	-0.70000	-0.72000	-0.83300	-0.91830	-0.77200	-0.71000	-0.55000	0.0
-7.0	-0.65000	-0.65000	-0.65000	-0.69000	-0.70000	-0.76500	-0.74000	-0.68000	-0.65500	-0.49500	0.0
-6.0	-0.55900	-0.55900	-0.58900	-0.58700	-0.62600	-0.65500	-0.65900	-0.59500	-0.58500	-0.44000	0.0
-5.0	-0.45000	-0.45000	-0.47000	-0.50000	-0.54000	-0.54000	-0.55300	-0.51000	-0.48000	-0.37000	0.0
-4.0	-0.34300	-0.34300	-0.35700	-0.38000	-0.40500	-0.41400	-0.42500	-0.39600	-0.37500	-0.31300	0.0
-3.0	-0.25000	-0.25000	-0.24000	-0.27000	-0.27000	-0.28000	-0.33000	-0.28000	-0.26500	-0.24000	0.0
-2.0	-0.12300	-0.12300	-0.12500	-0.13200	-0.14600	-0.15500	-0.14300	-0.14430	-0.16000	-0.15500	0.0
-1.0	-0.03000	-0.03000	-0.01000	-0.03000	-0.03100	-0.03200	-0.10000	-0.04000	-0.06000	-0.06000	0.0
0.0	0.07800	0.07800	0.08500	0.08900	0.09300	0.09900	0.03900	0.07200	0.05900	0.05000	0.0
1.0	0.18000	0.18000	0.21000	0.21300	0.23300	0.24000	0.23300	0.20500	0.18000	0.13000	0.0
2.0	0.30900	0.30900	0.31800	0.33800	0.36300	0.36500	0.36200	0.31500	0.27000	0.22800	0.0
3.0	0.40000	0.40000	0.43300	0.46700	0.50200	0.48500	0.46000	0.42530	0.38000	0.31500	0.0
4.0	0.52300	0.52300	0.55100	0.58300	0.62700	0.62300	0.60400	0.53700	0.48500	0.41000	0.0
5.0	0.62000	0.62000	0.66500	0.68000	0.73500	0.73000	0.70000	0.62000	0.59530	0.50000	0.0
6.0	0.73500	0.73500	0.78130	0.82500	0.88300	0.87400	0.79700	0.70933	0.66000	0.60000	0.0
7.0	0.83000	0.83000	0.88500	0.92000	0.96000	0.94000	0.87200	0.76000	0.74000	0.69000	0.0
8.0	0.95600	0.95600	1.01200	1.02000	1.05400	1.00500	0.94800	0.82000	0.81000	0.78000	0.0
9.0	1.05000	1.05000	1.08800	1.08300	1.11000	1.05300	1.01000	0.89900	0.88000	0.88000	0.0
10.0	1.15900	1.15900	1.12500	1.09500	1.16700	1.18500	1.05700	0.89900	0.93000	0.96300	0.0
11.0	1.23600	1.23600	1.11000	1.04800	1.09500	1.06000	1.13500	0.0	0.0	0.0	0.0
12.0	1.25400	1.25400	1.08600	1.00600	1.04400	1.34600	1.14200	0.0	0.0	0.0	0.0
13.0	1.15000	1.15000	1.04000	0.96000	0.99000	1.02500	1.13000	0.0	0.0	0.0	0.0
14.0	0.94500	0.94500	0.97700	0.91000	0.95800	1.06600	1.04500	0.0	0.0	0.0	0.0
15.0	0.84000	0.84000	0.89000	0.0	0.0	0.0	0.0	0.0	0.0	0.0	0.0
16.0	0.80000	0.80000	0.80300	0.0	0.0	0.0	0.0	0.0	0.0	0.0	0.0
17.0	0.78000	0.78000	0.0	0.0	0.0	0.0	0.0	0.0	0.0	0.0	0.0
18.0	0.78000	0.78000	0.0	0.0	0.0	0.0	0.0	0.0	0.0	0.0	0.0
19.0	0.78200	0.78200	0.0	0.0	0.0	0.0	0.0	0.0	0.0	0.0	0.0
20.0	0.78600	0.78600	0.0	0.0	0.0	0.0	0.0	0.0	0.0	0.0	0.0
180.0	0.0	0.0	0.0	0.0	0.0	0.0	0.0	0.0	0.0	0.0	0.0

DRAG TABLE

MACH NUMBERS 11, ANGLES OF ATTACK 33

ANGLES OF ATTACK	MACH NUMBERS										
	0.0	0.30000	0.40000	0.50000	0.60000	0.66000	0.71000	0.76000	0.82000	0.85000	1.00000
-180.0	0.0	0.0	0.0	0.0	0.0	0.0	0.0	0.0	0.0	0.0	0.0
-10.0	0.13200	0.13200	0.13200	0.13500	0.15300	0.18400	0.23100	0.0	0.0	0.0	0.0
-9.0	0.10100	0.10100	0.10000	0.10500	0.11200	0.12800	0.17300	0.23230	0.0	0.0	0.0
-8.0	0.05900	0.05900	0.06800	0.08000	0.05800	0.06600	0.09800	0.14300	0.23000	0.25900	0.0
-7.0	0.03200	0.03200	0.04000	0.05300	0.05000	0.04700	0.07000	0.10700	0.19600	0.23200	0.0
-6.0	0.01000	0.01000	0.01200	0.02100	0.02200	0.02800	0.04100	0.06600	0.17000	0.20800	0.0
-5.0	0.01000	0.01000	0.01000	0.01600	0.01300	0.01300	0.01400	0.03730	0.13530	0.19300	0.0
-4.0	0.01000	0.01000	0.00900	0.00900	0.00800	0.01000	0.01100	0.01400	0.11830	0.17700	0.0
-3.0	0.00900	0.00900	0.00800	0.00800	0.00700	0.00900	0.00900	0.01000	0.10530	0.16300	0.0
-2.0	0.00800	0.00800	0.00800	0.00800	0.00700	0.00700	0.00800	0.00930	0.09730	0.14500	0.0
-1.0	0.00700	0.00700	0.00700	0.00700	0.00600	0.00600	0.00700	0.01050	0.09530	0.14900	0.0
0.0	0.00600	0.00600	0.00600	0.00600	0.00600	0.00600	0.00600	0.01300	0.09100	0.14900	0.0
1.0	0.00600	0.00600	0.00600	0.00600	0.00600	0.00700	0.00700	0.01930	0.10050	0.16300	0.0
2.0	0.00600	0.00600	0.00600	0.00600	0.00700	0.00600	0.00800	0.03900	0.12800	0.17500	0.0
3.0	0.00800	0.00800	0.00700	0.00700	0.00600	0.00600	0.01000	0.05800	0.15200	0.19500	0.0
4.0	0.00900	0.00900	0.00800	0.00800	0.00800	0.00700	0.01600	0.06000	0.17500	0.21800	0.0
5.0	0.01000	0.01000	0.00800	0.00900	0.01000	0.01000	0.02330	0.08500	0.19800	0.23500	0.0
6.0	0.01000	0.01000	0.01000	0.01000	0.01130	0.01300	0.03500	0.09500	0.21500	0.25300	0.0
7.0	0.01100	0.01100	0.01200	0.01500	0.01900	0.02000	0.03900	0.13900	0.23800	0.27500	0.0
8.0	0.01300	0.01300	0.01300	0.01900	0.02700	0.03500	0.06800	0.16800	0.26100	0.29900	0.0
9.0	0.01400	0.01400	0.01800	0.03500	0.04800	0.06400	0.13100	0.20030	0.28700	0.31600	0.0
10.0	0.01700	0.01700	0.03600	0.06000	0.05800	0.09300	0.16100	0.23000	0.30900	0.33900	0.0
11.0	0.02300	0.02300	0.11000	0.09800	0.12300	0.13500	0.20500	0.0	0.0	0.0	0.0
12.0	0.03400	0.03400	0.13200	0.13400	0.16800	0.16700	0.22400	0.0	0.0	0.0	0.0
13.0	0.13700	0.13700	0.16600	0.19100	0.20000	0.19500	0.24300	0.0	0.0	0.0	0.0
14.0	0.21100	0.21100	0.21100	0.21800	0.22900	0.23500	0.26600	0.0	0.0	0.0	0.0
15.0	0.23000	0.23000	0.24500	0.0	0.0	0.0	0.0	0.0	0.0	0.0	0.0
16.0	0.24800	0.24800	0.25300	0.0	0.0	0.0	0.0	0.0	0.0	0.0	0.0
17.0	0.27300	0.27300	0.0	0.0	0.0	0.0	0.0	0.0	0.0	0.0	0.0
18.0	0.28500	0.28500	0.0	0.0	0.0	0.0	0.0	0.0	0.0	0.0	0.0
19.0	0.29000	0.29000	0.0	0.0	0.0	0.0	0.0	0.0	0.0	0.0	0.0
20.0	0.32000	0.32000	0.0	0.0	0.0	0.0	0.0	0.0	0.0	0.0	0.0
180.0	0.0	0.0	0.0	0.0	0.0	0.0	0.0	0.0	0.0	0.0	0.0

Figure 11.   Tabular Form of Aerodynamic Coefficients.

The pitch damping of the strip is approximated using an approximation which includes the effect of stall.[11] The pitch damping moment is given by

$$dM_i' = C_{\dot{\alpha}i} \, \dot{\alpha}_i \tag{74}$$

where $\dot{\alpha}_i$ is the rate of change of the strip angle of attack and $C_{\dot{\alpha}i}$ is a coefficient obtained from the table shown in Figure 12. Note the $C_{\dot{\alpha}i}$ is a function of the strip angle of attack α_i, and a reduced velocity K_i, defined as

$$K_i = \frac{2V_i}{\omega_\theta C_i} \tag{75}$$

where ω_θ is the frequency of a selected torsional mode of the blade; usually the fundamental torsional mode.

The strip thrust, inplane, and radial forces and pitching moment, in the blade rotating coordinate system x, y, z are then given as

$$F_i = \left(dL_i \cos\phi_i + dD_i \sin\phi_i\right)\cos\beta \tag{76}$$

$$H_i = \left(-dL_i \sin\phi_i + dD_i \cos\phi_i\right) \tag{77}$$

$$f_i = \left(dL_i \cos\phi_i + dD_i \sin\phi_i\right)\sin\beta \tag{78}$$

$$dQ_i = dM_i + dM_i' + \varepsilon_{ei}\left(dL_i \cos\alpha_i + dD_i \sin\alpha_i\right) \tag{79}$$

where ε_{ei} is the distance from the blade aerodynamic center to the blade elastic axis. Positive if aerodynamic center is ahead of the elastic axis.

3. Wing-Pylon-Hub Equations of Motion

a. Dynamics

The normal mode method is again used to simulate the wing-pylon-hub dynamics. As with the blade elastic equations, this greatly simplifies the development of the equations of motion.

Figure 13 shows the math model for the wing-pylon-hub system. The wing is represented by lumped masses located spanwise along the wing and having inertia and unbalance properties. Beamwise, chordwise, and torsional deflections of the wing are accounted for, as well as pylon pitching and yawing with respect to the wing.

37
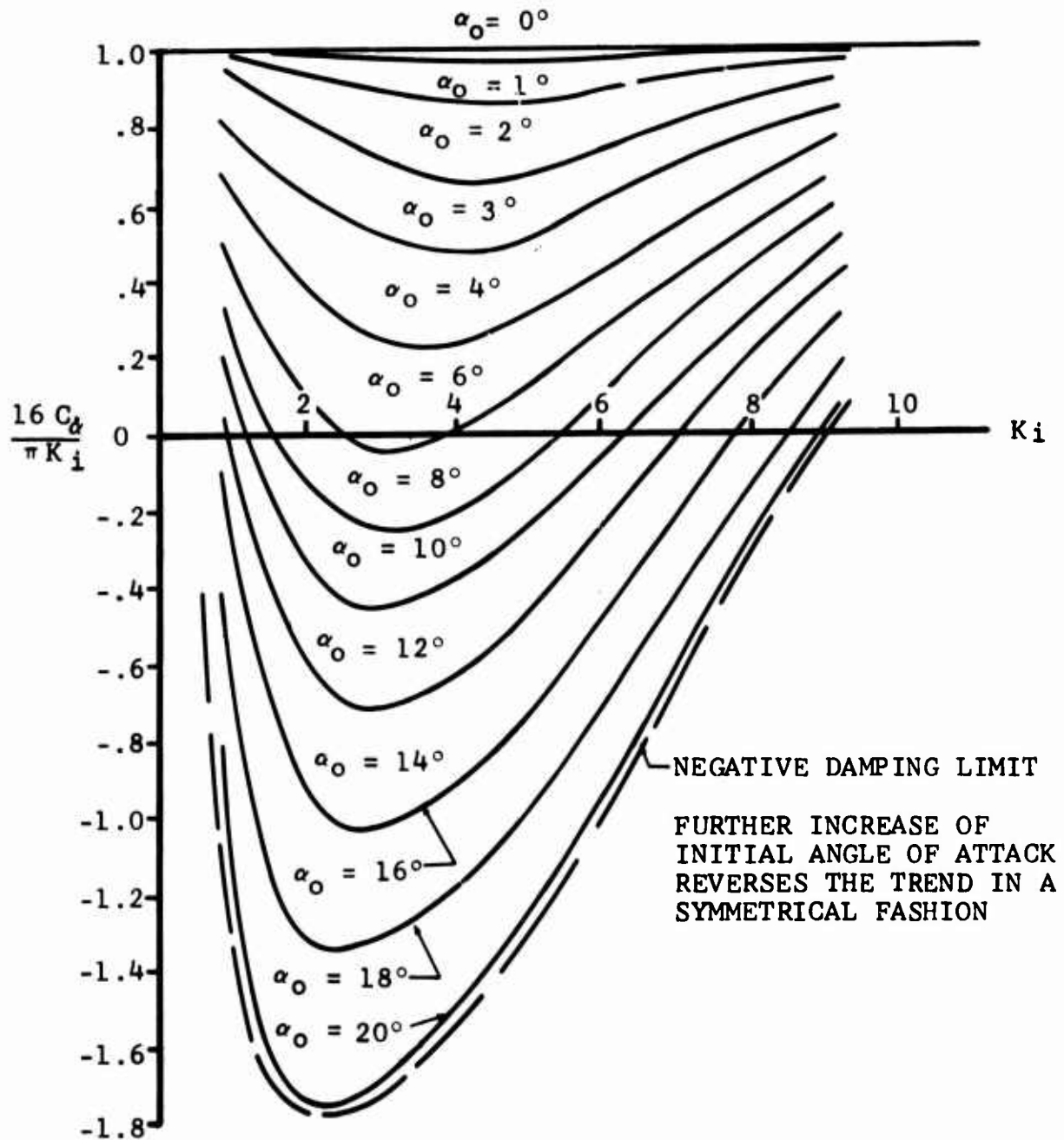
Figure 12.   Blade Pitch Damping Approximation.
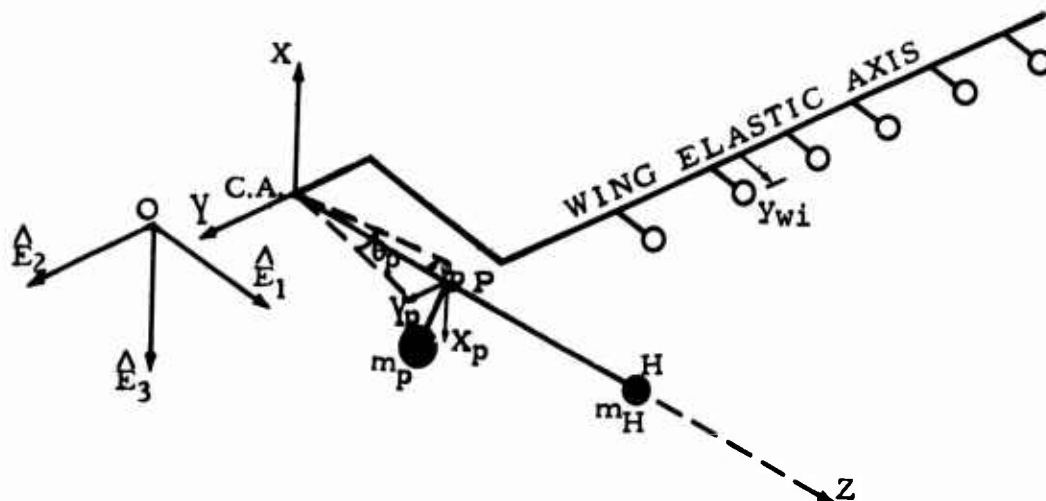
NOTES:

The distance from the pylon conversion axis to the pylon center of gravity is defined as Z_p. The signs of eccentricities, X_p, Y_p, as well as Z_p, are determined in the XYZ coordinate system. The distance from the pylon conversion axis to the hub is defined as z_H.

Figure 13.   Math Model for Wing-Pylon-Hub System.

39

The pylon is considered to be inelastic with the pylon center of gravity located a distance z_p along the shaft axis from the conversion axis, and with eccentricities X_p and Y_p from the shaft. The hub is treated as a point mass located on the shaft centerline, a distance z_H from the conversion axis.

By using the normal mode approach only one derivation is required, the generalized forces for the normal modes. These generalized forces consist of the wing airloads, gravitational forces, and the proprotor aerodynamic gravitational and inertial forces and moments acting at the hub.

By definition the generalized force for the jth normal mode is

$$Q_j = \sum_i \vec{F_i} \cdot \frac{\partial \vec{R_i}}{\partial \zeta_j} \tag{45}$$

where $\vec{F_i}$ is the external force acting at the ith element.

The external force applied at the ith segment on the wing is

$$\vec{F}_{wi} = -H_{wi}\hat{E}_1 + Q_{wi}\hat{E}_2 - (T_{wi} - m_{wi}g_Z)\hat{E}_3 - m_{wi}g_Y\hat{E}_2 \tag{80}$$

in which

T_{wi} is the lift force

H_{wi} is the drag force

Q_{wi} is the pitching moment

g_Z and g_Y are components of gravitational acceleration

m_{wi} is the wing discrete mass

The external force applied on the pylon is

$$\vec{F}_p = m_p g_Z \hat{E}_3 - m_p g_Y \hat{E}_2 \tag{81}$$

where m_p is the pylon mass.

The external force applied on the pylon tip is

$$\vec{F}_H = -TFF_X \hat{e}_2 + TFF_Y \hat{e}_4 + TFF_Z \hat{e}_3 - TFM_X \hat{e}_2$$

$$+ TFM_Y \hat{e}_4 + TFM_Z \hat{e}_3 + m_H g_Z \hat{E}_3 - m_H g_Y \hat{E}_2 \tag{82}$$

40

$$TFF_X = FF_X + W_X + F_x \cos\psi - F_y \sin\psi \tag{83}$$

$$TFF_Y = FF_Y + W_Y + F_x \sin\psi + F_y \cos\psi \tag{84}$$

$$TFF_Z = FF_Z + W_Z + F_z \tag{85}$$

$$TFM_X = \left(N_x + M_x\right)\cos\psi - \left(N_y + M_y\right)\sin\psi \tag{86}$$

$$TFM_Y = \left(N_x + M_x\right)\sin\psi + \left(N_y + M_y\right)\cos\psi \tag{87}$$

$$TFM_Z = N_z + M_z \tag{88}$$

in which

FF_X, FF_Y, FF_Z	are airloads
W_X, W_Y, W_Z	are gravitational forces
F_x, F_y, F_z	are inertial forces
N_x, N_y, N_z	are aerodynamic and gravitational moments
M_x, M_y, M_z	are inertial moments

The position vectors for the wing, pylon, and hub are given as

$$\vec{R}_{wi} = -r_{wi}\,\hat{E}_2 + \xi_{wi}\,\hat{E}_1 + \eta_{wi}\,\hat{E}_3 + y_{wi}\,\hat{e}_{11} \tag{89}$$

$$\vec{R}_p = \left(X_0 + Z_p \cos\psi_p \cos\theta_p - X_p \sin\theta_p - Y_p \sin\psi_p \cos\theta_p\right)\hat{E}_1$$

$$+ \left(Y_0 + Z_p \sin\psi_p + Y_p \cos\psi_p\right)\hat{E}_2$$

$$+ \left(Z_0 - Z_p \cos\psi_p \sin\theta_p - X_p \cos\theta_p + Y_p \sin\psi_p \sin\theta_p\right)\hat{E}_3 \tag{90}$$

41

$$\vec{R}_H = \left(X_0 + z_H \cos\psi_p \cos\theta_P \right)\hat{E}_1$$

$$+ \left(Y_0 + z_H \sin\psi_p \right)\hat{E}_2$$

$$+ \left(Z_0 - z_H \cos\psi_p \sin\theta_p \right)\hat{E}_3 \qquad (91)$$

where

X_0, Y_0, and Z_0 give the position of the conversion axis-shaft axis intersection

θ_p equals $\theta_{pc} + \theta_{pp}$ with θ_{pp} as the pitch due to wing torsional deflections

The generalized coordinates are now replaced by the orthonormal mode shapes

$$X_0 = \sum \phi_{XAn} q_n$$

$$Y_0 = \sum \phi_{YAn} q_n$$

$$Z_0 = \sum \phi_{ZAn} q_n$$

$$\psi_p = \sum \phi_{\psi An} q_n \qquad (92)$$

$$\theta_{pp} = \sum \phi_{\theta An} q_n$$

$$\eta_{wi} = \sum \phi_{Zin} q_n$$

$$\xi_{wi} = \sum \phi_{Xin} q_n$$

$$\theta_{wi} = \sum \phi_{\theta in} q_n$$

in which

ϕ_{XAn} is the X_F component of nth coupled mode at the CA

42

ϕ_{Xin} is the X_F component of the nth coupled mode at the ith segment on the wing

q_n is the nth normal coordinate

By the same token as to derive equation 52, the equations of motion for the wing-pylon-hub system can be written as

$$\ddot{q}_j + 2\tau\omega_j\dot{q}_j + \omega_j^2 q_j = \frac{1}{M_{ej}} Q_j \tag{93}$$

The generalized force, Q_j, has the following form

$$Q_j = \sum_i^w \left[Q_{wi}\phi_{\theta ij} - H_{wi}\phi_{Xij} - T_{wi}\phi_{Zij} \right.$$

$$\left. + m_{wi}\, g_Z\left(\phi_{Zij} - y_{wi}\cos\alpha_w\,\phi_{\theta ij}\right) \right]$$

$$+ m_p\, g_Z\left[\phi_{ZAj} - \left(Z_p\cos\theta_{pc} - X_p\sin\theta_{pc}\right)\phi_{\theta Aj} - Y_p\sin\theta_{pc}\,\phi_{\psi Aj}\right]$$

$$- m_p\, g_Y\left(Z_p\,\phi_{\psi Aj} + \phi_{YAj}\right)$$

$$+ TFF_X\left(z_H\,\phi_{\theta Aj} - \phi_{XAj}\sin\theta_{pc} - \phi_{ZAj}\cos\theta_{pc}\right)$$

$$+ \left(TFF_Y - m_H g_Y\right)\left(\phi_{YAj} + z_H\,\phi_{\psi Aj}\right)$$

$$+ TFF_Z\left(\phi_{XAj}\cos\theta_{pc} - \phi_{ZAj}\sin\theta_{pc}\right) - TFM_X\,\phi_{\psi Aj} + TFM_Y\,\phi_{\theta Aj}$$

$$+ m_H\, g_Z\left(\phi_{ZAj} - z_H\,\phi_{\theta Aj}\cos\theta_{pc}\right)$$

$$- \left[TFF_X\left(\phi_{XAj}\cos\theta_{pc} - \phi_{ZAj}\sin\theta_{pc}\right) \right.$$

$$- TFF_Z\left(z_H\,\phi_{\theta Aj} - \phi_{ZAj}\cos\theta_{pc} - \phi_{XAj}\sin\theta_{pc}\right)$$

$$\left. + TFM_Z\,\phi_{\psi Aj}\right] \Sigma\phi_{\theta An}\, q_n$$

43

$$- \left[\text{TFF}_Y \left(\phi_{XAj} \cos\theta_{pc} - \phi_{ZAj} \sin\theta_{pc} \right) \right.$$

$$\left. - \text{TFF}_Z \left(z_H \phi_{\psi Aj} + \phi_{YAj} \right) - \text{TFM}_Z \phi_{\theta Aj} \right] \Sigma \phi_{\psi An} q_n \quad (94)$$

The generalized mass, M_{ej}, may be obtained directly from the vibration analysis used to generate the normal modes, or may be calculated (as is done in ARAP06) using the relationship

$$M_{ej} = \sum_i^W \left[m_{wi} \left(\phi^2_{Xij} + \phi^2_{Zij} \right) + I_{wi} \phi^2_{\theta ij} - 2 m_{wi} y_{wi} \phi_{Zij} \phi_{\theta ij} \right]$$

$$+ m_p \left[\phi^2_{XAj} + \phi^2_{YAj} + \phi^2_{ZAj} + \left(Z^2_p + Y^2_p \right) \phi^2_{\psi Aj} \right.$$

$$+ \left(Z^2_p + X^2_p \right) \phi^2_{\theta Aj} - \left(2 Z_p \sin\theta_{pc} \right.$$

$$+ 2 X_p \cos\theta_{pc} \right) \phi_{\theta Aj} \phi_{XAj} - 2 X_p Y_p \phi_{\theta Aj} \phi_{\psi Aj}$$

$$+ 2 Y_p \cos\theta_{pc} \phi_{\psi Aj} \phi_{XAj} + 2 Z_p \phi_{YAj} \phi_{\psi Aj}$$

$$- \left(2 Z_p \cos\theta_{pc} - 2 X_p \sin\theta_{pc} \right) \phi_{ZAj} \phi_{\theta Aj}$$

$$\left. - 2 Y_p \sin\theta_{pc} \phi_{ZAj} \phi_{\psi Aj} \right]$$

$$+ m_H \left[\phi^2_{XAj} + \phi^2_{YAj} + \phi^2_{ZAj} + z^2_H \left(\phi^2_{\psi Aj} + \phi^2_{\theta Aj} \right) \right.$$

$$- 2 z_H \left(\sin\theta_{pc} \phi_{\theta Aj} \phi_{XAj} - \phi_{YAj} \phi_{\psi Aj} \right.$$

$$\left. \left. + \cos\theta_{pc} \phi_{ZAj} \phi_{\theta Aj} \right) \right] + I_p \left(\phi^2_{\theta Aj} + \phi^2_{\psi Aj} \right) \quad (95)$$

in which

I_{wi} is the wing torsional mass moments-of-inertia about its elastic axis

I_p is the pylon pitching mass moment-of-inertia about the pylon center of gravity

44

b. Aerodynamics

Two-dimensional steady strip theory is used for the wing air-
loads. Figure 14a shows the wing strip arrangement. Pylon
and hub airloads are neglected.

The normal and tangential components of the relative wind
acting at the wing quarter chord are obtained by inspection
(neglecting higher order terms)

$$V_{Pi} = -\dot{\eta}_{wi} - y_{wi} \dot{\theta}_{wi} \cos\alpha_w \tag{96}$$

$$V_{Ti} = U + \dot{\xi}_{wi} - y_{wi} \dot{\theta}_{wi} \sin\alpha_w \tag{97}$$

where α_w is the wing steady angle-of-attack

The inflow angle is

$$\phi_{wi} = \tan^{-1} \frac{V_{Pi}}{V_{Ti}} \tag{98}$$

with the local angle-of-attack given by

$$\alpha_{wi} = \theta_{wi} + \phi_{wi} + \alpha_w \tag{99}$$

and

$$V_{wi} = \left(V_{Pi}^2 + V_{Ti}^2\right)^{\frac{1}{2}} \tag{100}$$

The local lift and drag force are then, respectively

$$L_{wi} = \tfrac{1}{2} \bar{C}_L \rho c_{wi} V_{wi}^2 \Delta L_i \tag{101}$$

$$D_{wi} = \tfrac{1}{2} \bar{C}_D \rho c_{wi} V_{wi}^2 \Delta L_i \tag{102}$$

in which

$\quad C_{wi}$ is the wing chord

$\quad \Delta L_i$ is the segment length

$\quad V_{wi}$ is the total relative velocity

45
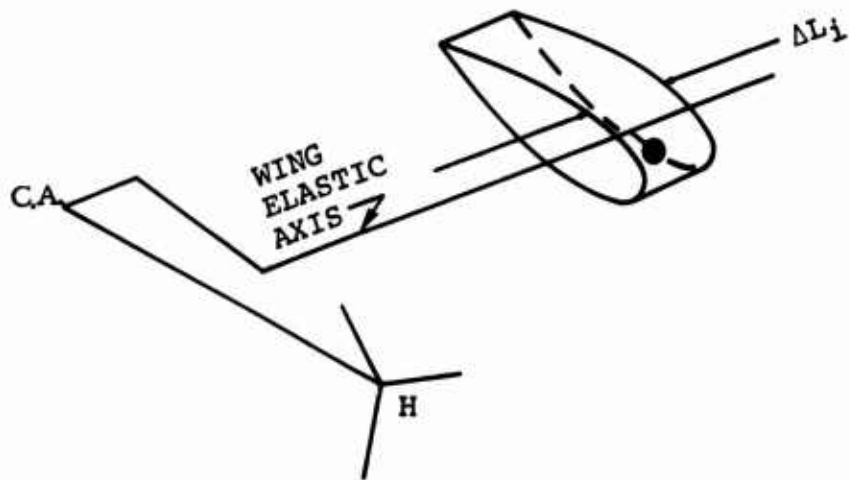
a.   WING STRIP ARRANGEMENT
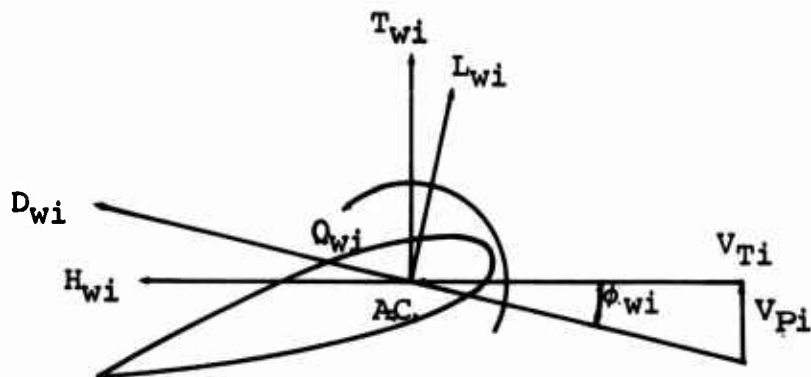
b.   AERODYNAMIC DETAILS

Figure 14.   Wing Strip Theory and Aerodynamic Details.

46

$\overline{C}_L$ and $\overline{C}_D$ are the lift and drag coefficients, defined as follows

$$\overline{C}_L = a\alpha_{wi} \tag{103}$$

$$\overline{C}_D = b_1 + b_2\alpha_{wi} + b_3\alpha_{wi}^2 \tag{104}$$

The local thrust, in-plane (flight path plane) drag, and pitching moment are then (see Figure 14b)

$$T_{wi} = L_{wi} \cos\phi_{wi} + D_{wi} \sin\phi_{wi} \tag{105}$$

$$H_{wi} = -L_{wi} \sin\phi_{wi} + D_{wi} \cos\phi_{wi} \tag{106}$$

$$Q_{wi} = \varepsilon_{wi}\left(L_{wi} \cos\alpha_{wi} + D_{wi} \sin\alpha_{wi}\right) \tag{107}$$

where ε_{wi} is the distance from the wing elastic axis to its aerodynamic center (AC), considered positive if the AC is toward the leading edge.

4. Wing-Blade Aerodynamic Interference

The aerodynamic interference between the wing and proprotor blades is simulated by determining the change in blade airloads caused by passage of the blade through the wing upwash field. The influence of the blade downwash on the wing is neglected. The problem is treated in two parts, the approximation of the flow field ahead of the wing and the location of the blade elements in that flow field.

a. Approximation of Flow Field Ahead of the Wing

The flow field of the wing is approximated by superimposing the flow field of an elliptical profile at zero angle of attack with that of a flat plate having the wing angle of attack. The ellipse simulates the wing thickness and the flat plate the circulation. Figure 15 illustrates this representation.

(1) Flow Field of an Elliptical Profile - Defining Z-plane as the math plane, ζ-plane as the physical plane, as shown in Figure 16, the streaming motion past a circular cylinder of radius R_1 in the Z-plane is given by the complex velocity potential

47

(a)   Flow Problem

ELLIPSE

(+)
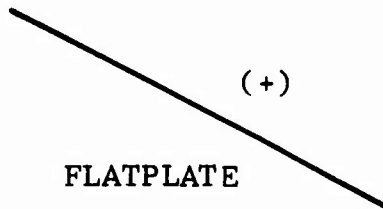
FLATPLATE

(b)   Math Model

Figure 15.   Approximation of Flow Field Ahead of the
             Wing.

48

$$\phi(Z) = u_\infty \left(Z + \frac{R_1^2}{Z} \right) \tag{108}$$

where u_∞ is the x-component free stream velocity
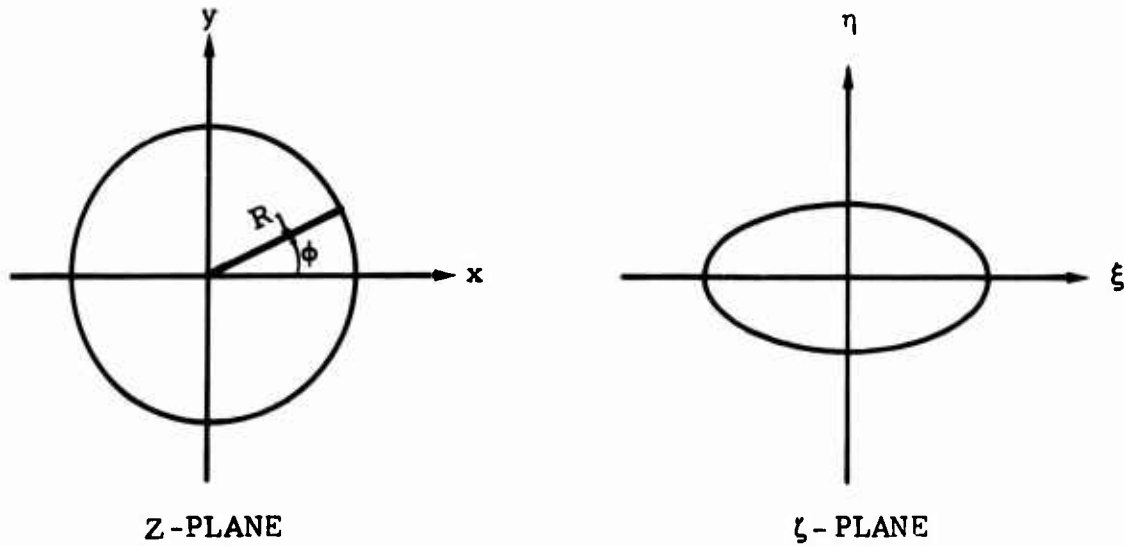
Figure 16. Conformal Mapping of an Ellipse to
a Circle.

The velocity field in the ζ-plane is given by

$$U_\zeta = \frac{d\phi}{d\zeta} = \frac{d\phi}{dZ} \frac{dZ}{d\zeta} \tag{109}$$

Let the Joukowsky transformation be the mapping function,
which has the following form

$$\zeta = Z + \frac{R_2^2}{Z} \tag{110}$$

where R_2 is a parameter.

The inverse transformation is then

$$Z = \frac{\zeta}{2} \pm \sqrt{\left(\frac{\zeta}{2}\right)^2 - R_2^2} \tag{111}$$

49

To map an ellipse of thickness ratio δ in the ζ-plane to a circle of radius R_1 in the Z-plane by using Joukowsky's transformation, the following relationships are established

$$R_1 = \tfrac{1}{4}\left(1 + \delta\right) \tag{112}$$

$$R_2 = \tfrac{1}{4}\sqrt{1 - \delta^2} \tag{113}$$

Differentiating equation 108 with respect to Z, and differentiating equation 111 with respect to ζ, substituting the results in equation 109 the flow field of an elliptical profile at zero angle of attack is then obtained

$$U_{\zeta e} = u_\infty \frac{\left(Z + R_1\right)\left(Z - R_1\right)}{\left(Z + R_2\right)\left(Z - R_2\right)} \tag{114}$$

where Z is a function of ζ defined by the inverse transformation equation 111.

The complex perturbation velocity is calculated by

$$\Delta U_{\zeta e} = U_{\zeta e} - u_\infty \tag{115}$$

(2) Flow Field of a Flat Plate

For a flat plate with an angle of attack, the complex velocity potential is obtained by superimposing the following,

- (a) uniform flow along x-axis with a doublet
- (b) uniform flow along y-axis with a doublet
- (c) a line vortex with clockwise circulation at the origin

Thus

$$\Phi(Z) = u_\infty\left(Z + \frac{R_1^2}{Z}\right) - iv_\infty\left(Z - \frac{R_1^2}{Z}\right) + \frac{i\Gamma}{2\pi}\log_e Z \tag{116}$$

where

u_∞ and v_∞ are the x and y components of the freestream velocity

Γ is the circulation, positive if counterclockwise

50

If the Joukowsky transformation, equation 110, is used to map a flat plate of chord length c in the ζ-plane to a circle of radius R_1 in the Z-plane, the following relationships are obtained

$$R_1 = R_2 = \frac{c}{4} \tag{117}$$

The mapping function for the case of a flat plate can, therefore, be written as

$$\zeta = Z + \frac{c^2}{16Z} \tag{118}$$

Thus

$$\frac{dZ}{d\zeta} = \frac{Z^2}{Z^2 - \left(\frac{c}{4}\right)^2} \tag{119}$$

Differentiating equation 116 with respect to Z yields

$$\frac{d\Phi}{dZ} = u_\infty \left(1 - \frac{c^2}{16Z^2}\right) - iv_\infty \left(1 + \frac{c^2}{16Z^2}\right) + \frac{i\Gamma}{2\pi}\frac{1}{Z} \tag{120}$$

With equations 119, 120 derived, the flow field of a flat plate having angle of attack can be obtained as

$$U_{\zeta p} = u_\infty - \frac{i}{\sqrt{\zeta^2 - \left(\frac{c}{2}\right)^2}} \left(v_\infty \zeta - \frac{\Gamma}{2\pi}\right) \tag{121}$$

The Kutta-Joukowsky condition requires that the value of the circulation is such as to make the term in the parentheses equal to zero at the trailing edge.[12] This is essential to avoid having infinite velocity component at $\zeta = c/2$.

Therefore,

$$\Gamma = 2\pi v_\infty \zeta = \pi v_\infty c \qquad (122)$$

Substituting this expression into equation 121, for a flat plate having unit chord length, we have

$$U_{\zeta p} = u_\infty - i v_\infty \sqrt{\frac{\zeta - \frac{1}{2}}{\zeta + \frac{1}{2}}} \qquad (123)$$

The perturbation velocity due to a flat plate with angle of attack α is given in the following form

$$\Delta U_{\zeta p} = U_{\zeta p} - (u_\infty + i v_\infty) \qquad (124)$$

in which

$$u_\infty = U \cos\alpha_w \qquad (125)$$

$$v_\infty = U \sin\alpha_w \qquad (126)$$

Where U is the free stream velocity.

b. Calculations of Blade Element Locations Ahead of the Wing

The wing upwash velocity is vectorily added to the proprotor blade element velocity to obtain the change in angle of attack and dynamic pressure caused by the presence of the wing. This requires the location of the blade element relative to the wing be known. Figure 17 shows the top and side views of a blade element location ahead of the wing.

The position vector of a blade mass element m_i from the wing leading-edge can be written

$$\vec{\zeta_i} = \vec{d_i} + z_H \hat{e}_3 + \vec{r_i} \qquad (127)$$

in which

$\vec{d_i}$ is a vector from the wing leading-edge to the pylon conversion axis

52
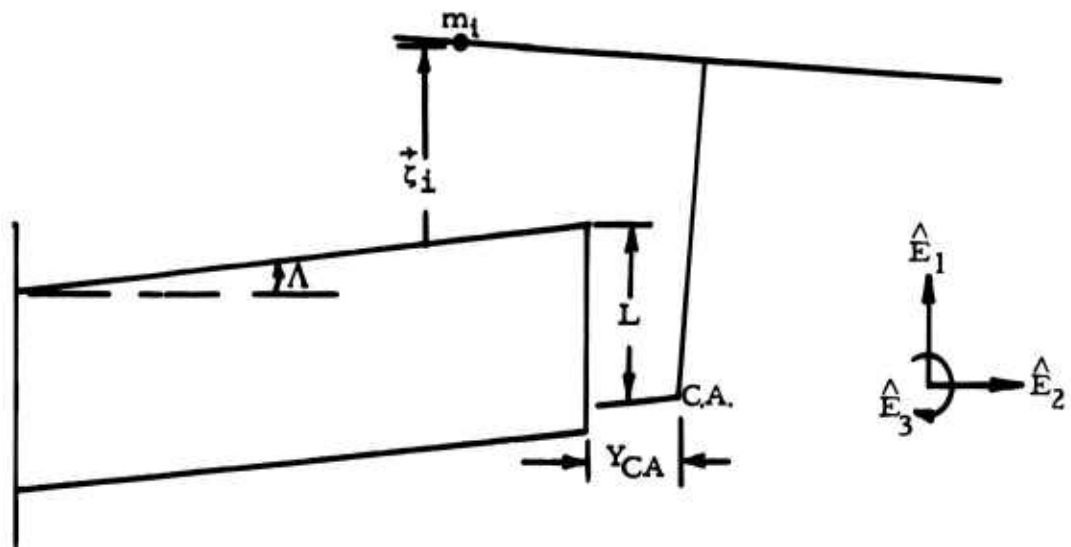
(a) Top View
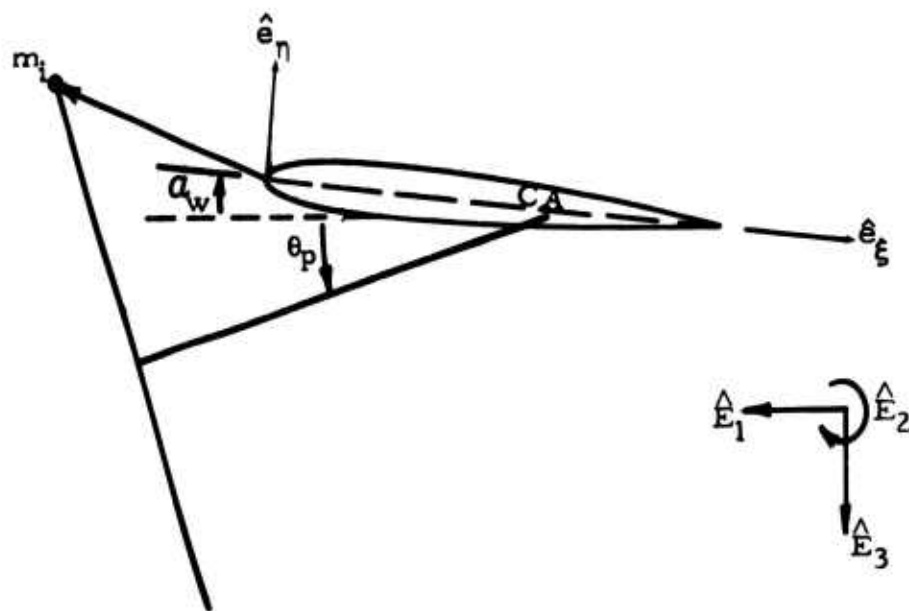
(b) Side View

Figure 17. Blade Element Location Ahead of the Wing.

53

$z_H \hat{e}_3$ is a vector from pylon conversion axis to rotor hub

$\vec{r_i}$ is the position vector of a blade mass element relative to the rotor hub, which is given by equation 3.

In terms of the fixed coordinate system, $X_F Y_F Z_F$, the following is obtained

$$z_H \hat{e}_3 + \vec{r_i} = \zeta_{iX_F} \hat{E}_1 + \zeta_{iY_F} \hat{E}_2 + \zeta_{iZ_F} \hat{E}_3 \tag{128}$$

in which

$$\zeta_{iX_F} = z_H \cos\psi_p \cos\theta_p + r_i \left(-\cos\beta \sin\psi \sin\psi_p \cos\theta_p \right.$$

$$\left. - \cos\beta \cos\psi \sin\theta_p + \sin\beta \cos\psi_p \cos\theta_p \right)$$

$$+ \bar{y}_i \left[\sin\theta_p \left(\cos\bar{\theta}_i \sin\psi + \sin\bar{\theta}_i \sin\beta \cos\psi \right) \right.$$

$$+ \cos\theta_p \sin\bar{\theta}_i \cos\beta \cos\psi_p$$

$$\left. + \sin\psi_p \cos\theta_p \left(\sin\bar{\theta}_i \sin\beta \sin\psi - \cos\bar{\theta}_i \cos\psi \right) \right]$$

$$- \frac{1}{2r_i} \left(\eta_i^2 + \xi_i^2 \right) \left(-\cos a_o \sin\psi \sin\psi_p \cos\theta_p - \cos a_o \cos\psi \sin\theta_p \right.$$

$$\left. + \sin a_o \cos\psi_p \cos\theta_p \right)$$

$$+ \eta_i \left(\cos a_o \cos\psi_p \cos\theta_p + \sin a_o \sin\psi \sin\psi_p \cos\theta_p \right.$$

$$\left. + \sin a_o \cos\psi \sin\theta_p \right)$$

$$- \xi_i \left(\sin\psi \sin\theta_p - \cos\psi \sin\psi_p \cos\theta_p \right) \tag{129}$$

$$\zeta_{iY_F} = z_H \sin\psi_p + r_i \left(\cos\beta \sin\psi \cos\psi_p + \sin\beta \sin\psi_p\right)$$

$$+ \bar{y}_i \left(\cos\bar{\theta}_i \cos\psi \cos\psi_p + \sin\bar{\theta}_i \cos\beta \sin\psi_p\right.$$

$$\left. - \sin\bar{\theta}_i \sin\beta \sin\psi \cos\psi_p\right)$$

$$+ \eta_i \left(\cos a_o \sin\psi_p - \sin a_o \sin\psi \cos\psi_p\right)$$

$$- \frac{1}{2r_i}\left(\eta_i^2 + \xi_i^2\right)\left(\cos a_o \sin\psi \cos\psi_p + \sin a_o \sin\psi_p\right)$$

$$- \xi_i \cos\psi \cos\psi_p \tag{130}$$

$$\zeta_{iZ_F} = -z_H \cos\psi_p \sin\theta_p + r_i \left(\cos\beta \sin\psi \sin\psi_p \sin\theta_p\right.$$

$$\left. - \cos\beta \cos\psi \cos\theta_p - \sin\beta \cos\psi_p \sin\theta_p\right)$$

$$+ \bar{y}_i \left[\cos\theta_p \left(\cos\bar{\theta}_i \sin\psi + \sin\bar{\theta}_i \sin\beta \cos\psi\right)\right.$$

$$- \sin\bar{\theta}_i \cos\beta \cos\psi_p \sin\theta_p$$

$$\left. + \sin\psi_p \sin\theta_p \left(\cos\bar{\theta}_i \cos\psi - \sin\bar{\theta}_i \sin\beta \sin\psi\right)\right]$$

$$- \frac{1}{2r_i}\left(\eta_i^2 + \xi_i^2\right)\left(\cos a_o \sin\psi \sin\psi_p \sin\theta_p - \cos a_o \cos\psi \cos\theta_p\right.$$

$$\left. - \sin a_o \cos\psi_p \sin\theta_p\right) + \eta_i \left(\sin a_o \cos\psi \cos\theta_p\right.$$

$$\left. - \cos a_o \cos\psi_p \sin\theta_p - \sin a_o \sin\psi \sin\psi_p \sin\theta_p\right)$$

$$- \xi_i \left(\cos\psi \sin\psi_p \sin\theta_p + \sin\psi \cos\theta_p\right) \tag{131}$$

If $\hat{e}_\xi$, $\hat{e}_\eta$ represent the unit vectors in the wing-chord coordinate system, referring to Figure 17, we have

55

$$\vec{d}_i = \left[L + \left(\zeta_{iY_F} + Y_{CA} \right) \tan\Lambda \right] \hat{e}_\xi - \zeta_{iY_F} \hat{E}_2 \qquad (132)$$

substituting equations 128 and 132 into equation 127, $\vec{\zeta}_i$ is given in the wing-chord coordinate system as

$$\vec{\zeta}_i = \left[L - \zeta_{iX_F} \cos\alpha_w + \zeta_{iZ_F} \sin\alpha_w + \left(\zeta_{iY_F} + Y_{CA} \right) \tan\Lambda \right] \hat{e}_\xi$$

$$- \left[\zeta_{iX_F} \sin\alpha_w + \zeta_{iZ_F} \cos\alpha_w \right] \hat{e}_\eta \qquad (133)$$

The two components in $\hat{e}_\xi$ and $\hat{e}_\eta$ directions are used to locate a blade element ahead of the wing in the ζ-plane. With these components calculated, the flow field is then obtained by using equations 114 and 123.

5. Special Provisions

a. Blade Feather/Unfeather Capability

To stop or start the proprotor the blades are feathered or unfeathered, respectively. In the feather/stop analysis the blade collective pitch may be specified as a function of time; constant at time t_1, then varying linearly to a new value at time t_2.

The windmilling blade collective pitch for a given rpm may be estimated using the following approximation:

$$\theta_c = \cos\theta_{pc} \ \tan^{-1}\left(\frac{U}{.73R\Omega} \right) - \theta_t \qquad (134)$$

where

θ_{pc}	is the steady shaft angle-of-attack
U	the airspeed in inches per second
R	the blade radius in inches
Ω	the proprotor angular velocity in radians per second
θ_t	the blade twist at the 73 percent radius (washout negative)

(This formula is based on zero angle of attack at 73 percent radius.)

56

b. Hub Restraint and Flapping Stops

Hub restraint is commonly employed with gimballed proprotors. The analysis includes the capability to simulate non-isotropic hub restraint. This is accomplished by introducing moments in the rotor fixed coordinate system, XYZ about the X and Y axes.

$$M_X = -K_b \, \beta_{lat} \tag{135}$$

and

$$M_Y = K_a \, \beta_{long} \tag{136}$$

where

K_a corresponds to longitudinal hub restraint

K_b corresponds to lateral hub restraint

β_{long} corresponds to the longitudinal tip-path-plane flapping

β_{lat} corresponds to the lateral tip-path-plane flapping

The components of these moments in the blade rotating coordinates, xyz, are

$$m_x = M_X \, \cos\psi + M_Y \, \sin\psi \tag{137}$$

$$m_y = -M_X \, \sin\psi + M_Y \, \cos\psi \tag{138}$$

These are applied to the right hand side of the b' and a' flapping equations, respectively.

The longitudinal and lateral restraint rates, K_a and K_b, may be specified as a function of rpm.

An approximation to flapping stops is also provided for the gimballed rotor. If the flapping of any blade exceeds a specified magnitude, a flapping moment is added to equations 33 and 34. For instance, if the second blade flapping of a three bladed gimballed rotor satisfies the following condition

57

$$\beta_2 - \beta_{stop} < 0 \qquad (139)$$

The flapping moment components are calculated

$$\Delta m_x = -\frac{\sqrt{3}}{2} K_{stop} \left(\beta_2 - \beta_{stop}\right) \qquad (140)$$

$$\Delta m_y = -\frac{1}{2} K_{stop} \left(\beta_2 - \beta_{stop}\right) \qquad (141)$$

where

K_{stop} is very large

c. Gust Simulation

Gust encounters with head-on and vertical gusts of sinusoidal, sine-square or sharp edged shape may be specified. The magnitude and time for the encounter may be specified and for the sine-square gust, the gust length. The magnitude and frequency are specified for a sinusoidal gust. Symbolically, the gust may be written in the following form

$$\vec{V}_g = -V_{g_h} \hat{E}_1 - V_{g_v} \hat{E}_3 \qquad (142)$$

where

V_{g_h} is a head-on gust

V_{g_v} is a vertical gust

The coordinate transformations discussed earlier in this section are used to transfer the $\vec{V}_g$ into the velocity vectors in the local blade coordinate system for the proprotor and the fixed coordinate system for the wing.

The gust is assumed to be encountered simultaneously by the wing and proprotor.

d. Frequency Response Excitation

The frequency response of the system analyzed can be determined using two means of aerodynamic excitation (1) cyclic pitch and, (2) aerodynamic vane located on the pylon. (The vane may be used to simulate aileron excitation.)

58

(1) <u>Cyclic Pitch Excitation</u> - The cyclic pitch excitation is to determine the position of the swashplate. If $A_1(t)$ and $B_1(t)$ are the lateral and longitudinal cyclic pitch components

for $t < t_\tau$

$$A_1(t) = A_1 \qquad (143)$$

$$B_1(t) = B_1 \qquad (144)$$

for $t \geqslant t_\tau$

$$A_1(t) = A_1 + A_{1c} \cos\left[\omega_{ac}(t - t_\tau)\right] + A_{1s} \sin\left[\omega_{as}(t - t_\tau)\right] \qquad (145)$$

$$B_1(t) = B_1 + B_{1c} \cos\left[\omega_{bc}(t - t_\tau)\right] + B_{1s} \sin\left[\omega_{bs}(t - t_\tau)\right] \qquad (146)$$

where

t_τ is the time excitation initiated

A_1 is the steady lateral cyclic

B_1 is the steady longitudinal cyclic

The four ω's are frequencies of excitation, defined as follows

$$\omega_{ac} = \omega_{ac0} + \frac{\partial \omega_{ac}}{\partial t}\left(t - t_\tau\right) \qquad (147)$$

$$\omega_{as} = \omega_{as0} + \frac{\partial \omega_{as}}{\partial t}\left(t - t_\tau\right) \qquad (148)$$

$$\omega_{bc} = \omega_{bc0} + \frac{\partial \omega_{bc}}{\partial t}\left(t - t_\tau\right) \qquad (149)$$

$$\omega_{bs} = \omega_{bs0} + \frac{\partial \omega_{bs}}{\partial t}\left(t - t_\tau\right) \qquad (150)$$

(2) <u>Aerodynamic Vane</u> - With the location and dimensions of the exciter on the pylon having been specified, the vertical and tangential velocity components can be computed. The angle of attack of the vane is then calculated by

59

$$\alpha_e = \theta_p + \alpha_{0e} + \alpha_{0s} \sin\left[\omega_e(t - t_e)\right] + \tan^{-1} \frac{V_{Pv}}{V_{Tv}} \qquad (151)$$

in which

θ_p is the pylon conversion angle

V_{Pv} is the vertical velocity component

V_{Tv} is the tangential velocity component

α_{0e} is the steady angle of attack of the vane relative to the pylon

α_{0s} is the oscillatory angle of attack of the vane relative to the pylon

t_e is the time when excitation of the vane begins

ω_e is the exciting frequency given by

$$\omega_e = \omega_{e0} + \frac{\partial \omega_e}{\partial t}(t - t_e) \qquad (152)$$

The lift curve slope of the vane is specified. By the same token as wing aerodynamic loads and moments are treated, the ones for the vane are calculated and used as part of the wing pylon forcing function.

6. ARAP06 Computer Program

The final form of the equations of motion are shown in Figure 18. Up to nineteen nonlinear simultaneous equations are involved, depending on the degrees of freedom selected by the user.

The equations of motion are solved using a step-by-step integration technique. Details of the method of solution are provided in Volume II. The output data consists of a time history of selected accelerations, displacements, and forces and moments. If desired, the time history may be machine plotted (CALCOMP).

a. Program Capabilities

The ARAP06 program has been structured to provide the user with considerable latitude in the math model to be analyzed. Table II gives examples of the math models available. (The math model is specified by control cards.)

$$
\begin{bmatrix} \text{Time Dependent} \\ \text{Inertial} \\ \text{Property} \end{bmatrix}_I \begin{Bmatrix} \ddot{\psi} \\ \ddot{b}_1{}' \\ \ddot{a}_1{}' \end{Bmatrix}_{\substack{\text{Rotor Rigid} \\ \text{Body DOF}}} = \begin{bmatrix} \text{Blade} \\ \text{Aerodynamic} \\ \text{Forces and} \\ \text{Moments} \end{bmatrix} + \begin{bmatrix} \text{Hub Motion} \\ \text{Due to} \\ \text{Wing Elastic} \\ \text{Deflections} \end{bmatrix}
$$

$$
+ \begin{bmatrix} \text{Inertial Forces} \\ \text{(Centrifugal and} \\ \text{Coriolis)} \\ \text{Plus Gravity} \end{bmatrix}_I
$$

$$
\begin{bmatrix} \text{Time Dependent} \\ \text{Internal} \\ \text{Property} \end{bmatrix}_{II} \begin{Bmatrix} \ddot{q}_1 \\ \ddot{q}_2 \\ \vdots \\ \ddot{q}_{12} \end{Bmatrix}_{\substack{\text{Elastic} \\ \text{Blades}}} = \begin{bmatrix} \text{Blade} \\ \text{Aerodynamic} \\ \text{Forces and} \\ \text{Moments} \end{bmatrix} + \begin{bmatrix} \text{Hub Motion} \\ \text{Due to} \\ \text{Wing Elastic} \\ \text{Deflections} \end{bmatrix}
$$

$$
+ \begin{bmatrix} \text{Inertial Forces} \\ \text{(Centrifugal and} \\ \text{Coriolis)} \\ \text{Plus Gravity} \end{bmatrix}_{II}
$$

$$
\begin{bmatrix} \text{Generalized} \\ \text{Masses} \end{bmatrix} \begin{Bmatrix} \ddot{q}_1 \\ \ddot{q}_2 \\ \ddot{q}_3 \\ \ddot{q}_4 \end{Bmatrix}_{\substack{\text{Wing-Pylon-} \\ \text{Hub}}} = \begin{bmatrix} \text{Forces} \\ \text{Generated} \\ \text{by the} \\ \text{Proprotor} \end{bmatrix} + \begin{bmatrix} \text{Wing-Pylon-} \\ \text{Hub} \\ \text{Gravity} \end{bmatrix}
$$

$$
+ \begin{bmatrix} \text{Wing} \\ \text{Aerodynamic} \\ \text{Forces} \end{bmatrix}
$$

Figure 18. Form of Equations of Motion.

61

In addition to the calculation of proprotor stability and dynamic response during the FPR feather/stop cycle, the ARAP06 program can be used to calculate:

(1) Proprotor aerodynamic derivatives, including frequency response characteristics.

(2) Oscillatory forces and moments acting at the hub. These data, when used with a finite element structural analysis such as NASTRAN, provides useful design information.

(3) Loads and response during blade folding. In this respect the ARAP06 program has a more general capability than the response analysis specifically developed as part of the Folding Dynamics Analysis.

(4) Dynamic characteristics of tilt-rotor VTOL including proprotor/pylon stability, blade flapping and loads, and pylon and fuselage vibration.

b. **Program Usage**

(1) **Data Requirements** - An input format and users guide is given in Volume II. The direct data requirements consist of the proprotor and wing/pylon/hub system inertial properties, geometry, and normal mode frequencies and mode shapes. The wing lift curve slope and proprotor hub restraint, if applicable, must also be supplied.

Indirect input data requirements consist of the stiffness properties of the wing and blades which are used in vibration analyses to generate the normal modes. The tabulated 2-D airfoil data currently incorporated in the program is satisfactory for most dynamics work, but the user can substitute his own tables directly in the source deck if desired. These tables currently include the following airfoils:

Airfoil	Applies to Radial Station
$t/c = 0.25$	$0.075 \le r/R < 0.45$
$t/c = 0.18$	$0.45 \le r/R < 0.70$
$t/c = 0.12$	$0.70 \le r/R < 0.90$
$t/c = 0.08$	$0.90 \le r/R \le 1.0$

(2) **Usage Techniques**

(a) **Proprotor Modeling** - As indicated in Table II, the ARAP06 program can be used to model a number of rotor types. The gimballed rotor type is automatically modeled if the gimballed rotor option is selected. To model a hingeless rotor (or a

62

TABLE II

ARAP06 MATH MODEL CAPABILITY

Math Model	Degrees of Freedom Used			
	*(1)	*(2)	*(3)	Σ
1. Isolated Proprotor (Rigid Blades)				
a. Rigid, constant rpm	0	0	0	0
b. Rigid, variable rpm	0	1	0	1
c. Gimballed, constant rpm	0	2	0	2
d. Gimballed, variable rpm	0	3	0	3
e. Offset flapping hinge, constant rpm	0	0	2	2
f. Offset flapping hinge, variable rpm	0	1	2	3
g. Fully articulated, constant rpm	0	0	4	4
h. Fully articulated, variable rpm	0	1	4	5
2. Wing/Pylon System Coupled with Proprotor with Rigid Blades				
a. Rigid, constant rpm	up to 4	0	0	4
b. Rigid, variable rpm	"	1	0	5
c. Gimballed, constant rpm	"	2	0	6
d. Gimballed, variable rpm	"	3	0	7
e. Offset flapping hinge, constant rpm	"	0	2	6
f. Offset flapping hinge, variable rpm	"	1	2	7
g. Fully articulated, constant rpm	"	0	4	8
h. Fully articulated, variable rpm	"	1	4	9
3. Wing/Pylon System Coupled with Proprotor with Elastic Blades				
a. Rigid, constant rpm	up to 4	0	4	8
b. Rigid, variable rpm	"	1	4	9
c. Gimballed, constant rpm	"	2	4	10
d. Gimballed, variable rpm	"	3	4	11
e. Offset flapping hinge, constant rpm	"	0	2 + 2	8
f. Offset flapping hinge, variable rpm	"	1	2 + 2	9
g. Fully articulated, constant rpm	"	0	4 +	8
h. Fully articulated, variable rpm	"	1	4 +	9

*(1) Wing-Pylon Degrees of Freedom
*(2) Proprotor Rigid-Body Degrees of Freedom
*(3) Rigid Blade Elastic Degrees of Freedom
+ Rigid

propeller) the rigid rotor option is used and blade normal modes employed to represent blade flexibility.

To represent the articulated and offset flapping hinge rotor types the rigid rotor option is used in conjunction with normal modes. The first normal mode is used to represent the blade rigid-body flapping. Accordingly the natural frequency of the first mode is

$$\omega_f = \Omega \sqrt{1 + \frac{3}{2} \frac{e_f}{R}} \tag{153}$$

where e_f is the flapping hinge offset.

The out-of-plane mode shape is zero at the hinge and inboard of the hinge, and is unity at the tip. A straight line is assumed between the hinge and the tip. The inplane shape is zero, root to tip.

For the fully articulated rotor the lead-lag motion is simulated using the second normal mode. The frequency is given by

$$\omega_L = \Omega \sqrt{\frac{3}{2} \frac{e_L}{R}} \tag{154}$$

where e_L is the lead-lag hinge offset.

The out-of-plane mode shape is zero and the inplane mode shape is zero at the lag hinge, zero inboard of the lag hinge and unity at the tip. A straight line approximation is used between the lag hinge and the tip.

Since four normal modes can be specified, the first and second flapwise and first edgewise modes can also be input, for offset flapping hinge rotors and the first flapwise and edgewise modes in the case an articulated rotor is being simulated.

(b) Wing-Pylon Modeling - Up to four wing-pylon modes can be specified. These can be used to represent a complete wing-pylon-hub system or if desired pylon pitching and/or yawing freedom only.

When the wing-pylon-hub system is modeled either cantilever wing or free-free (symmetric or asymmetric) modes may be used. Usually the fundamental beam, chord, and torsion modes, and either the fuselage vertical bending or a second wing bending mode should be used. These modes must be calculated at the pylon conversion angle input to the program.

64

The pylon pitching and/or yawing modes may be modeled without
having to first perform a normal mode vibration analysis.
First the wing mode shape is set to zero. Then the conversion
axis reference point is assumed to be located at the pylon
center of gravity. (The mast length is then input as the
distance between the pylon center of gravity and the hub.)
The pylon pitch and yaw angular deflection is set equal to
the distance from the pylon center of gravity to the hub,
divided by the actual mast length. The desired pylon natural
frequencies are input directly.

The inherent capability to build up the math model from a
limited number of degrees of freedom to a fully-coupled wing-
pylon-hub-proprotor system can be used when first using the
analysis. At each stage of build-up the math model should
be checked to verify the accuracy of the representation.
For example, the in-vacuo coupled wing-pylon-hub frequencies
and mode shapes can be determined by running the program
with the air density and structural damping set to zero.

B. BLADE FOLDING DYNAMICS ANALYSIS

The development of a dynamic theory for blade folding/unfolding
is divided into two parts: a flutter (and divergence) analysis
and a dynamic response (loads) analysis. The flutter analysis
is the basis for the response analysis.

1. Flutter Analysis

The flutter analysis is based on a conventional collocation
method, flutter and vibration analysis.[8] The formulation
utilizes structural, aerodynamic, and inertial characteristics
in the form of structural and aerodynamic influence coefficients
and mass matrices.

This analysis differs from the original analysis,[8] in two
ways: (1) a specific structural influence coefficient matrix
which represents the folding-proprotor wing-pylon-blade
system has been developed, and (2) a faster, more accurate,
eigenvalue routine is employed.

a. Description of the Math Model

An overview of the math model is shown in Figure 19. This
model includes the following degrees of freedom:

    1. Wing beam, chord, and torsion (5 elements)
    2. Pylon pitch and yaw relative to the wing-tip
    3. Motions about the fold hinge and feathering axis
    4. Blade beam, chord, and torsion (5 elements)

65

The standard sign convention is used, positive starboard down, and aft. Nose up, yaw right, and roll left are positive.

The wing representation consists of five beam elements located along the elastic axis of the wing. Lumped masses represented by dumbells are located at each node point (element junction). These reflect the mass, inertia, and static unbalance properties of the wing. The sweep of the x axis orientation follows from the right hand rule. The principal benefit of this coordinate system is that the aerodynamic and mass matrices can be formed directly without coordinate transformation (except to account for the dumbbell representation).

b.   Formulation of Equations of Motion

The equation of motion for the system shown in Figure 19 may be written as

$$[m]\{\ddot{q}\} + [1 + ig][K]\{q\} = [\bar{F}]\{q\}$$ (155)

where

$$\begin{bmatrix} m \\ K \\ \bar{F} \end{bmatrix}$$

[m]   is a mass matrix
[K]   is a stiffness matrix
[F̄]   is a complex forcing function
 g   is the complex structural damping parameter
{q}   is the generalized coordinates

The generalized coordinates used in this analysis are those compatible with the aerodynamic representation. The vertical (z) axis is taken normal to a strip and the y axis in the streamwise direction; the wing elastic axis is included in the structural formulation. (The segment of the elastic axis continuing from the fifth node point is considered to be identical to the fifth segment and of one-half the fifth segment's length.)

The wing aerodynamic representation consists of strips centered on the node points. The chord and width of each strip are input variables. The strips lie parallel to the freestream. Two dimensional incompressible, oscillating, thin airfoil theory is used to approximate the airloads.

The pylon (shaft) is attached to the wing by an inelastic chordwise element between the wing elastic axis and the pylon conversion axis and by a spanwise element to the shaft centerline. The torsional stiffness of the spanwise element is used to simulate the pylon pitch attachment stiffness; and its chordwise stiffness the pylon yawing stiffness.

66

BLADES TWO AND THREE HAVE
SAME MATH MODEL AS INDI-
CATED FOR BLADE ONE

FIVE WING STRIPS WITH MASS,
MASS UNBALANCE AND INERTIA.
2-D, INCOMPRESSIBLE, UNSTEADY
STRIP THEORY AERODYNAMIC
FORCES AND MOMENT

PYLON PITCH AND YAW MOUNTING
FLEXIBILITY, AND INERTIAL
CHARACTERISTICS

FIVE BLADE STRIPS WITH
SAME INERTIAL AND AERO-
DYNAMIC REPRESENTATION
AS WING

BLADE FOLD HINGE
WITH CONCENTRATED
ROOT FLEXIBILITY

Figure 19. Overview of Math Model for Blade Folding Flutter Analysis.

67

Two strips, located on the pylon, may be used to approximate the vertical and lateral aerodynamic forces acting on the pylon.

The hub details include blade feathering (control system) and fold hinge flexibilities. Feathering flexibilities are immediately located inboard and outboard of the fold hinge. The fold hinge radial location is specified by the hub offset.

The blades' structural and aerodynamic representation is identical to that of the wing except that the element outboard of the fifth node is inelastic. The blade is assumed to start at the fold hinge. The fold angle is a variable. Only three blades are considered and they are assumed to fold knife-like into the nacelle.

c. Mass and Aerodynamic Matrices

The mass and aerodynamic formulation of the original flutter analysis are essentially unchanged. For completeness, however, a brief review of these formulations is given here.

(1) Mass Matrix - Figure 20 shows the details of the dumbbell arrangement. The dumbbells are parallel to the y-axis (free stream). Working backwards, the deflections at the element elastic axis may be written as

$$\delta = h_1 + \overline{X}\xi \tag{156}$$

and

$$\xi = \frac{h_2 - h_1}{d} \tag{157}$$

where

h_1 and h_2 are the generalized coordinates.

Solving in terms of h_1 and h_2 only,

$$\delta = \frac{h_1 \overline{Y} + \overline{X} h_2}{d} \tag{158}$$

and

$$\overline{Y} = d - \overline{X} \tag{159}$$

or in a matrix notation

68
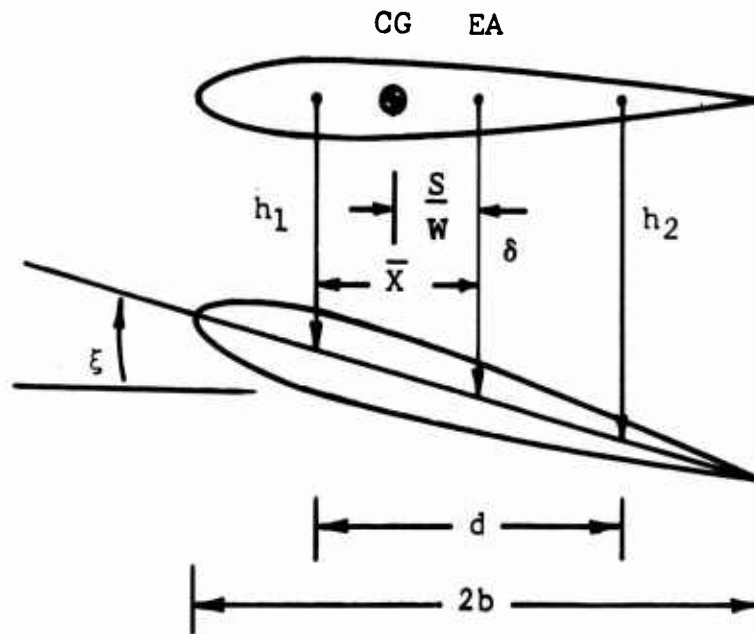
(a)   Dumbbell Arrangement for Mass Matrix.
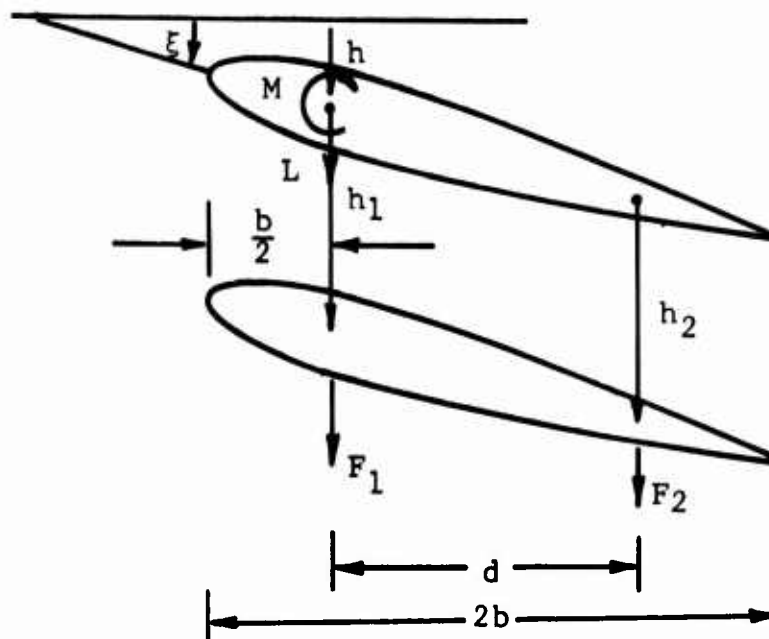
(b)   Original and Equivalent Force Systems and
      Geometry for Aerodynamic Matrix

Figure 20.   Dumbbell Relationships.

69

$$
\begin{Bmatrix} \delta \\ \xi \end{Bmatrix} = \begin{bmatrix} \dfrac{\overline{Y}}{d} & \dfrac{\overline{X}}{d} \\ -\dfrac{1}{d} & \dfrac{1}{d} \end{bmatrix} \begin{Bmatrix} h_1 \\ h_2 \end{Bmatrix}
\tag{160}
$$

From Lagrange's equation the kinetic energy of a system is given by

$$
T = \tfrac{1}{2} \lfloor \dot{\delta}, \dot{\xi} \rfloor \begin{bmatrix} m & S \\ S & I_e \end{bmatrix} \begin{Bmatrix} \dot{\delta} \\ \dot{\xi} \end{Bmatrix}
\tag{161}
$$

where

  m   is the mass

  S   is the unbalance (positive forward)

  I_e is the inertia about the elastic axis

Performing the differential $\dfrac{d}{dt}\left(\dfrac{\partial T}{\partial \dot{q}}\right)$, gives the following form

for the mass matrix in dumbbell coordinates.

$$
[m] = \begin{bmatrix} \dfrac{\overline{Y}}{d} & -\dfrac{1}{d} \\ \dfrac{\overline{X}}{d} & \dfrac{1}{d} \end{bmatrix} \begin{bmatrix} m & S \\ S & I_e \end{bmatrix} \begin{bmatrix} \dfrac{\overline{Y}}{d} & \dfrac{\overline{X}}{d} \\ -\dfrac{1}{d} & \dfrac{1}{d} \end{bmatrix} = [U]_1^T \begin{bmatrix} m & S \\ S & I_e \end{bmatrix} [U]_1
\tag{162}
$$

For the chordwise deflections no transformation is required.

(2) Aerodynamic Matrix - The matrix of aerodynamic influence coefficients for a strip is defined in terms of the generalized coordinates as

$$
\begin{Bmatrix} F_1 \\ F_2 \end{Bmatrix} = \rho \omega^2 b_r{}^2 s \, [C_h] \begin{Bmatrix} h_1 \\ h_2 \end{Bmatrix}
\tag{163}
$$

in which

  ρ is the air density

  ω is the oscillatory frequency

  b_r is the reference semichord

  s   is the reference semispan

70

The matrix of aerodynamic influence coefficients $[C_h]$ are in partitioned form, i.e.

$$[C_h] = \begin{bmatrix} C_{h_1} & \vdots & 0 \\ \text{---} & \vdots & \text{---} \\ 0 & \vdots & C_{h_2} \end{bmatrix} \tag{164}$$

$[C_h]$ is related to the lift and moment acting on the strip as follows. Using the geometry indicated in Figure 20b, the relationship between the lift and moment, L and M, respectively, may be written as

$$\begin{Bmatrix} L \\ M \end{Bmatrix} = \begin{bmatrix} 1 & 1 \\ 0 & d \end{bmatrix} \begin{Bmatrix} F_1 \\ F_2 \end{Bmatrix} \tag{165}$$

The oscillatory lift and moment referred to the blade quarter chord are defined as

$$\begin{Bmatrix} L \\ M \end{Bmatrix} = \pi \cos\Lambda(\rho\omega^2 b^2 \Delta Y) \begin{bmatrix} 1 & 0 \\ 0 & b \end{bmatrix} \begin{bmatrix} L_h & L_\alpha \\ M_h & M_\alpha \end{bmatrix} \begin{bmatrix} h \\ \xi \end{bmatrix} \tag{166}$$

when the coefficients L_h, L_α, M_h, and M_α are those given in Reference 10, and h and ξ are related to h_1 and h_2 as follows:

$$\begin{Bmatrix} h \\ \xi \end{Bmatrix} = \begin{bmatrix} 1 & 0 \\ -\dfrac{b}{d} & \dfrac{b}{d} \end{bmatrix} \begin{Bmatrix} h_1 \\ h_2 \end{Bmatrix} \tag{167}$$

Solving for $\{F\}$ in terms of $\{h\}$ an expression for $[C_h]$ is obtained

$$[C_h] = \pi \cos\Lambda \left(\frac{b}{b_r}\right)^2 \left(\frac{\Delta Y}{A}\right) \begin{bmatrix} 1 & -\dfrac{b}{d} \\ 0 & \dfrac{b}{d} \end{bmatrix} \begin{bmatrix} L_h & L_\alpha \\ M_h & M_\alpha \end{bmatrix} \begin{bmatrix} 1 & 0 \\ -\dfrac{b}{d} & \dfrac{b}{d} \end{bmatrix} \tag{168}$$

The steady-state aerodynamic influence coefficients are a limiting case of the oscillatory coefficients, i.e. $\omega \to 0$.

$$\begin{Bmatrix} F_1 \\ F_2 \end{Bmatrix} = \tfrac{1}{2}\rho V^2 \left(\frac{A}{C}[C_{h_S}]\right) \begin{Bmatrix} h_1 \\ h_2 \end{Bmatrix} \tag{169}$$

d. Flexibility Matrix

The flexibility matrix for the wing-pylon-blades system is formed using finite element theory.[13] As noted earlier, the

71

structural representation consists of 30 beam elements and 31 nodes. Figure 21 shows the structure arrangement. Each beam element is considered to have a uniform cross section and resist moments and shears about the principal axes, torsion about the normal axis, and axial loads. Each element stiffness matrix is 12 x 12 and is of the form shown in Figure 22. Each node is assumed to have six degrees of freedom.

To construct a stiffness matrix for the complete structure each element is first oriented along the reference x-axis (see Figure 21) and then rotated into its structural orientation through three successive coordinate system rotations. These rotations are in order, first about the z-axis, then about the y'-axis, and finally about the z''-axis. These rotations are designated as α, ψ, and β, respectively, and the rotated coordinate systems are disgnated as $x^I y^I z^I$, $x^{II} y^{II} z^{II}$, and $x^{III} y^{III} z^{III}$.

These coordinate transformations are given by the following relationships (for brevity only the xyz transformations are shown. The θ_x, θ_y, and θ_z transformations are similar.)

α rotation

$$
\begin{Bmatrix} x \\ y \\ z \end{Bmatrix}^I = \begin{bmatrix} \cos\alpha & \sin\alpha & 0 \\ -\sin\alpha & \cos\alpha & 0 \\ 0 & 0 & 1 \end{bmatrix} \begin{Bmatrix} x \\ y \\ z \end{Bmatrix}^0
\tag{170}
$$

ψ rotation

$$
\begin{Bmatrix} x \\ y \\ z \end{Bmatrix}^{II} = \begin{bmatrix} \cos\psi & 0 & -\sin\psi \\ 0 & 1 & 0 \\ \sin\psi & 0 & \cos\psi \end{bmatrix} \begin{Bmatrix} x \\ y \\ z \end{Bmatrix}^I
\tag{171}
$$

β rotation

$$
\begin{Bmatrix} x \\ y \\ z \end{Bmatrix}^{III} = \begin{bmatrix} \cos\beta & \sin\beta & 0 \\ -\sin\beta & \cos\beta & 0 \\ 0 & 0 & 1 \end{bmatrix} \begin{Bmatrix} x \\ y \\ z \end{Bmatrix}^{II}
\tag{172}
$$

The final transformation from the reference coordinate system to the final structural coordinate system is then

72
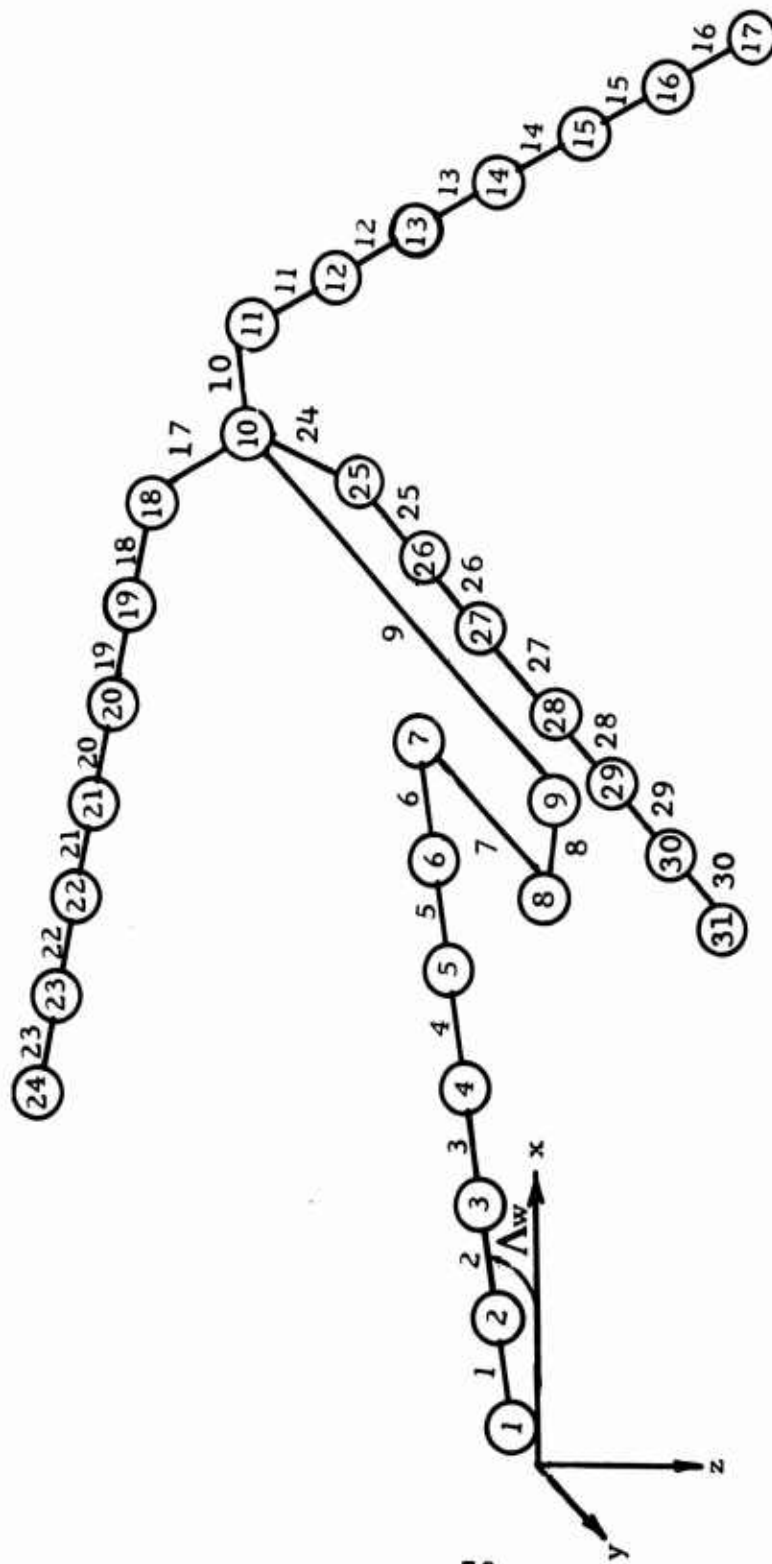
Figure 21. Structural Representation of the Wing-Pylon-Blades System by Using Finite Element Theory.

73

	X_L	Y_L	Z_L	θ_{XL}	θ_{YL}	θ_{ZL}	$X_{\bar{R}}$	$Y_{\bar{R}}$	$Z_{\bar{R}}$	$\theta_{X\bar{R}}$	θ_{YR}	$\theta_{Z\bar{R}}$
	$\dfrac{AE}{\ell}$											
	0	$\dfrac{12EI_\beta}{\ell^3}$								SYMMETRIC		
	0	0	$\dfrac{12EI_c}{\ell^3}$									
	0	0	0	$\dfrac{GJ}{\ell}$								
	0	0	$-\dfrac{6EI_c}{\ell^2}$	0	$\dfrac{4EI_c}{\ell}$							
	0	$\dfrac{6EI_\beta}{\ell^2}$	0	0	0	$\dfrac{4EI_\beta}{\ell}$						
	$-\dfrac{AE}{\ell}$	0	0	0	0	0	$\dfrac{AE}{\ell}$					
	0	$-\dfrac{12EI_\beta}{\ell^3}$	0	0	0	$-\dfrac{6EI_\beta}{\ell^2}$	0	$\dfrac{12EI_\beta}{\ell^3}$				
	0	0	$-\dfrac{12EI_c}{\ell^3}$	0	$\dfrac{6EI_c}{\ell^2}$	0	0	0	$\dfrac{12EI_c}{\ell^3}$			
	0	0	0	$-\dfrac{GJ}{\ell}$	0	0	0	0	0	$\dfrac{GJ}{\ell}$		
	0	0	$-\dfrac{6EI_c}{\ell^2}$	0	$\dfrac{2EI_c}{\ell}$	0	0	0	$\dfrac{6EI_c}{\ell^2}$	0	$\dfrac{4EI_c}{\ell}$	
	0	$\dfrac{6EI_\beta}{\ell^2}$	0	0	0	$\dfrac{2EI_\beta}{\ell}$	0	$-\dfrac{6EI_\beta}{\ell^2}$	0	0	0	$\dfrac{4EI_c}{\ell}$

Figure 22. Element Stiffness Matrix.

74

$$\left\{ \begin{array}{c} x \\ y \\ z \end{array} \right\}^{III} = \begin{bmatrix} \cos\beta\cos\psi\cos\alpha & \cos\beta\cos\psi\sin\alpha & -\cos\beta\sin\psi \\ \quad - \sin\beta\sin\alpha & \quad + \sin\beta\cos\alpha & \\ -\sin\beta\cos\psi\cos\alpha & -\sin\beta\cos\psi\sin\alpha & \sin\beta\sin\psi \\ \quad - \cos\beta\sin\alpha & \quad + \cos\beta\cos\alpha & \\ \sin\psi\cos\alpha & \sin\psi\sin\alpha & \cos\psi \end{bmatrix} \left\{ \begin{array}{c} x \\ y \\ z \end{array} \right\}^{0} \qquad (173)$$

or

$$\left\{ \begin{array}{c} x \\ y \\ z \\ \theta_x \\ \theta_y \\ \theta_z \end{array} \right\}^{III} = \begin{bmatrix} [T]_2 & \\ & [T]_2 \end{bmatrix} \left\{ \begin{array}{c} x \\ y \\ z \\ \theta_x \\ \theta_y \\ \theta_z \end{array} \right\}^{0} \qquad (174)$$

For reference the rotations of the various structural elements shown in the math model (Figure 21) are

Element(s)	Segment No.	α	ψ	β
Wing	1 - 6	0	0	Wing sweep angle
EA - CA Offset	7	90	0	0
Mast Offset	8	0	0	0
Mast	9	-90	0	0
Hub Element 1	10	0	0	0
Hub Element 2	17	180	60	0
Hub Element 3	24	180	-60	0
Blade No. 1	11 - 16	0	0	Blade fold
Blade No. 2	18 - 23	180	60	- Blade fold
Blade No. 3	25 - 30	180	-60	- Blade fold

75

The stiffness matrix for each element, in the beam coordinate system is then

$$[K_e] = [T]_2^T [k_e][T]_2 \tag{175}$$

where $[k_e]$ is the element stiffness matrix shown in Figure 22.

The stiffness matrix for the complete structural system is then formed by adding the individual stiffness matrices at each node. This gives a 186 x 186 matrix

$$[K] = \begin{bmatrix} [K_e]_1 \\ & [K_e]_2 \\ & & [K_e]_3 \\ & & & \ddots \end{bmatrix} \tag{176}$$

where the overlay of the individual element stiffness matrices indicate addition of adjoining element stiffness matrices.

This stiffness matrix (176) must now be transformed into a coordinate system compatible with the inertial and aerodynamic math models. As noted earlier these are normal to the aerodynamic surface. For the wing and blade 1(see Figure 21) the reference xyz coordinate system is compatible with the inertial and aerodynamic coordinate systems. However, for blades 2 and 3 a coordinate transformation to the $x^{IV}y^{IV}z^{IV}$ system is required. The transformation is about the y^I axis and is (only the linear transformation is shown for brevity):

$$\begin{Bmatrix} x \\ y \\ z \end{Bmatrix}^{IV} = \begin{bmatrix} \cos\beta & 0 & -\sin\beta \\ 0 & 1 & 0 \\ \sin\beta & 0 & \cos\beta \end{bmatrix} \begin{Bmatrix} x \\ y \\ z \end{Bmatrix} \tag{177}$$

or

$$\begin{Bmatrix} x \\ y \\ z \end{Bmatrix} = \begin{bmatrix} \cos\beta & 0 & \sin\beta \\ 0 & 1 & 0 \\ -\sin\beta & 0 & \cos\beta \end{bmatrix} \begin{Bmatrix} x \\ y \\ z \end{Bmatrix}^{IV} = [U]_3 \begin{Bmatrix} x \\ y \\ z \end{Bmatrix}^{IV} \tag{178}$$

For a three-bladed rotor $\beta = -60^\circ$ for the second blade and $+60^\circ$ for the third blade.

The final stiffness matrix is obtained by pre and post multiplication of $[K]$ by $[U]_3$. This gives

$$[K]_{final} = [U]_3^T [K][U]_3 \qquad (179)$$

and is a 186 x 186 symmetric matrix.

The stiffness matrix is now condensed to the number of degrees of freedom required for this study. This is accomplished by transferring the contribution of the undesired coordinates to the retained coordinates. Single coordinate elimination is employed such that

$$[K_{ij}]_{reduced} = [K_{ij}]_{final} - \frac{1}{K_{nn}} \{K\}_i \lfloor K \rfloor^j \qquad (180)$$

Where i and j refer to columns and rows and n is the coordinate of the row and column being eliminated. By successive application of 180 the stiffness matrix is reduced to 74 x 74. Figure 23 shows the coordinates retained. The reader can refer to Figure 23 for identification of the degrees of freedom which are retained in the reduced stiffness matrix.

The reduced stiffness matrix is now inverted to form the flexibility matrix. A final transformation into the collocation (dumbbell) coordinates is now made.

By definition the system deflections are given as

$$\{\delta\} = [SIC] \{F\} \qquad (181)$$

where

    $\{\delta\}$ is the deflection matrix, consisting of linear and angular deflections

    $[SIC]$ is the flexibility matrix

    $\{F\}$ is the applied force matrix

The relationship between the two linear deflections at the collocations points and the linear and angular deflections at the element elastic axis, derived for the mass matrix also apply for the stiffness matrix. Thus

77

	1	X				49	X			97	X	*	31
	2	Y				50	Y	*	11	98	Y	*	32
①	3	Z			⑨	51	Z	*	12	⑰99	Z	*	33
	4	θX				52	θX	*	13	100	θX	*	34
	5	θY				53	θY			101	θY		
	6	θZ				54	θZ	*	14	102	θZ		
	7	X				55	X			103	X		
	8	Y				56	Y			104	Y		
②	9	Z	*	1	⑩	57	Z			⑱105	Z		
	10	θX	*	2		58	θX			106	θX		
	11	θY				59	θY			107	θY		
	12	θZ				60	θZ			108	θZ		
	13	X				61	X			109	X		
	14	Y				62	Y			110	Y		
③	15	Z	*	3	⑪	63	Z			⑲111	Z		
	16	θX	*	4		64	θX			112	θX		
	17	θY				65	θY			113	θY		
	18	θZ				66	θZ			114	θZ		
	19	X				67	X			115	X	*	35
	20	Y				68	Y			116	Y	*	36
	21	Z	*	5		69	Z			117	Z	*	37
④	22	θX	*	6	⑫	70	θX			⑳118	θX	*	38
	23	θY				71	θY			119	θY		
	24	θZ				72	θZ			120	θZ		
	25	X				73	X	*	15	121	X	*	39
	26	Y				74	Y	*	16	122	Y	*	40
⑤	27	Z	*	7	⑬	75	Z	*	17	㉑123	Z	*	41
	28	θX	*	8		76	θX	*	18	124	θX	*	42
	29	θY				77	θY			125	θY		
	30	θZ				78	θZ			126	θZ		
	31	X				79	X	*	19	127	X	*	43
	32	Y				80	Y	*	20	128	Y	*	44
	33	Z	*	9		81	Z	*	21	129	Z	*	45
⑥	34	θX	*	10	⑭	82	θX	*	22	㉒130	θX	*	46
	35	θY				83	θY			131	θY		
	36	θZ				84	θZ			132	θZ		
	37	X				85	X	*	23	133	X	*	47
	38	Y				86	Y	*	24	134	Y	*	48
⑦	39	Z				87	Z	*	25	135	Z	*	49
	40	θX			⑮	88	θX	*	26	㉓136	θX	*	50
	41	θY				89	θY			137	θY		
	42	θZ				90	θZ			138	θZ		
	43	X				91	X	*	27	139	X	*	51
	44	Y				92	Y	*	28	140	Y	*	52
⑧	45	Z			⑯	93	Z	*	29	141	Z	*	53
	46	θX				94	θX	*	30	㉔142	θX	*	54
	47	θY				95	θY			143	θY		
	48	θZ				96	θZ			144	θZ		

Fourth column:

㉕	145	X		
	146	Y		
	147	Z		
	148	θX		
	149	θY		
	150	θZ		
	151	X		
	152	Y		
㉖	153	Z		
	154	θX		
	155	θY		
	156	θZ		
	157	X	*	55
	158	Y	*	56
㉗	159	Z	*	57
	160	θX	*	58
	161	θY		
	162	θZ		
	163	X	*	59
	164	Y	*	60
	165	Z	*	61
㉘	166	θX	*	62
	167	θY		
	168	θZ		
	169	X	*	63
	170	Y	*	64
㉙	171	Z	*	65
	172	θX	*	66
	173	θY		
	174	θZ		
	175	X	*	67
	176	Y	*	68
	177	Z	*	69
㉚	178	θX	*	70
	179	θY		
	180	θZ		
	181	X	*	71
	182	Y	*	72
㉛	183	Z	*	73
	184	θX	*	74
	185	θY		
	186	θZ		

*Indicates coordinates retained

Figure 23. Coordinates Retained in Stiffness Matrix.

78

$$\left\{ \begin{array}{c} \xi \\ \alpha \end{array} \right\} = \left[\begin{array}{cc} \dfrac{\overline{Y}}{d} & \dfrac{\overline{X}}{d} \\ -\dfrac{1}{d} & \dfrac{1}{d} \end{array} \right] \left\{ \begin{array}{c} h_1 \\ h_2 \end{array} \right\} = \left[U \right]_1 \left\{ \begin{array}{c} h_1 \\ h_2 \end{array} \right\} \tag{182}$$

and

$$\left\{ \begin{array}{c} F \\ T \end{array} \right\} = \left[\begin{array}{cc} 1 & 1 \\ -\overline{X} & \overline{Y} \end{array} \right] \left\{ \begin{array}{c} F_1 \\ F_2 \end{array} \right\} = \left[U \right]_4 \left\{ \begin{array}{c} F_1 \\ F_2 \end{array} \right\} \tag{183}$$

$$\left[U \right]_1^{-1} = \left[U \right]_4^{T}$$

Rewriting

$$\left[\begin{array}{cc} \dfrac{\overline{Y}}{d} & \dfrac{\overline{X}}{d} \\ -\dfrac{1}{d} & \dfrac{1}{d} \end{array} \right] \left\{ \begin{array}{c} h_1 \\ h_2 \end{array} \right\} = \left[SIC \right] \left[\begin{array}{cc} 1 & 1 \\ -\overline{X} & \overline{Y} \end{array} \right] \left\{ \begin{array}{c} F_1 \\ F_2 \end{array} \right\} \tag{184}$$

or

$$\left\{ \begin{array}{c} h_1 \\ h_2 \end{array} \right\} = \left[U \right]_4^{T} \left[SIC \right] \left[U \right]_4 \left\{ \begin{array}{c} F_1 \\ F_2 \end{array} \right\} \tag{185}$$

Hence, the final form of the flexibility matrix is

$$\left[SIC \right]_{final} = \left[U \right]_4^{T} \left[SIC \right] \left[U \right]_4 \quad (74 \times 74) \tag{186}$$

(e) __Method of Solution__ - Solution of the matrix of differential equations follows the usual flutter practice. Equation 155 is rearranged such that

$$\left[\left[SIC \right] \left(\left[m \right] + \left[\overline{F} \right] \right) - \dfrac{(1 + ig)}{\omega^2} \right] \{q\} = 0 \tag{187}$$

or

$$\left(\left[\overline{m} \right] - \lambda \right) \{q\} = 0 \tag{188}$$

79

where

$$\lambda = \frac{(1 + ig)}{\omega^2} = \lambda_R + \lambda_I \text{ (Real and imaginary parts)}$$

$$[\bar{m}] = [SIC]([m] + [\bar{F}])$$

The complex eigenvalue λ is solved for using a QR algorithm
called ALLMAT which uses Given's rotations for the elementary
unitary transformations. The Weilandt inverse power method
is used to compute the complex vectors.

The frequency and damping is then obtained from the following
relationships.

As assumed,

$$\lambda_R + \lambda_I = \frac{1}{\omega^2} + \frac{ig}{\omega^2} \qquad (189)$$

therefore

$$\omega^2 = \frac{1}{\lambda_R} \qquad (190)$$

$$g = \frac{\lambda_I}{\lambda_R} \qquad (191)$$

and

$$V = \frac{1}{k} \cdot b \cdot \sqrt{\frac{1}{\lambda_R}} \qquad (192)$$

As is the usual flutter practice, a wide range of reduced
frequencies must be swept to construct a V-g diagram.

2. Response Analysis

The Folding Dynamics Response Analysis solves for the internal
forces, moments, and torques acting at a specified node on
the wing-pylon-blade system due to externally applied airloads.
These externally applied airloads may be due to an atmospheric
gust or a maneuver.

It must be pointed out that the response analysis determines
only the incremental loads. The steady structural loading
must be added to these incremental loads to arrive at the net
load. The Feather-Stop Analysis (ARAP06) may be used to
determine the steady loads for a trimmed flight condition.
The Feather-Stop Analysis also has the capability to compute
the response during blade folding and is recommended for pre-
liminary studies where unsteady aerodynamic effects can be
neglected.

80

a. Formulation of the Response Analysis

The response analysis employs the Laplace transform-transfer function method to determine the response of the generalized coordinates to external forces. These responses are then used to calculate the transient internal loads. The general method may be explained as follows:

The dynamics of the wing-pylon-proprotor system with respect to a trim or static position can be represented by differential equations:

$$[m]\frac{d^2 q_n}{dt^2} + [D]\frac{dq_n}{dt} + [K]q_n = \left[F(t)\right] + \left[F_e(\omega^2)q_n\right] \qquad (193)$$

where

$[m]$	is the mass matrix
$[D]$	is the damping matrix
$[K]$	is the stiffness matrix
F_e	is the external aerodynamic resulting from wing motion
$F(t)$	is the externally applied forces
q	is the generalized coordinates

Assuming the classical flutter form and harmonic motion, then equation 193 is rewritten as

$$(B - \lambda I)q = F' \qquad (194)$$

where

$$B = K^{-1}m + iD\frac{K^{-1}}{\omega} - K^{-1}F_e$$

$$I = \text{identity matrix}$$

$$\lambda = \text{eigenvalue} = \frac{1 + ig}{\omega^2}$$

$$F' = \frac{K^{-1}}{\omega^2} F(t)$$

The damping matrix $[D]$ will be assumed equal to zero, hence

$$B = K^{-1}m - K^{-1}F_e$$

81

Note that if F' is set to zero equation 194 ~~will be~~ recognized as the classical flutter equation. The generalized coordinate q_i can be solved for by applying Cramer's rule

$$q_i = \frac{|(B - \lambda I)|_{F'}}{|(B - \lambda I)|} \qquad (195)$$

where the numerator $|(B - \lambda I)|_{F'}$ is the determinant of the matrix $(B - \lambda I)$ with the i column replaced by F'.

Since only a finite number of modes will define the system response, equation 195 can be simplified by evaluating it at its natural frequencies and determining the residue. The technique can be explained by writing equation 195 in matrix form and evaluating the residue at the first pole or eigenvalue, i.e.

$$q_i = \frac{|(B - b_1 I)|_{F'}}{(b_1 - \lambda) |(b_i - b_1)|} \qquad (196)$$

where

b_1 is the first eigenvalue

b_i is the remainder of eigenvalues

λ is an integration operator

The expression is thus evaluated at one frequency minus the first. Equation 196 can now be written as

$$q_i = R_1 = \frac{K_1}{b_1 - \lambda} \qquad (197)$$

where

R_1 is the contribution of the first mode to the total response of coordinate q_i

$$K_1 = \frac{|(B - b_1 I)|_{F'}}{|(b_i - b_1)|} \qquad (198)$$

The total response of q_i is then given by equation 199

$$q_i = \sum_{n=1}^{n=NP} D_n = D_1 + D_2 + D_3 \ldots \qquad (199)$$

where NP is the total number of eigenvalues.

However λ, the integration operator, is difficult to evaluate as a function of time. It is, therefore, necessary to express 199 as a transfer function to determine the coordinate transient response

$$\frac{q_i}{F} = \frac{p(\overline{Z})}{q(\overline{Z})} \tag{200}$$

This can be expressed in terms of an inverse Laplace transform

$$q_i(t) = F(t) \; L^{-1}\left(\frac{p(\overline{Z})}{q(\overline{Z})}\right) \tag{201}$$

where $\overline{Z}$ is the differential operator $\frac{d}{dt}$.

It is now necessary that a relationship be established between the operators λ and $\overline{Z}$. By definition.

$$\lambda = \frac{1 + i2\sigma}{\omega^2} \quad \text{and} \quad \overline{Z} = i\omega \tag{202}$$

where

    ω is the frequency

    2σ is the damping factor, g

hence

$$\frac{1}{\lambda} = \frac{\omega^2}{1 + i2\sigma} = - \frac{\overline{Z}^2 + \overline{Z}2\sigma\omega}{1 + 4\sigma^2} \tag{203}$$

Then rewriting equation 197

$$R_1 = \frac{K_1}{b_1 - \lambda} \tag{197}$$

then

$$\frac{\dfrac{K_1}{b_1\lambda}}{\dfrac{1}{\lambda} - \dfrac{1}{b_1}} = \frac{\dfrac{K_1}{b_1}\left(\dfrac{\overline{Z}^2 + \overline{Z}2\sigma\omega}{1 + 4\sigma^2}\right)}{\left(\dfrac{\overline{Z}^2 + \overline{Z}2\sigma\omega}{1 + 4\sigma^2}\right) + \dfrac{1}{b_1}} \tag{204}$$

Since

$$\frac{1}{b_1} = \frac{\omega_1^2}{1 + i2\sigma_1} = \frac{\omega_1^2(1 - i2\sigma_1)}{1 + 4\sigma_1^2} \tag{205}$$

We have the form

$$R_1 = \frac{\frac{K_1}{b_1}(\bar{Z}^2 + 2\sigma\omega_1\bar{Z})}{\bar{Z}^2 + 2\sigma\omega_1\bar{Z} + \omega^2(1 - j2\sigma)} \tag{206}$$

We neglect the term $j2\sigma\omega^2$, since it represents an imaginary response and steady-state component of no interest. Thus,

$$R_1 = \frac{\frac{K_1}{b_1}\bar{Z}(\bar{Z} + 2\sigma_1\omega_1)}{(\bar{Z} + \sigma\omega)^2 + \omega^2(1 - \sigma^2)} \tag{207}$$

Equation 207 is of the form $\dfrac{p(\bar{Z})}{q(\bar{Z})}$.

To inverse transform equation 207, S in the numerator is neglected and differentiated with respect to time. Only the real part of the inverse transform is used:

$$R_1 = -\frac{\mathrm{Re}\left(\frac{K_1}{b_1}\right)\omega^2}{(Z + \sigma^1\omega)^2 + \omega^2(1 - \sigma^2)} \tag{208}$$

This manipulation is made for all modes of importance. Equation 189 can be written as

$$\frac{q(t)}{F(t)} = \frac{N_O}{D_O + D_1\bar{Z} + Z^2} \tag{209}$$

where N_O, D_O, and D_1 are linear coefficients from equation 197.

The expression for the coordinate motion in finite differencing notation is then

$$q(t) = \frac{\Delta t^2(N_O F(t) + \ddot{E}_{-1}) + 4(E_{-1} + \dot{E}_{-1}\Delta t) + R_1\Delta t(2E_{-1} + \dot{E}_{-1}\Delta t)}{D_O\Delta t^2 + 2D_1\Delta t + 4} \tag{210}$$

where

Δt is the time increment

E is $\dfrac{d}{dt}F(t)$

For finite differencing

$$E = \frac{2}{\Delta t}\left(\frac{d}{dt}F(t) - \frac{d}{dt}F(t)_{-1}\right) - E_{-1}$$

$()_{-1}$ indicates the previous time step

The advantages of this method are:

1. The steady-state gain value is immediately known as

$$\frac{q'}{F} = \frac{p(o)}{q(o)} \qquad (211)$$

2. The response can be obtained very rapidly by evaluating only a few roots rather than a large system.

3. Large multiroot systems can safely be reduced by making simple approximations.

4. The magnitude of the highest retained frequency can be used to define an optimum value of Δt used for the time response.

5. The solution is valid for any time form of the forcing function without need to resolve.

6. The solution form is flexible and can be changed with a minimum of difficulty.

Approximations made during solution to reduce the root system are:

1. If roots of $p(S)$ are equal to roots of $q(S)$ within one percent, their roots effectively cancel from the transfer function and are thus removed.

2. If natural frequencies of the system (roots of $q(S)$) are greater than some value, usually 200 HZ, they are considered sufficiently far removed from the forcing frequencies to have little effect on response. These roots are neglected.

Special Notes:

1. The evaluation of the determinant of a complex 74th order matrix is a time consuming operation. Thus the matrix is reduced to a 6th order for each input made by matrix pivotal reduction techniques. The reduced 6x6 matrix then provides an equivalent system as far as evaluation by Cramer's rule is concerned. The forcing vector is also condensed to retain system eigenvalence.

2. The roots of the unforced system are available directly from the flutter analysis. These are, however, based on the assumption of simple harmonic motion, i.e. the damping parameter g is the value of structural damping required to maintain neutral stability. These may be modified for use in the response analysis using the method developed by Frueh and Miller[14]

$$\omega_{response} = \omega_{flutter} \qquad (212)$$

$$S_{response} = \tfrac{1}{2}\left[\left(1 - \left(\frac{V}{\omega}\right)\left(\frac{d\omega}{dV}\right)\right)\right] g_{flutter} \qquad (213)$$

where

V = velocity

ω = model natural frequency

$\frac{d\omega}{dV}$ = rate of change of model natural frequency with velocity evaluated at the airspeed V

This transformation must be made manually. However, it is seldom required for FPR studies since the rate of change of frequency is small in the transition mode.

3. The external forcing function F(t) is written as a unit vector and the superposition theorem employed to facilitate the representation of complicated forcing functions. The vector is calculated assuming steady-state aerodynamic theory, i.e. $C_{h_i} = 1$. The gust induced lift for aerodynamic section is then:

$$L_i = VV_g \rho C_{L_\alpha} \Delta Y_i c_i \qquad (214)$$

where

V_g = gust velocity

ΔY_i = width of strip i. For blades 2 and 3 this input is $\tfrac{1}{2} \Delta Y_i$ for blade 1 to account for blade orientation

ρ = air density

86

$$C_{L_\alpha} = \text{lift curve slope}$$

$$c_i = \text{strip semichord}$$

$$V = \text{forward velocity}$$

4. The R. T. Jones approximation to Wagner's function[10]

$$\Phi(\tau) = 1 - 0.165e^{-0.0455\tau} - 0.335e^{-0.3\tau} \qquad (215)$$

is used to account for aerodynamic lag (τ is the distance traveled in semichords).

b. Calculation of the Internal Loads

In order to determine the internal loads at a given node the linear displacements, q_n, at the dumbbell coordinates the node and at the node to its left are computed. These are then transformed into the displacements and rotations at the node and node to its left.

The torque is calculated directly from the differential twist of the nodes.

$$T = \frac{GJ_i}{\ell_i} \left[\xi_\ell - \xi_{\overline{R}} \right] \qquad (216)$$

The moment and shear are approximated by solving simultaneous equations for the deflection and slope at the tip of a cantilevered beam.

$$\delta = e_1\ell_i^3 + e_2\ell_i^2 \qquad (217)$$

and

$$\xi = 3e_1\ell_i^2 + 2e_2\ell_i \qquad (218)$$

Note that the ξ expression is equal to $\partial\delta/\partial\ell$.

The displacement at the node and node lift are then substituted into equation 217 to determine the constant e_1 and e_2. Once e_1 and e_2 are known they are used to solve for slope, θ. In general form the slopes at the nodes are

87

$$\begin{Bmatrix} \theta_1 \\ \\ \theta_2 \end{Bmatrix} = \begin{bmatrix} \ell_1{}^2/2 - \ell_2\ell_1 & -\ell_1 \\ \\ -\ell_2{}^2/2 & -\ell_2 \end{bmatrix} \begin{bmatrix} \ell_2\ell_1{}^2 - \ell_1{}^3/6 & \ell_1{}^2/2 \\ \\ \ell_2{}^3/3 & \ell_2{}^2/2 \end{bmatrix} \begin{Bmatrix} \delta_1 \\ \\ \delta_2 \end{Bmatrix} \tag{219}$$

The moment and shear are then given as

$$\bar{M} = \frac{2EI_\beta}{\ell_i}\left[\frac{3}{\ell_i}\left(\delta_{\bar{R}} - \delta_L\right) + 2\theta_{\bar{R}} + \theta_L\right] \tag{220}$$

and

$$SII = \frac{6EI_\beta}{\ell_i{}^2}\left[\frac{2}{\ell_i}\left(\delta_{\bar{R}} - \delta_L\right) + \theta_{\bar{R}} + \theta_L\right] \tag{221}$$

(This approximation is exact for a uniform beam. For a nonuniform beam, with nonuniform loading it is only approximate. However, numerous checks have established the error as small.)

88

SECTION III

CORRELATION OF THEORY WITH EXPERIMENTAL DATA

Prior to this program a considerable amount of experimental data on proprotor stability and dynamic response were available. These data proved valuable during the development and checkout of the computer programs. A wind tunnel test of a dynamically scaled model was made during this program to obtain additional data on proprotor stability at low rpm, and on the effect of feathering rate on dynamic response. A joint NASA-Bell Helicopter Company test, using the same model, provided experimental data on the stability and load characteristics during blade folding.

Appendix I contains descriptive data for the models used to obtain the experimental data shown in this section. These descriptive data are sufficient to allow the reader to conduct independent dynamic analysis.

A. WING/BLADE AERODYNAMIC INTERFERENCE

Data on wing/blade aerodynamic interference were available from a test of the model shown in Figure 24. This model was constructed specifically to investigate wing/blade aerodynamic interference. Provisions incorporated in the model to vary the proprotor to wing spacing, wing chord length, wing leading edge shape, and pylon and wing angle of attack. A three-component strain gage balance was employed to measure the hub normal and side force, pitching and yawing moments, and axial force. The wind-tunnel balance was used to measure the combined wing and proprotor forces and moments. A strain gage was located at the blade root fitting to measure the blade root bending moment in the plane of the rotor.

Figure 25 shows the correlation between theory (Program ARAP06) and the measured variation in the blade inplane bending moment as the blade passes in front of the wing. The experimental data were obtained by indexing the blade in five degree increments of azimuth and recording the bending moment. (Zero azimuth is defined to be the designated master blade normal to the upper surface of the wing.) The data have been normalized on dynamic pressure since the moments were found to vary linearly with dynamic pressure.

The oscillatory normal force correlation is shown in Figures 26 and 27. The relative influences of wing-rotor spacing, shaft angle of attack, and wing angle of attack on the oscillatory normal force are indicated.

The normal force correlation with regard to waveform is shown
in Figure 28. Although there appears to be a sizeable varia-
tion between the calculated and measured waveform, the harmonic
content at the blade passage frequency is nearly equal. Table
III compares the frequency content in terms of the blade
passage frequency. The phase angle is also shown. It is
evident that the principal difference lies with the magnitudes
and phase angles of the higher harmonics of the blade
passage frequency.

TABLE III

NORMAL FORCE HARMONIC CONTENT

Harmonic	Measured	Calculated
1 BP (3 per rev)	26 in^2, 60 degrees	25 in^2, 60 degrees
2 BP (6 per rev)	9.5 in^2, 60 degrees	14 in^2, 40 degrees
3 BP (9 per rev)	15 in^2, 10 degrees	10 in^2, 5 degrees

Measured data show very little variation in wing lift and
pitching moment due to wing-blade aerodynamic interference.
The decision to neglect the effect of the blades on the wing
in the Feather-Stop Analysis was based on this experimental
evidence.

B. DYNAMIC STABILITY CORRELATION

The model shown in Figure 29 was used to obtain dynamic
stability data for the proprotor over a range of rpm from zero
to a scale tip speed of 600 feet per second, and with the
proprotor stopped, over the full range of blade fold angles.
It should be noted that the model configuration employed for
the fold test differed somewhat from that of the rotating
test. This was the result of having to insert a fold-hinge
fitting between the blade and the hub for the blade folding
test. This fitting could not be used for the rotating tests
since it was not designed to carry centrifugal force.

The model is not scaled to represent a specific FPR design
but is representative of the dynamic and aeroelastic character-
istics of the FPR concept. The basis for the scaling is
discussed in Appendix I. The wing and blades are dynamically
scaled in beam, chord, and torsion. The pylon is not elastically
scaled but does have representative inertial properties. The
proprotor is of the gimballed, semirigid type, i.e. the blades
are rigidly attached to a central yoke which is in turn

90

attached to the hub with a gimbal. The hub may be elastically restrained and the blade pitch-flap coupling varied. The collective pitch of the blades can be remotely adjusted to control rpm.

For the folding tests a fold hinge fitting is added between the blades and the yoke and the gimbal is locked out. Controlled flexibility is included in the fitting to simulate fold hinge and blade pitch control flexibility.

1. Proprotor/Pylon Stability

Proprotor stability was determined for two model configurations. In the first configuration, the proprotor gimbal was restrained by a hub restraint spring with a rate typical of that employed in Bell's proprotor designs. This spring rate was found to be a significant factor in the stability at low rpm and was varied over a range to determine its influence. The blade pitch-flap coupling was also varied to establish its influence.

The model was also tested with the flapping locked out. However, this configuration was not typical of current helicopter hingeless rotors as the blade first elastic flapping natural frequency was approximately 1.8 per rev, and these rotors generally have natural frequency ratios of 1.15 to 1.2 per rev. The configuration was, of course, typical of a gimballed rotor configuration, where the gimbal freedom is locked out prior to blade feathering and folding.

The experimental stability data were obtained by maintaining constant rpm and incrementally increasing the wind-tunnel velocity until the model motion was lightly damped. At each velocity the model was manually excited using thin cables attached to the wing tip. The decay of the wing and proprotor motion was recorded and used to obtain frequency and damping information. Figure 30 shows a typical decay history. Figure 31 a typical variation in wing frequency and damping with velocity. Similar plots were obtained for the wing chord mode.

The calculated stability data were obtained in a similar manner. The computer program was started with the wing undeflected so that the simulated gravitational force and the airloads would excite the system natural modes. Frequency and damping were obtained from the time history of the model motions.

a. Proprotor Stability with Gimbal Free

Figure 32 shows the stability correlation with the model gimbal free. For reference the proprotor rpm at which wing-pylon modes are in resonance with proprotor excitation are indicated.

91

Where possible, the tunnel velocity was increased until the
model was neutrally stable or until the neutral stability
velocity was evident from extrapolation of a damping versus
velocity plot. However, in many cases, the instability
velocity could not be reached because of excessive vibration
and/or loads. In these cases the maximum airspeed tested is
indicated by an arrow at the data point.

In the range from 250 to 350 rpm, instability occurs in the
wing beamwise bending mode. In this instability simultaneous
wing beamwise bending and torsion are the dominant model
motions. There is very little blade flapping with respect to
space since the rotor cannot follow pylon pitching or yawing
motions at the wing beam natural frequency.

The wing beamwise instability is well understood and readily
predicted as evidenced by the correlation. The mechanism of
this instability is discussed in References 4, 5, and 6.

From 50 to 250 rpm wing torsion mode instability is predicted.
This instability is similar to the wing beam mode instability
in that it involves blade rigid-body flapping coupled with
elastic wing motion. However, the frequency of instability is
much higher; occurring at the wing torsion mode frequency,
about $2\frac{1}{2}$ times that of the wing beam mode.

At very low rpm and near zero rpm the blade rigid-body flapping
motion becomes unstable. The frequency of this instability is
close to the uncoupled frequency of the proprotor flapping on
the hub flapping restraint. Wing vertical bending and torsion
are in-phase with the flapping. At zero rpm the instability
appears as a pitching of the proprotor tip-path-plane; at low
rpm it appears as a forward precession of the tip-path-plane.
A time history of this flapping instability is shown in Figure 33.

The mechanism of the low rpm instability was not understood at
the time of the test. To gain insight into the instability
mechanism and to provide additional correlation data the model
pitch-flap coupling and hub restraint were varied.

Figures 34 and 35 show the variation in stability with these
parameters. The principal influence appears to be the flapping
restraint, with pitch-flap coupling also being destabilizing.
At the point of minimum stability, K_{HUB} = 2500 foot-pound/degree,
the uncoupled flapping natural frequency of the rotor on the
hub restraint spring is equal to the uncoupled wing beamwise
natural frequency. Thus, the instability mechanism appears
to be the frequency coincidence of the flapping and wing beam-
wise bending modes. Correlation with the low rpm data is good
from a trend standpoint and slightly conservative.

b. Proprotor Stability with Flapping Locked Out

With the blade flapping locked out blade loads limited the
maximum speed at which the model could be tested. Consequently,

92

the instability boundary could not be defined experimentally. Figure 36 compares the maximum velocity reached, with the calculated proprotor/pylon stability boundary. Note that the zero rpm instability is effectively suppressed by locking out flapping.

Correlation between the calculated and measured frequency and damping serves as a measure of the accuracy of the program with flapping locked out. Figures 37 and 38 compare the calculated and measured frequency and damping versus airspeed for $\Omega R = 600$ feet per second and zero feet per second, respectively. Note that with flapping locked out the model is more stable than it was with the blade free to flap. However, care must be taken in concluding that a hingeless rotor type would necessarily exhibit the same stability. As noted earlier, the flapping natural frequency of the blades with flapping locked out was considerably higher than that typical of hingeless rotors. Since the flapping natural frequency is known to be an important consideration in proprotor/pylon instability this model characteristic must be taken into account.[15]

c. Instability Frequency and Mode Shape Correlation

Another measure of program accuracy is instability frequency and mode shape correlation. Figure 39 compares the measured and calculated frequencies, the 1:1 line being perfect correlation. Some of the differences between the calculated and measured frequency is due to the use of calculated model mass and stiffness values in the calculations. These do not give exactly the same natural frequencies as measured in a ground vibration test of the model (see Appendix I).

The calculated instability mode shapes were also compared to the measured instability mode shapes, and found to be very close. In no case was the calculated mode of instability other than that measured.

2. Flutter and Divergence During Blade Folding

A model configuration which was felt to be prone to flutter was chosen for the blade folding tests. This involved using a blade feathering restraint with a stiffness such that the blade bending natural frequencies traverse the wing fundamental beam and chord modes as the blades fold. A representative fold hinge stiffness was used.

Prior to the wind tunnel test a model vibration survey was made. The correlation was found to be poor and as a result, the math model for the Folding Dynamics Analysis was expanded from 44 to 74 degrees of freedom. This modification improved the correlation considerably.

93

During the wind tunnel test it was not possible to approach a flutter or divergence condition. This was the result of a limitation on maximum velocity imposed by fold hinge and wing load considerations. Consequently, frequency and damping variation with velocity and fold angle must serve to indicate the accuracy of the Folding Dynamics program.

a. <u>Natural Frequency Correlation</u>

Figures 40 and 41 show the calculated and measured wing-pylon-blade natural frequency variation with fold angle, respectively. Identification of the modes was extremely difficult because of the high coupling between the blade and wing-pylon motions. As a consequence, the modes are somewhat arbitrarily defined on the basis of the frequency of the uncoupled modes. The modes are identified in Table IV.

TABLE IV

MODE IDENTIFICATION

Mode	Description	Remarks
1	Wing Fundamental Beam Bending	---
2	Mast Torsion	This mode changes to blade flapping on the feathering hinge as the blades are folded.
3	Wing Fundamental Chord Bending	---
4	Blade Beam Bending	This mode couples with mast torsion as the blades are folded. The blade bending is in-phase.
5	Blade Chord Bending	Blades out-of-phase
6,7	Blade Beam Bending	Blades out-of-phase
8	Blade Chord Bending	Blades in-phase
9	Wing Fundamental Torsion	---
10	Blade Second Beam Bending	---

94

The general trends of the calculated frequency as the blades
are folded is in agreement with the measured trends.
(Unfortunately many of the modes could not be identified
adequately during the vibration survey and are thus not shown
for all fold angles in Figure 40.)

Frequency and damping was measured versus fold angle and
velocity. Figure 42 shows the measured frequency and damping
variation with velocity. The calculated characteristics are
given for both the Feather-Stop Analysis (ARAP06) and the
Folding-Dynamics Analysis (DFAL17). The higher damping
calculated with the latter is due to neglecting stall in the
blade root region. ARAP06 included stall effects. Adjustment
of the strip width in the root region to compensate for stall
would reduce the damping calculated with DFAL17.

The correlation with regard to fold angle, shown in Figure 43,
shows the same damping trend for both analyses.

C. DYNAMIC RESPONSE

During the wind tunnel test the steady-state response of the
model was determined as a function of proprotor rpm. At each
rpm from zero to 350, in increments of 10 rpm, the pylon
accelerations, wing and blade loads, and flapping were
recorded. Then the feathering rate was progressively increased
to the power limit of the collective pitch control motor.
Testing time limitations permitted only a selected number of
speed and angle of attack combination to be evaluated.
Consequently only limited experimental data are available to
indicate the influence of airspeed and angle of attack.

During the correlation study the system steady-state response
was first calculated by making runs at selected proprotor rpm
and allowing the system to stabilize. The system steady-state
response was then determined from the calculated time history.
These calculations were made early in the correlation study
and showed the computer representation of wing-blade inter-
ference to be in error. After the program was corrected, the
steady-state response was not recalculated because of the large
amount of computer time required. However, extrapolation of
the response at various rates of feathering to zero rate,
indicates reasonable correlation with the steady-state response.

A flight condition felt to be typical of the FPR transition mode was chosen for the model test; an airspeed of 180 knots and a shaft angle of attack of zero degrees. The wing angle of attack was 3.6 degrees, less than that required for 1g flight at 80 knots. Flaps, which were not available on the model, would be used to achieve the required lift coefficient while maintaining zero shaft angle of attack.

Figures 44 and 45 show the steady-state pylon vibration at the blade passage frequency and harmonics of the blade passage frequency, respectively, versus rpm. Note that the response at the blade passage frequency is dominant. The one-third blade passage frequency (one per rev) response shown for the wing beam and chord modes in Figure 45 is due to model rotor out-of-balance and out-of-track and is felt to be higher than representative of full-scale since small scale model tolerances are generally proportionally larger than full-scale.

Figure 46 shows the measured steady-state blade loads versus rpm. Noteworthy is the absence of large buildups in load when the rotor rpm is such that a rotor blade natural frequency is in resonance with aerodynamic excitation.

As noted earlier, the basic configuration involved a gimballed rotor with moderate hub restraint. For the steady-state response run the mast was aligned close to parallel to the test section centerline. (The measured mast pitch was 0.6 degrees; the mast yaw was not measured.) Nevertheless, large amplitude flapping was encountered. Figure 47 shows the total flapping of the red blade as a function of proprotor rpm.

1. Response Correlation

The influence of blade feathering rate was evaluated by progressively increasing the feathering rate up to the collective motor limit. The slowest rate attained was approximately 2 degrees per second, which caused the rotor to stop in 30 seconds (0.75 degrees per second and 82 seconds respectively, full-scale). The highest rate was approximately 150 degrees per second, which caused the rotor to stop in 0.4 seconds (55 degrees per second and 1.1 seconds respectively, full-scale).

96

Several observations during the tests should be noted at this time: (1) once the zero rpm collective pitch setting was determined, and the collective limit set, there was no requirement to change the setting for different tunnel speeds or shaft angles. (2) The rotor blades were virtually self-indexing. The rotor always stopped with one blade pointed outward from the wing. This is a result of the wing-blade aerodynamic interference.

Figure 48 shows a time history of model accelerations and loads during a slow stop (20 seconds full-scale). The buildups caused by traversing resonant rpm are noted. For comparison time histories of a fast stop (1.5 seconds full-acale) and of a fast start (1.1 seconds) are shown in Figures 49 and 50, respectively. The response during unfeathering of the proprotor was observed to be, in general, si.ghtly less than during feathering.

A computed time history of a fast stop (1 second, full-scale) is shown in Figure 51. Note that the general character of the response is similar to that of Figure 49. The primary difference between the calculated and measured response is the absence of one-per-rev response in the calculated history.

Sensitivity to rate was evaluated by plotting the response occurring at the system natural frequencies, versus feathering rate. Figures 52 through 56 compare the calculated and measured rate sensitivity to the inverse of the time to feather or unfeather the rotor. The feathering rate is related to the inverse of the time to feather, ΔT, as follows:

$$\text{Feather Rate Degrees Per Second} = (108.8^\circ)(1/\Delta T) \qquad (222)$$

In general, the correlation between theory and measured response is excellent.

Several noteworthy observations can be made from the feathering rate data: (1) Even at the fastest feathering rates, blade stall was not evident. Figure 54 shows that the wing chordwise peak transient bending moment varied almost linearly with rate. Had the blades stalled at the higher rates the transient moment would fall off. (2) The valley in the wing chordwise moment was the only indicator of an "optimum feathering rate" observed during the test. Based on the chordwise moment valley,

97

the optimum feather time would be about 2.75 to 3 seconds.
Figures 52 and 53 indicate that faster feathering rates do
not provide a significant reduction in other system responses.
(3) Increasing the feathering rate reduces the resonant buildup
in blade loads. But very fast rates produce an impulsive
response in the wing chordwise bending moment. This results
from the impulsive nature of the proprotor aerodynamic loading
at the higher rates. However, over the range of rates tested,
blade loads were very low and were not a limitation on the
testing. (4) Flapping freedom must be restrained prior to
feathering the blades. Figure 56 shows that faster rates
increase the transient flapping during proprotor stopping.
The characteristics may be explained by considering the way in
which the blade flap-damping varies during feathering. The
flap-damping coefficient is given as[7]

$$C = \frac{\gamma}{16} \cos\phi_{3/4} \tag{223}$$

where

$$\phi_{3/4} = TAN^{-1}\left(\frac{U}{\Omega\overline{R}}\right) \tag{224}$$

the inflow angle at the blade 3/4 radius, γ is blade lock number.

As the blade is feathered the inflow angle varies approximately
in proportion to the blade collective pitch. According to
equation 223 the flap damping then decreases as the blade is
feathered and increases as the blade is unfeathered. And
according to Reference 16, this time variation in the damping
parameter of a single degree-of-freedom system will cause the
apparent damping to be less when the damping decreases with
time, and more when the damping increases with time. Since
flapping amplitude is controlled by the flap damping, the
characteristics shown in Figure 56 are to be expected.

2. Other Factors Influencing Dynamic Response Characteristics

(1) Flapping Lockout - Prior to this study, it was thought
that flapping could be locked out during the feather/stop
sequence, at about 25-30 percent of the hover rpm. The effect
of feathering rate on the dynamic flapping response (Figure 56)
and practical considerations, however, indicate flapping should
be locked out prior to feathering.

Locking out flapping did not significantly influence the wing
and pylon dynamic response. Both test data and calculated
pylon responses show the acceleration to be close to that with

98

the flapping free. The blade tip deflections were not measured during the model test, but were observed to be small.

The principal influence of locking out flapping freedom is a mast angle of attack limit resulting from blade loads. (Locking out the flapping freedom increases the one per rev out-of-plane loads since flapping acts to relieve the one-per-rev airloads.) Figure 57 shows the measured angle of attack limit established by the model test. Note that this limit would only apply during the feather/stop sequence. The angle of attack limit with the gimbal free is much higher.

(2) Angle of Attack - Shaft angle of attack has a significant influence on the dynamic response. Figure 58 shows a time history of a blade feathering at a shaft angle of attack of 5.6 degrees. The most apparent difference with the zero angle-of-attack history, Figure 49, is the impulsive response at the wing beam natural frequency, seen in the wing beam bending moment and torsion traces. This is the result of the sudden buildup in normal force as the proprotor stops. (The normal force is essentially proportional to the inflow angle.) Figure 59 shows how the beam response varies with feathering rate. Note that while a slow feather rate is indicated to be desirable, a shaft angle of attack of 5.6 degrees during the feather/stop sequence is considered of transient nature only. Operationally, the feather/stop sequence should be made with a shaft angle of attack near zero degrees.

Another noteworthy observation can be made from Figure 58. The blade loads buildup remain moderate even at large shaft angles of attack.

(3) Airspeed - Three airspeeds were investigated during the feather/stop test. From the test data it appears that the response amplitude increased essentially linearly with airspeed for a constant wing lift coefficient. This is logical, since the system damping is proportional to velocity, whereas the airload forcing function is proportional to velocity squared. At resonance the response amplitude is proportional to the ratio of the forcing function divided by the damping. Hence the response would be expected to be proportional to velocity.

In Section IV, the influence of airspeed on response is studied in more detail. When the lower wing lift coefficient with increasing airspeed and consequent lower wing upwash is accounted for, the net effect is a negligible influence of airspeed on response.

3. Response During Blade Folding

In the blade folding configuration the model was tested over the range of airspeed, fold angle, and shaft angle-of-attack indicated in Figure 60. Wing and blade load considerations limited the envelope investigated.

As noted earlier in this section, there was no evidence of flutter, divergence, or buffet during the testing. The data presented in this report therefore deals only with the steady load correlation.

The airstream oscillation capability of the 16-foot TDT wind tunnel was employed to investigate the frequency response characteristics versus fold angle. Unfortunately the measured airstream flow angularity data appears questionable. The flow angle data do not agree with previous flow angle measurements and the zero frequency response per degree of indicated flow angle is too low. Consequently, no correlation with measured frequency response is presented here. To indicate the correlation between theory and measured loads data, the wing beam bending at 15 percent semispan, blade beam and chord bending at 35 percent radius, and the blade spindle chord moments and torques were used.

Figures 61, 62, and 63 compare the calculated and measured loads for the wing beam versus fold angle, velocity, and shaft angle of attack. The correlation is felt to be very good. (The wing lift curve slope used in the analysis is based on measured data for the model.)

The calculated and measured spindle torque is shown as representative of the blade load correlation. Figures 64, 65, and 66 show how the spindle torque varies with fold angle, angle of attack, and airspeed. The peak at a fold angle of 35 to 45 degrees is evident. A significant load characteristic during blade folding is evident in Figure 66. The blade loads variation with airspeed, at partial fold angles, does not follow the usual velocity-square ratio. This is the result of deflections of the blade and control system reducing the blade angle of attack. This is similar to the gust load alleviation characteristic of swept wings.

Another characteristic noted in the tests is higher than predicted blade loads at fold angles near 90 degrees as shown in Figure 64. This is theorized as being caused by the wing-tip vortex tending to lift the outboard blade as the blade folds close to the vortex. The analysis does not include a tip vortex representation, hence the lower calculated loads. Figure 67 further illustrates this effect.
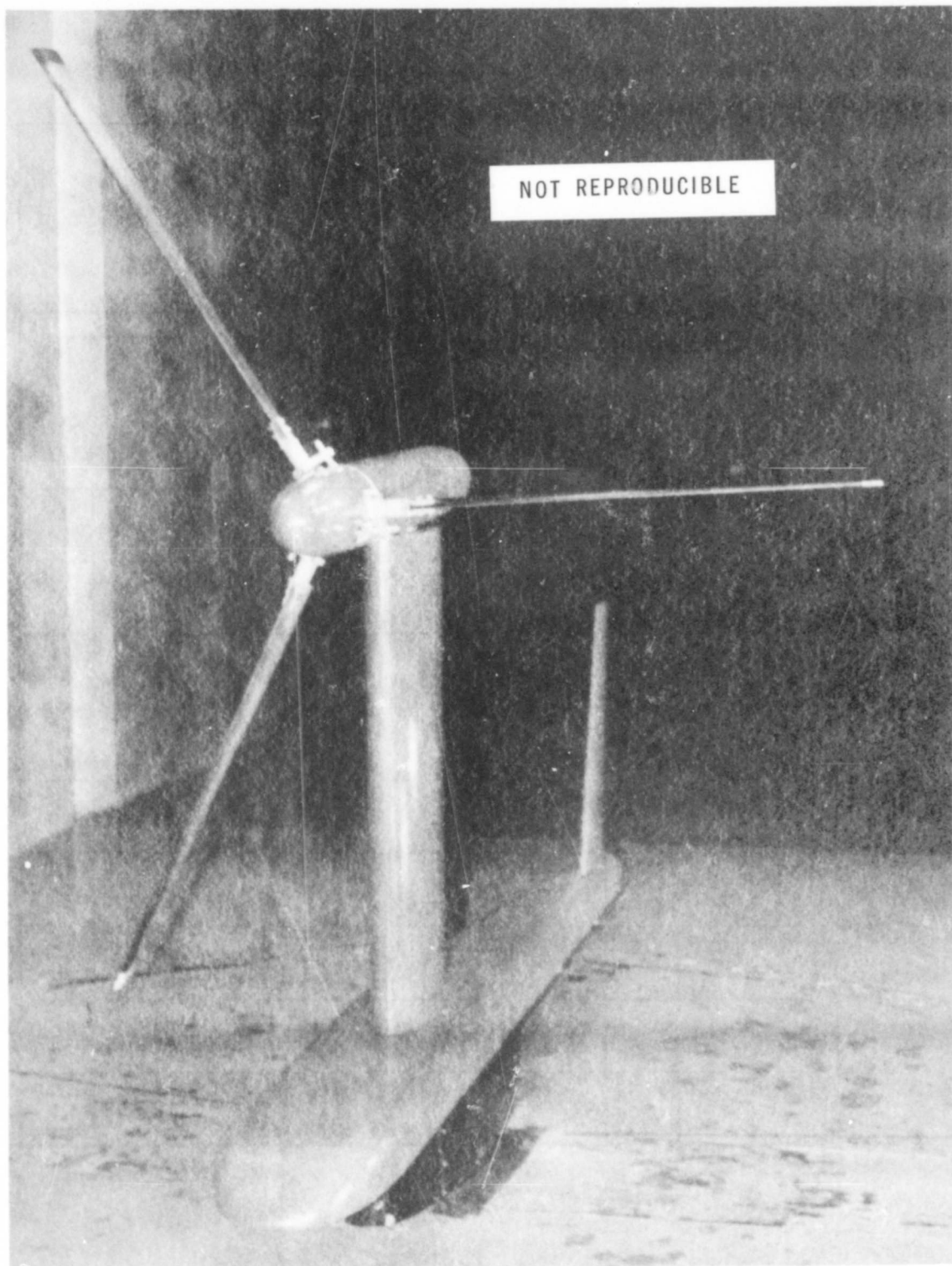
Figure 24. Model Used to Obtain Wing-Blade
Aerodynamic Interference Data

101
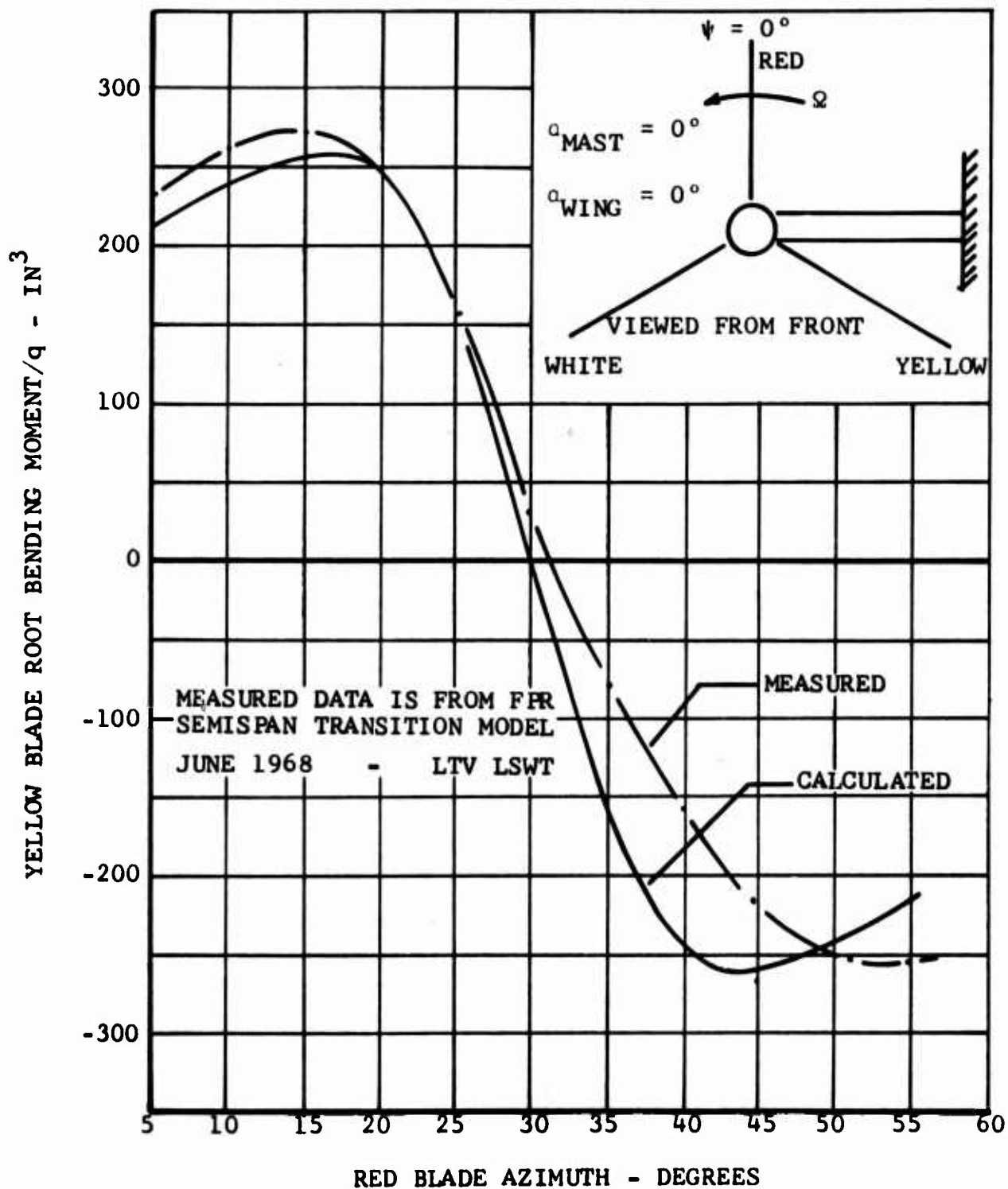
Figure 25. Correlation Between Theory and Measured
Blade Root Inplane Bending Moment
(Model Parameters)

102
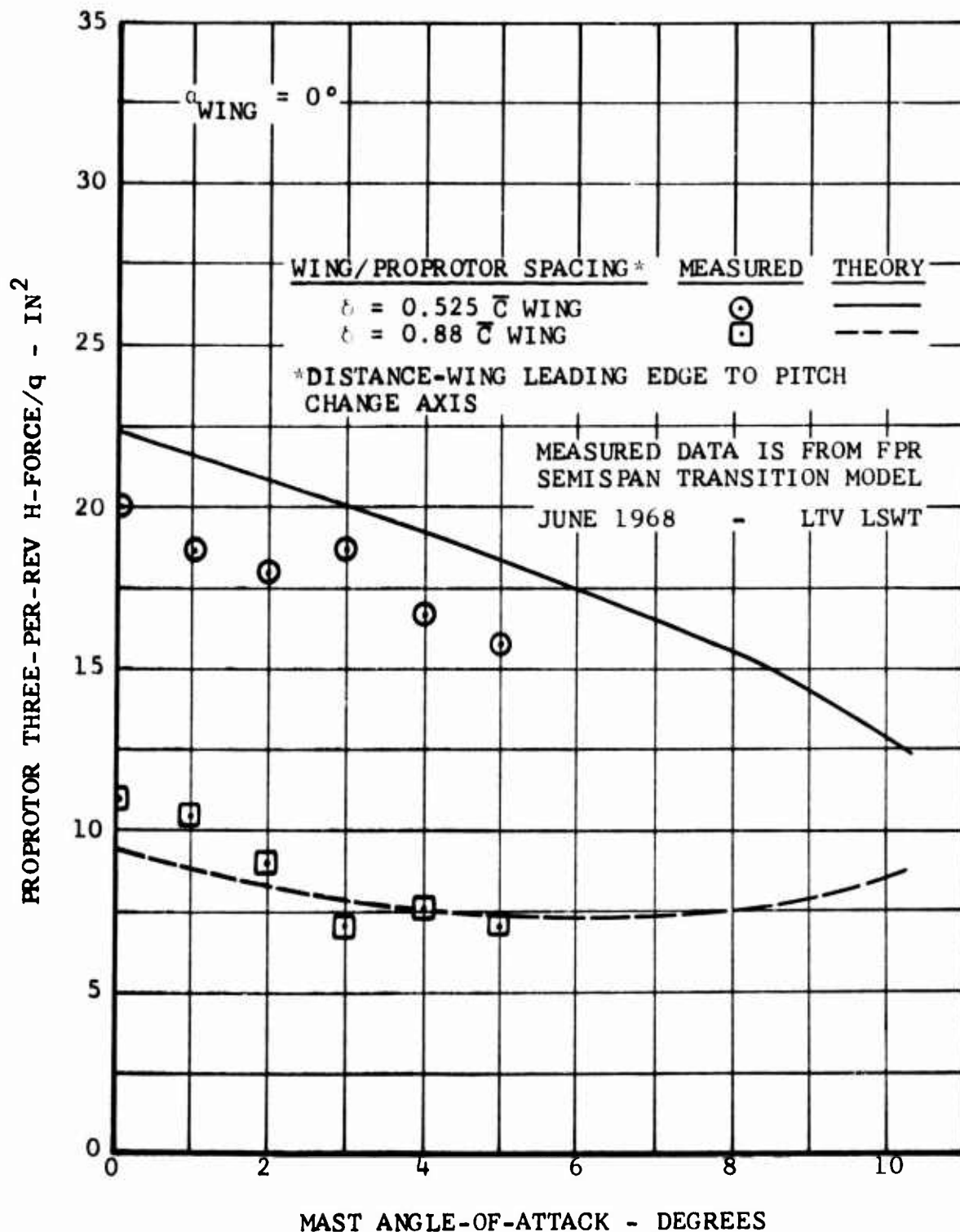
Figure 26. Correlation Between Theory and Measured Effect of Shaft Angle of Attack on Oscillatory Normal Force (Model Parameters)

103
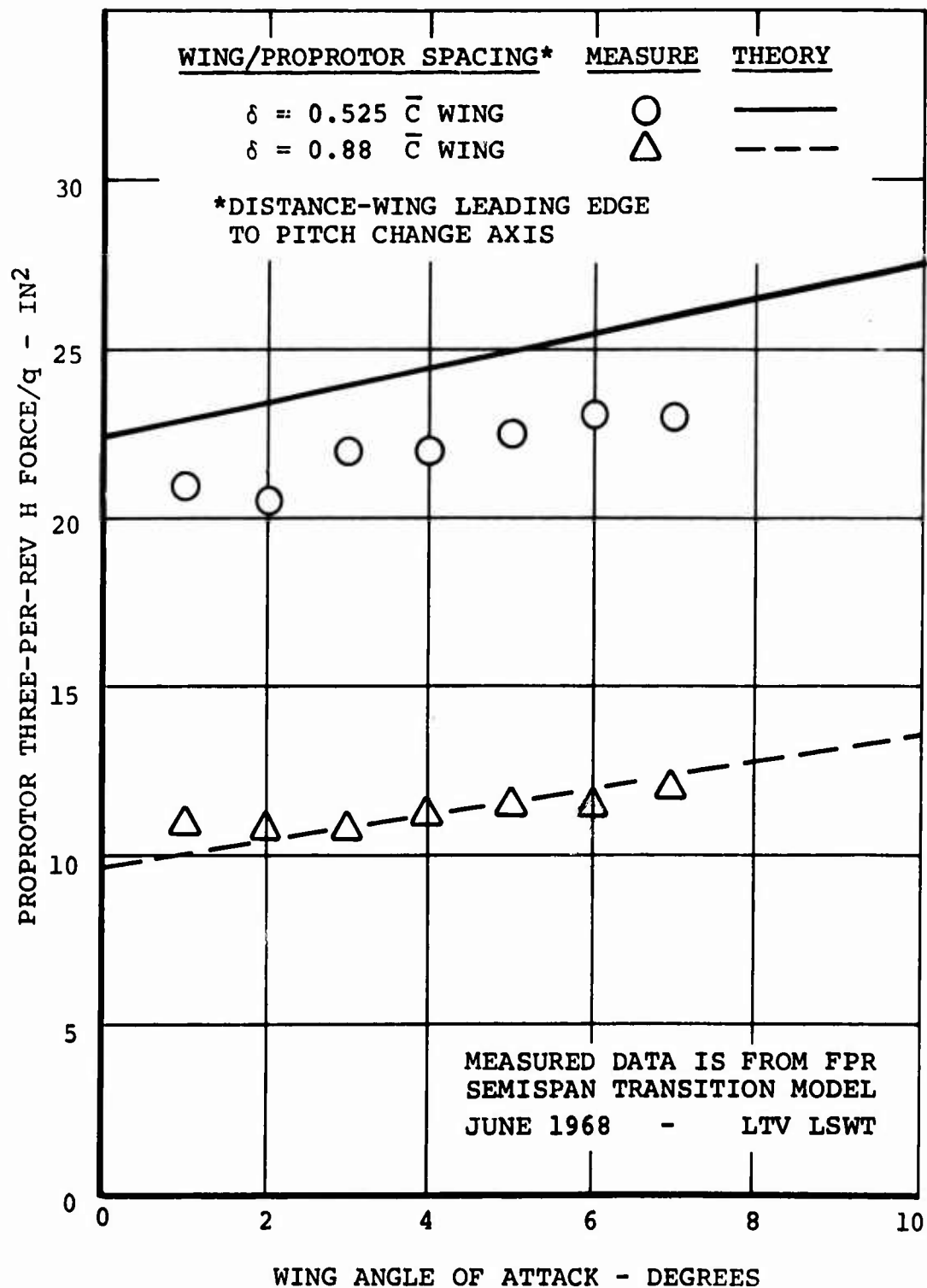
Figure 27. Correlation Between Theory and Measured Effect of Wing Angle of Attack on Oscillatory Normal Force (Model Parameters).

104
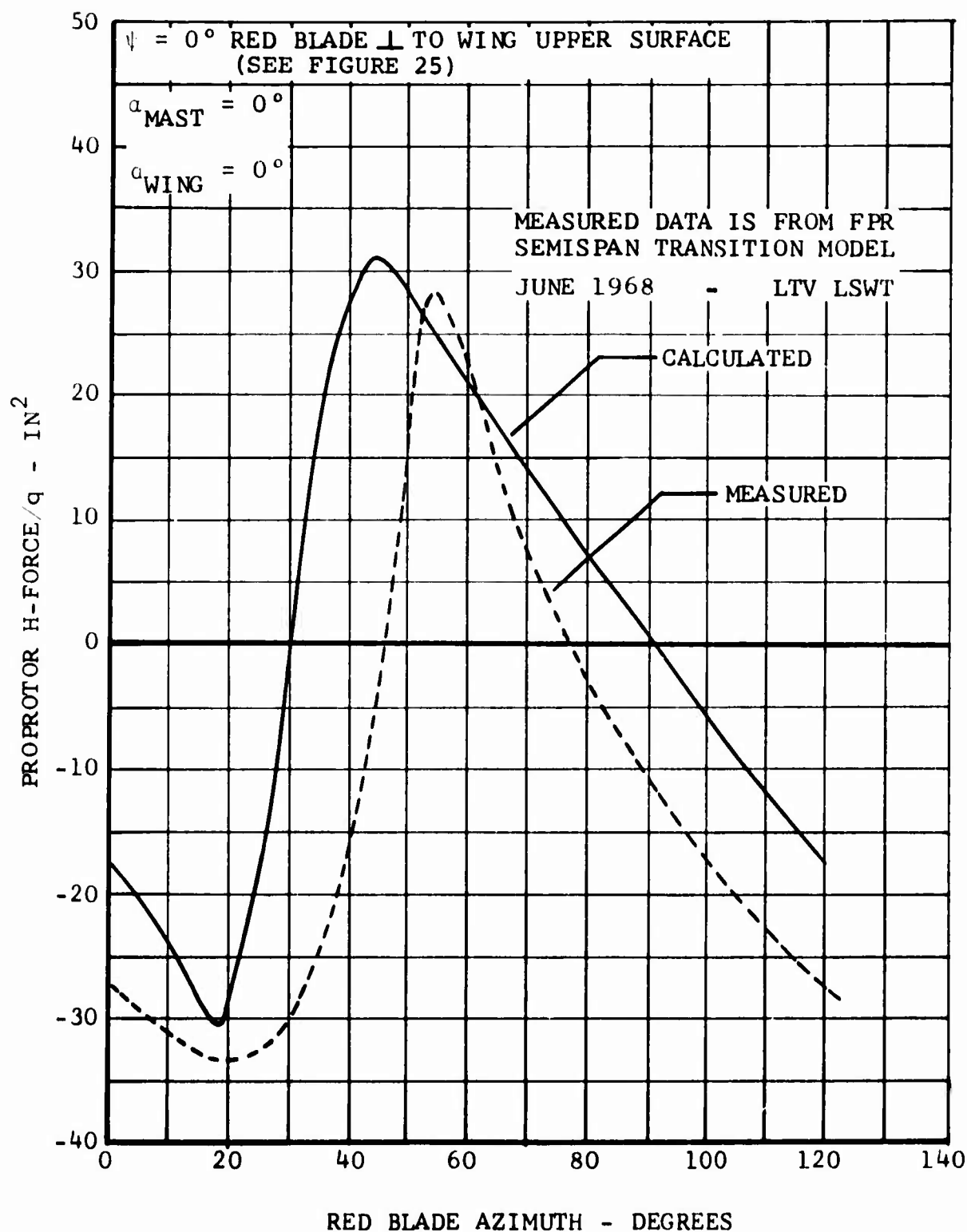
Figure 28. Correlation Between Theory and Measured Shapes of Oscillatory Normal Force (Model Parameters).
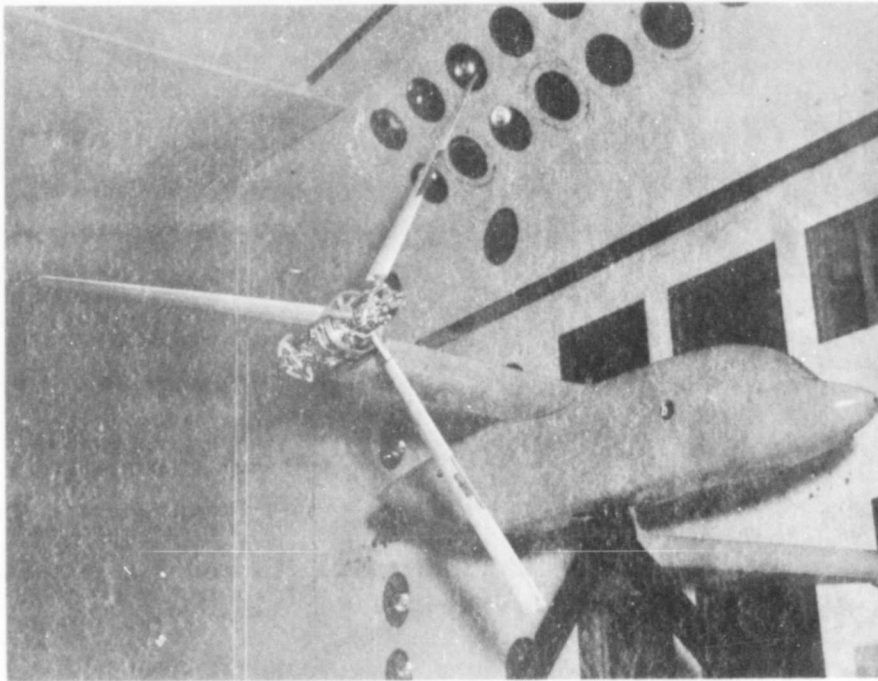
a. Feather-Stop Configuration

NOT REPRODUCIBLE
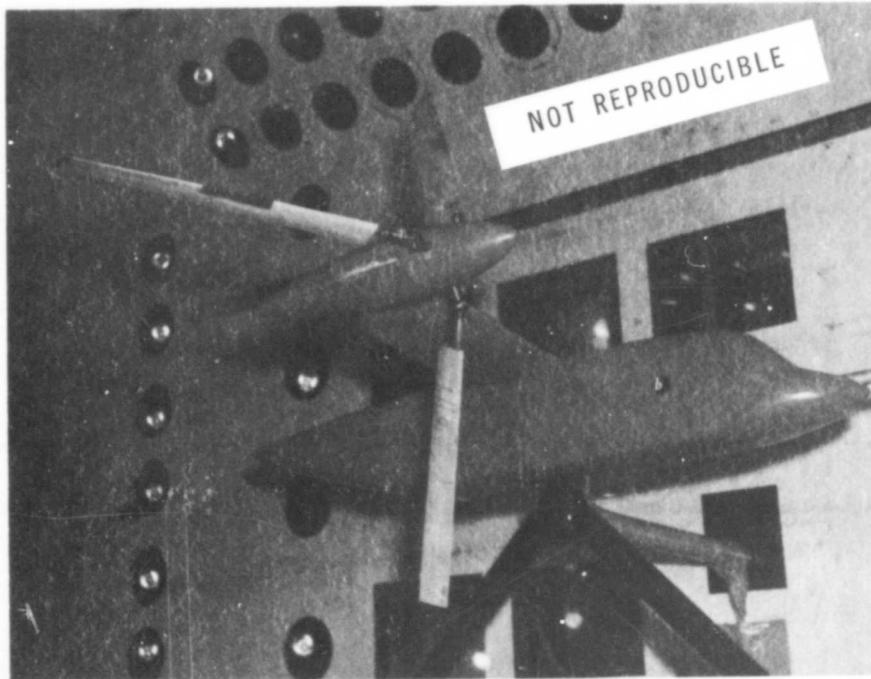
b. Folding Configuration

Figure 29. Model Used to Obtain Dynamic
Stability Data

106

WING BEAM (15%)
1100 in-lb/in

WING CHORD (28%)
581 in-lb/in

WING TORSION (15%)
192 in-lb/in

BLADE BEAM (35%)
102.12 in-lb/in

PITCH LINK
5.55 lb/in

FLAPPING

AZIMUTH

AIRSPEED =
α_{MAST} = 0.
α_{WING} = 3.
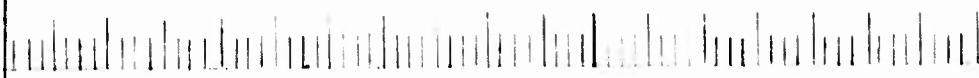
Figure 30. Time
Insta
Frequ

AIRSPEED = 175 KT, SIMULATED
$^\gamma{}_{MAST}$ = 0.6°
$^\gamma{}_{WING}$ = 3.6°

.1 SEC

1 REV

0. Time History of Proprotor Pylon
   Instability at Wing Beam Natural
   Frequency

107

3

3   4
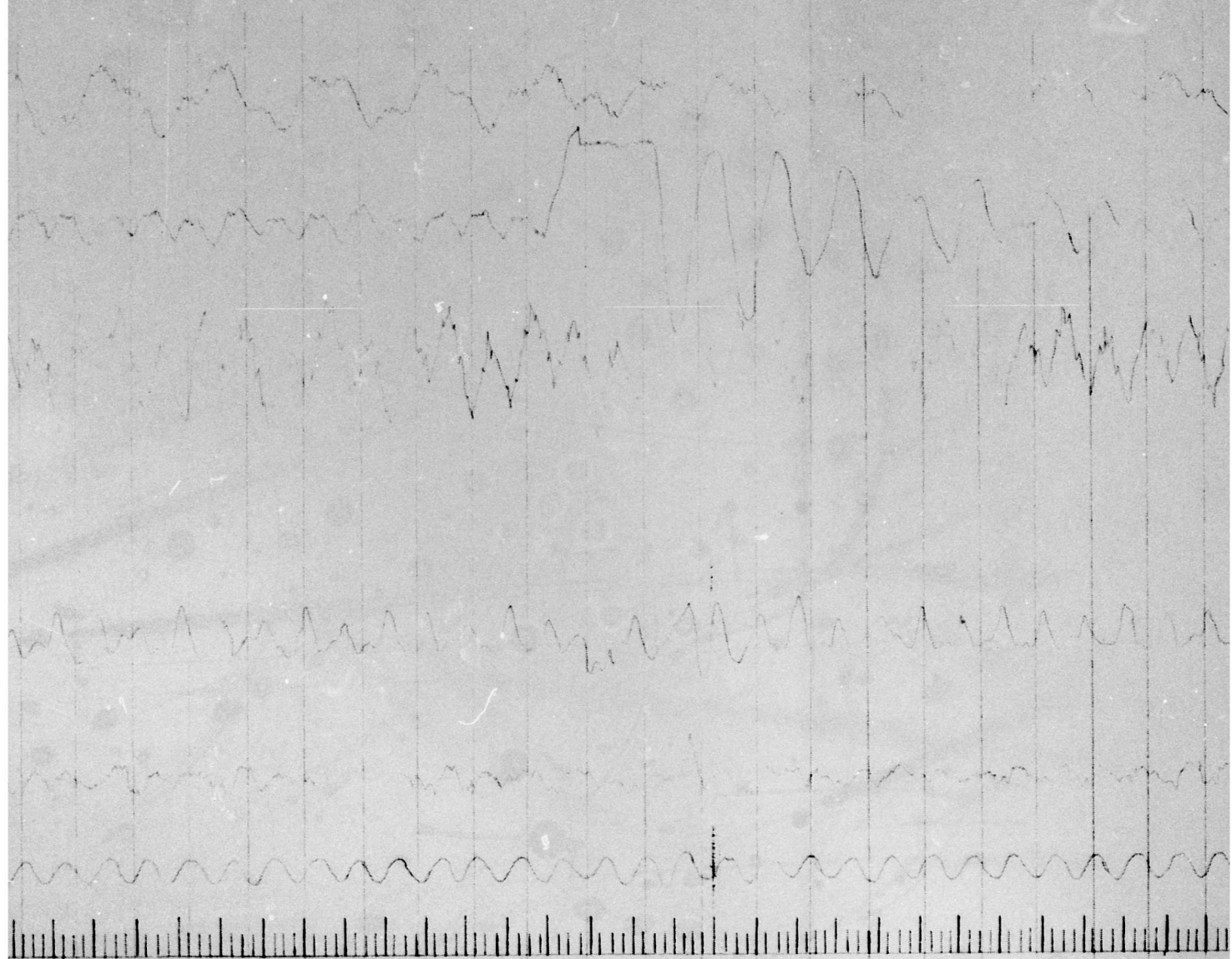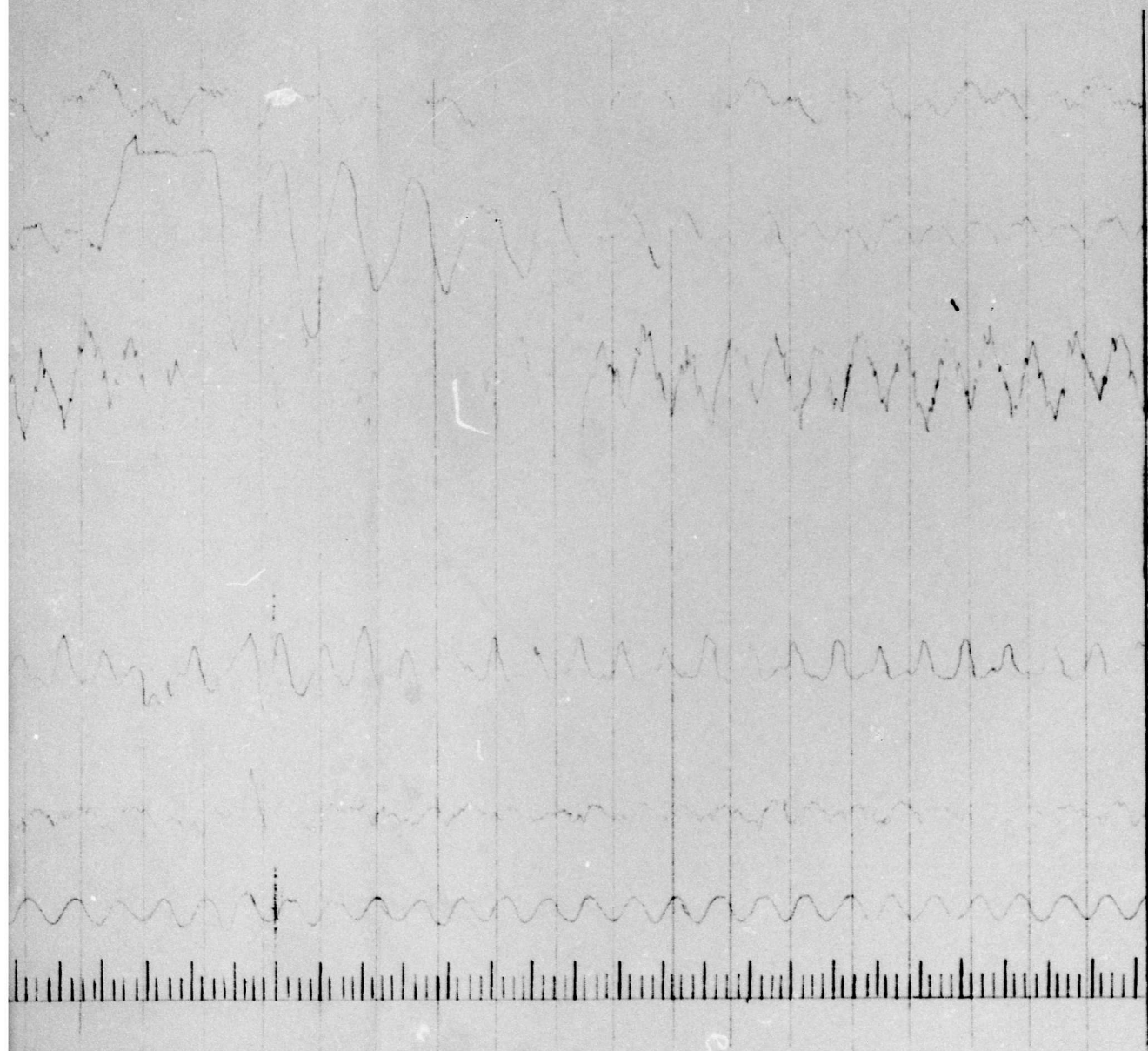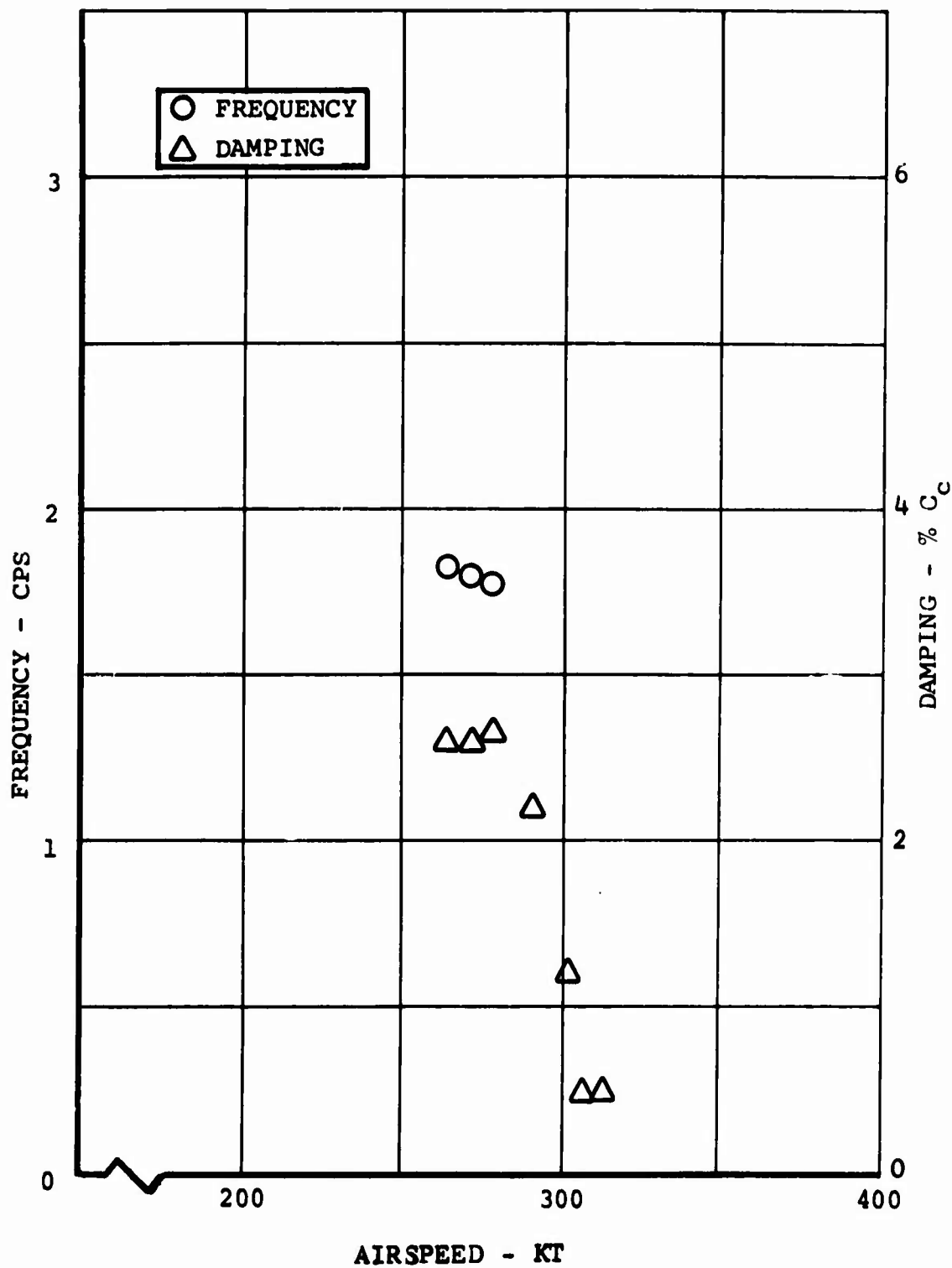
Figure 31. Example of Measured Wing-Beam Frequency
and Damping Variation with Airspeed,
300 rpm.
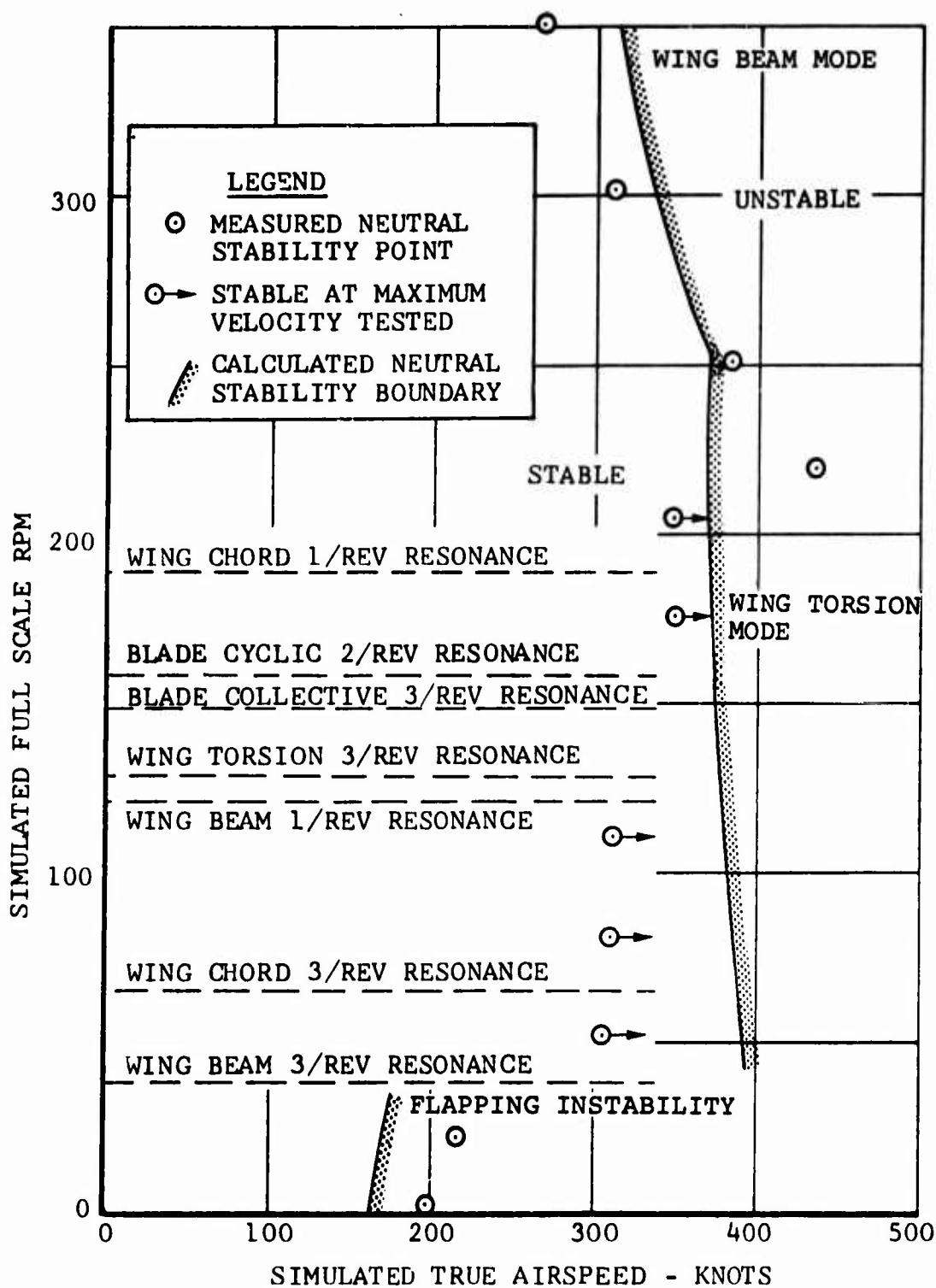
Figure 32. Correlation Between Theory and Measured
            Proprotor Stability Boundary, Gimbal
            Free.

WING BEAM (15%)
1100 in-lb/in

WING CHORD (28%)
581 in-lb/in

WING TORSION (15%)
192 in-lb/in

XMSN VERT ACC
±1.38 g/in

CA VERT ACC
±1.40 g/in

CA LONG
ACC ± 1.32 g/in

BLADE BEAM (35%)
102.12 in-lb/in

BLADE CHORD (35%)
75.3 in-lb/in

PITCH LINK
5.55 lb/in

FLAPPING

.1 SEC
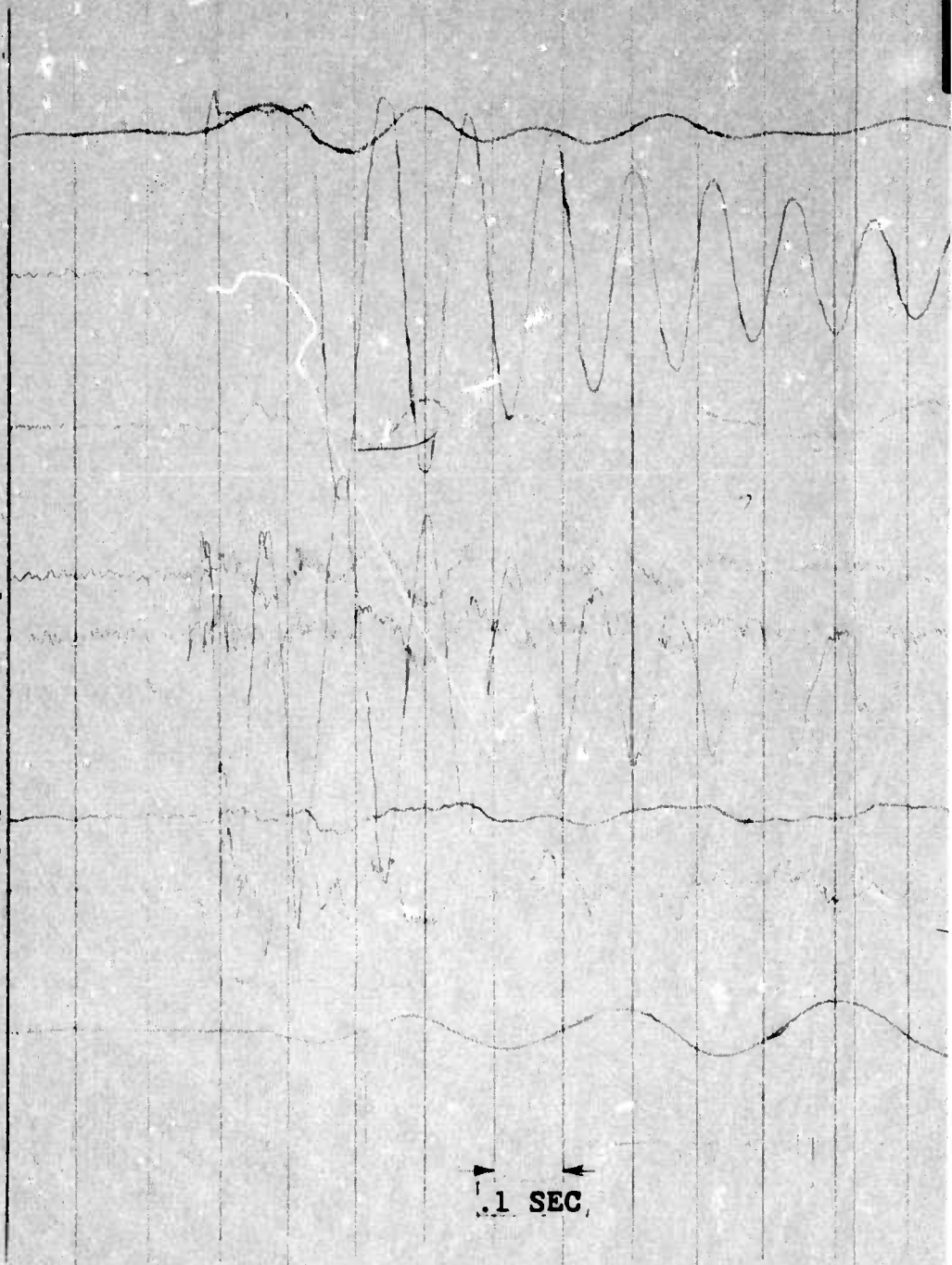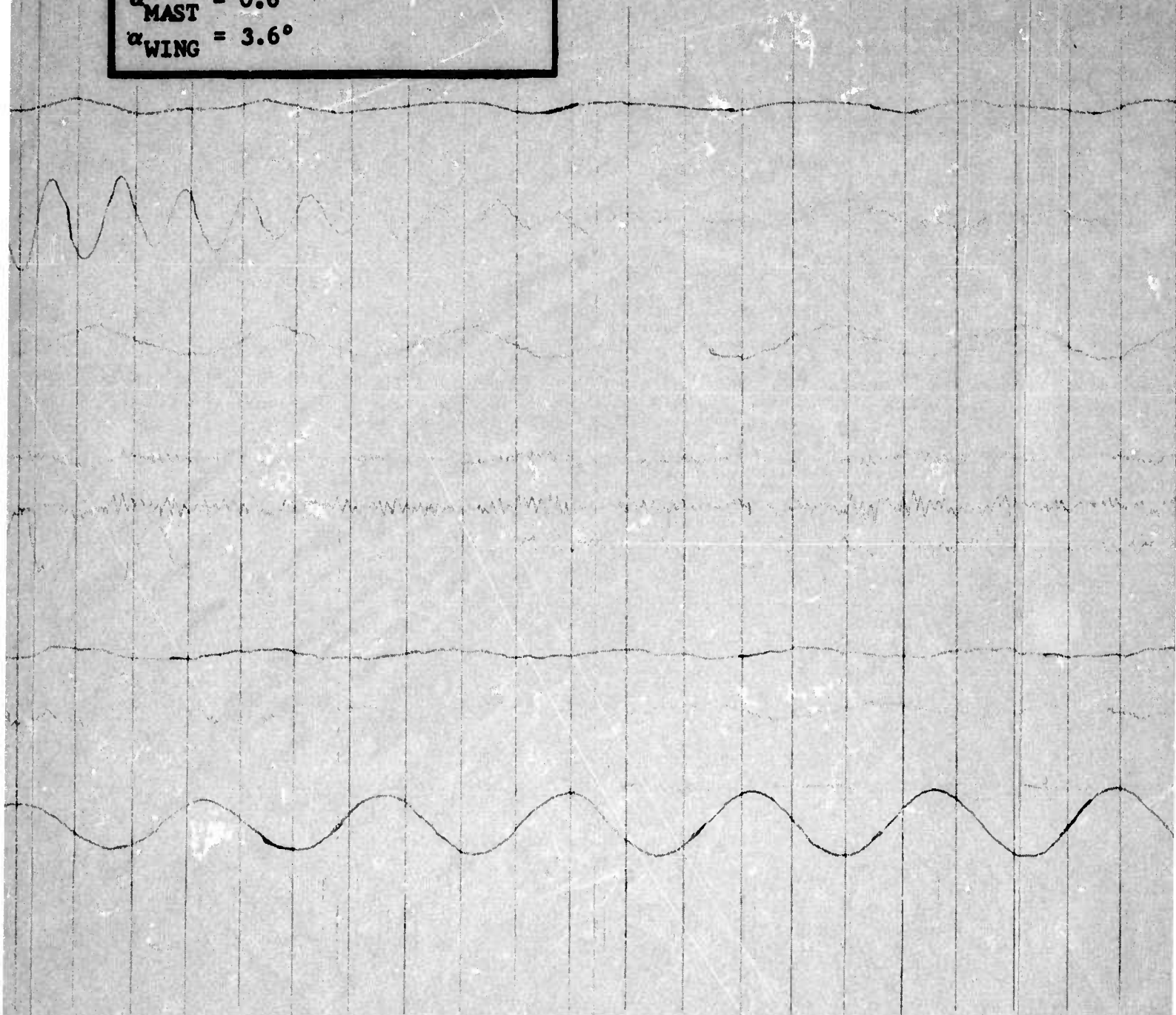
Figure 3

Figure 33.   Time History of Zero RPM Flapping
            Instability

110

3
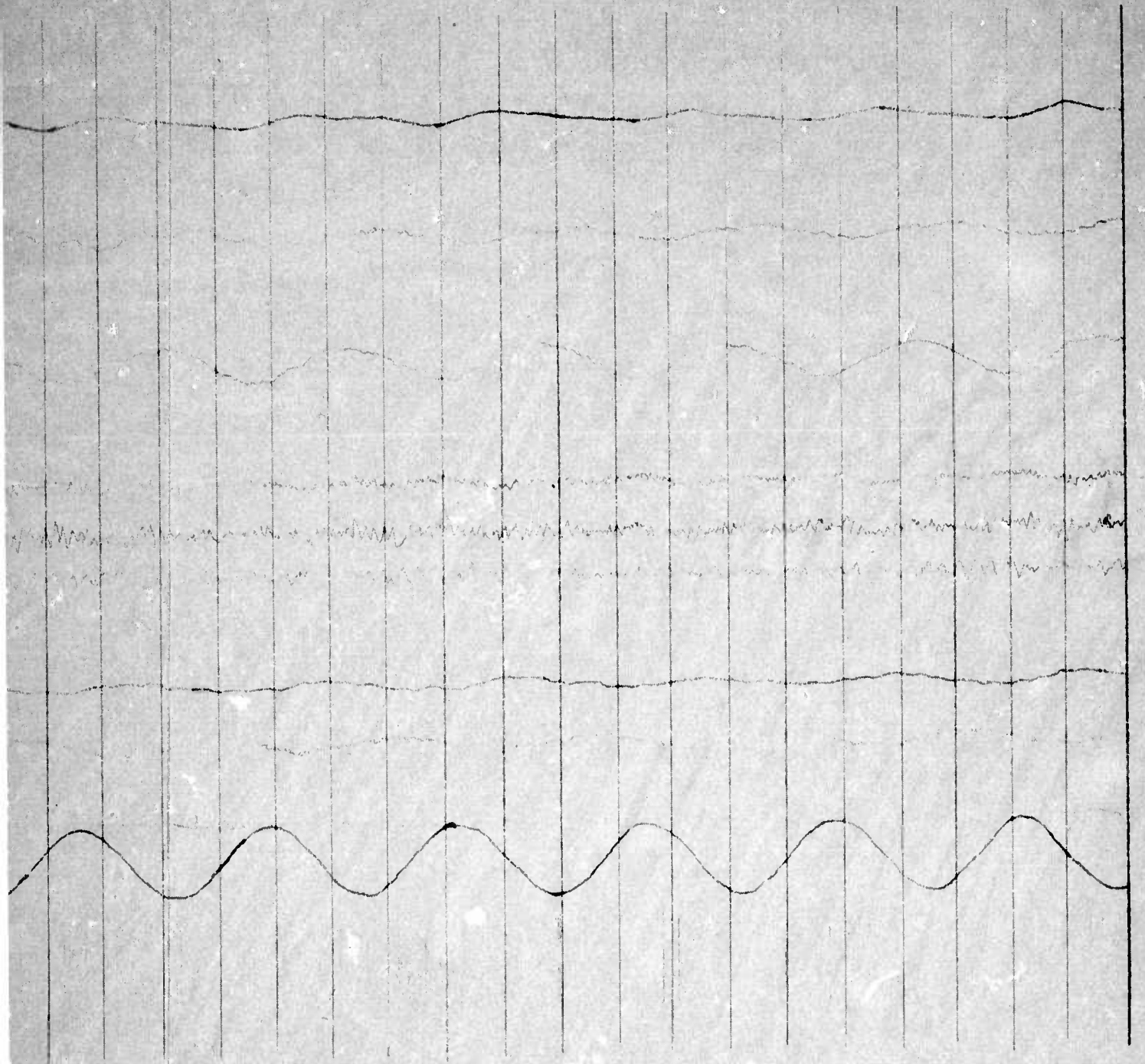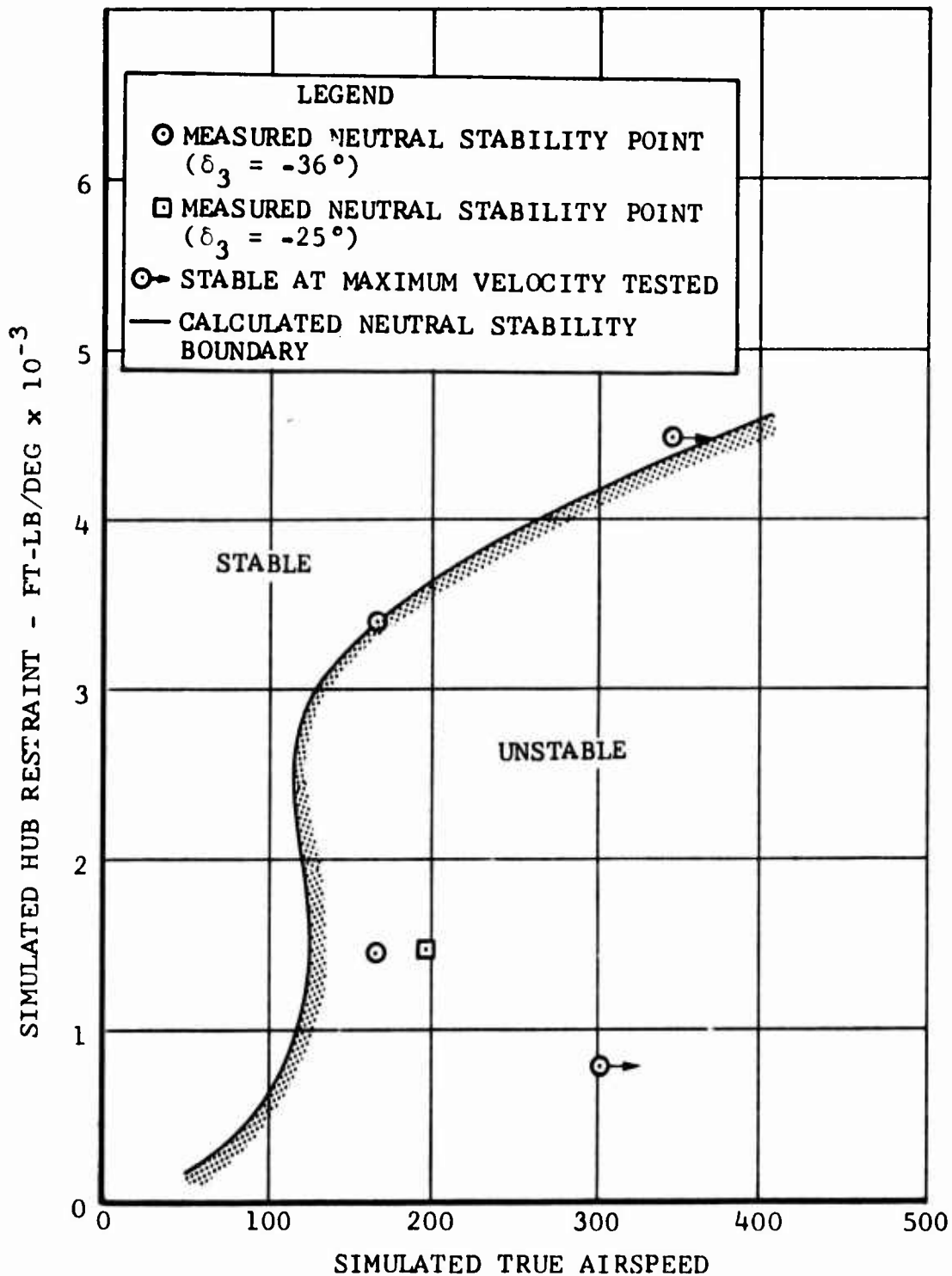
Figure 34. Correlation Between Theory and Measured
Effect of Hub Restraint on Zero RPM
Flapping Stability.

111
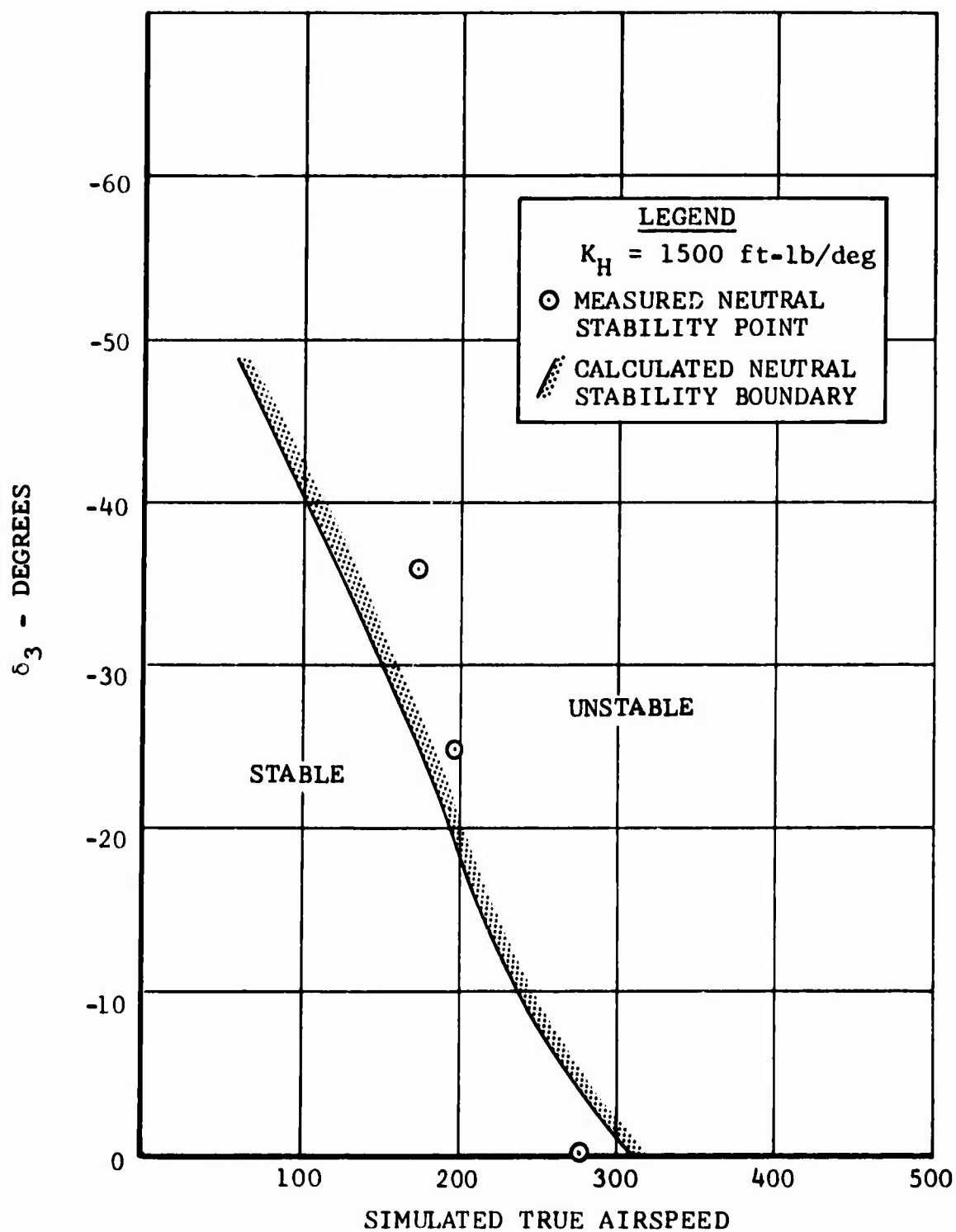
Figure 35. Correlation Between Theory and Measured
Effect of Pitch-Flap Coupling on Zero
RPM Flapping Stability.

112
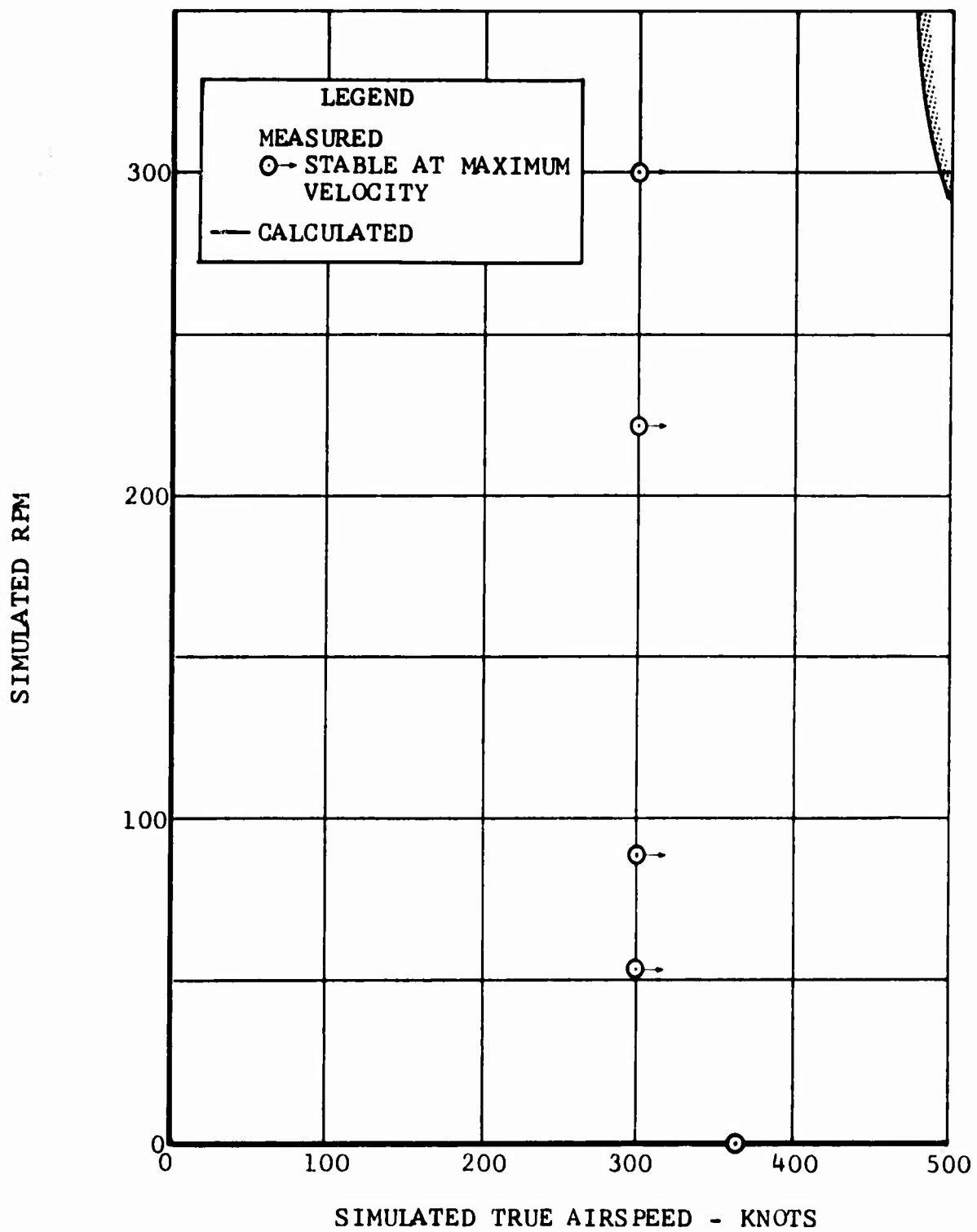
Figure 36. Airspeed - RPM Envelope Explored With
Gimbal Flapping Freedom Locked Out.

113
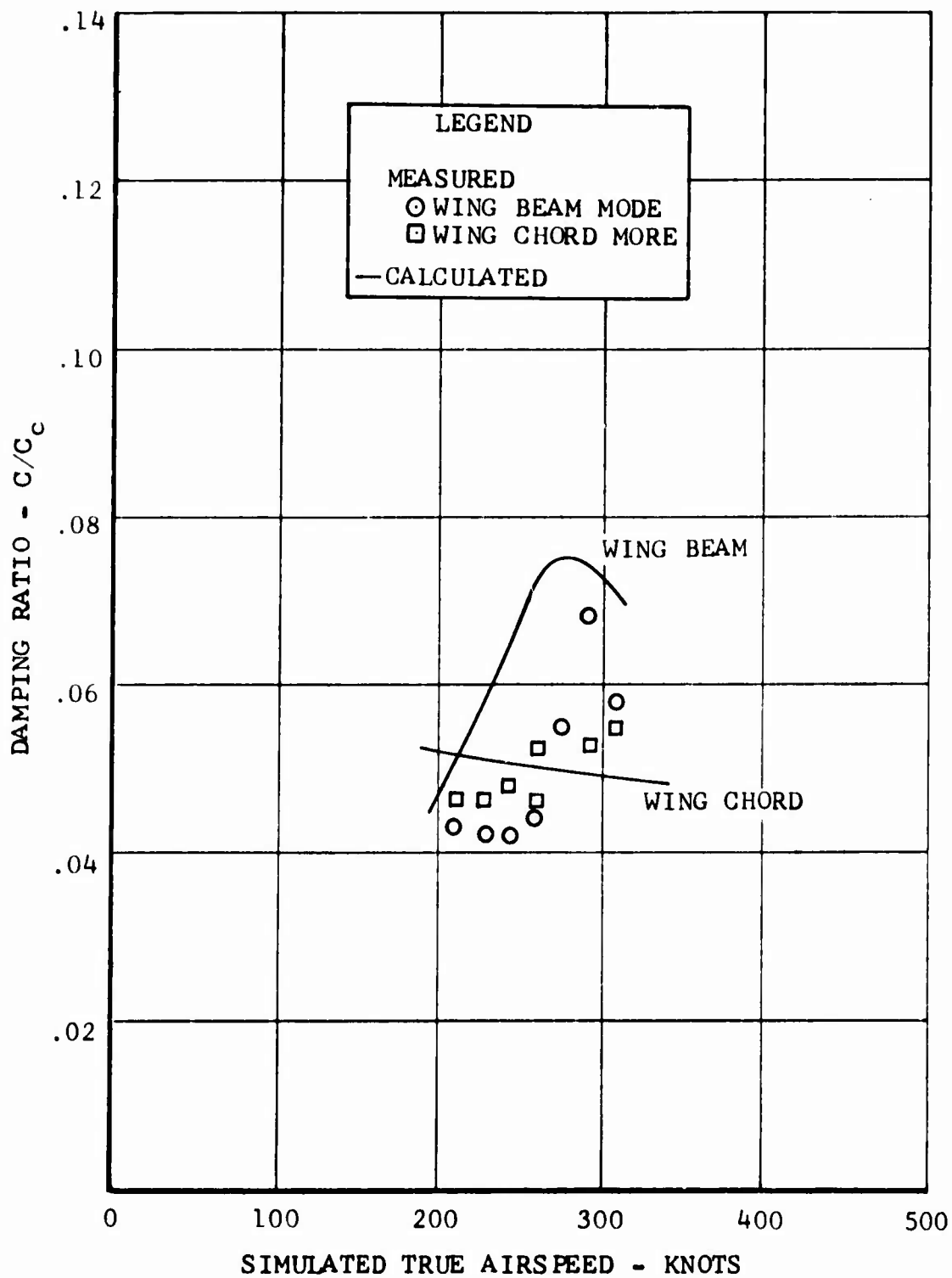
Figure 37. Correlation Between Theory and Measured
Wing Beam and Chord Damping, Gimbal
Flapping Freedom Locked Out, 300 RPM.
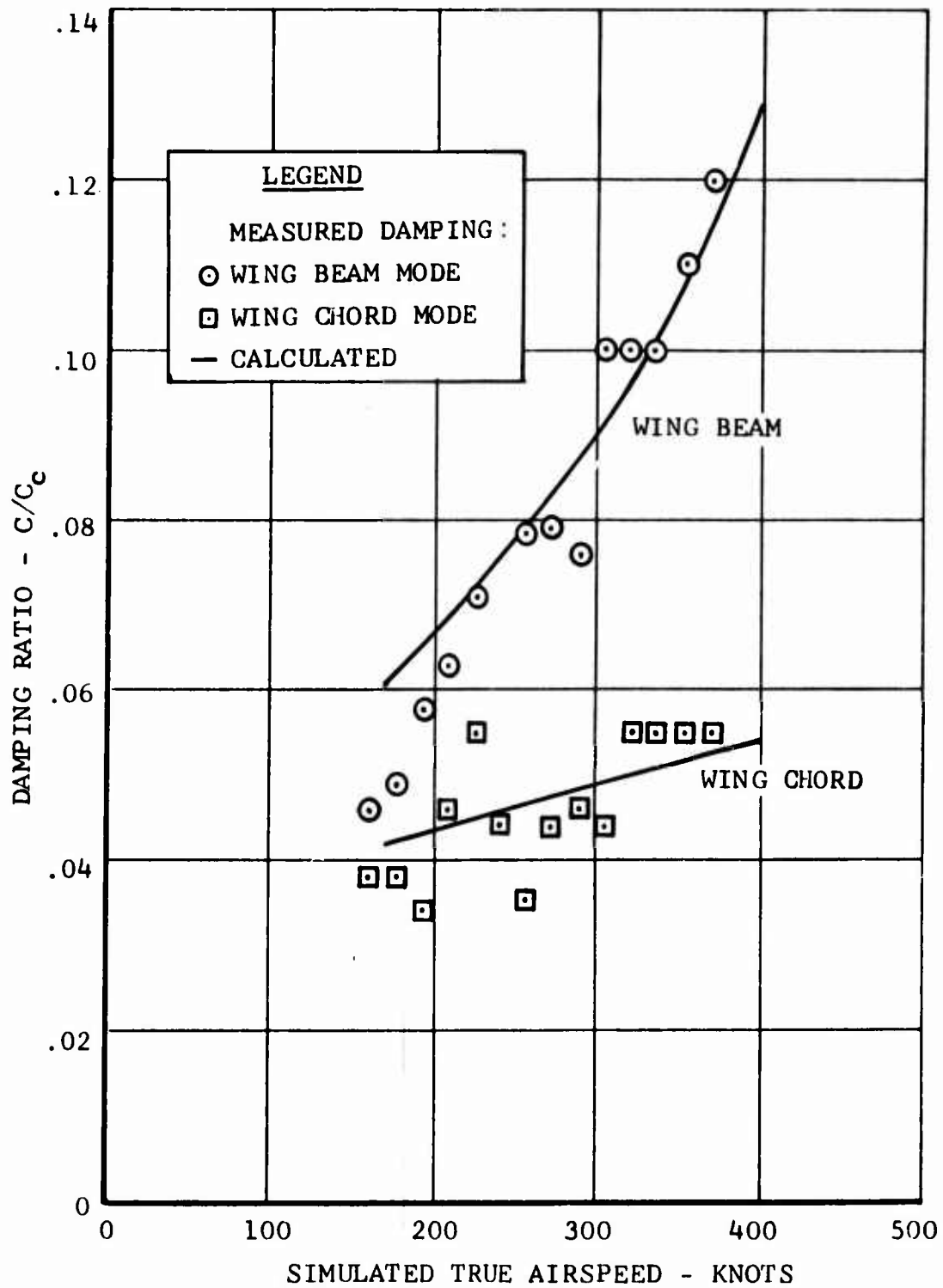
Figure 38. Correlation Between Theory and Measured
Wing Beam and Chord Model Damping, Gimbal
Flapping Locked Out, Zero RPM.

115
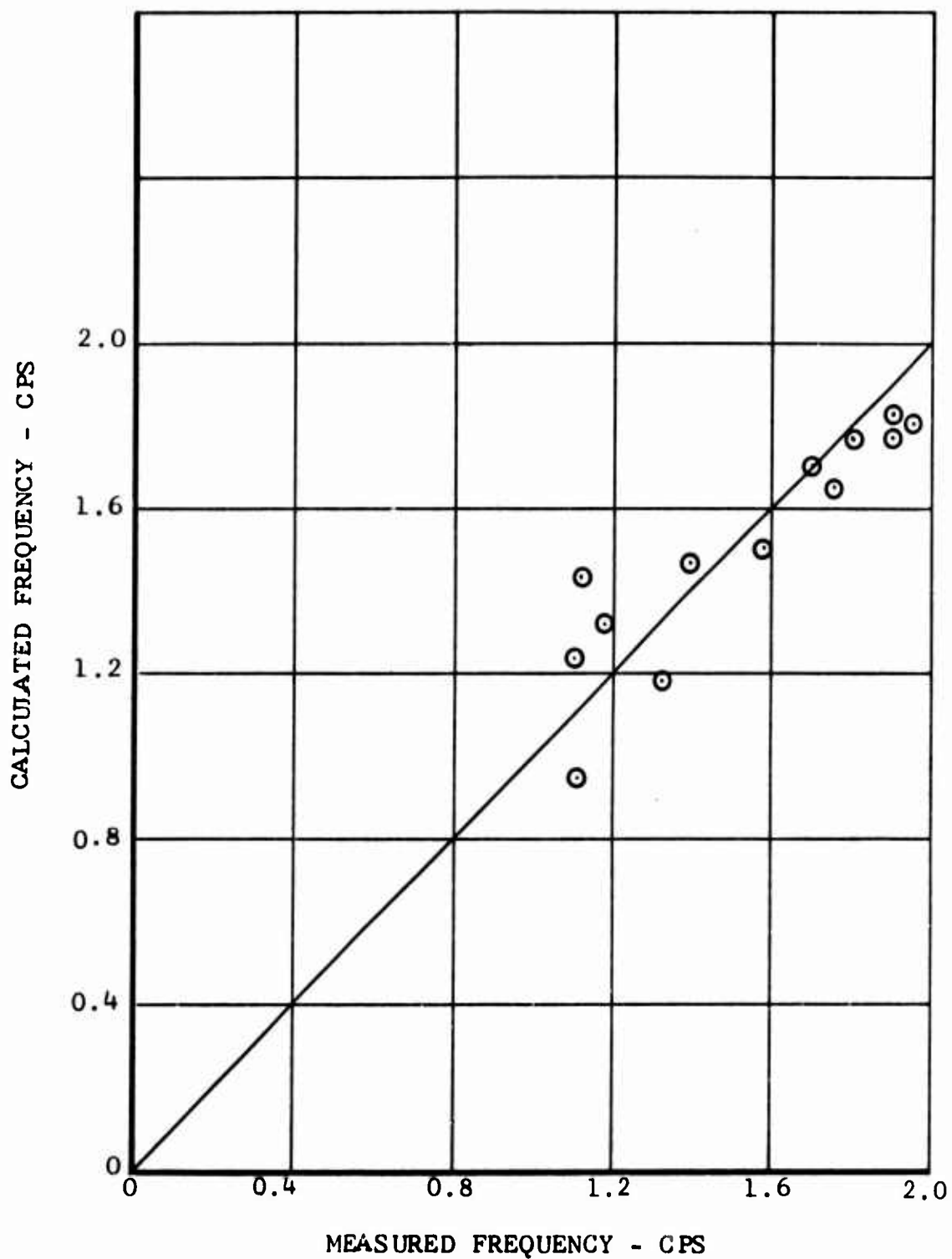
Figure 39.   Correlation Between Theory and Measured
             Instability Frequency.

116
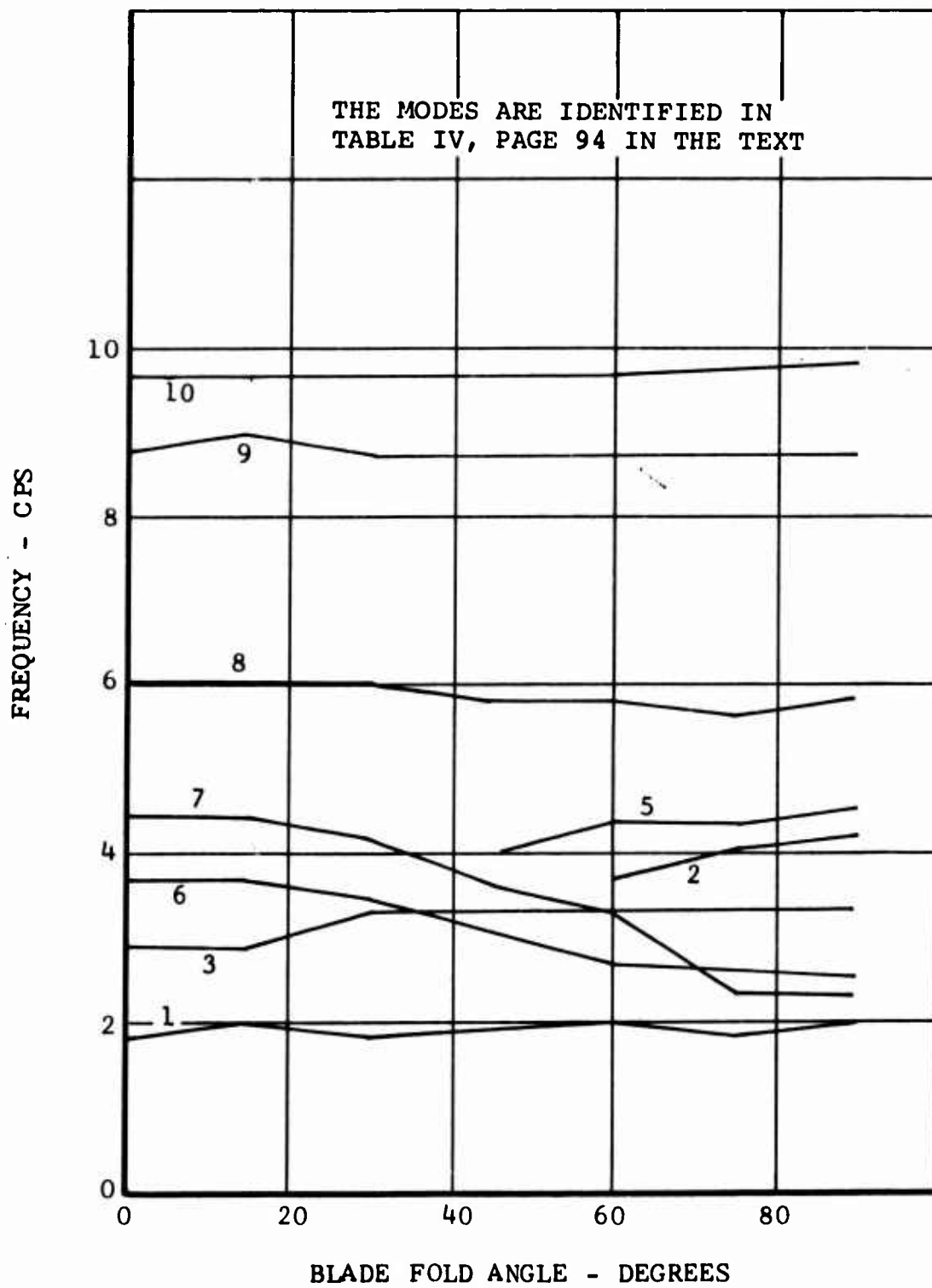
Figure 40. Measured Wing/Pylon/Blade Natural Frequencies Versus Blade Fold Angle.

117
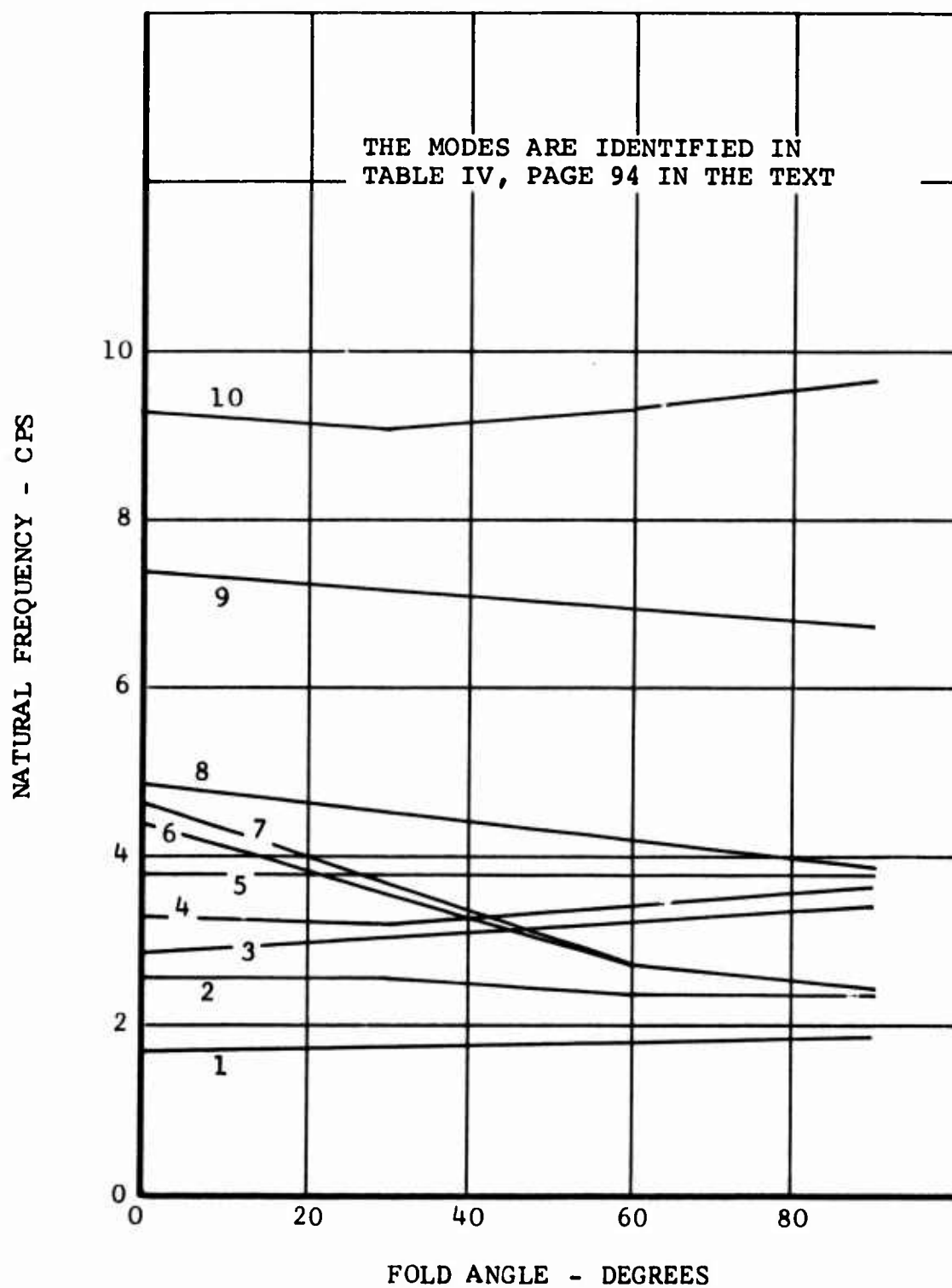
Figure 41.   Calculated Blade Natural Frequencies Versus
Blade Fold Angle.

118
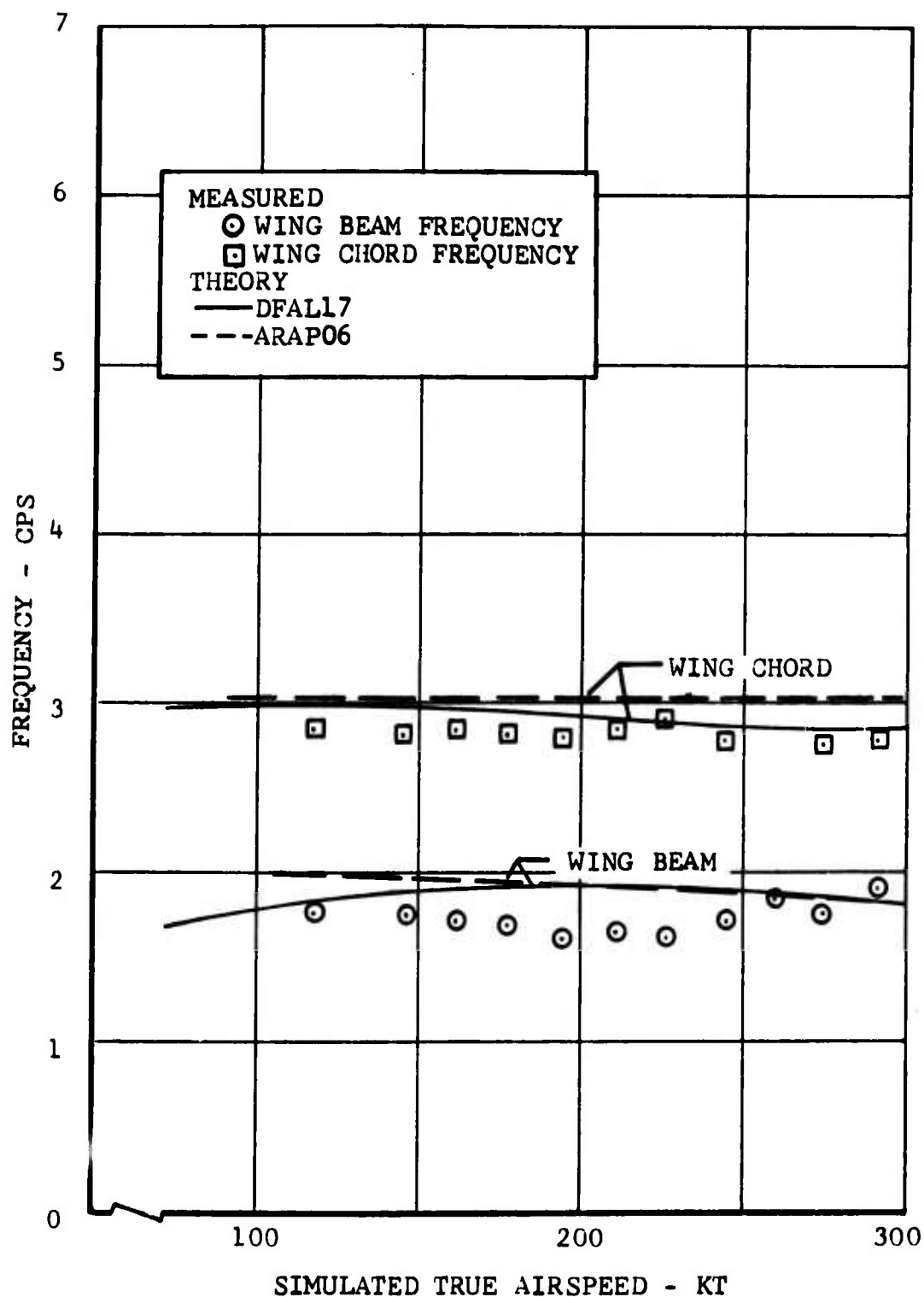
Figure 42. Correlation of Theory With Measured
Frequency and Damping Versus Velocity
Zero Fold Angle.

119
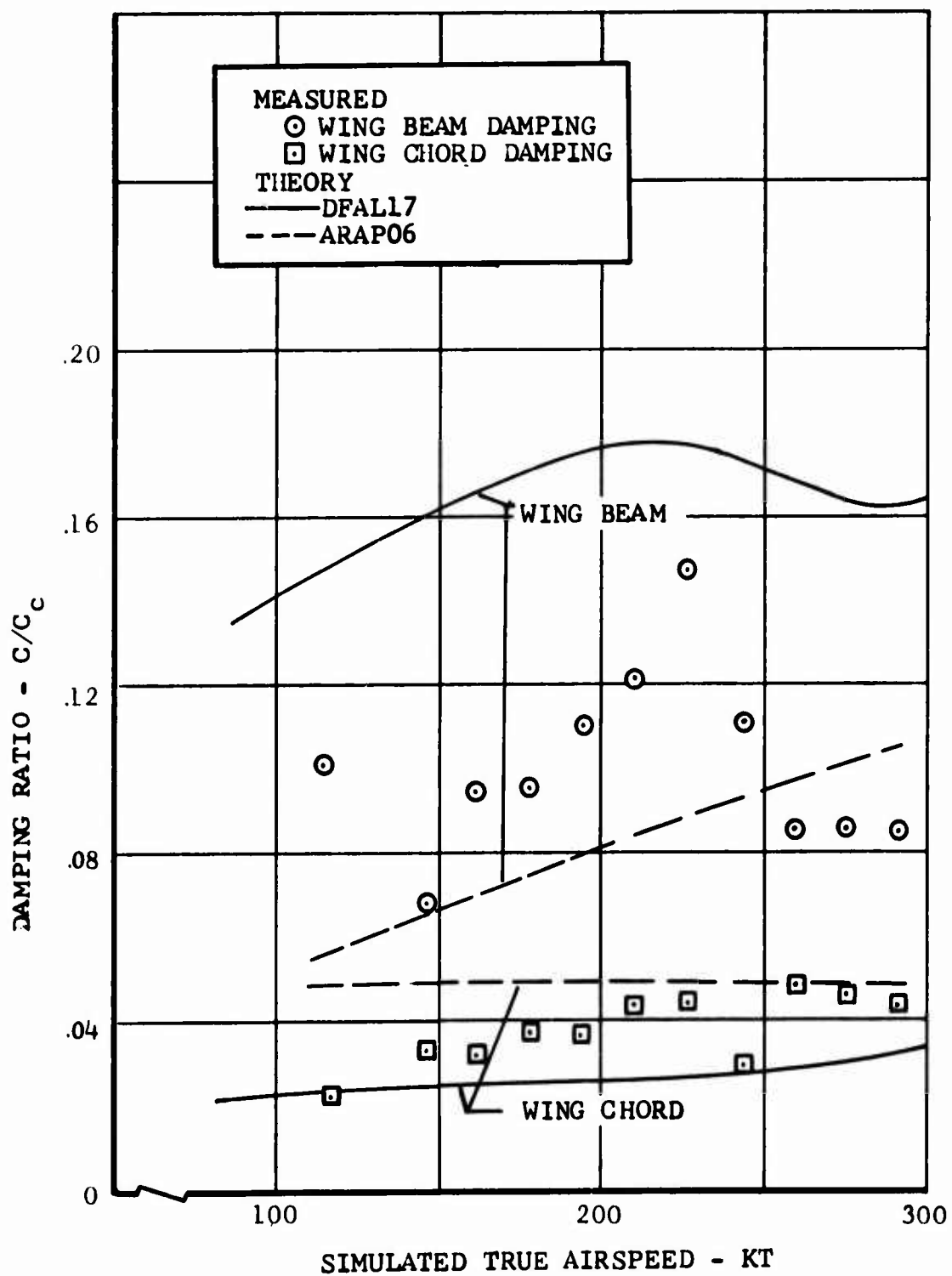
Figure 42. Concluded.

120
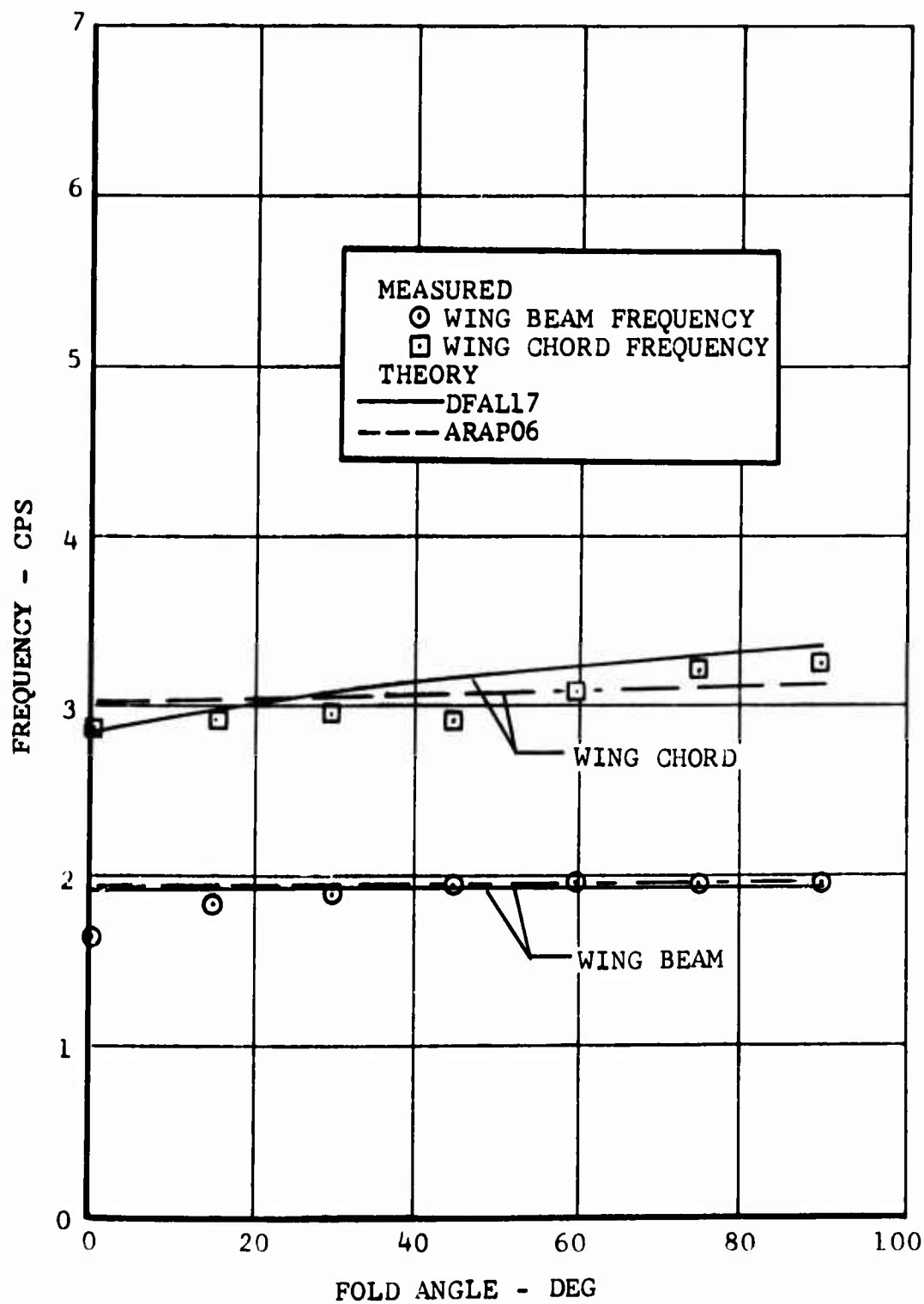
Figure 43. Correlation Between Theory and Measured
Frequency and Damping Versus Fold Angle,
211 Knots Simulated Airspeed.
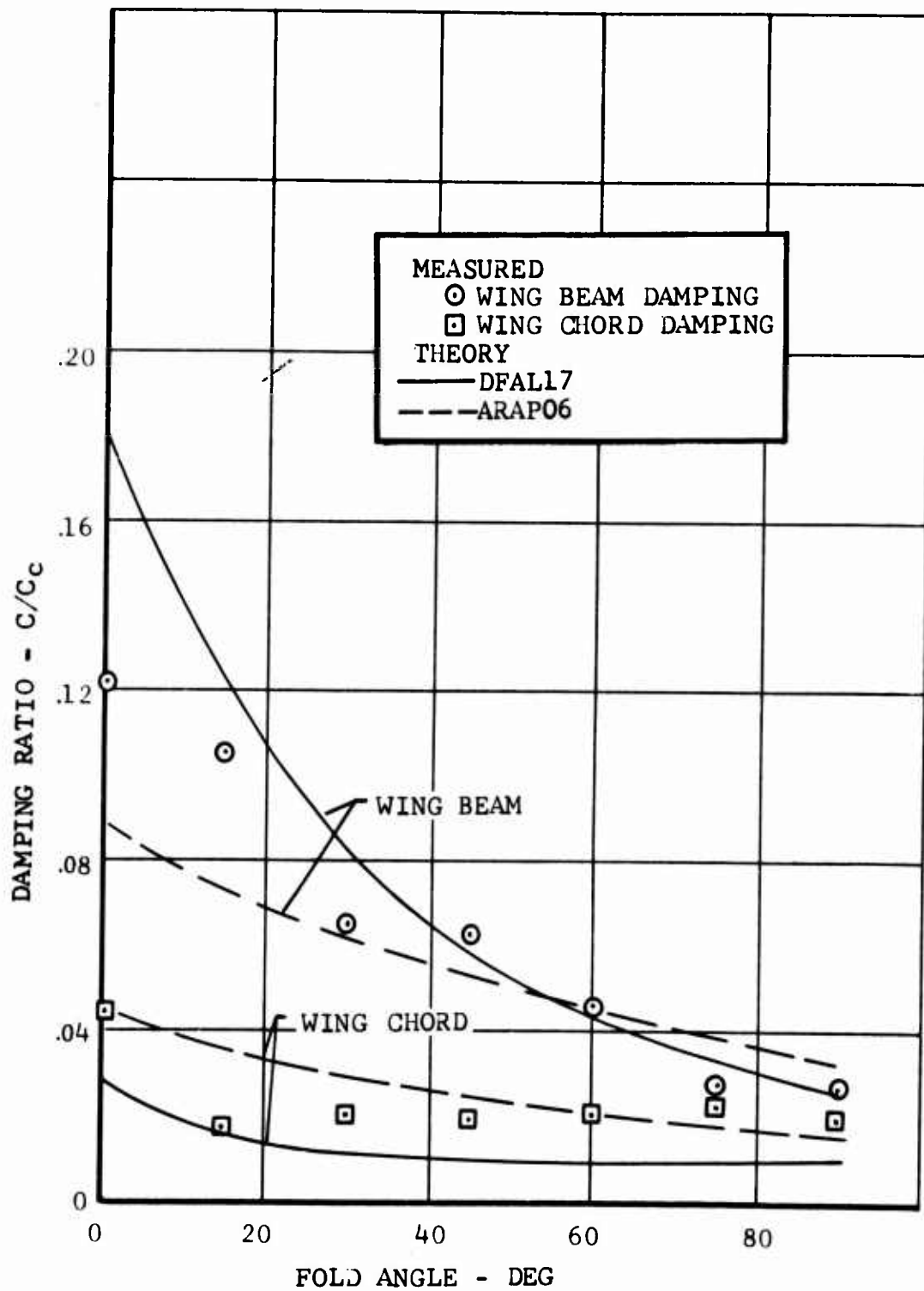
Figure 43.   Concluded.

122
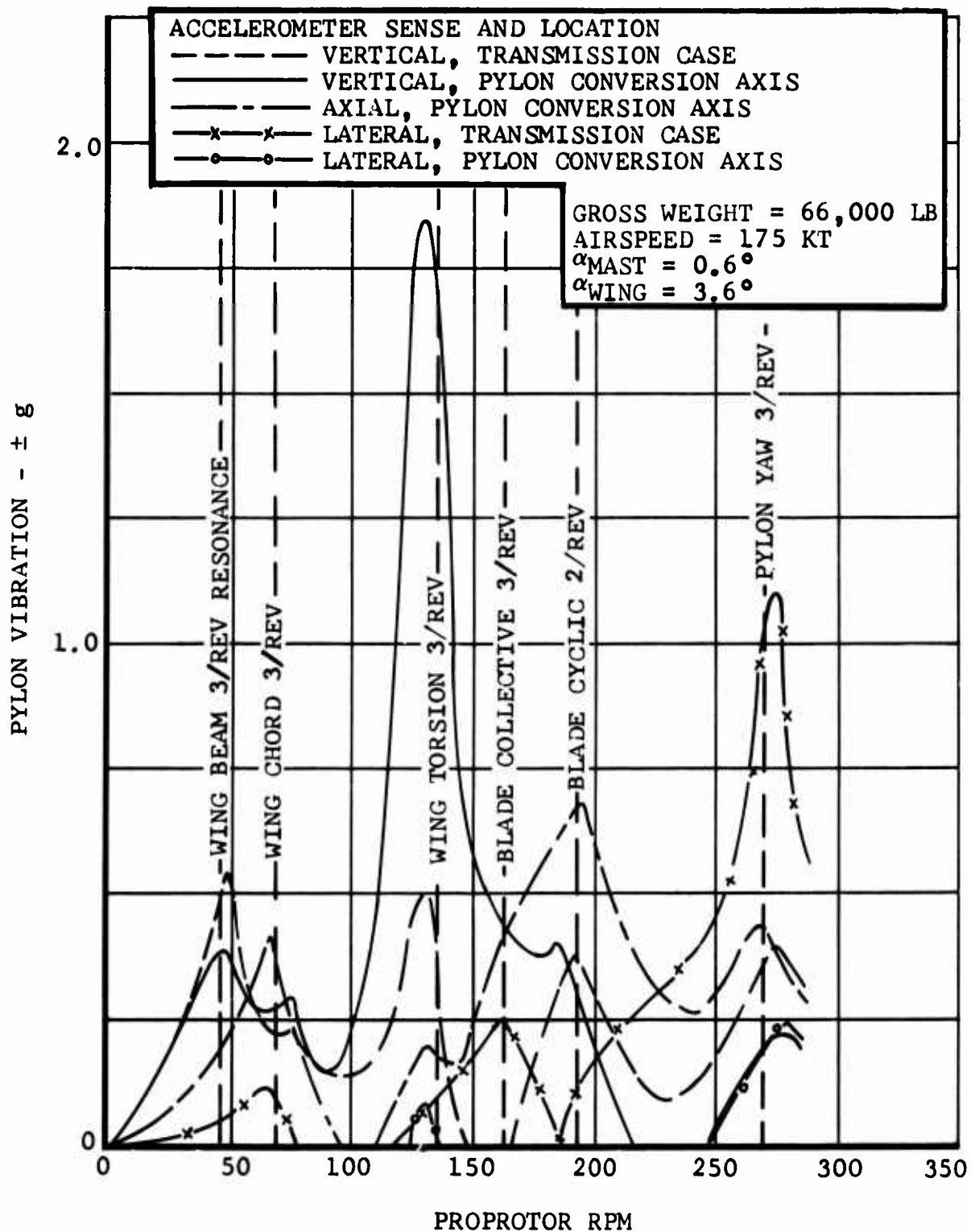
Figure 44.   Measured Steady State Pylon
Vibration at Blade Passage
Frequency.

123
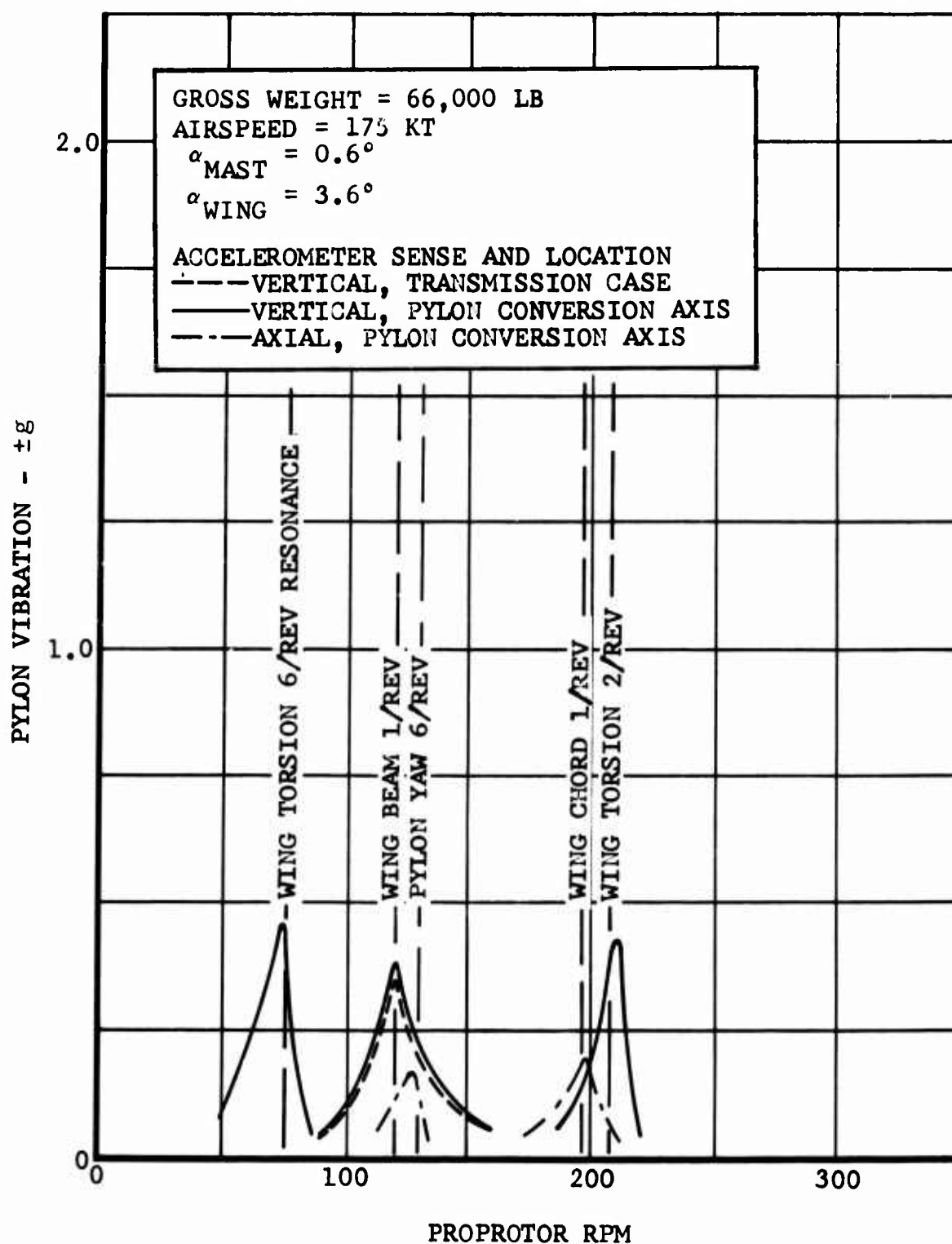
Figure 45. Measured Steady-State Pylon Vibration at Harmonics of Blade Passage Frequency.

124
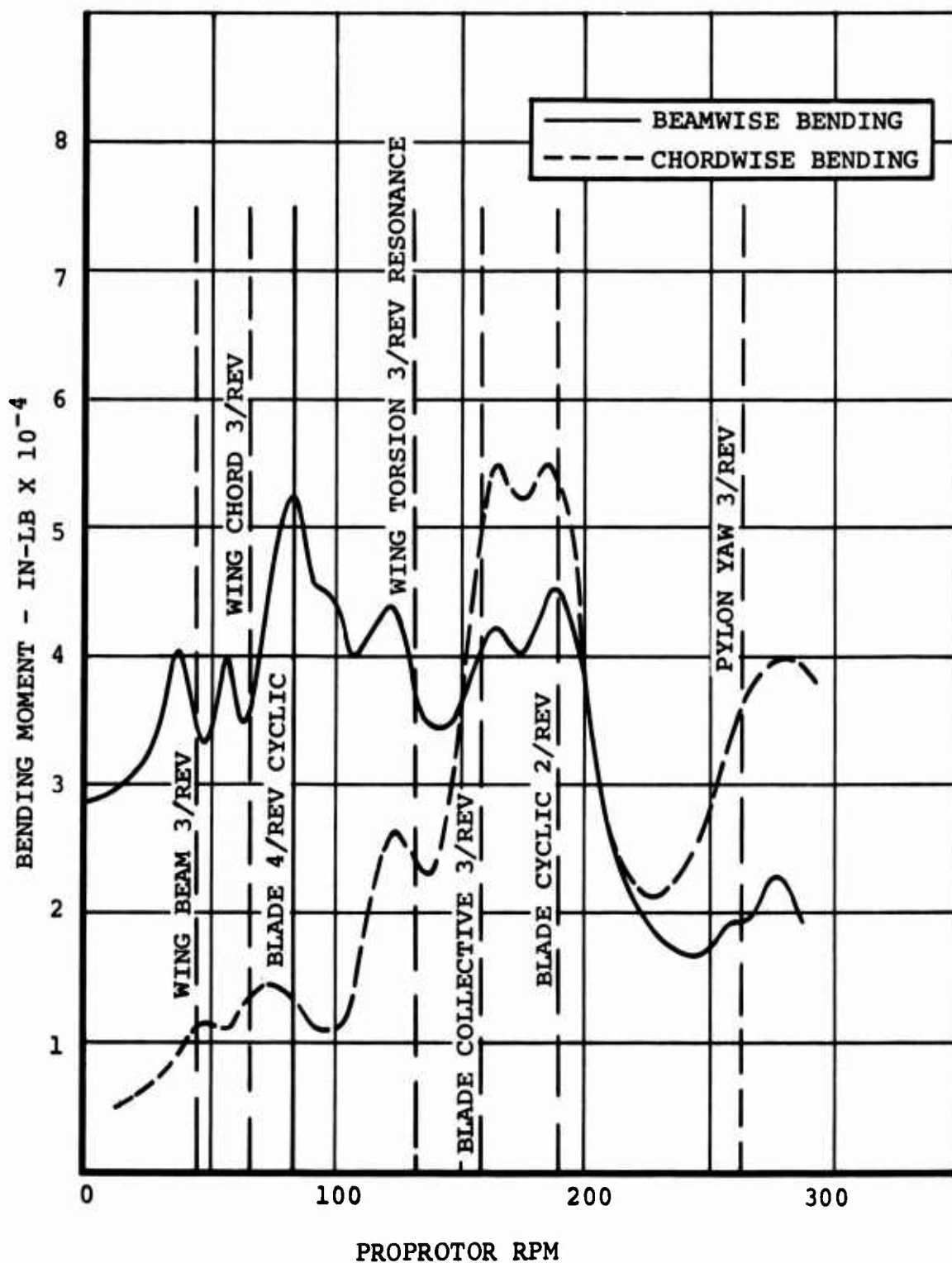
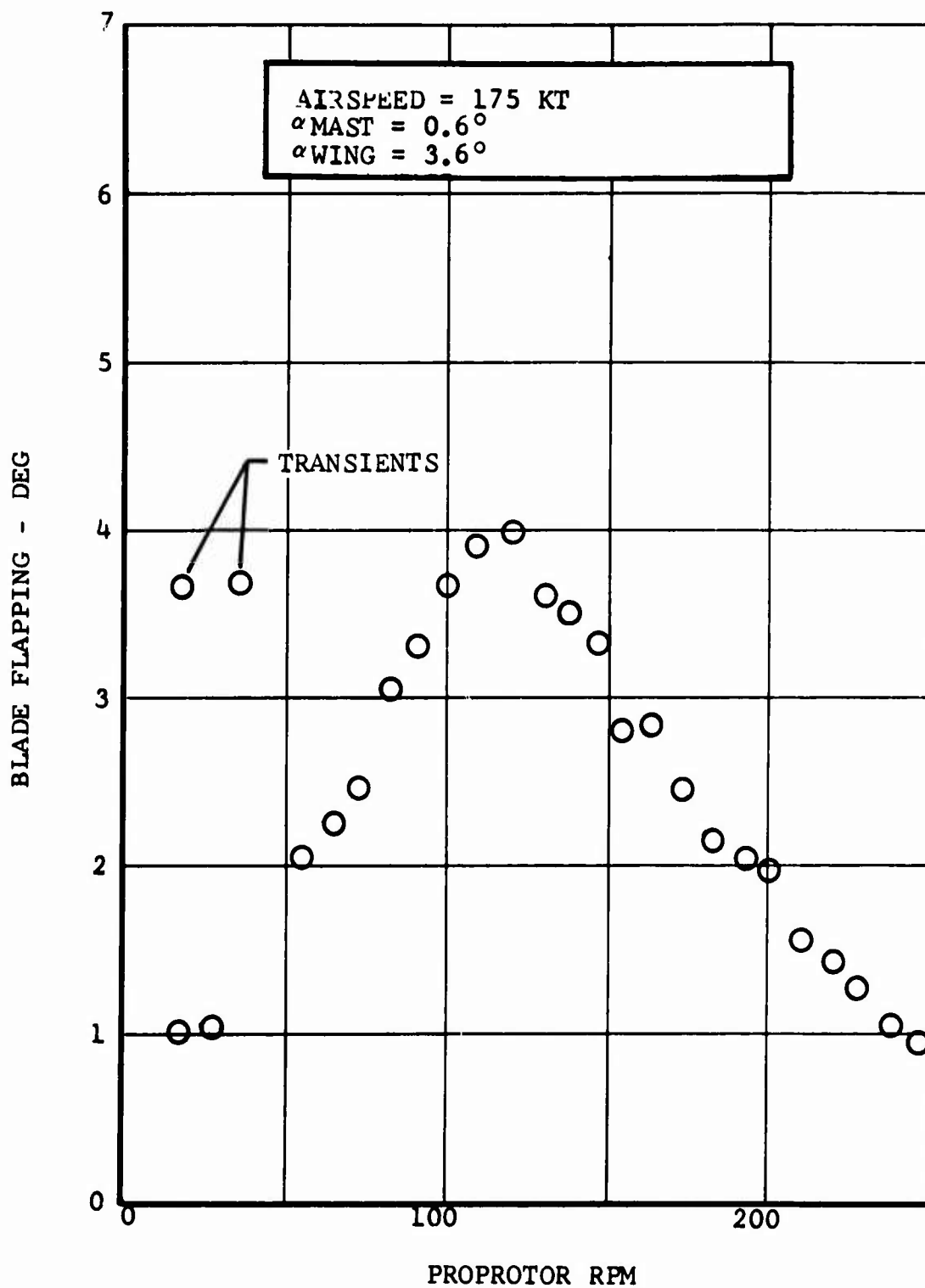Figure 46. Measured Steady State Blade Loads at Blade 35-Percent Radius.

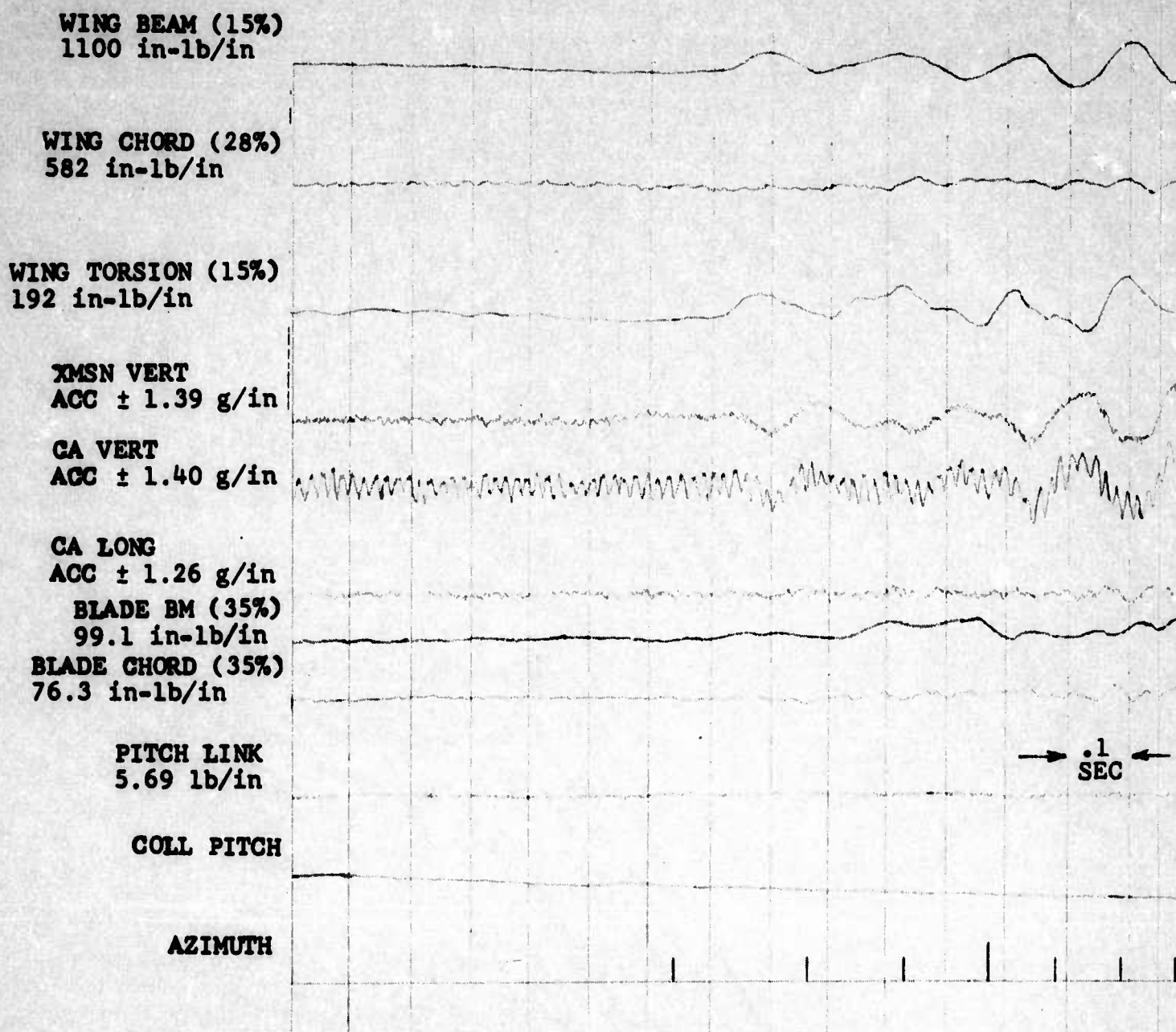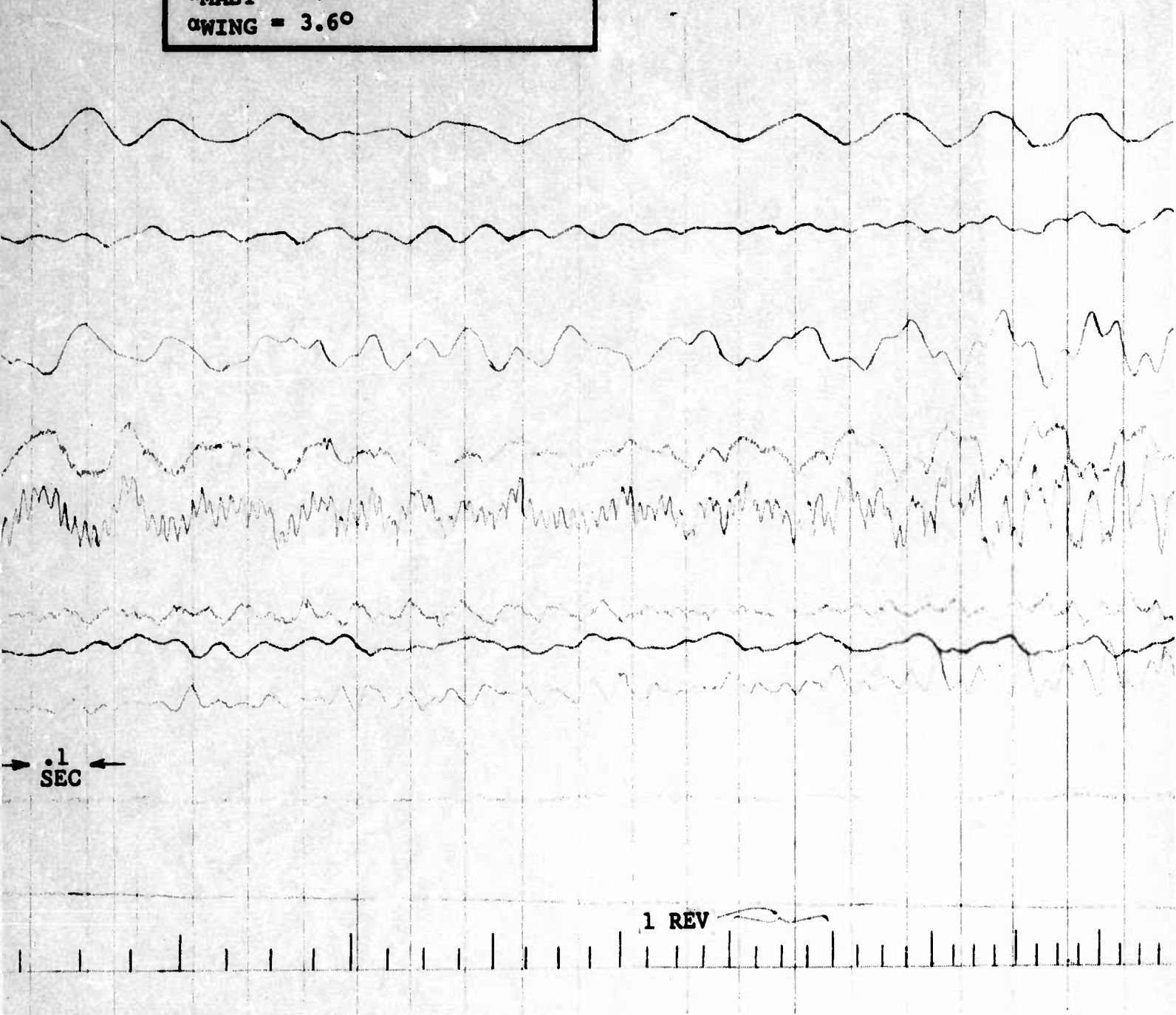Figure 47.   Measured Steady-State Flapping Response.

WING BEAM (15%)
1100 in-lb/in

WING CHORD (28%)
582 in-lb/in

WING TORSION (15%)
192 in-lb/in

XMSN VERT
ACC ± 1.39 g/in

CA VERT
ACC ± 1.40 g/in

CA LONG
ACC ± 1.26 g/in

BLADE BM (35%)
99.1 in-lb/in

BLADE CHORD (35%)
76.3 in-lb/in

PITCH LINK
5.69 lb/in

COLL PITCH

AZIMUTH

→ .1 ←
SEC

Figure 48.   Time Hi
Unfeath

$\Omega_O = 283$ RPM
AIRSPEED = 175 KT, SIMULATED
$\alpha_{MAST} = 0.6^\circ$
$\alpha_{WING} = 3.6^\circ$

.1
SEC

1 REV

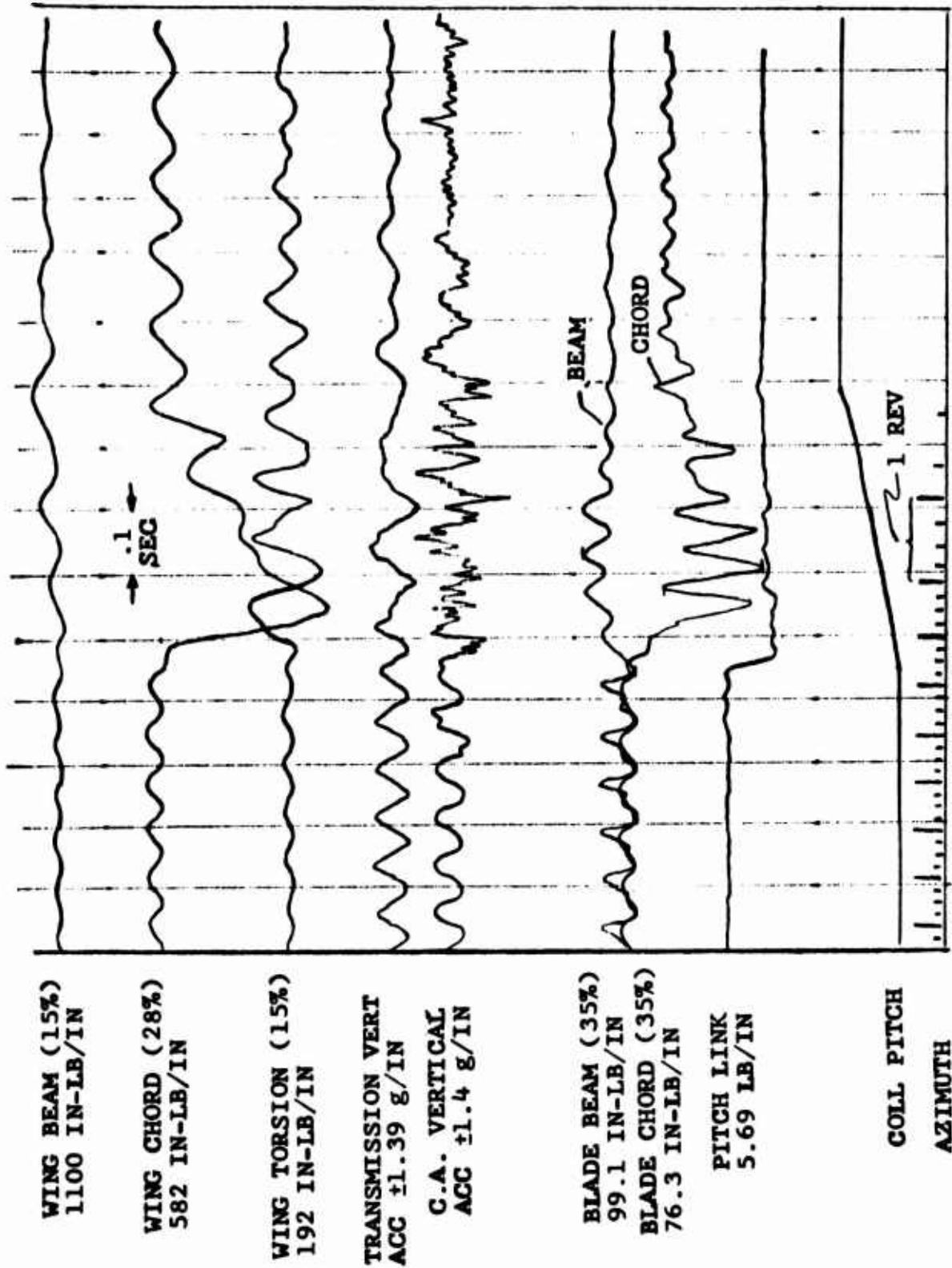Time History of Model Vibration During Slow
Unfeathering of the Blades.

127

3

WING BEAM (15%)
1100 IN-LB/IN

WING CHORD (28%)
582 IN-LB/IN

WING TORSION (15%)
192 IN-LB/IN

TRANSMISSION VERT
ACC ±1.39 g/IN

C.A. VERTICAL
ACC ±1.4 g/IN

BLADE BEAM (35%)
99.1 IN-LB/IN

BLADE CHORD (35%)
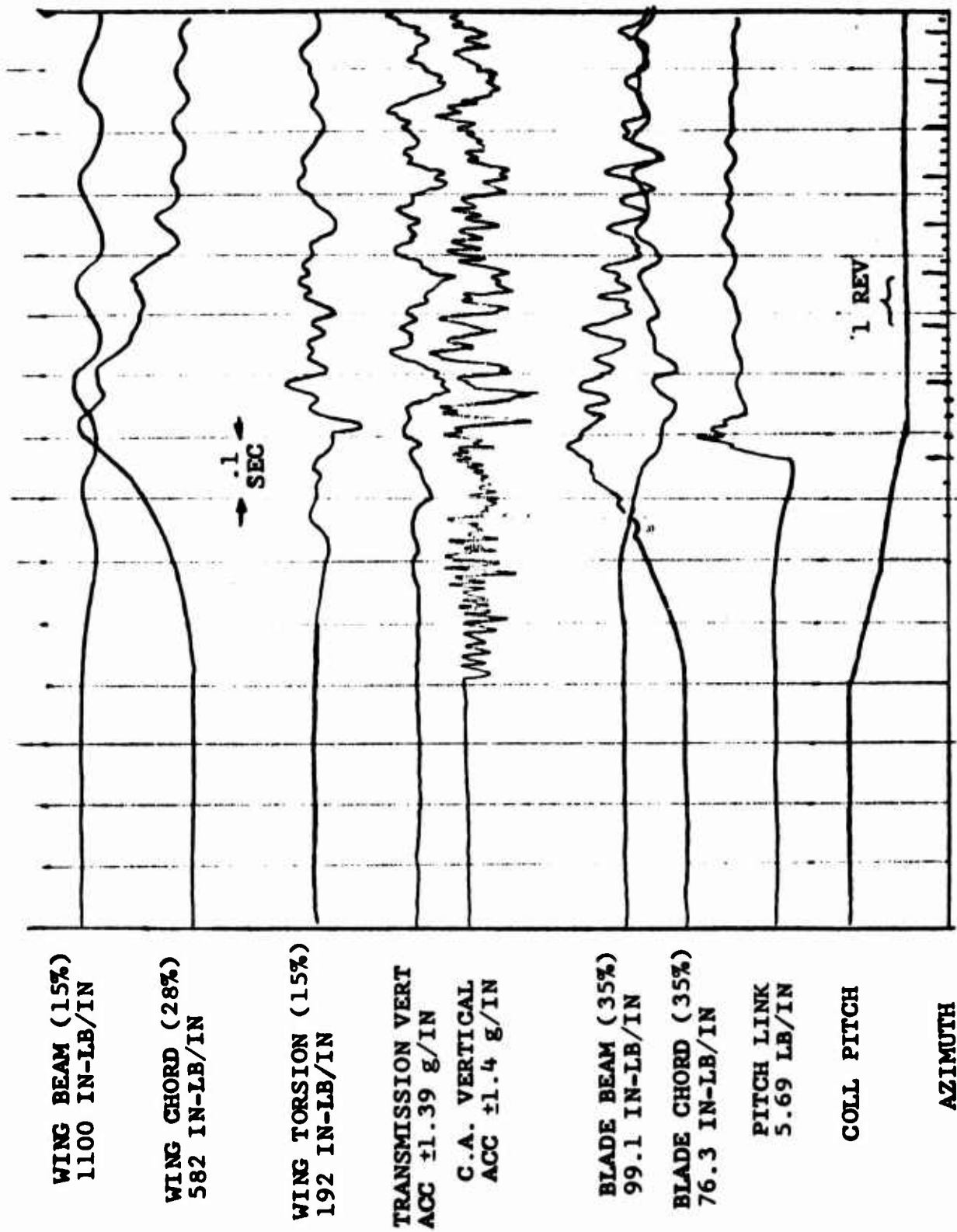76.3 IN-LB/IN

PITCH LINK
5.69 LB/IN

COLL PITCH

AZIMUTH

Figure 49. Time History of Model Response to Rapid Feathering
($\Delta T = 0.42$ Seconds), 175 Knots Simulated Airspeed.

128

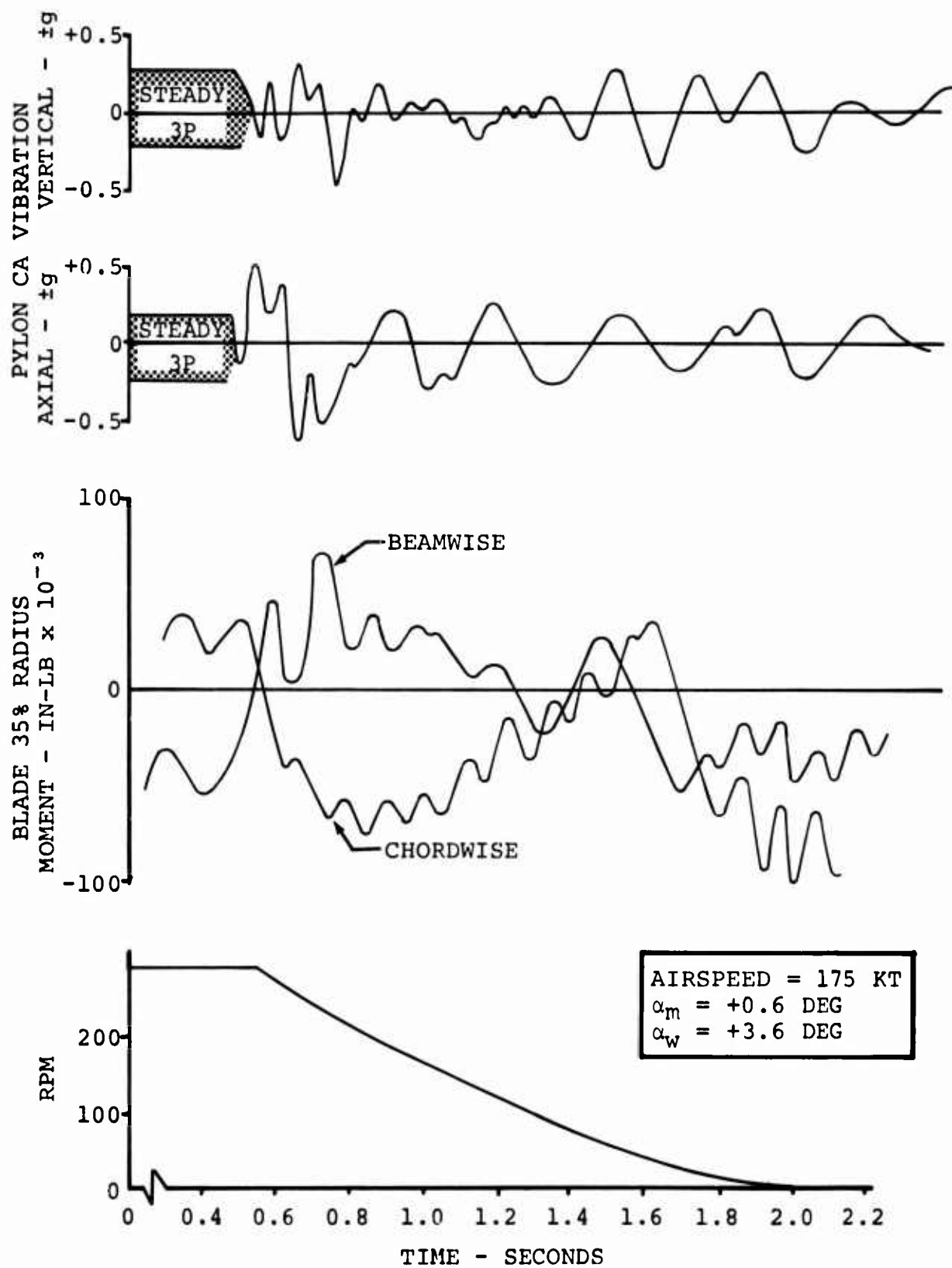Figure 50. Time History of Model Response to Rapid Unfeathering (ΔT = 0.4 Seconds), 175 Knots Simulated Airspeed.

WING BEAM (15%)
1100 IN-LB/IN

WING CHORD (28%)
582 IN-LB/IN

WING TORSION (15%)
192 IN-LB/IN

TRANSMISSION VERT
ACC ±1.39 g/IN

C.A. VERTICAL
ACC ±1.4 g/IN

BLADE BEAM (35%)
99.1 IN-LB/IN

BLADE CHORD (35%)
76.3 IN-LB/IN

PITCH LINK
5.69 LB/IN

COLL PITCH

AZIMUTH

.1
SEC

1 REV

129

Figure 51.   Calculated Time History of Dynamic Response.
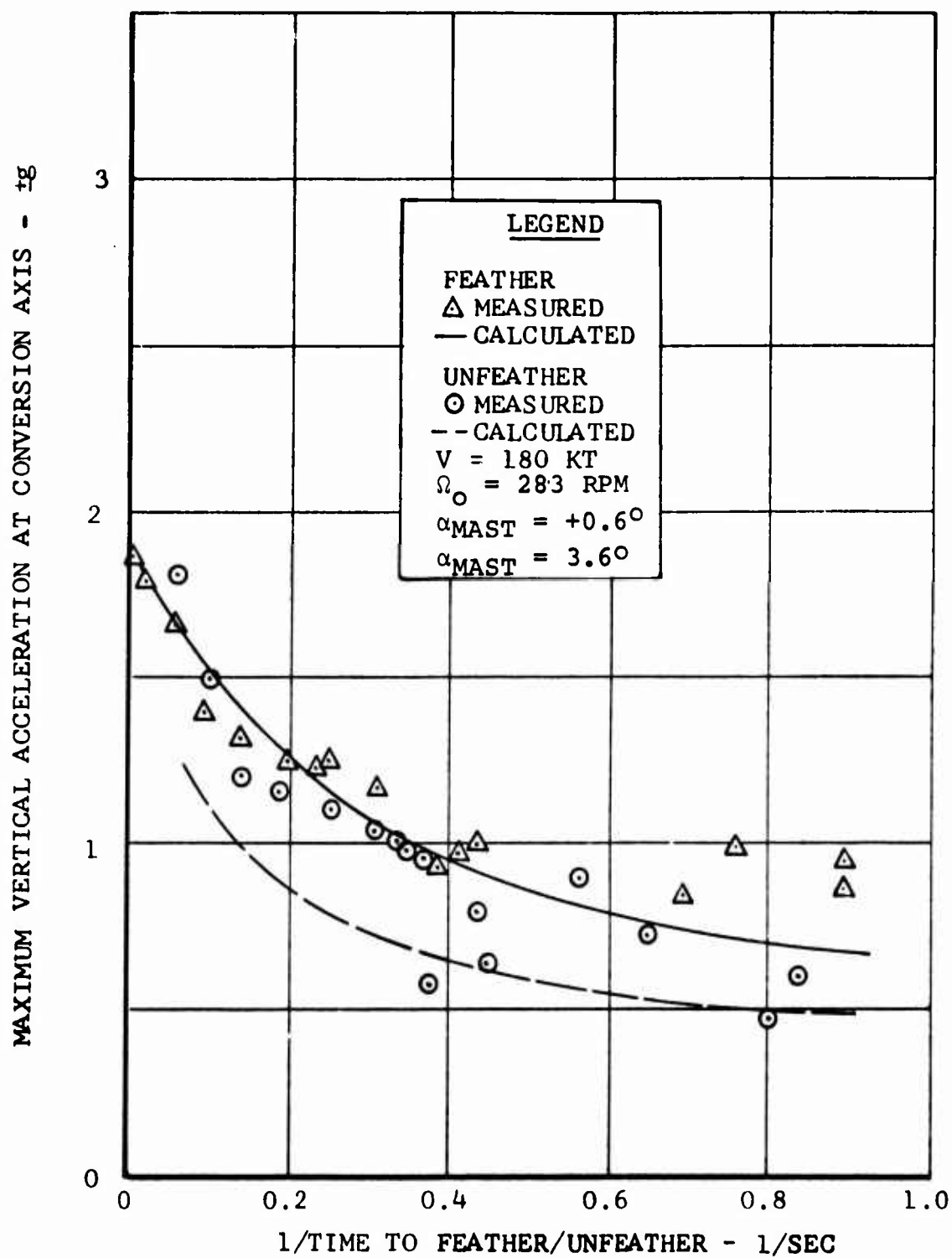
130

Figure 52.   Correlation Between Theory and Measured
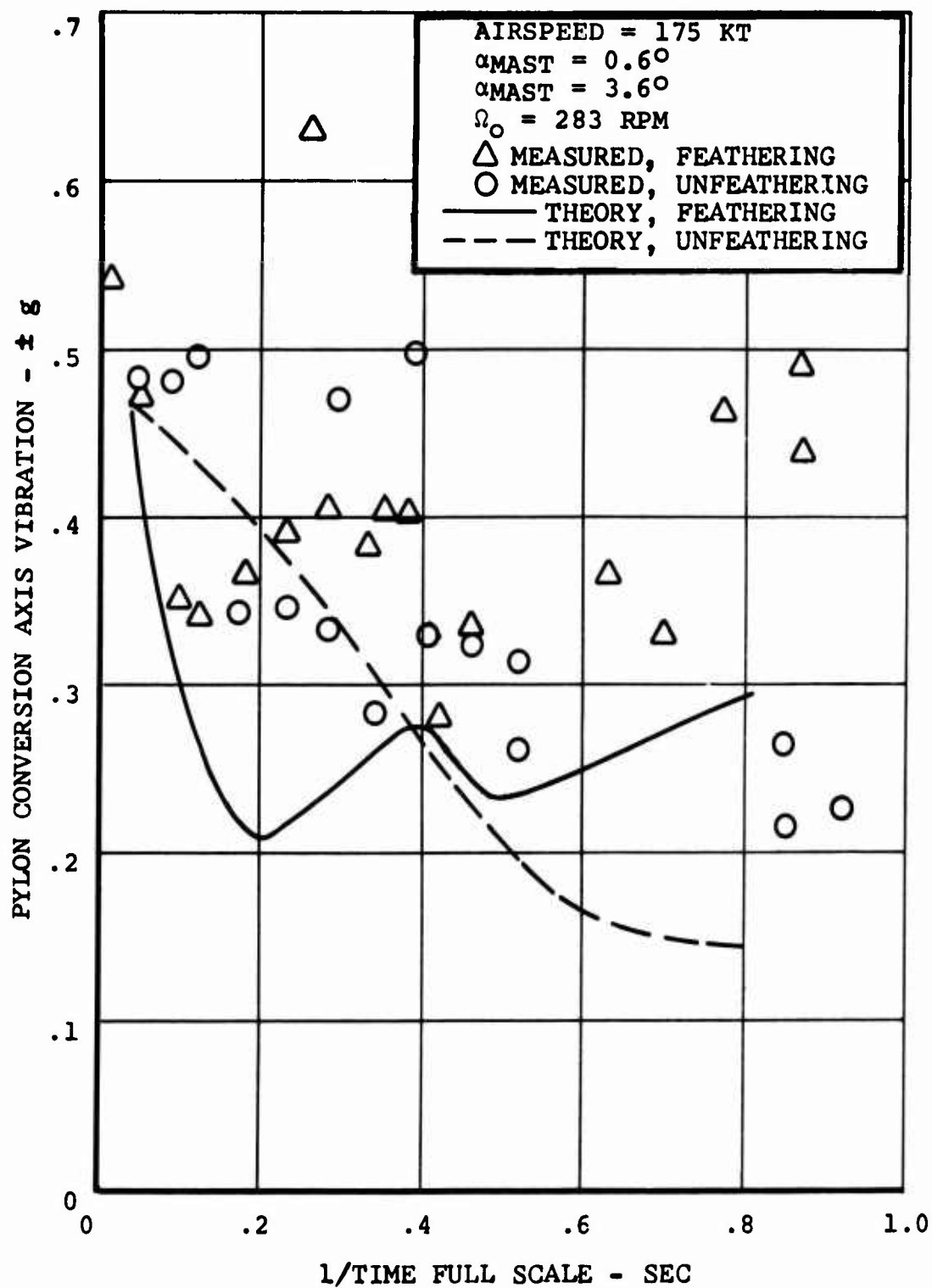Response at Wing Torsional Natural
Frequency.

131

Figure 53.   Correlation Between Theory and Measured
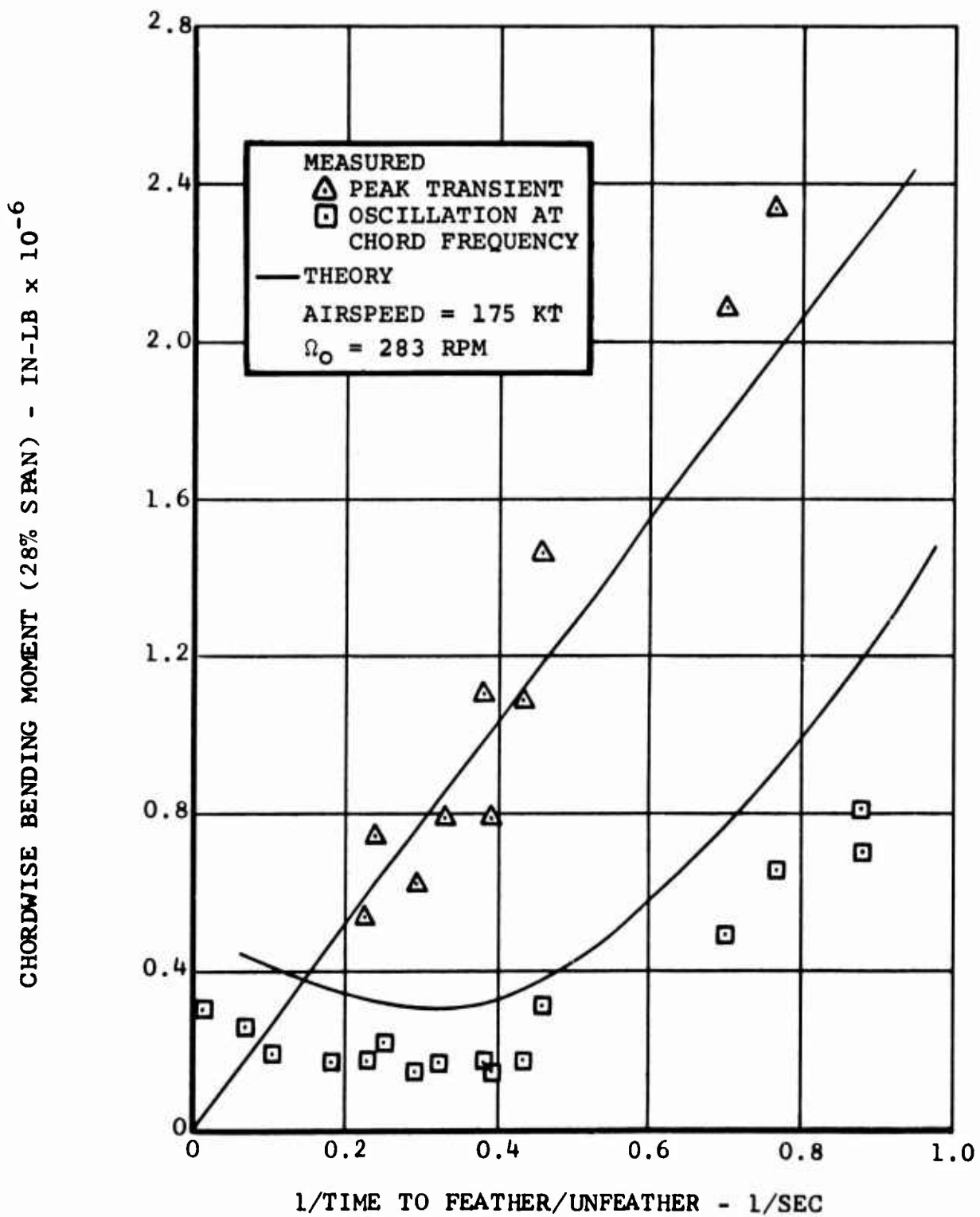Response at Wing Beam Natural Frequency.

132

Figure 54.   Correlation Between Theory and Measured
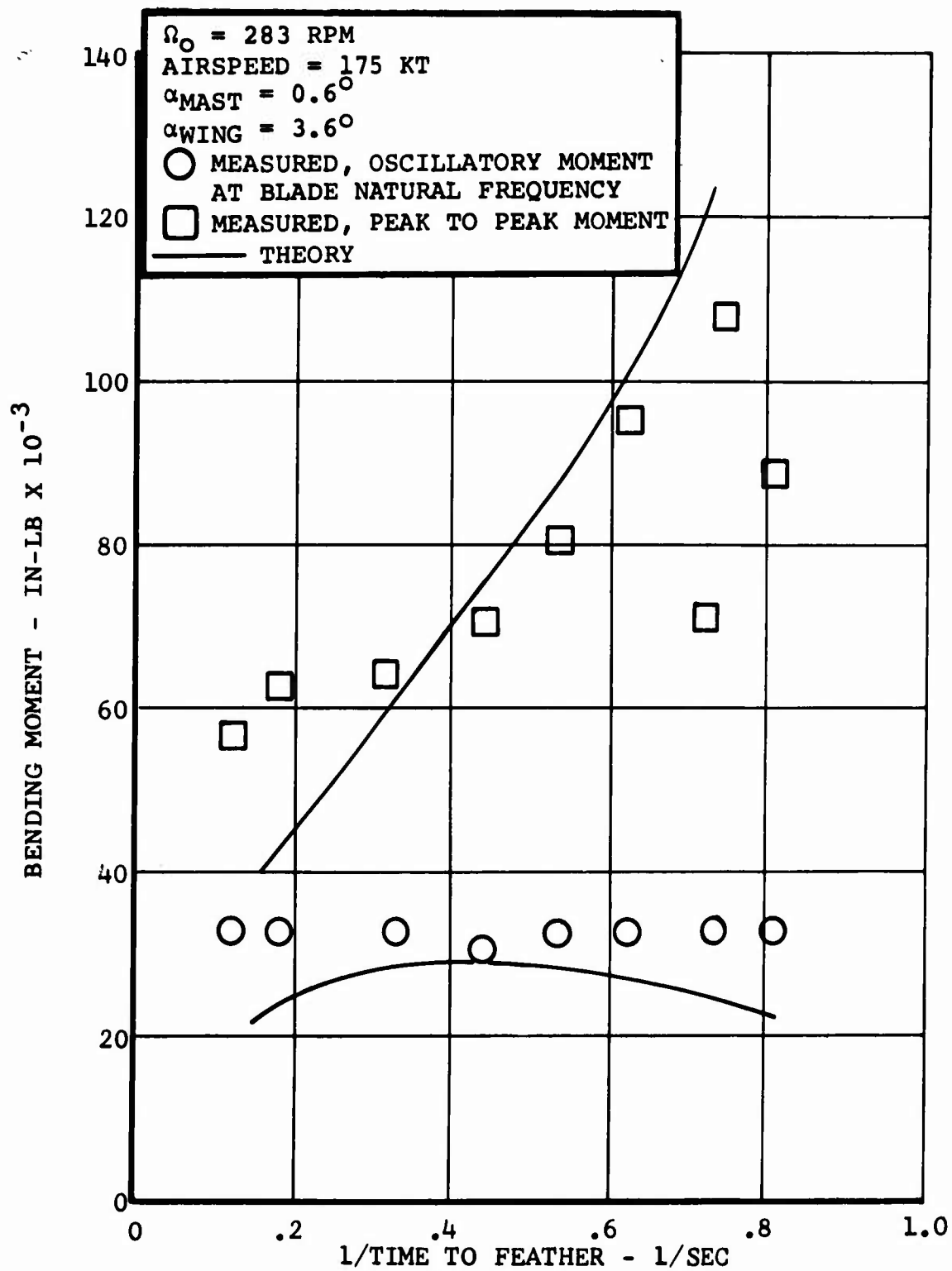Wing Chord Bending Response.

133

Figure 55. Correlation Between Theory and Measured
Blade Beam Bending Moments During
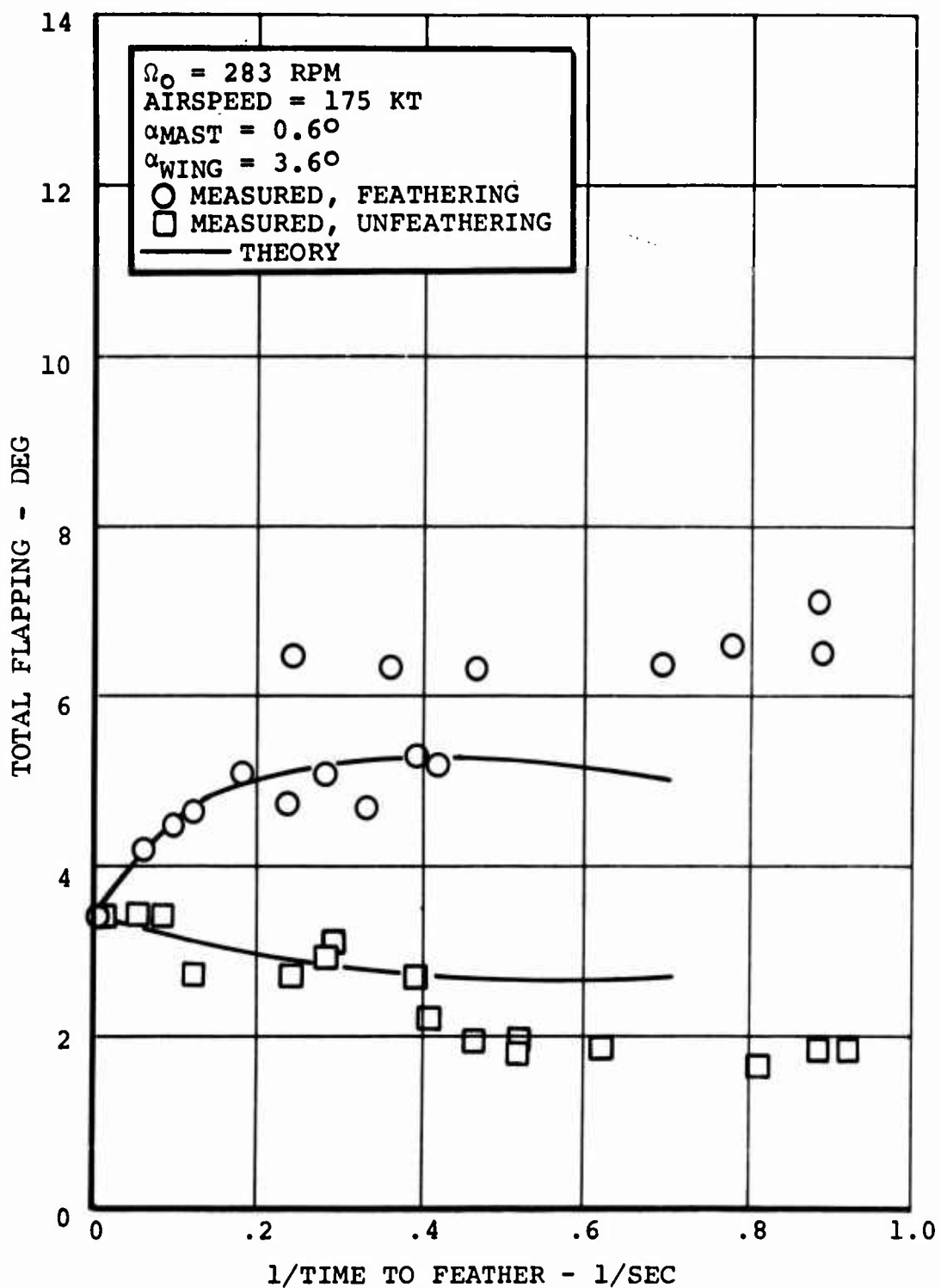Feathering.

Figure 56. Correlation Between Theory and Measured
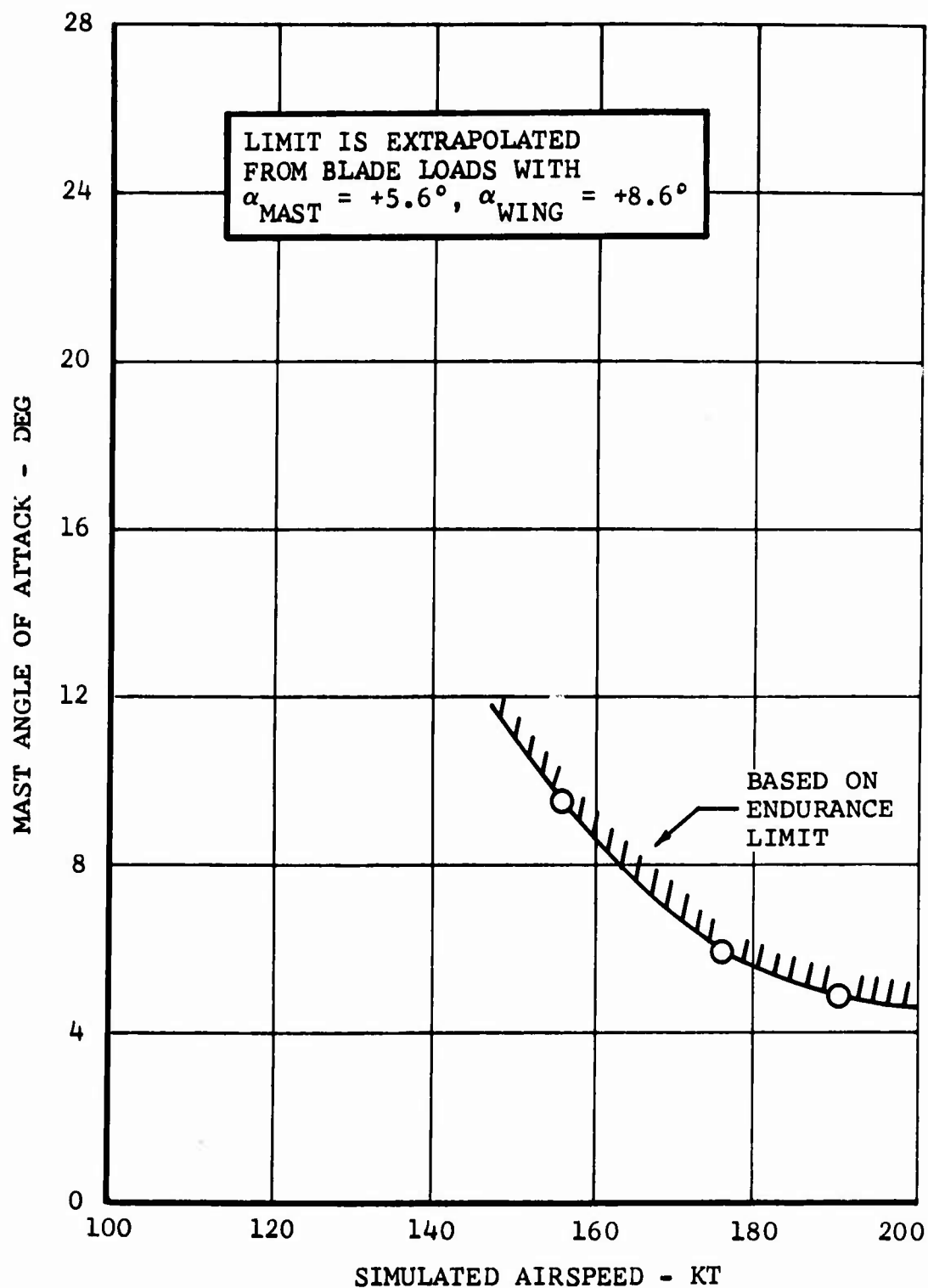   Effect of Feathering Rate on Flapping.

135

Figure 57. Measured Mast Angle of Attack Limit with
Flapping Freedom Locked Out, 300 RPM.

136
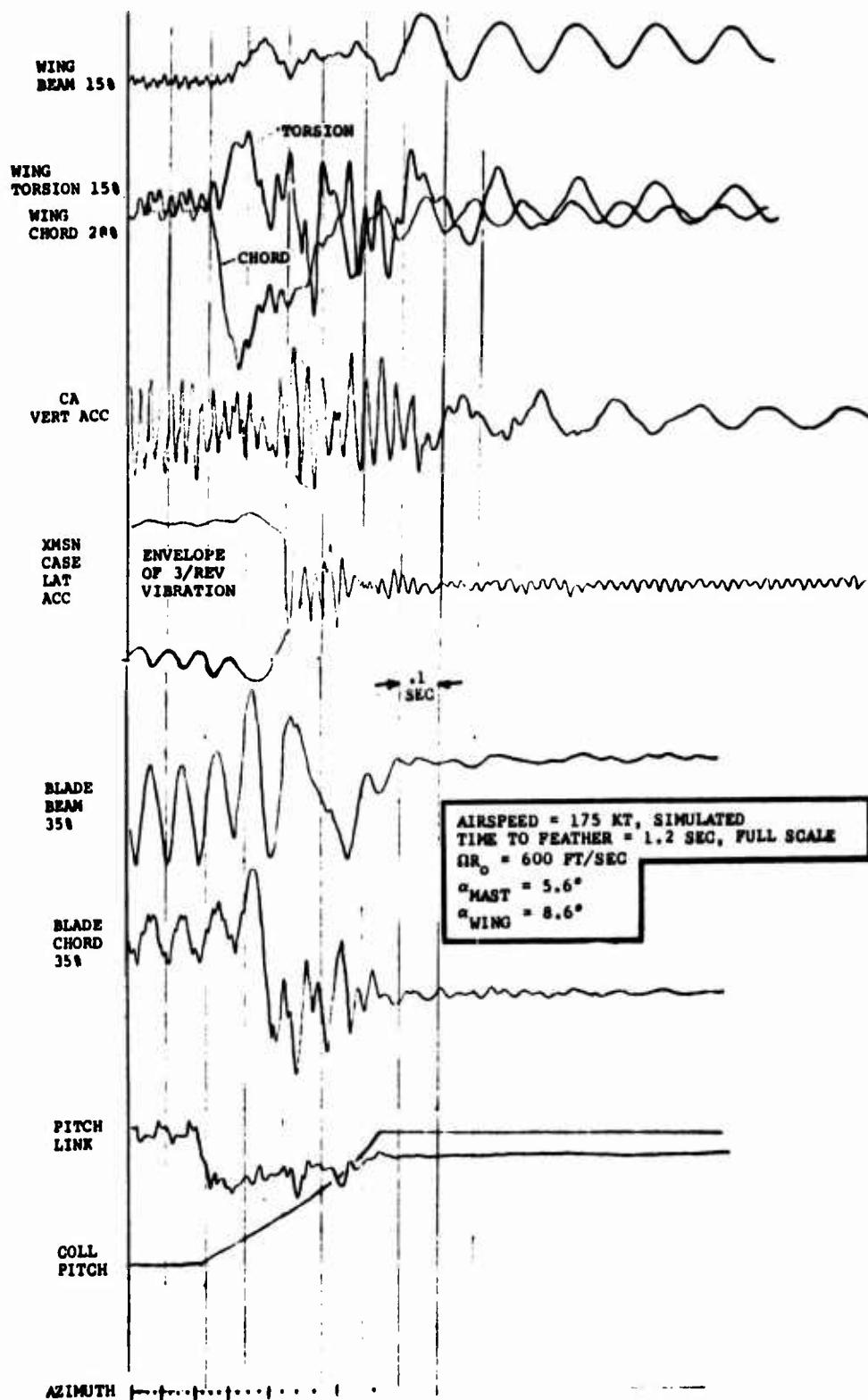
Figure 58. Time History of Model Vibration During Feathering with Shaft Angle of Attack of 5.6°.

137
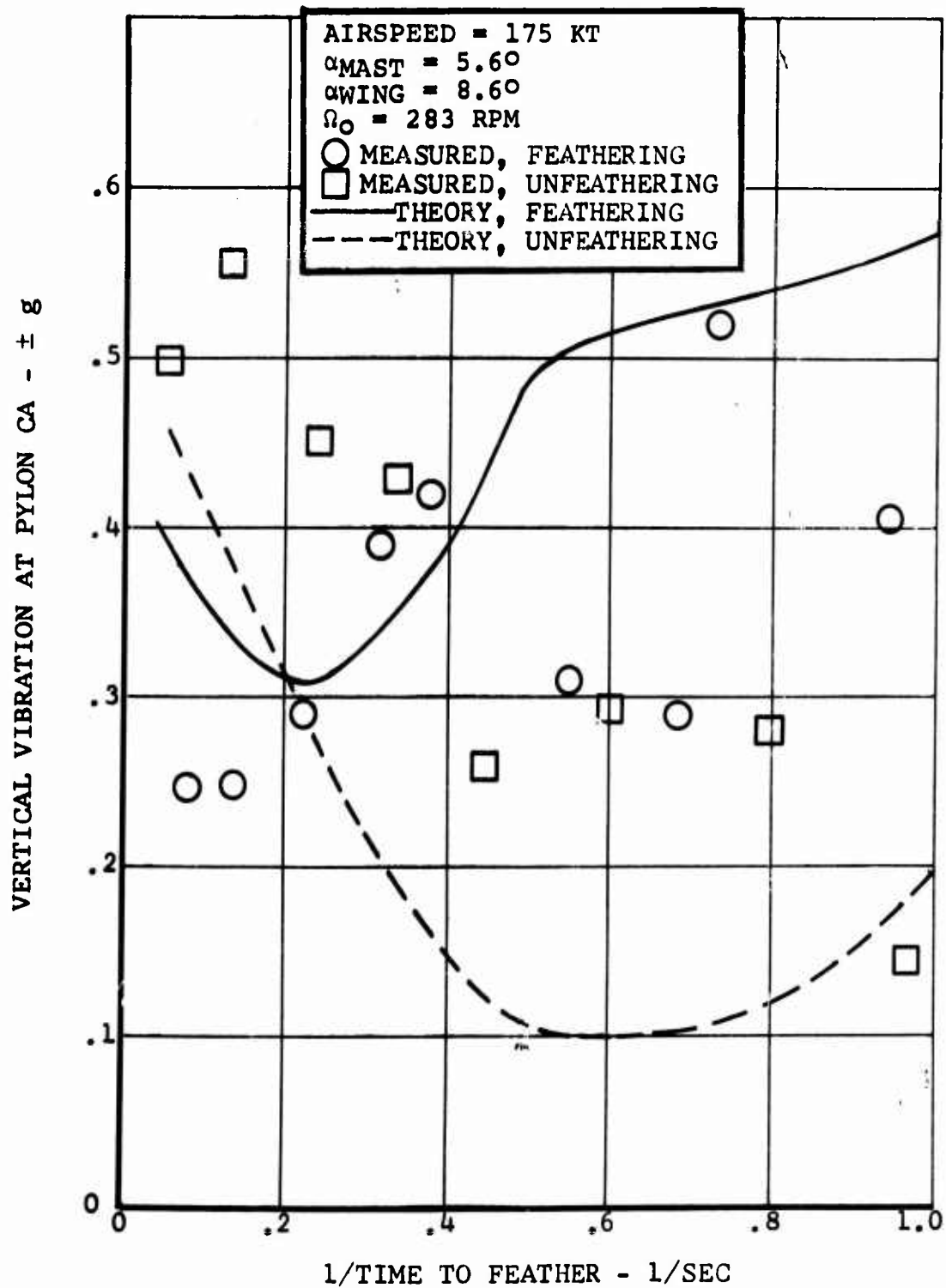
Figure 59. Correlation Between Theory and Measured
Response at Wing Beam Natural Frequency
With Shaft Angle-Of-Attack Of 5.6 Degrees.

138
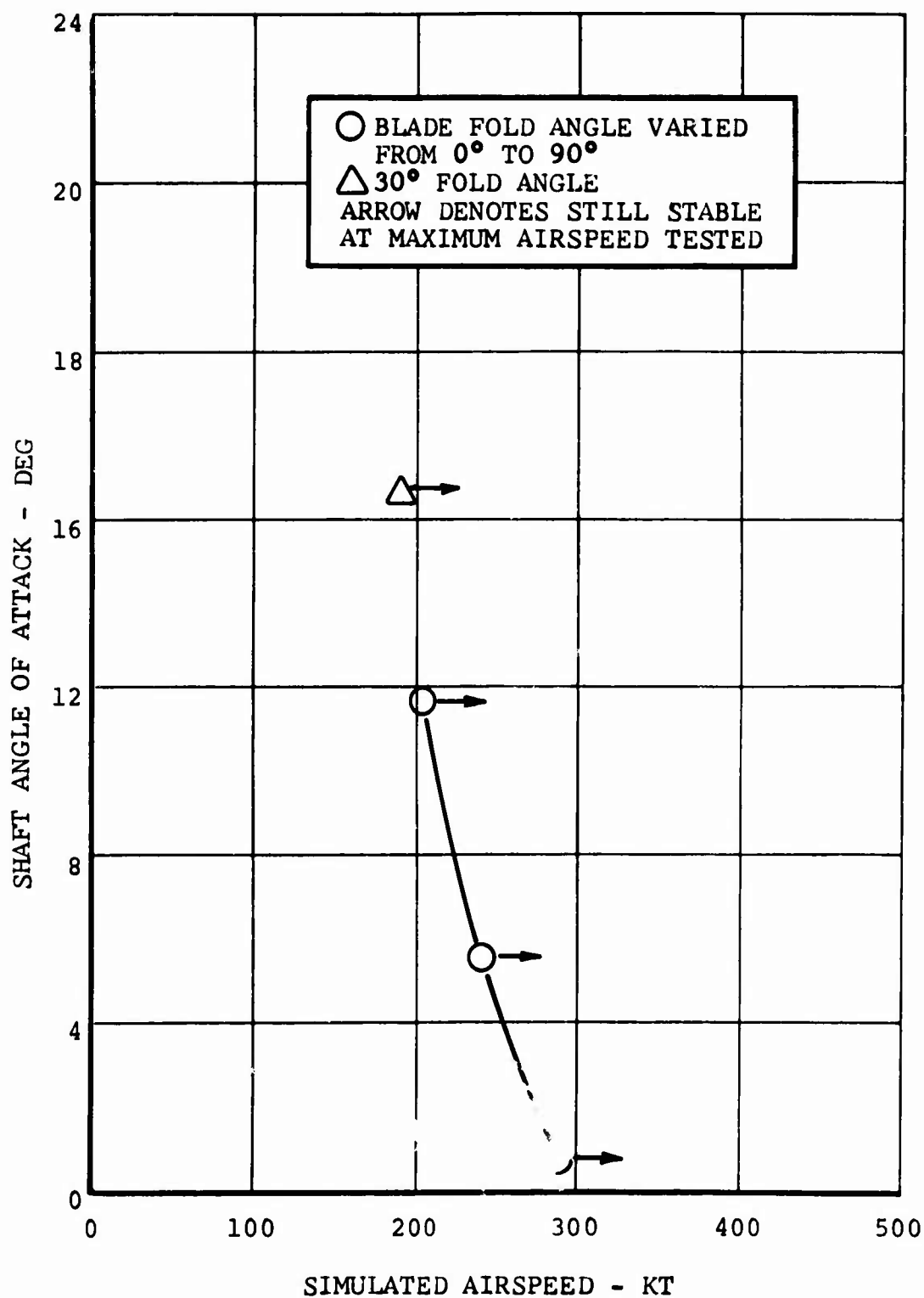
Figure 60. Angle-of-Attack and Airspeed Envelope
Explored in Blade Folding Test.

139
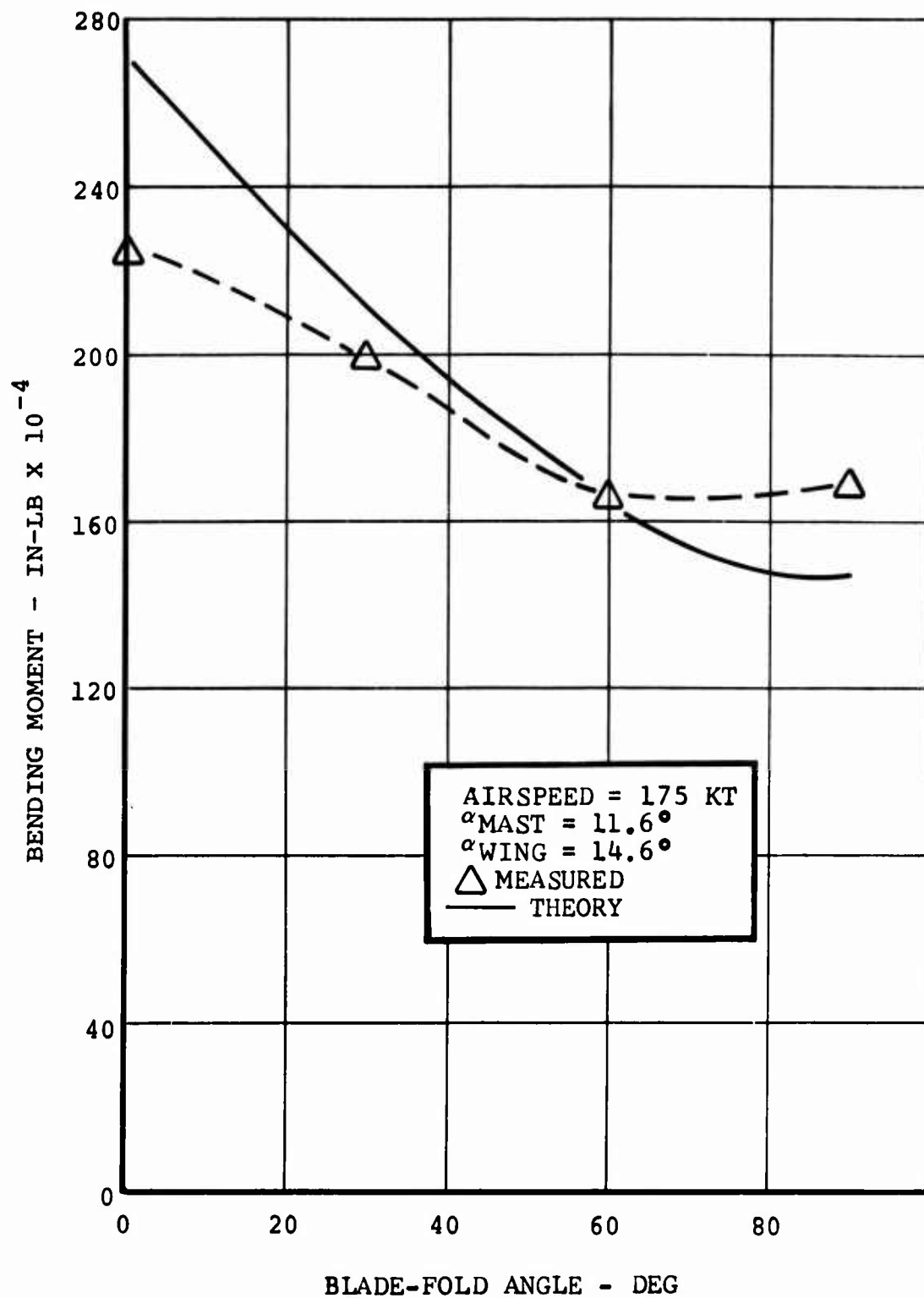
Figure 61. Correlation Between Theory and Measured Wing Root Beam Bending Moment Variation with Blade Fold Angle.

140
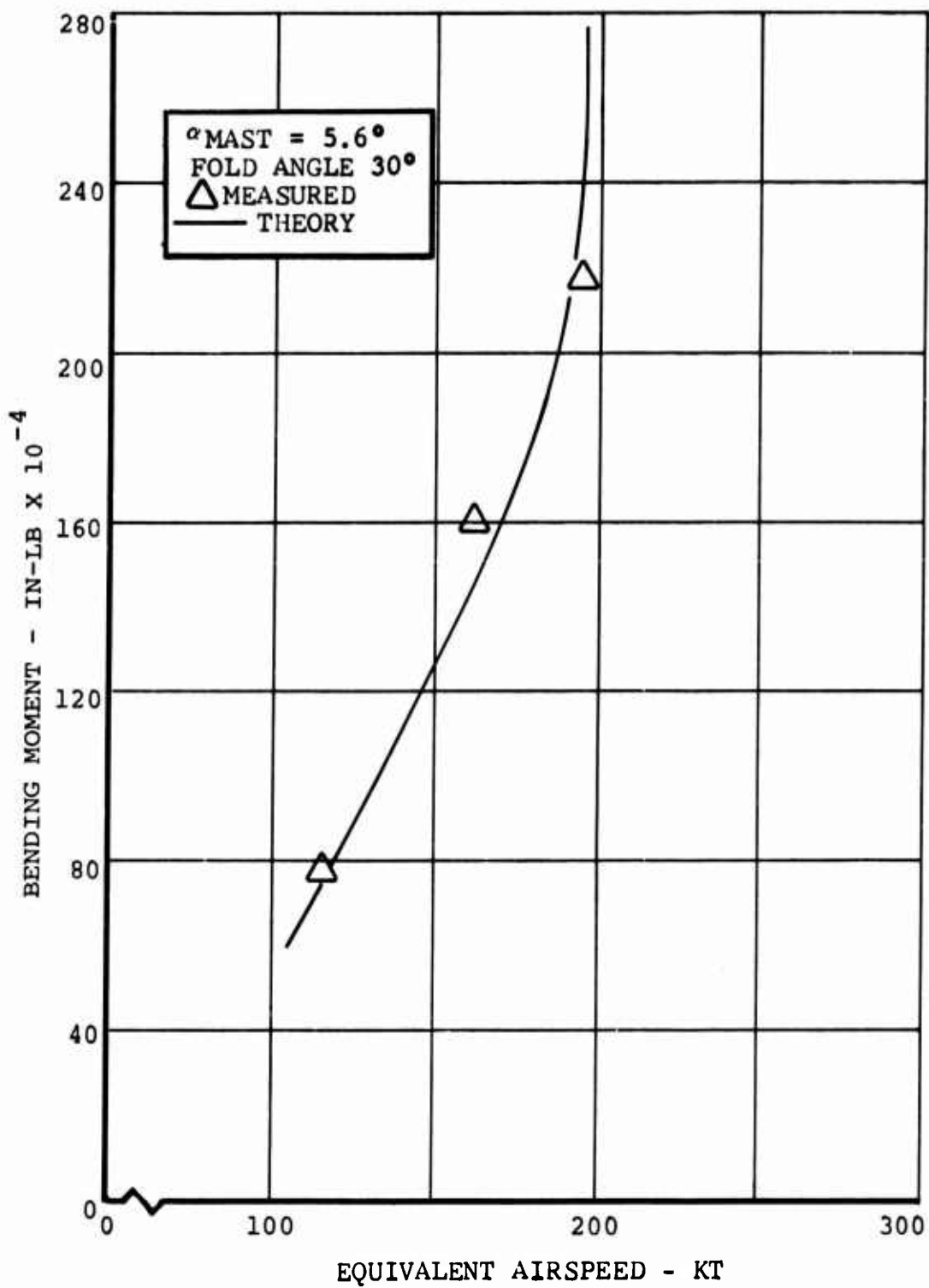
Figure 62. Correlation Between Theory and Measured
Wing Root Beam Bending Moment Variation
With Airspeed.

141

Figure 63. Correlation Between Theory and Measured
Wing Root Beam Bending Moment Variation
With Shaft Angle of Attack.

142

Figure 64.   Correlation Between Theory and Measured
Pitch Change Torque, Variation with
Fold Angle.

143

Figure 65.   Correlation Between Theory and Measured
             Pitch Change Torque, Variation with
             Shaft Angle of Attack

144

Figure 66.   Correlation Between Theory and
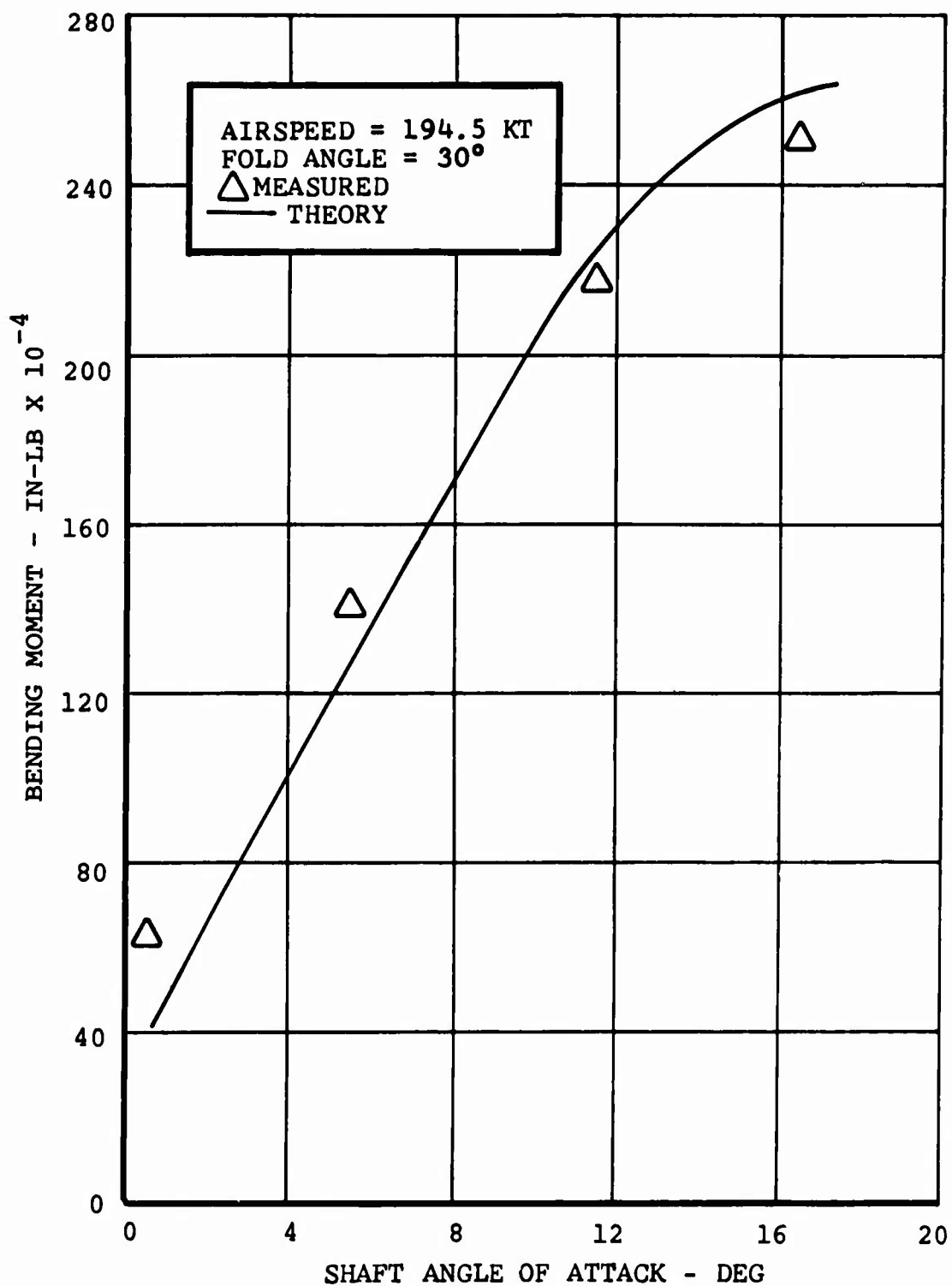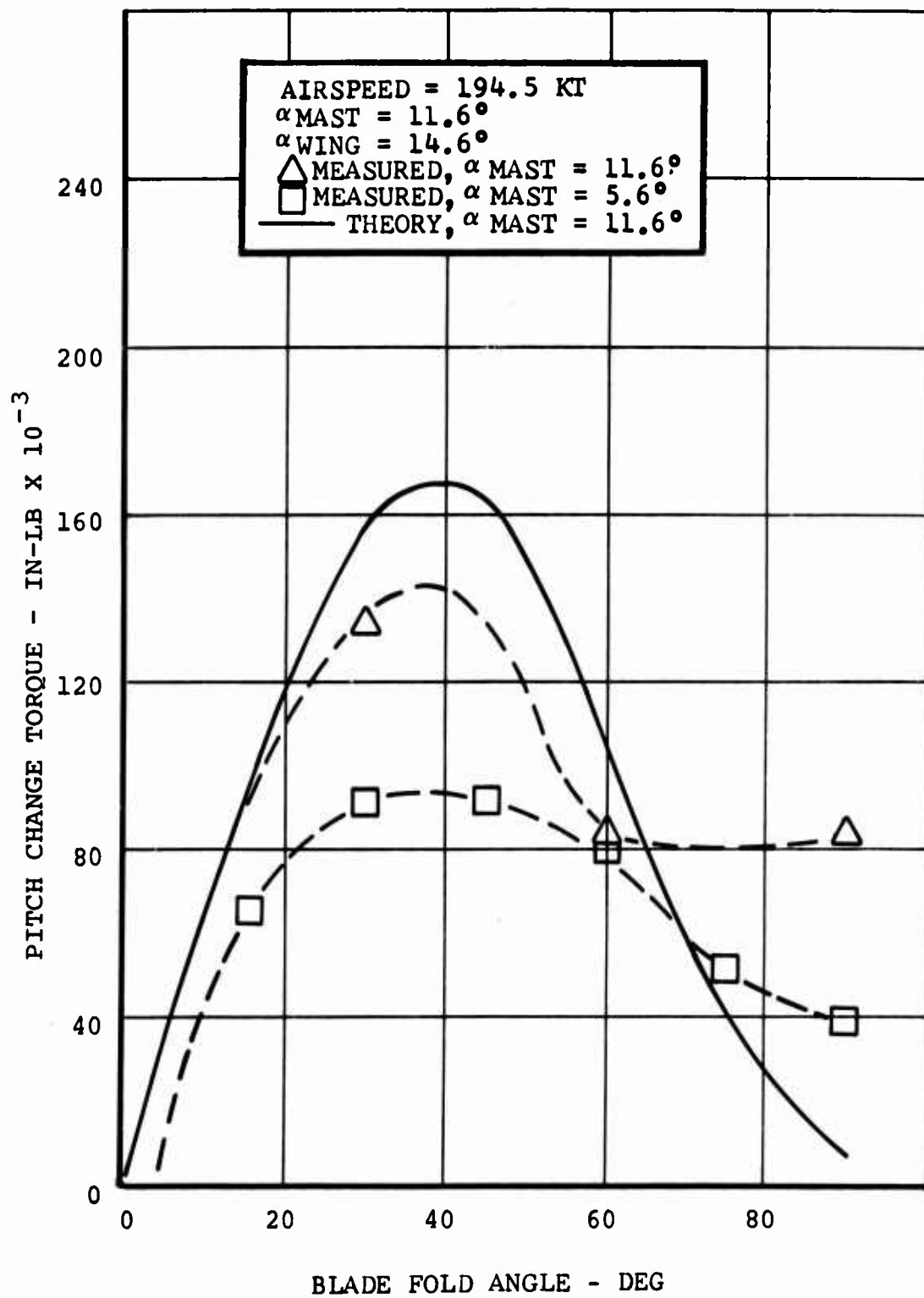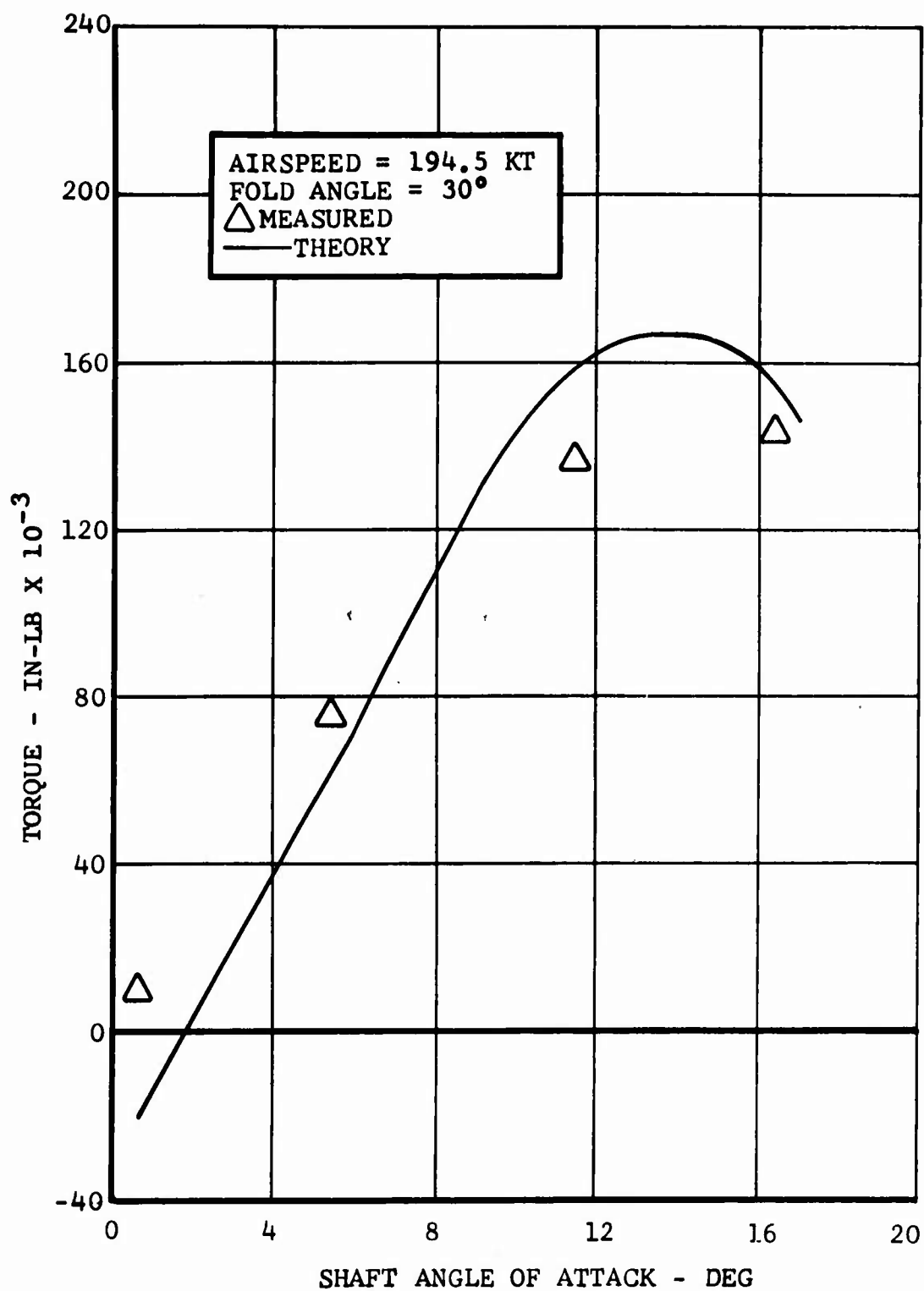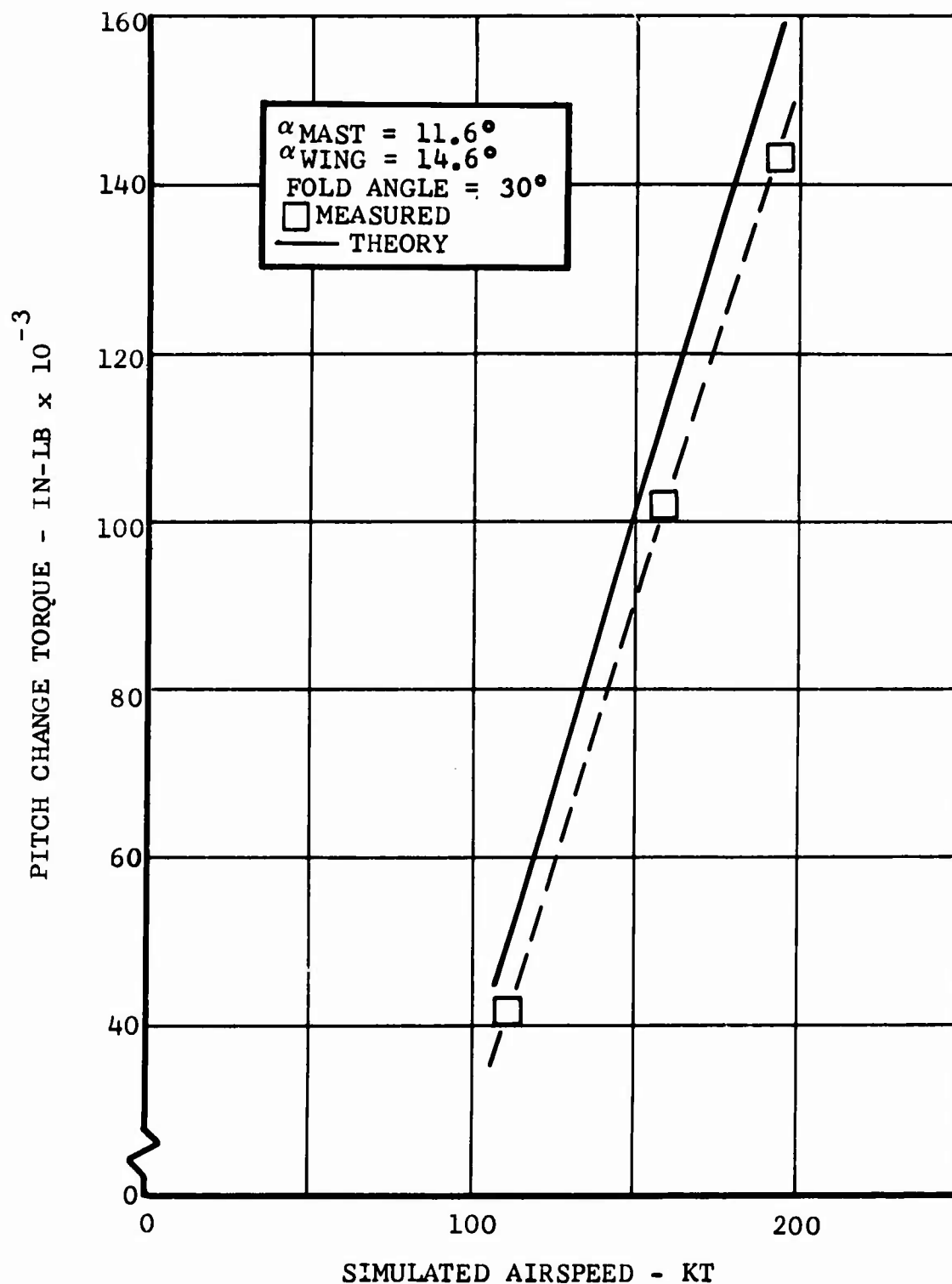   Measured Pitch Change Torque Vari-
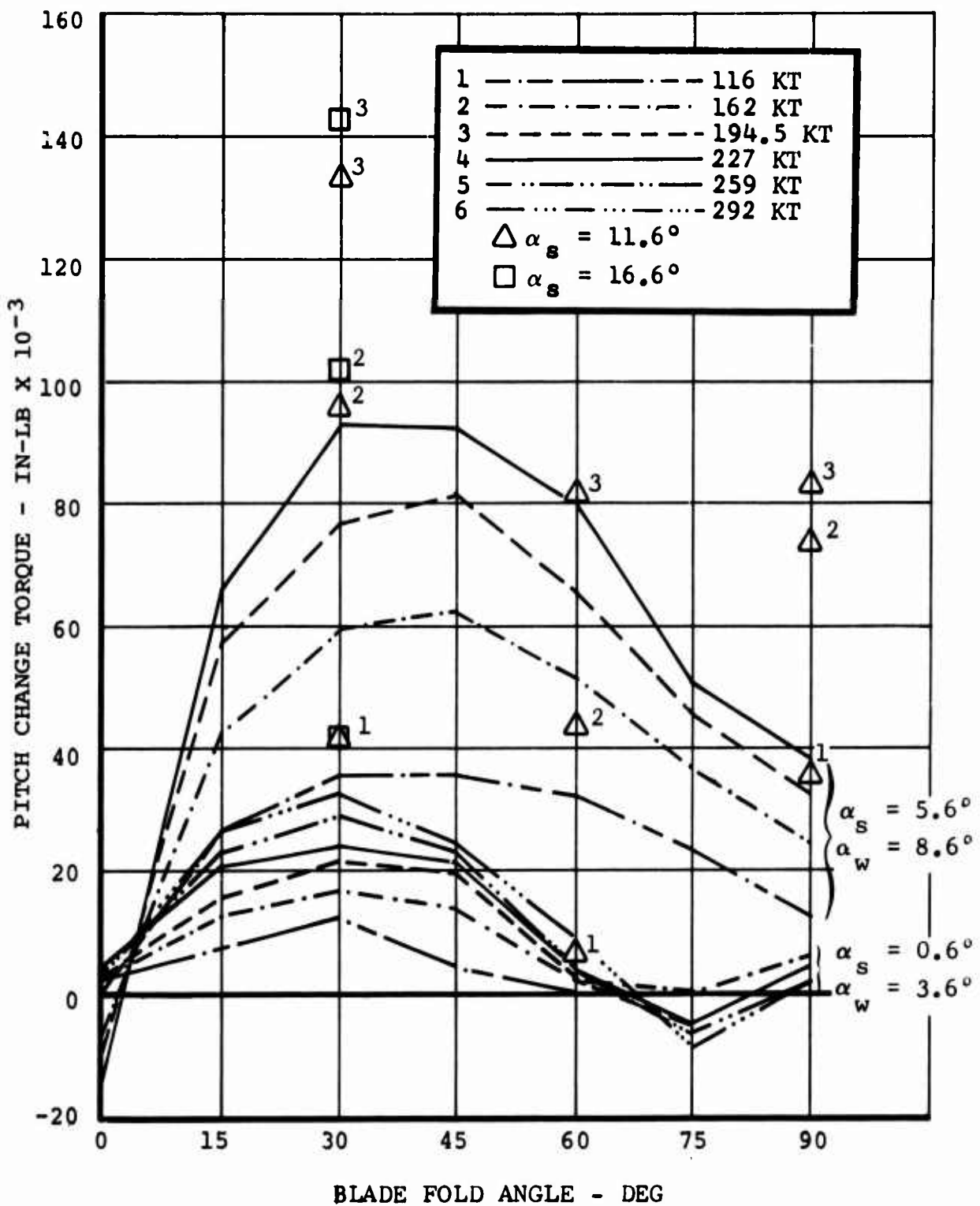   ation with Airspeed

145

Figure 67. Measured Blade Pitch Change Torque Versus
Blade Fold Angle and Angle of Attack.

146

SECTION IV

DYNAMIC ANALYSIS AND PARAMETRIC STUDY

A dynamic analysis of a representative, 66,000-pound gross weight, FPR VTOL design was made to indicate dynamic stability and response characteristics during the feathering and folding of the blades of that class aircraft. It also serves as the basis for a parametric study to identify design factors which control the dynamic stability and response during blade feathering/folding.

The design used for this analysis is one developed by Bell Helicopter Company under contract to the Air Force Flight Dyanmics Laboratory.[17] It carries the Bell Helicopter design designation D270A. Descriptive data and major component drawings are given in Appendix II.[18] The data provided are sufficient to allow the reader to conduct an independent analysis.

A. D270A DYNAMIC ANALYSIS

The following D270A feather/fold dynamic characteristics were identified in the course of this analysis.

- proprotor/pylon stability boundaries
- wing/blade flutter and divergence boundaries
- dynamic response during blade feathering
- gust and maneuver limits

Although the analysis was focused on the feather/fold sequence, the proprotor stability boundary in proprotor cruise mode and system natural frequencies in all modes were determined.

A number of D270A design features are incorporated on the basis of dynamic considerations. These will be discussed first.

1. Design Features Influenced by Dynamic Considerations

a. Wing

The wing thickness and planform are selected primarily on the basis of proprotor dynamic stability considerations. A wing thickness ratio of 0.18, constant root to tip, combined with a tapered chord section and spars located at 5- and 50-percent chord, provide a large torque box. All of the required bending material is concentrated in the skins and spar webs to maximize the effective torque box skin thickness. The skin gage in the outboard 50-percent span is greater than

147

required for strength, further increasing the wing torsional stiffness. The high torsional stiffness is reflected in a tip torsional spring rate of 6.25×10^6 in-lb/radian. The wing bending stiffnesses, beamwise and chordwise, were established by strength requirements.

A wing forward sweep of six degrees was chosen to minimize the distance from the tip-path-plane of the proprotor to the wing elastic axis, thus minimizing the destabilizing influence of the proprotor shear forces, while maintaining adequate flapping clearance.

b. Pylon

The pylon is rigidly attached to the wing tip to take advantage of the wing torsional stiffness. The shaft is as short as possible, consistent with flapping clearance requirements.

c. Proprotor

A gimbaled hub, three-bladed, semirigid type proprotor was chosen on the basis of blade loads, blade motion stability, and mechanical stability considerations. When the gimbal freedom is locked out, as it is before feathering the blades, this proprotor configuration approaches a propeller in stiffness characteristics.

The proprotor blades are extremely strong and stiff to resist oscillatory loads in helicopter mode and gust and maneuver loads in proprotor mode. The blades are preconed $2\frac{1}{2}$ degrees and employ positive pitch-flap coupling (δ_3 = -25 degrees) to preclude blade motion instability.[7]

2. Feather-Fold Flight Procedure

For this analysis it was assumed the following flight procedures will be followed when feathering and folding the blades:

- The airspeed will be typically between 150 and 200 knots. In this analysis, 175 knots were used as a representative airspeed.

- The aircraft attitude will be trimmed, using the wing flaps, to zero degrees fuselage angle of attack. This places the shaft at zero angle of attack to minimize the variation in proprotor steady aerodynamic forces and moments during feathering and folding.

148

- Flapping will be automatically locked out prior to feathering the blades, and restored only after the blades are unfeathered.

This operational procedure was established in light of the results of exploratory tests and studies, including the wind tunnel test conducted under this program.

3. Airframe and Proprotor Natural Frequencies

a. Airframe Natural Frequencies

The natural frequencies of the wing-pylon-fuselage system were calculated using a finite element (beam representation only) vibration analysis. The empennage and proprotor were assumed to be lumped rigid masses.

Figures 68 and 69 show the symmetric and asymmetric natural frequencies versus mast conversion angles. The changes in natural frequency when the proprotor gimbal is locked out prior to and during the feather/fold sequence are also indicated. Table V, below, identifies the modes.

TABLE V

AIRFRAME NATURAL FREQUENCY IDENTIFICATION

Mode No.	Symmetric	Asymmetric
1	Wing 1st Beam	Wing 1st Torsion
2	Wing 1st Chord	Wing 1st Chord
3	Wing 1st Torsion	Fuselage Lateral
4	Fuselage Vertical	Wing 1st Beam
5	Wing 2nd Beam	Wing 2nd Torsion
6	Wing 2nd Torsion	Wing 2nd Beam
7	Wing 2nd Chord	Wing 2nd Chord

Several resonance problems are indicated: 1) The proximity to one-per-rev of the first symmetric chord and first asymmetric torsion modes and resonance during partial conversion of the first asymmetric chord mode, indicate that rpm may have to be scheduled during conversion to avoid prolonged operation at resonance. However, this may not be

149

as serious a problem as it appears since recent full-scale
tests indicate operation in and near one-per-rev resonance is
possible with proprotors.[19] 2) The wing second beam and
torsion modes are indicated to be in three-per-rev resonance.
These modes have nodal points near the hub, thus they are
weakly excited by the proprotors. These modes can probably
be moved out of resonance by spanwise relocation of the
engines.

b. Proprotor Natural Frequencies

The proprotor blade natural frequencies were calculated using
a Myklestad-type analysis for a rotating-twisted beam. The
analysis includes the coupling between beamwise and chord-
wise deflections that results from the built-in twist and
collective pitch. Good correlation has been achieved with
the measured frequencies of many rotor designs, including
three-bladed, semirigid rotors such as those of the Model
D270A.

Figures 70 and 71 show the calculated natural frequencies as
a function of rpm and collective pitch. Figure 72 shows the
change in the frequencies when gimbal freedom is locked out.

The frequencies are presented here in terms of collective and
cyclic modes. The collective modes are those excited by air-
loads whose frequency per revolution is an integer multiple of
the number of blades. Noninteger multiple harmonic airloads
excite the cyclic modes. The coupled natural frequencies are
noted by crosses (x) and diamonds (◊). The crosses denote
modes whose largest deflection is normal to the plane of
rotation. The solid lines denote the frequency of an untwisted
blade at zero collective pitch (i.e., uncoupled beamwise and
chordwise frequencies) and are provided for reference. By
comparing the uncoupled and coupled frequencies, the effect
of built-in twist on the blade frequencies is apparent.

Past experience of the design and testing of the three-bladed
semirigid rotors has shown that frequency placement of the
first inplane (cyclic) and second beamwise (collective) modes
poses the most severe requirements. The first inplane mode
must be sufficiently removed from one-per-rev to avoid high
one-per-rev loads, but cannot be too high or two-per-rev loads
will be a problem. A frequency of 1.5-per-rev results in the
lowest oscillatory loads. However, frequencies as low as
1.25-per-rev are acceptable. Meeting this requirement can be
difficult in proprotors because of the wide rpm and collective
range required for efficient operation. The second beam mode
must be located above three-per-rev to avoid high loads and
airframe vibration. In helicopters, keeping this mode out
of resonance has been a problem; however, it is less of a

150

problem with proprotors because of the thicker and stiffer blade root sections required for static strength.

The frequency location of the major blade modes of the D270A proprotor is satisfactory: the first inplane mode varies from 1.8 to 1.38-per-rev in helicopter mode (134 rpm) and from 1.5 to 1.85-per-rev in airplane mode (225 rpm). The second beam mode is about 4.0-per-rev in both helicopter and airplane mode. Thus, these two modes are well located. Close proximity to 4-per-rev resonance is indicated for the second cyclic mode at high pitch in airplane mode (225 rpm) and 6-per-rev resonance for the third collective mode at high collective pitch. However, low airload excitation at these resonances would be expected.

When gimbal freedom is locked out, the second cyclic mode is in resonance with 2-per-rev at tip speeds above 750 feet per second. Consequently, when flapping is locked out, the proprotor may have to be restricted to 250 rpm, maximum. The collective modes are not affected by locking out flapping.

The frequency of the blade first torsional mode was not calculated but is estimated to be located at 4.5-per-rev. This mode is rigid body blade pitching based on the control system flexibility. The second torsional frequency which involves blade torsional deflection is much higher in semirigid rotor types due to the inherent torsional stiffness of the blades.

The design blade loads for the D270A were scaled from loads obtained in tilt-proprotor design studies. These past studies have shown that for tilt-proprotors two flight conditions impose the designing loads. For oscillatory loads, the maximum level flight airspeed in helicopter mode is the most severe. These must be below the endurance limit to achieve a reasonable fatigue life for the proprotor. Design limit loads are generally established by a vertical gust encounter in airplane mode.

4. Proprotor Stability, Flutter, and Divergence Character-
    istics

a. Proprotor/Pylon Stability

The proprotor/pylon stability (whirl flutter) boundaries were calculated for proprotor mode as well as during blade feathering. In proprotor mode the gimbal is restrained with a moderate, isotropic, hub restraint of 3850 ft-lb/deg of hub flapping. Before feathering the blades, the hub gimbal freedom is locked out with a hydraulic flapping lockout (see Drawing D270A-410-002).

151

The mathematical model for the proprotor stability analysis included the wing fundamental beam, chord, and torsion modes and the pylon yaw (second chord mode). Both symmetric and asymmetric modes were considered. The symmetric modes were found to be the less stable.

Figure 73 shows the proprotor/pylon stability boundary in proprotor mode versus rpm. The mode of instability that first becomes unstable is the symmetric wing chord mode. The symmetric wing beam mode becomes unstable at a slightly higher airspeed. The root motion with airspeed, calculated using a Bell Helicopter Company linearized proprotor stability analysis, is shown in Figure 74.

The stability margin requirement of $1.15V_L$ as specified in MIL-8870 (ASG) is met by the D270. If it is desired to increase the stability margin in proprotor mode, reducing the pitch-flap coupling is the most effective means. The effect of reducing the pitch-flap coupling to $\delta_3 = -15^\circ$ or -20°, is shown in Figure 73. This would require some redesign of the proprotor rotating controls but could be accomplished with a small weight increase.

When the gimbal flapping freedom is locked out during blade feathering, the stability margin is increased. Figure 75 shows the proprotor stability boundary with the flapping locked out. The mode of instability in the 100 to 300 rpm range is that of the wing beam mode but also involves wing chord motion. Figure 76 shows the root motion with airspeed. The beam mode in this case corresponds to the retrograde whirl mode of classical whirl flutter theory.[20]

At very low rpm, divergence of the wing beam mode is the mode of instability. The indicated stability margin is more than ample.

b. Flutter and Divergence

Flutter and divergence characteristics during blade folding were calculated using the Folding-Dynamics Analysis, DFAL17. Since the math model consists of a cantilever wing, the divergence boundary in this case is somewhat conservative.

Figure 77 shows the D270 flutter and divergence boundaries as a function of the blade fold angle. For zero fold the mode of instability is wing torsional divergence, a result of the proprotor aerodynamic center being well forward of the wing elastic axis. Figure 78 shows the natural frequency variation with airspeed with the blades folded. While the mode denoted wing beam bending is indicated to diverge, inspection of the mode shape shows increasing wing torsional deflection as

airspeed increases. As the blades are folded, the divergence speed increases rapidly since the proprotor aerodynamic center moves aft.

The flutter boundary indicated in Figure 77 is a weak, wing chord mode flutter. It results from coupling between the blade beamwise bending and the second wing chord mode. The second chord mode contains a large amount of nacelle yawing coupling the mode with blade beam bending at large fold angles. Figure 79 shows the natural frequency variation with airspeed for a fold angle of 60 degrees. Figure 80 shows the damping versus airspeed. Note that the blade natural frequencies increase rapidly with airspeed and coalesce with the second chord mode at a speed of about 890 knots. Since aerodynamic damping of wing chord motions is small, the blade drives the chord mode unstable. It should be noted that only a small amount of damping is indicated to be required to stabilize this flutter. Coupling of the first chord mode with blade beam bending was investigated experimentally as discussed in Section III.

The blade over mass balancing required for helicopter mode effectively prevents blade flutter during folding.

The relatively low divergence airspeed suggested that aileron reversal might be a problem. The reversal speed was estimated using the method outlined in Reference 22 but using the wing tip torsional spring rate rather than the 0.7 span value used for conventional aircraft. This gave a reversal speed of 320 knots for the zero-degree fold angle. This low reversal speed emphasizes the requirement for including aeroelastic effects in stability and control analysis of the feather/fold sequence.

5. Dynamic Response During Blade Feathering

a. Math Model and Method

The first four coupled wing-pylon-fuselage modes are included in the math model as well as the proprotor first collective and first and second cyclic modes. The coupled wing-pylon-fuselage modes consist of the wing fundamental beam and chord bending and torsion modes, and the first fuselage vertical bending mode. As indicated in Figures 68 and 69, the wing second beam bending and torsion modes are also transited by three-per-rev during blade feathering. However, these modes are relatively weak compared to the fundamental modes and were, therefore, neglected. Since the proprotors are inter-connected and indexed such that only symmetric excitation is possible, the asymmetric mode response was not analyzed.

A time history of the pylon response during blade feathering is shown in Figure 81. The flight condition follows the procedure discussed earlier; airspeed 175 knots, flapping freedom locked out.

b. Response Amplitude

Figures 82 and 83 show the calculated vibratory response during blade feathering at the pylon conversion axis-shaft intersection and at the crew station, respectively, as a function of feathering rate. Also, shown in Figure 83 is the longitudinal acceleration caused by the transient thrust generated by blade feathering. This in combination with the vibratory response characteristics suggests that a feathering time of three to five seconds is desirable.

The acceleration levels on the pylon, at the engine locations, and on the fuselage, are all well below normal design limits. The stresses in the wing and at the pylon to wing attachment are also below design limits. For example, the peak wing tip deflection (referenced to the shaft centerline) is ±1.6 inches. For reference, the limit beamwise deflection is 32 inches. Oscillatory blade loads are also well below endurance limits for this condition. It was concluded that wing and pylon loads and vibration are not a limitation on blade feathering.

However, the crew station response at the wing beam frequency, does indicate a potential human factors problem. At the beam frequency the acceleration level is close to the level established in Reference 23 as alarming. The transient nature may reduce the significance of this observation, but a requirement for a study of the crew acceptance of this type of response is indicated.

The response sensitivity to airspeed and load factor was also investigated and is shown in Figures 84 and 85. The relative insensitivity to airspeed is explained by the reduction in wing angle of attack as airspeed is increased. Thus, the wing upwash is reduced as the dynamic pressure increases. (In making the airspeed sensitivity calculation, it was assumed the flaps were adjusted to maintain a shaft angle of attack of zero.)

In making the load factor calculation, the shaft angle of attack was increased along with the wing angle of attack. Apparently the increased shaft angle offsets the increase in wing upwash at increased load factor to keep the response constant and combines with reduced upwash at reduced load factors to decrease the response.

154

Load factor does have a marked effect on blade loads. This is discussed next.

6. Gust and Maneuver Limits

a. Critical Components

The blade fold hinge loads determine the gust and maneuver limits during feathering and folding the blades. Drawing D270-410-003, in Appendix II, shows the fold hinge arrangement. Tearout of the spindle folding knuckle lugs is the estimated failure mode. The spindle is titanium; an ultimate stress of 130,000 was assumed. The limit bending moment is calculated to be 2.2×10^6 inch-pounds (nonrotating). Since the folding hinge is inboard of the blade spindle, blade bending moments do not enter the control system.

The wing root becomes critical when the blades are folded past 20-degree fold angle.

b. Methods

A discrete, 25-wing chord length, 1-cosine shape, vertical gust was used in the analysis. A sharp edged gust was also investigated; the loads imposed were about 15 percent higher than those using the 1-cosine shaped gust. The rigid body vertical motion of fuselage was included in the analysis to introduce inertia and aerodynamic relief. However, rigid body pitching was neglected.

Program ARAP06 was used to evaluate the limits during blade feathering. For gusts, the aircraft was assumed to be in unaccelerated flight. The gust was imposed with the prop-rotor at constant rpm, with the rpm varied from 0 to 80 percent of hover rpm. The allowable limit load was then used to define the limit gust. For maneuvers the wing and shaft angles of attack were adjusted to provide the required lift. A fatigue oscillatory load limit was used to define the maneuver limit.

The limits during folding were determined neglecting stall and are thus conservative. The blade lift curve slope was adjusted with fold angle in accordance with the lift curve slope variation measured in the dynamic model test. The allowable limit loads were used to define both gust and maneuver limits.

c. Limits

Figure 86 shows the gust and maneuver limits versus rpm and fold angle. The influence of airspeed on the limits is shown

155

in Figure 87. As shown, the gust limit and the maneuver limit during blade folding are acceptable. A small increase in fold hinge strength would result in meeting the required 50 foot per second gust at V_{LR}, 230 knots.

Determination of the maneuver load factor limits during feathering raised several questions: (1) What oscillatory load limit should be used? And (2), at what rpm should the static limit be used rather than an oscillatory limit? For example, if the proprotor stopping time is five seconds, only ten load cycles will occur during feathering, and thus a low cyclic limit can be applied. However, when flapping is locked out prior to feathering, a large number of cycles can accumulate so the endurance limit must be used for that condition. And at some low rpm, the number of cycles will be very low, so the static limit may be used.

For this study the following procedure was followed: (1) Between 80- and 40-percent hover rpm, the endurance limit (16,000 psi for titanium) was used. The limit was increased to that for 10,000 cycles (30,000 psi) at 20-percent rpm, and further increased to the static limit at zero rpm.

The resulting maneuver limits, based on the fold hinge lug, are considered too low. When the strength of the fold hinge lug increased to that of the blade and hub, a more acceptable maneuver limit results. Further increases (or possibly a decrease) in the maneuver limit could result from a revised allowable limit schedule.

7. Blade Deflections

Because the D270A blades and hub assembly are extremely stiff relatively small blade deflection occurs during feathering and folding. This is significant from the standpoint of wing-blade clearance. For reference, the calculated peak deflections under extreme conditions during folding and feathering are tabulated in Table VI. The inplane deflections are greater than the out-of-plane deflections because of the high blade collective pitch during folding and feathering.

TABLE VI

BLADE TIP PEAK DEFLECTIONS - AIRSPEED 175 KNOTS

Condition	Inplane (inches)	Out-of-Plane (inches)
Feathering, n = 1	5.5	2.4
Feathering, n = 2	20.1	4.8
Feathering, 50-fps gust	24.4	4.8

156

TABLE VI - Continued

Condition	Inplane (inches)	Out-of-Plane (inches)
Folding, n = 1	2.6	0.2
Folding, n = 2	9.6	0.52
Folding, 50-fps gust	19.4	7.6

B. PARAMETRIC STUDY

The sensitivity of the dynamic characteristics during blade
feathering and folding was assessed for several parameters.
These include:

- design disc loading
- proprotor type
- wing stiffness
- wing to proprotor blade spacing

The effect of feathering rate was investigated in the
correlation study and the dynamic analysis of the D270A.
The influence of detail design parameters such as pylon
center of gravity and pylon incidence was also investigated
and is reported in this section.

1. Sensitivity to Design Disc Loading

The design disc loading was found to have a strong influence
on proprotor stability, a lesser influence on dynamic response
during feathering, and no significant influence on flutter and
divergence during folding, or on the gust and maneuver limits.

The D270A design disc loading of 16.8 was varied by ±25 per-
cent using equal mission capability as a design constraint. The
design value of 16.8 was selected to minimize design gross weight,
using the technique described in Reference 24. Table VII shows
the mass and stiffness properties for the disc loadings investi-
gated. These were estimated using the methods outlined in Ref-
erence 18. It was assumed that design factors such as placement
of the blade natural frequencies were the same regardless of
disc loading.

Figure 88 shows the influence of disc loading on proprotor/
pylon stability. Note that the influence is strongest in
proprotor mode, when the hub gimbal is free to flap. However,
a significant influence is also evident when the gimbal is

157

locked out. The high sensitivity to disc loading is explained by the variation in blade Lock number. The D270A blade Lock number is 6.2; for a disc loading of 12 the Lock number increases to 8.7 and for 20 it decreases to 5.0. Since the Lock number represents the ratio of aerodynamic and inertia forces acting on the blades and consequently the wing/pylon, a higher Lock number generally implies reduced stability.

The variation in response during feathering is shown in Figure 89. Note that lower disc loading leads to a higher response. The reason for this is partially explained by the higher Lock number, and partially by the lower wing loading at the same lower disc loading.

The reason for the negligible influence of disc loading on flutter and divergence and gust and maneuver limits is the wing and blade strength to airload ratio remains a design constant regardless of disc loading.

2. Proprotor Type

There are several configurations possible for a folding proprotor. The gimbaled, semirigid configuration such as used on the D270A is one configuration. Other possible configurations are the hingeless or "rigid" rotor which may be either soft or stiff in the plane of the rotor, and the fully articulated and free-to-flap configurations.

Analysis of all of these configurations was not practical. The hingeless, soft-inplane type was chosen for analysis since it represents an extreme in flexibility compared to the gimbaled semirigid type. It should be noted that locking out the flapping freedom before feathering on the fully articulated (and lag freedom) and the free-to-flap configurations appears necessary to prevent excessive blade motions. When this is done these rotor configurations approach either the gimbaled-semirigid or the hingeless-soft inplane configurations in dynamic characteristics, depending on the blade flexibility.

a. Hingeless-Soft Inplane Proprotor Parameters

The parameters of a 49.2-foot diameter, four-bladed, hingeless folding proprotor, developed under contract to the Air Force were used in this study. Figure 90 shows the blade stiffness and mass distributions of the proprotor. The blade natural frequencies are shown in Figure 91.

In comparison to the D270 proprotor blades (see Appendix II), this proprotor may be characterized as extremely flexible. The blade weight is approximately 55 percent of the D270

158

blade weight, and the stiffness at 10 percent radius only about 7.8 percent of that of the D270A blade in the feathering spindle region, 7½ percent radius.

For this study a three-bladed hingeless soft-inplane proprotor was substituted for the D270A gimballed proprotor. The wing/pylon dynamic characteristics were not modified.

TABLE VII

WEIGHT AND STIFFNESS VERSUS DISC LOADING*

		DL = 12.0	DL = 16.8	DL = 20.0
Gross Weight	lb	82500	66000	69300
Weight empty	lb	55000	44900	45200
Rotor radius	ft	33.0	25.0	23.5
Blade chord	in.	30.3	40.0	42.5
Wing span	ft	80.25	64.25	61.25
Wing area	ft²	1101	706	641
Wing loading	lb/ft²	74.9	93.5	108.1
Wing root stiffness	lb-in²	133×10^9	68×10^9	65×10^9
Wing tip stiffness	lb-in²	15.6×10^9	10×10^9	10×10^9
Rotor weight	lb	9005	7521	7819
Pylon weight	lb	4601	3849	4002
Wing weight	lb	8016	5137	4963

*Basis: Equal mission capability

b. <u>Dynamic Stability Characteristics</u>

The proprotor/pylon stability boundary with the hingeless-soft-inplane proprotor is shown in Figure 92 as a function of rpm. In the proprotor cruise mode rpm range the mode of instability is the same as that with the gimbaled proprotor, the wing chordwise bending mode. The stability boundary is slightly higher, however. Below 150 rpm the mode of instability changes to one involving coupled flapping, blade

159

inplane, and wing beam motion. The boundary decreases with rpm, and is a minimum near zero rpm.

The low rpm instability appears to be of the same nature as that measured with the dynamic model when the gimbal was free to flap; coalescence of the blade flapping and wing beam modes. A plot of flapping natural frequency versus wing beam natural frequency indicates the frequencies would coalesce at about 80 rpm.

With the blades stopped, blade flutter and divergence are more of a problem than with the D270A proprotor. The blade divergence boundary is greatly reduced. Figure 93 shows the variation in blade beam bending natural frequency with airspeed for sideslip angles of 5, 10, and 20 degrees. This characteristic is similar to that measured with hingeless stiff inplane edgewise stoppable rotors.[24]

Since the divergence dynamic pressure is essentially proportional to the blade stiffness, it appears divergence is a fundamental problem associated with a hingeless type folding proprotor.

A second aeroelastic characteristic during folding, is also a potential problem for the gimballed type folding proprotor, a coupled blade beam bending wing-chord bending flutter. Figures 94 and 95 show the calculated variation of frequency and damping with airspeed for a 60-degree fold angle. As was observed with the gimballed rotor, the blade bending modes increase in frequency and transit the wing beam and chord bending, and torsion modes. At each crossing the damping of the wing modes decreased. For the beam and torsion modes the reduction in damping does not overcome the available aerodynamic damping. But for the wing chord mode negative damping is predicted. Whether or not this would result in flutter depends on the structural damping.

c. Response Characteristics

The pylon vibration levels during blade feathering are similar to those with the gimballed proprotor, but are more sensitive to load factor. Figure 96 compares the vibration levels calculated for both types. The increased sensitivity of the hingeless proprotor is caused by the larger blade tip deflections associated with the blade flexibility. Figure 97 compares the blade tip peak out-of-plane deflections during feathering for the two proprotor types as a function of load factors. Blade tip deflections toward the wing leading edge represent an effective decrease in wing-rotor spacing, which is shown later in this section to increase response.

160

Blade oscillatory deflections during feathering were also investigated. Since the fundamental inplane natural frequency is below operating rpm in the normal operating rpm range, about 0.7-per-rev, 1-per-rev resonance is transmitted during feathering. For very low rates of feathering, 1-per-rev resonance of the first inplane mode could be a load problem. However for rapid rates the resonant build up is relatively small. Figure 98 shows the blade tip peak inplane deflections versus rpm during a four second blade feathering. The oscillation limit for the rotor is not known but the magnitude shown is clearly within the capability of such a flexible blade.

d. Gust and Maneuver Limit

Since the strength characteristics of the subject proprotor are not known, it is not possible to accurately assess a change in the gust and maneuver limits. The calculated blade tip deflections for several gust and maneuver conditions are given in Table VIII and are large compared to those for the gimbaled semirigid type but appear to be within the strength capability of the hingeless blade. The associated fold hinge loads are somewhat lower, due to the relieving effect of the blade motion. Thus slightly higher gust and maneuver limits (during folding) could result with the hingeless proprotor.

An increase in the limit maneuver load factor during feathering might appear to be a benefit of using the hingeless proprotor type since flapping freedom is retained during feathering. However, the very large deflections at low rpm indicate that high, low cycle, blade loads may result in maneuver limit during feathering, in the same range as those of the stiffer, gimbaled semirigid proprotor. Figure 99 shows the blade tip peak deflection envelope versus rpm for a load factor of 1.5 to illustrate this consideration.

TABLE VIII

BLADE TIP PEAK DEFLECTIONS
HINGELESS, SOFT-INPLANE PROPROTOR
AIRSPEED 175 KNOTS

Condition	Inplane	Out-of-Plane
Feathering, n = 1	15.5	9.8
Feathering, n = 1.5	65.0	22.5
Feathering, 50-fps gust	83.6	26.2

161

TABLE VIII - Continued

Condition	Inplane	Out-of-Plane
Folding, n = 1	2.9	0.91
Folding, n = 1.5	57.4	18.0
Folding, 50-fps gust	153.0	47.8

3. Wing Stiffness

Wing stiffness has a controlling influence on proprotor stability and flutter and divergence. Wing stiffness can be used to a lesser extent to control dynamic response during blade feathering. The influence on gust and maneuver limits is small, since in general the blade loads are more critical.

a. Influence on Stability

Figure 100 shows the effect of varying the wing beam, chord, and torsional stiffness (reference to the wing tip spring rates) separately and simultaneously, on stability in proprotor mode (flapping free). Wing torsion has the strongest influence, up to the design stiffness. Above that stiffness, it is ineffective since the mode of instability becomes that of the wing chord mode. To effect a further increase in stability, the wing torsion and chord stiffness would have to be increased simultaneously. Note that wing beam stiffness does not have a strong influence.

When flapping is locked out the proprotor stability becomes a propeller whirl flutter problem and relative isotropicity of the wing/pylon modes becomes a controlling factor.[20] Figure 101 shows the effect of varying the wing stiffness when flapping is locked out. Since the fundamental beam and chordwise modes are close together in frequency, varying the beam and chord stiffness so as to reduce the isotropicity increasing the stability. Increasing the wing torsional stiffness increases stability since it reduces the amount of shaft pitching in the beamwise mode. When the torsion stiffness is increased more than 25 percent, the mode of instability changes to a forward whirl.

The influence of wing stiffness on the flutter and divergence characteristics during folding was found to be straightforward. The divergence speed varied proportionally to the square root of the wing torsional stiffness, and was not significantly

influenced by the wing beamwise or chordwise stiffness. The
flutter velocity was not sensitive to nominal variation in
the wing stiffness properties.

b. Influence on Response

The influence of wing stiffness on the dynamic response is
somewhat difficult to assess. Figure 102 shows the influence
of wing beamwise and torsional stiffness on the dynamic
response. Increasing the wing torsional stiffness has the
opposite effect of what one might expect on the basis of
superficial considerations. However, the reason for the
increased response with increased torsional stiffness is
logical if the effect of torsional stiffness on the system
damping is considered. For example, for the wing beam mode
an increase in torsional stiffness decreases the amount of
coupled pylon pitching motion. This decrease in pitching
decreases the proprotor aerodynamic damping of the wing beam
mode (C_{mq} contribution). Since the forced response is
essentially proportional to the system damping the response
is increased.

Varying the wing beam stiffness has a smaller influence since
the system damping is not significantly affected by beam
stiffness. However, it should be pointed out that increasing
the beam stiffness, and thus the beam frequency may be desir-
able from a human factor standpoint, since for a given vibra-
tional level the displacement is reduced in proportion to the
frequency squared; i.e., directly proportional to the stiff-
ness. Furthermore, the human tolerance to vibration is
frequency dependent and adjustment of the beam stiffness could
be used to tune the wing beam mode to a more "comfortable"
frequency.

c. Wing Thickness Influence

Increasing the wing thickness is the most efficient means of
increasing wing stiffness for a given material/structural con-
cept. The influence of wing thickness on the response during
feathering is shown in Figure 103. The relatively small
increase in response with increased thickness suggests that
the wing circulation is the strongest source of excitation.

4. Wing to Proprotor Blade Spacing

Wing to rotor spacing has a strong influence on proprotor
stability, divergence and dynamic response. The influence
on gust and maneuver limits is small since the blade is
critical. There are two means of varying the spacing; wing
sweep and mast length.

a. Influence on Stability

The influence of mast length on stability is indicated in Figure 104. The influence of forward sweep on stability, for sweep angles of up to 12 degrees (twice that of the D270A's forward sweep of 6 degrees) was found to be negligible. This is because the wing beam stiffness is very high and thus does not impact on the effective torsional stiffness as strongly as for conventional aircraft designs.

With flapping free, for proprotor mode, increasing the mast stiffness decreases the proprotor stability and would require an increase in wing stiffness to maintain the stability margin. With flapping locked out, however, the stability increases up to a point, with increasing mast length. This increase in stability with mast length follows the travel for propellers noted in Reference 20. Further increases in mast length cause a reduction in the wing divergence speed.

b. Influence on Response

Increasing the wing to rotor spacing reduces the dynamic response during feathering. Figure 105 shows the effect of these parameters on the response at the wing beam frequency. It should be noted at this point that the wing to rotor spacing has a strong influence on the aircraft stability and control characteristics and may not be readily used to control dynamic characteristics.

5. Other Parameters Investigated

Several secondary design parameters were also varied to investigate their influence.

a. Pylon Incidence

The influence of load factor on dynamic response suggested that pylon incidence might be a means of reducing dynamic response. Figure 106 shows that ±5 degrees of incidence reduces the response by about 25 percent. However this approach to reducing response is limited by blade load considerations.

b. Wing Structural Damping

The wing structural damping was assumed to be one percent of critical throughout the dynamic analysis. An increase in structural damping (or the application of external damping) was investigated to determine if that could be used to reduce dynamic response. The results, shown in Figure 107 indicate that a resonable increase in damping is ineffective.

164

c. Pylon Center of Gravity

Since the location of the pylon center of gravity is con-
trollable to some extent, an investigation was made to
determine its influence. This investigation showed the pylon
center of gravity location has a negligible influence on
stability and response.

d. Blade Fold-Hinge Arrangement

As noted earlier, the D270A fold hinge is located inboard of
the pitch change spindle to prevent the blade airloads from
acting through the control system during blade folding.

If the fold hinge were located outboard of the pitch change
spindle, the gust limit (and maneuver load factor limit)
would be greatly reduced. Figure 108 compares the limit
gust for the alternate configuration with that of the D270A.

To raise the allowable gust limit to the level of the D270A,
a feathering lockout would be required to prevent the blade
airloads from acting on the control system.
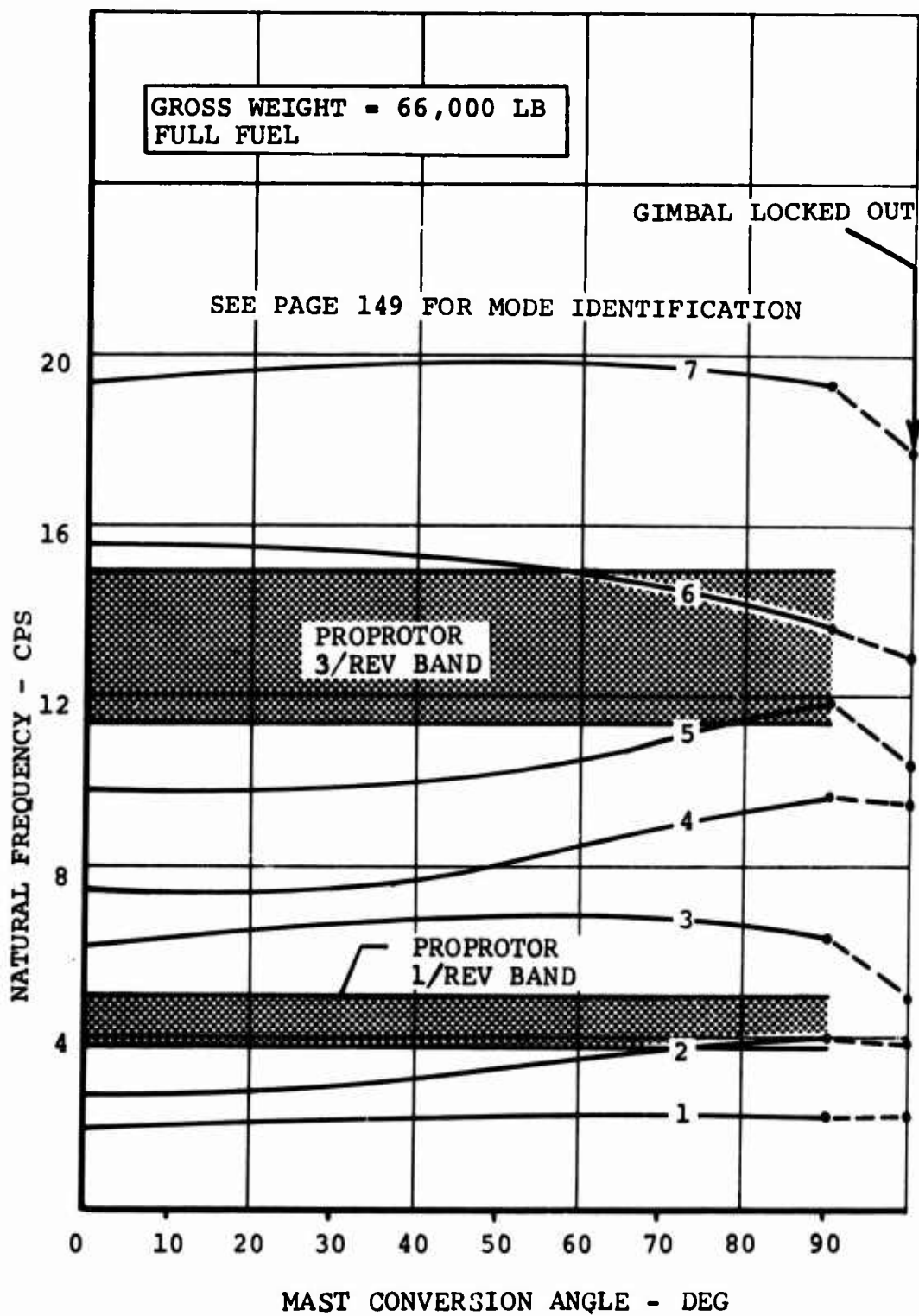
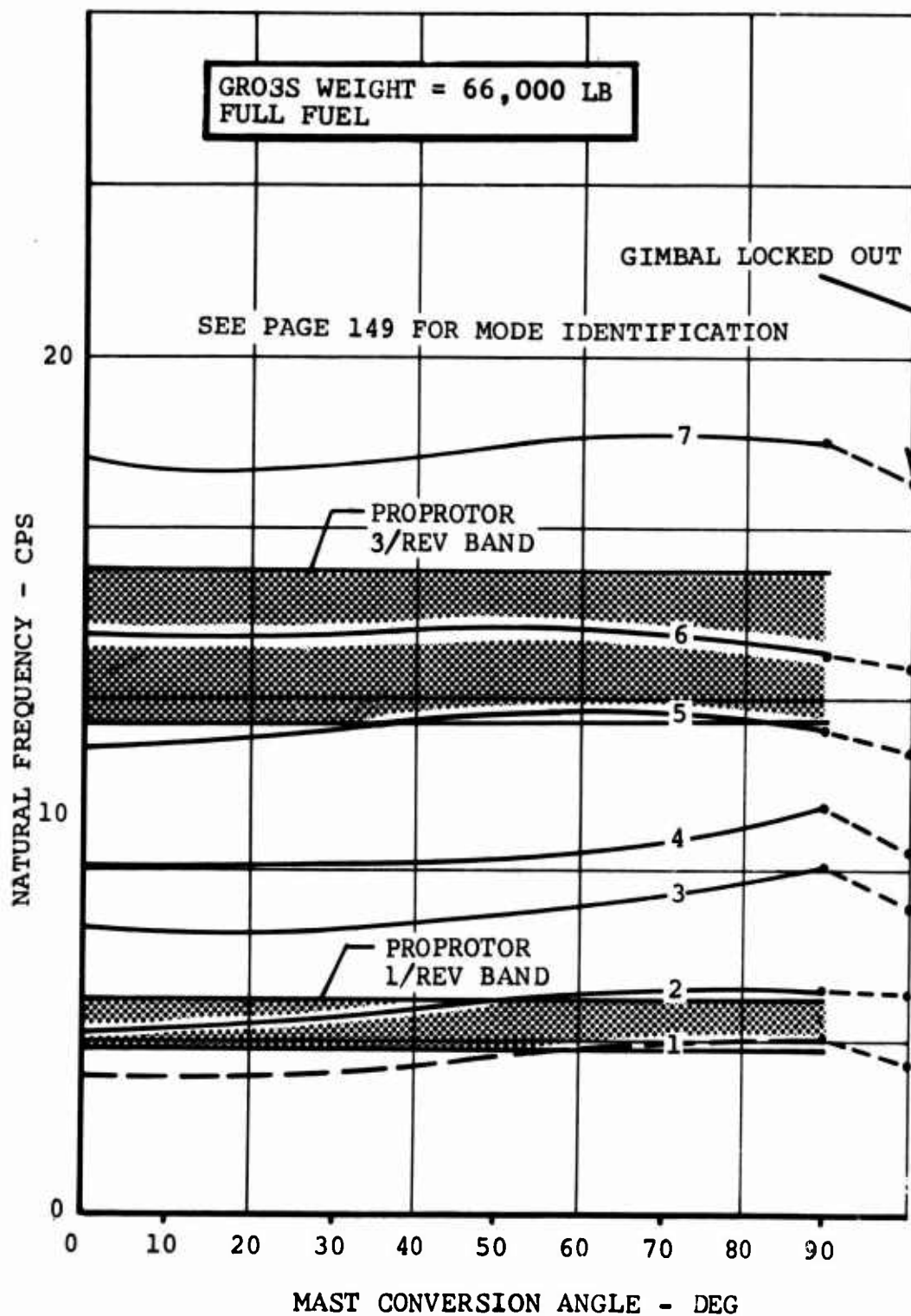Figure 68. Airframe Symmetric Natural Frequencies
Versus Pylon Conversion Angle.

166

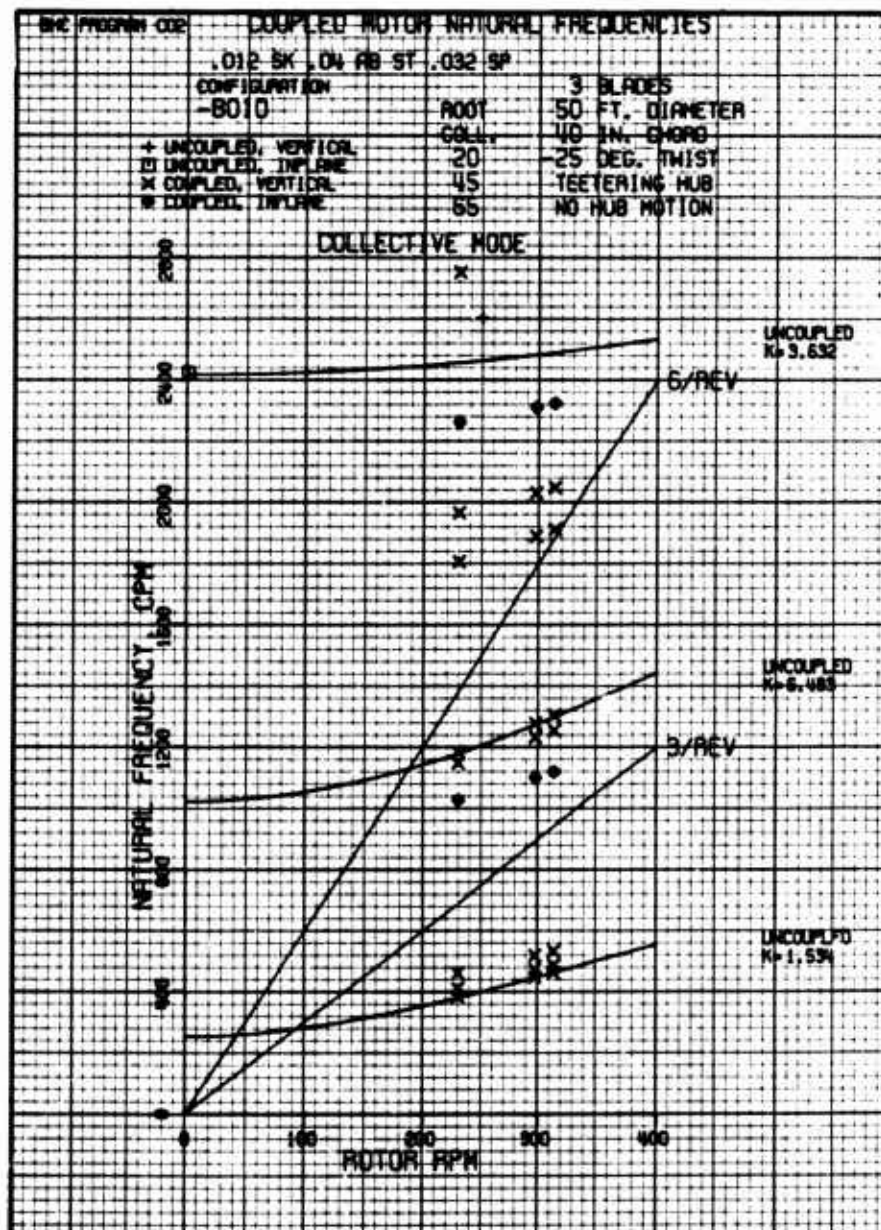Figure 69. Airframe Asymmetric Natural Frequencies Versus
Pylon Conversion Angle.

167

Figure 70. Proprotor Collective Natural
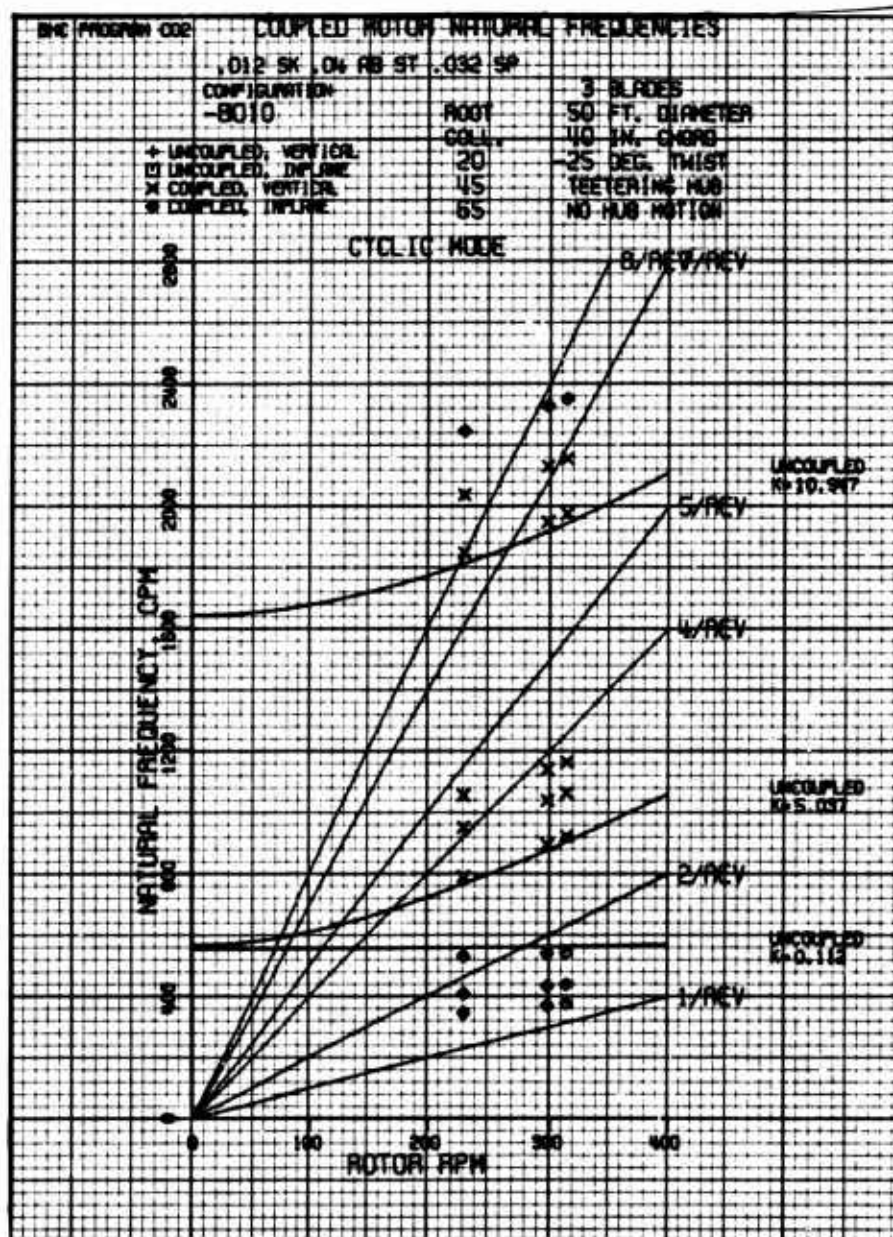Frequencies, Gimbal Free to Flap

168

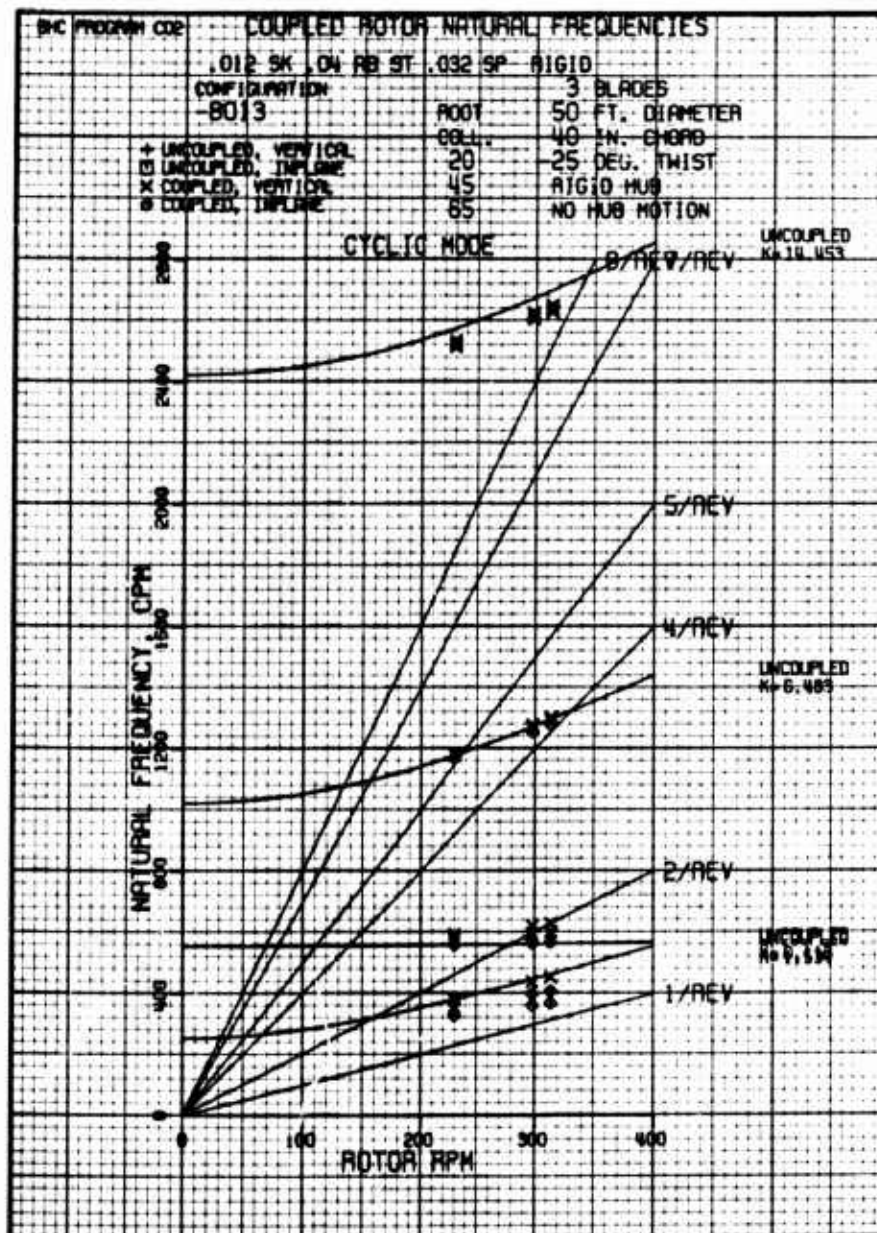Figure 71. Proprotor Cyclic Natural
Frequencies, Gimbal Free-To
Flap

169

Figure 72. Proprotor Cyclic Natural Frequencies
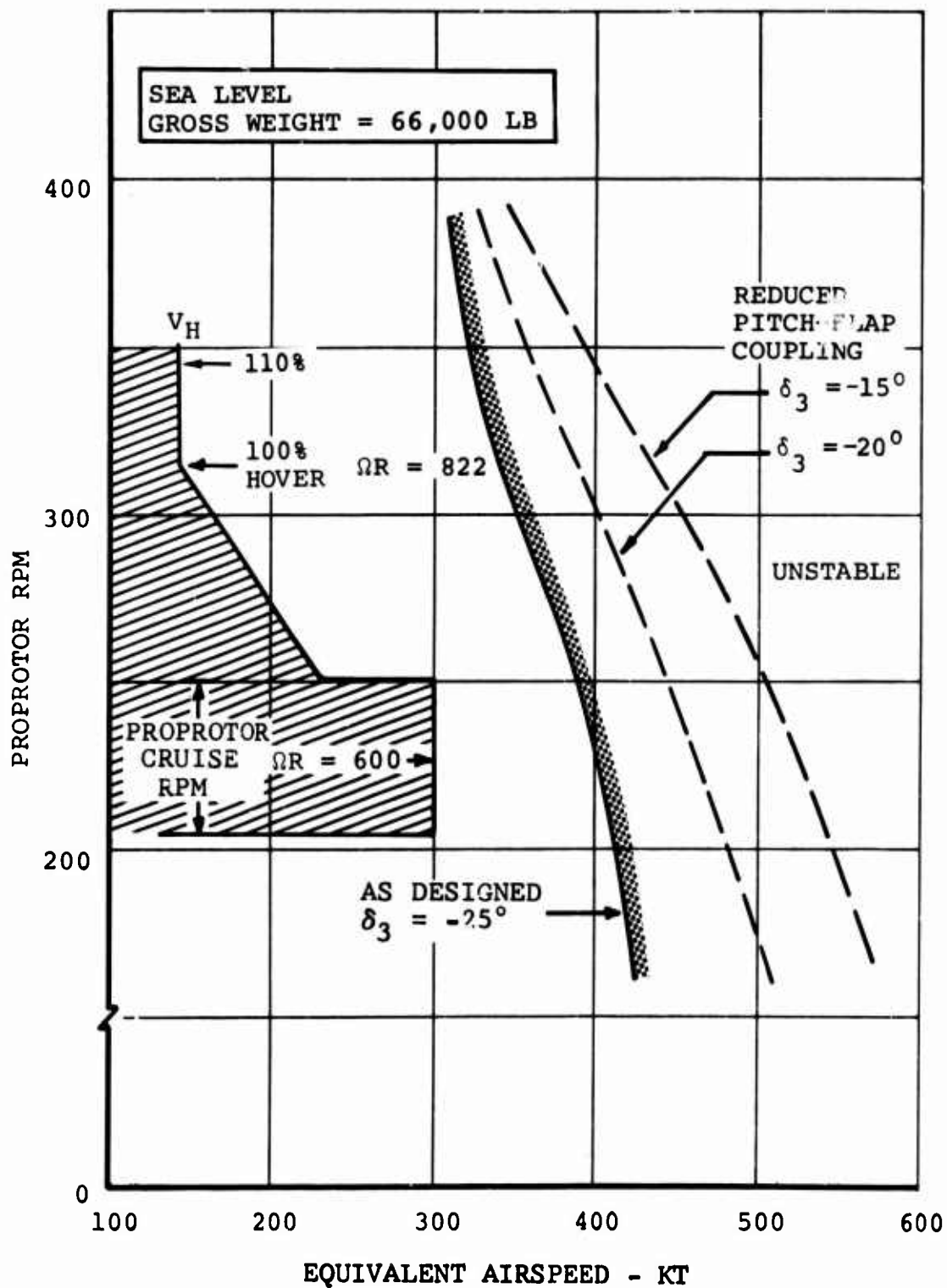Gimbal Flapping Freedom Locked Out

170

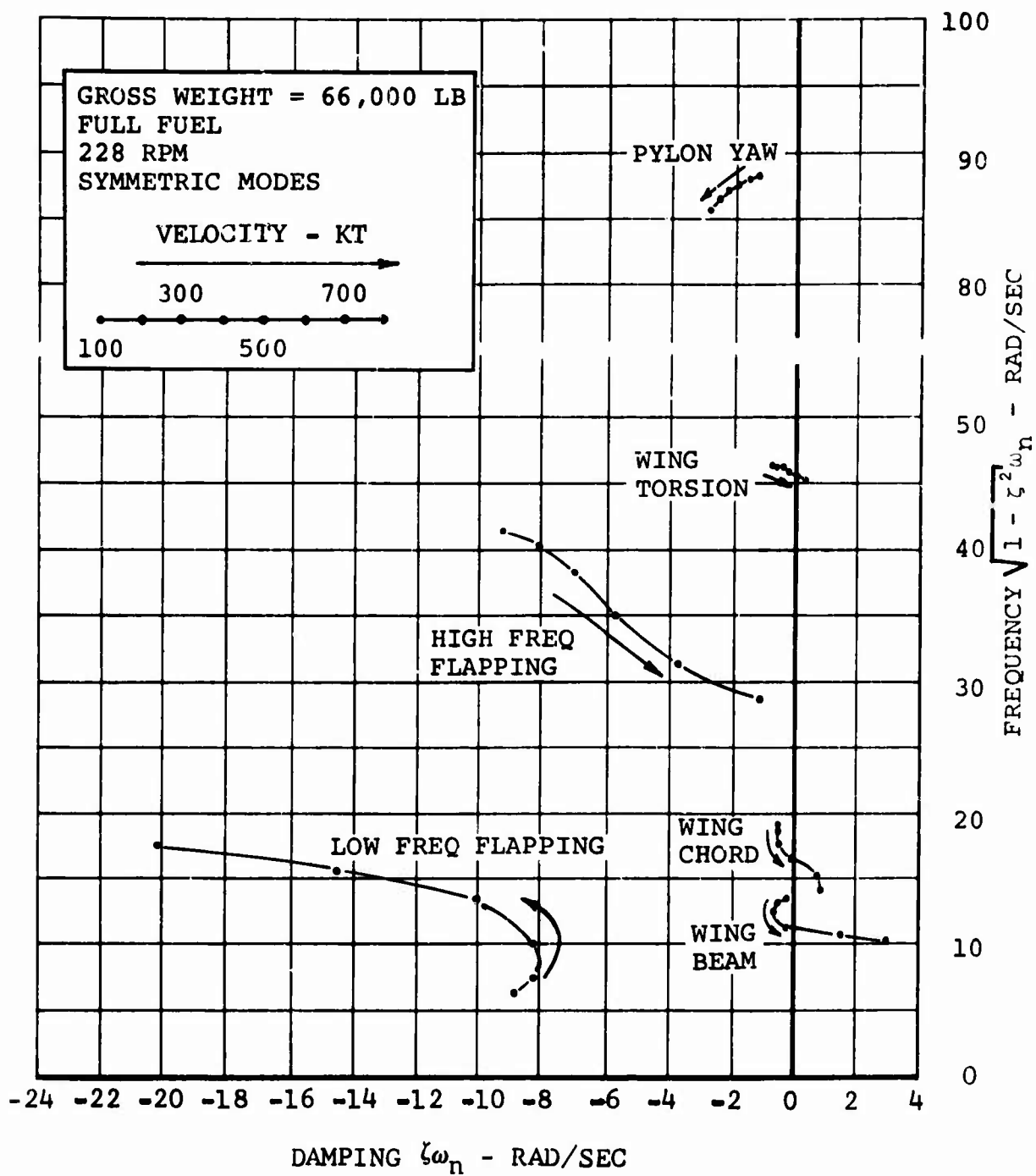Figure 73.   Proprotor Stability Boundary, Proprotor Cruise
Mode.

171

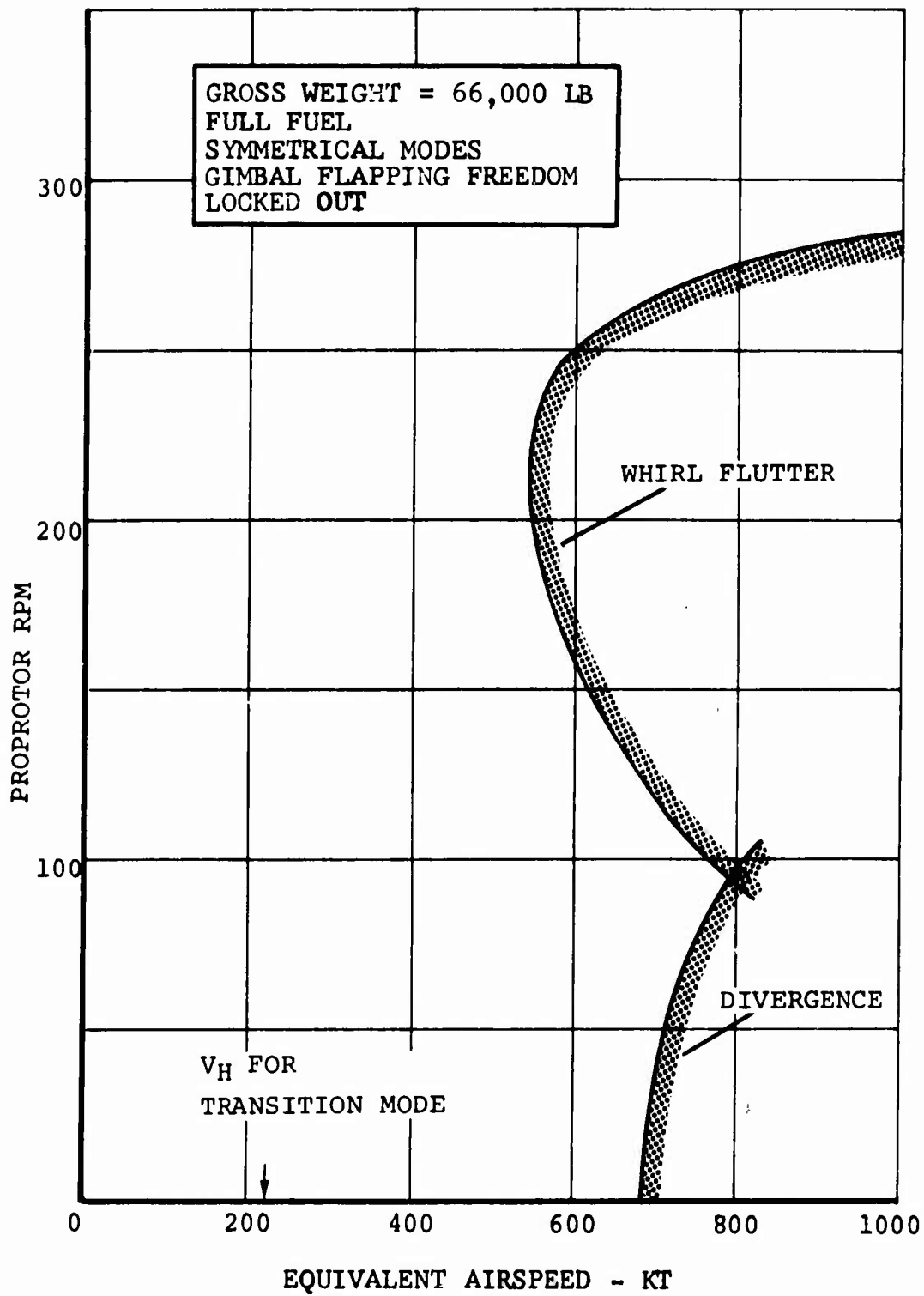Figure 74. Root Motion With Airspeed, Proprotor
Mode.

172

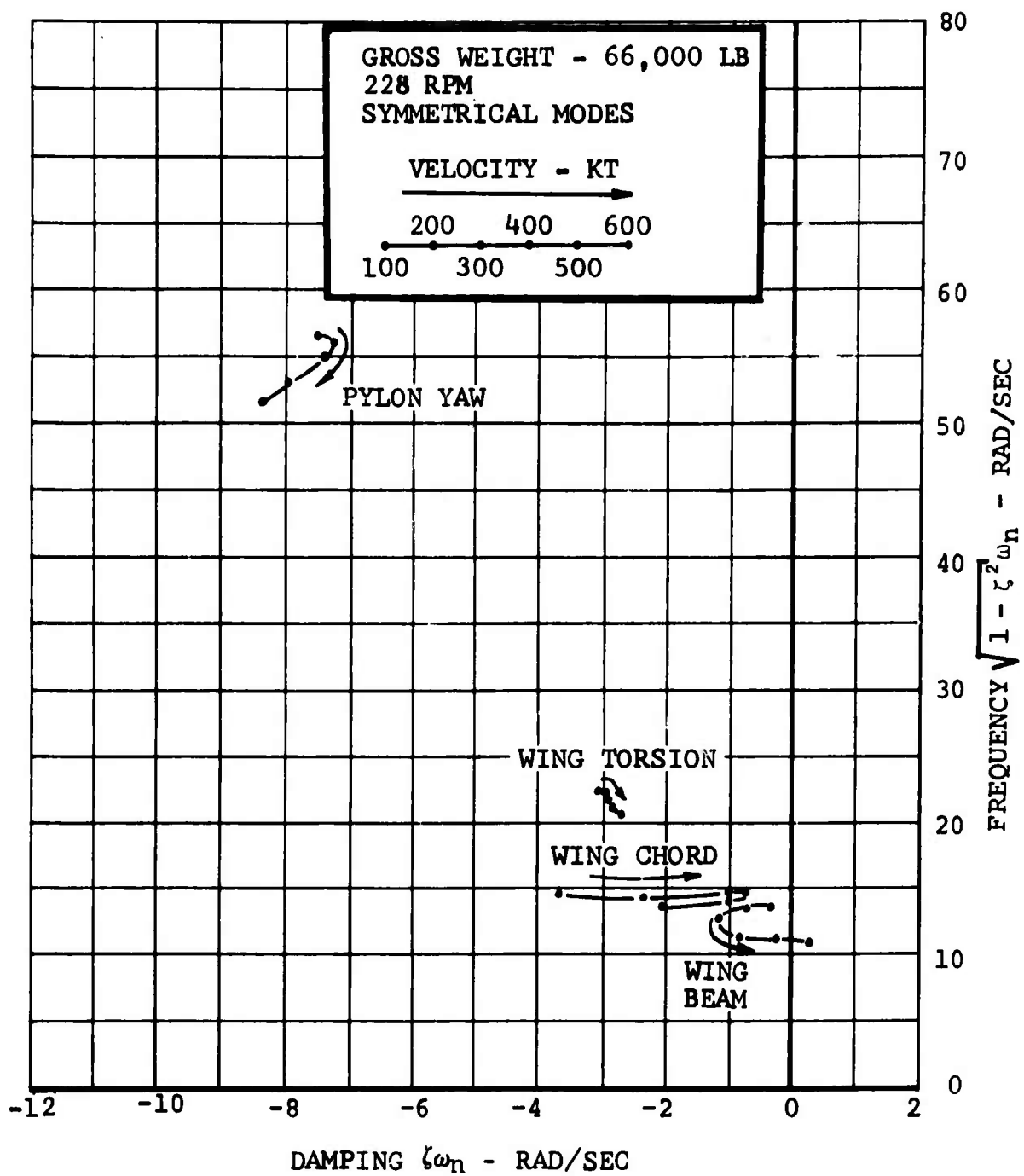Figure 75. Proprotor Stability Boundary During Blade
Feathering.

173

Figure 76.   Root Motion With Airspeed, Gimbal Flapping
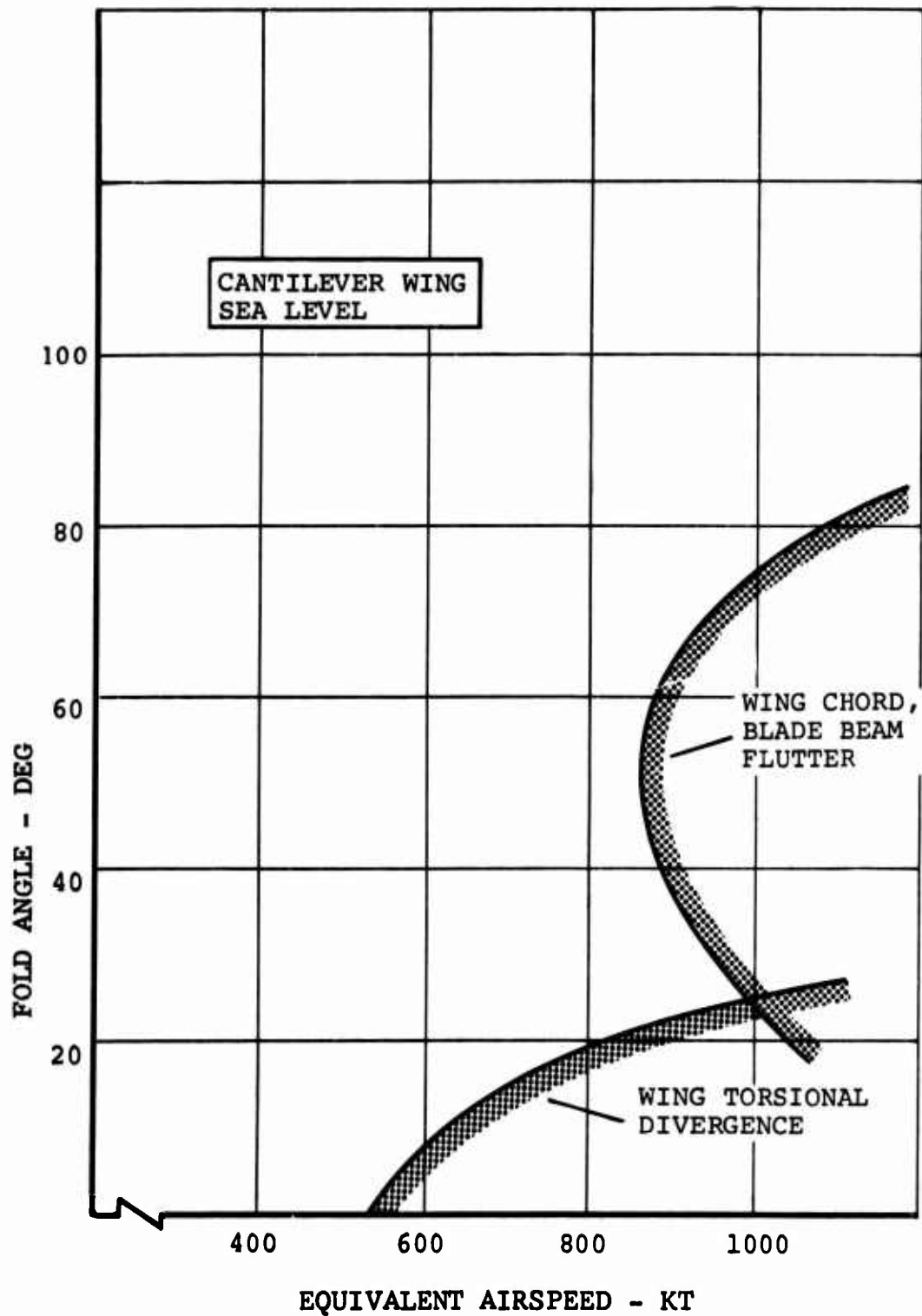Freedom Locked Out.

174

Figure 77. Flutter and Divergence Boundary During
            Blade Folding.

175

Figure 78. Frequency Variation with Airspeed,
Zero Degree Blade Fold.
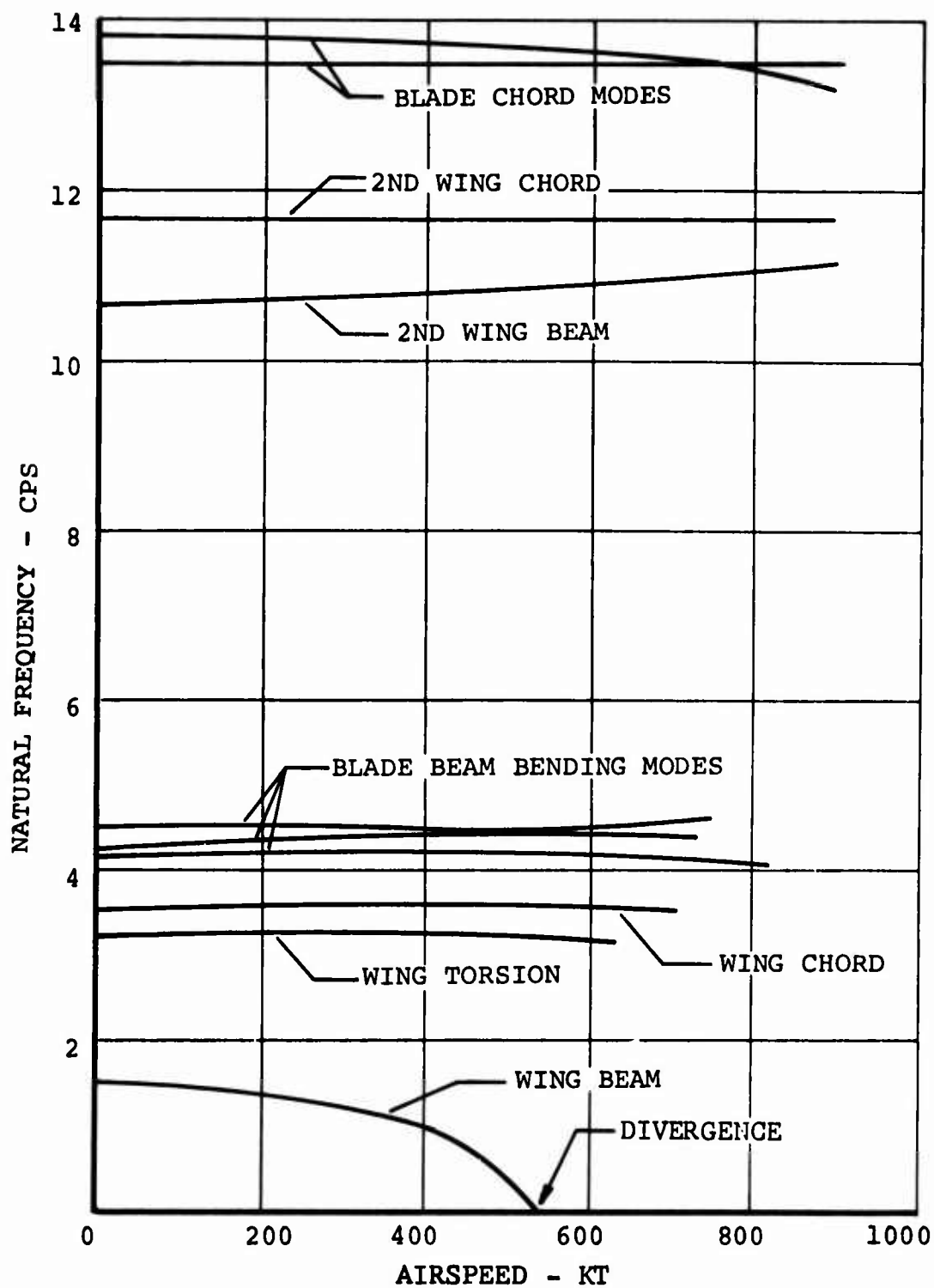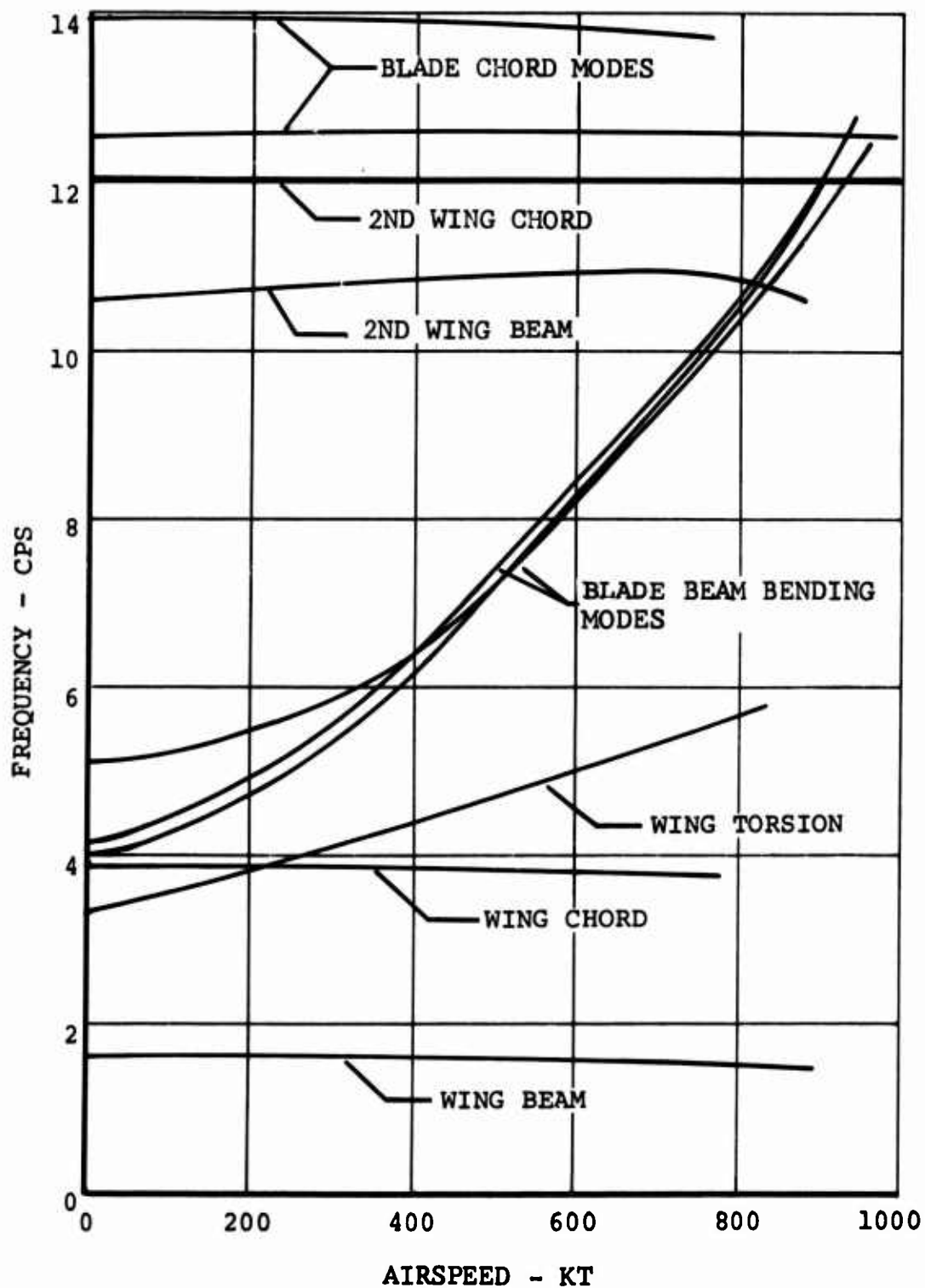
Figure 79. Frequency Variation with Airspeed,
60 Degrees Blade Fold.

Figure 78. Frequency Variation with Airspeed,
Zero Degree Blade Fold.

176
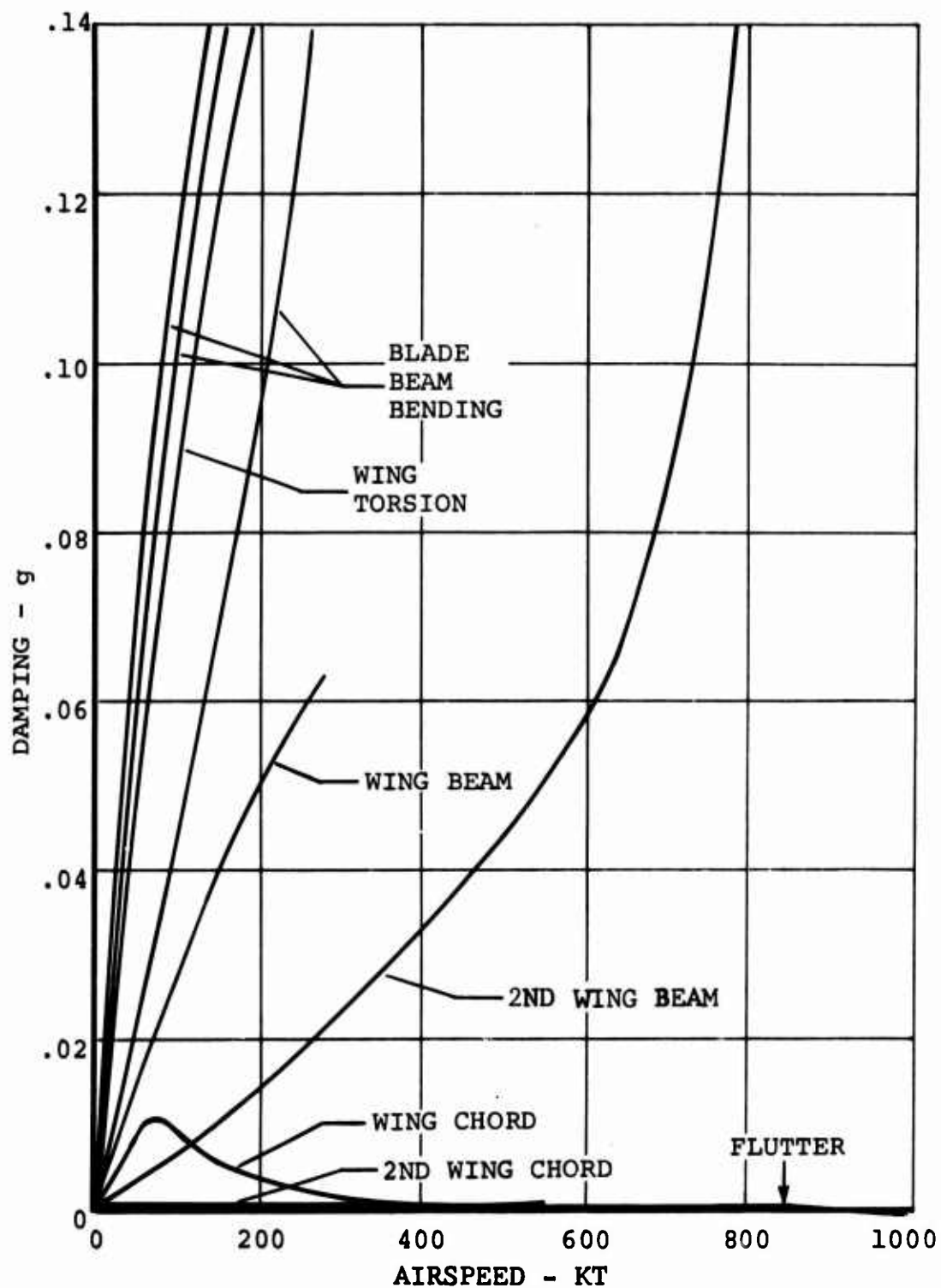
Figure 80.   Damping Variations with Airspeed, 60-Degrees Blade Fold.

178
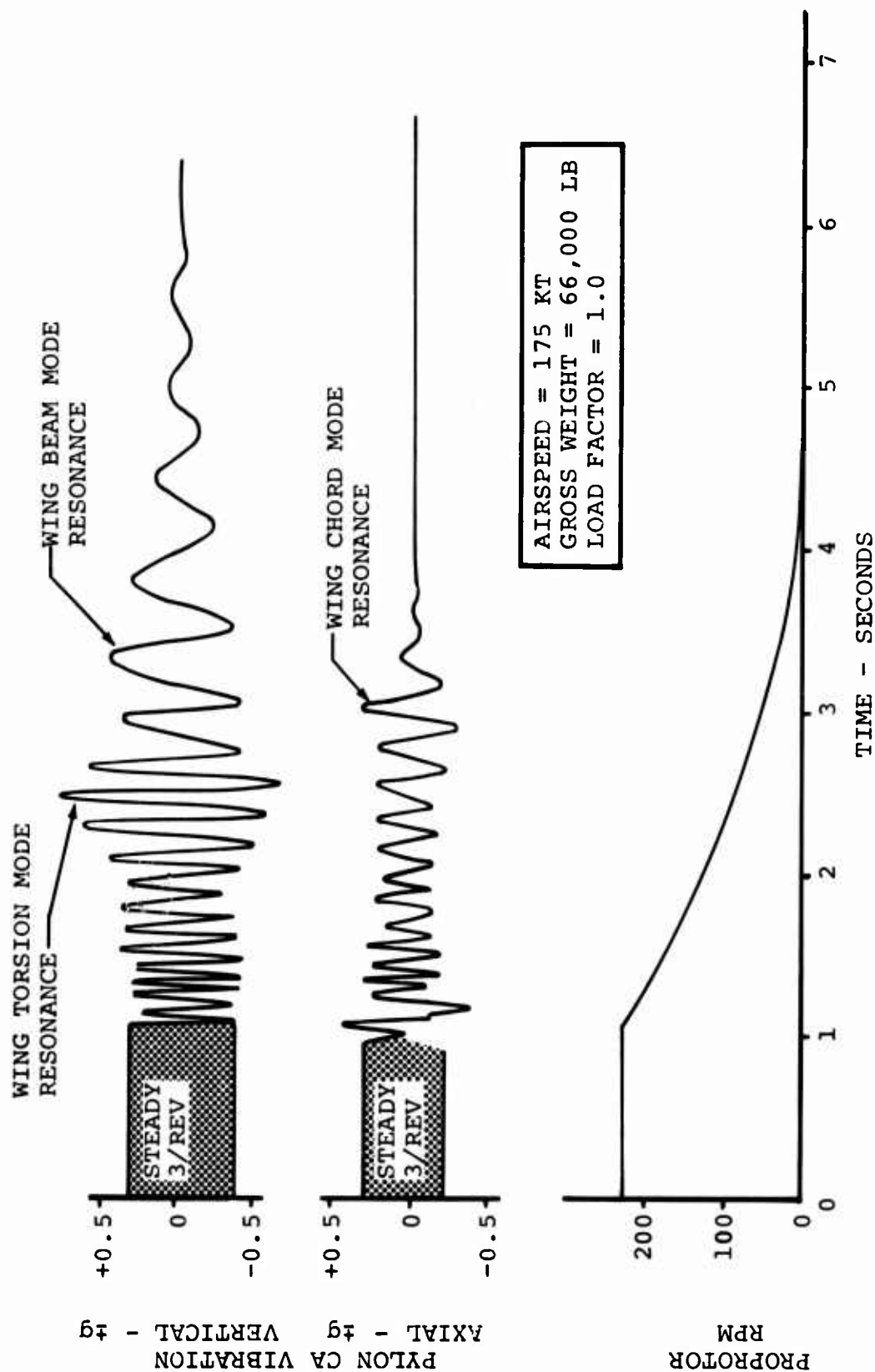
Figure 81. Time History of D270A Pylon Conversion Axis Vibration During Blade Feathering.

179
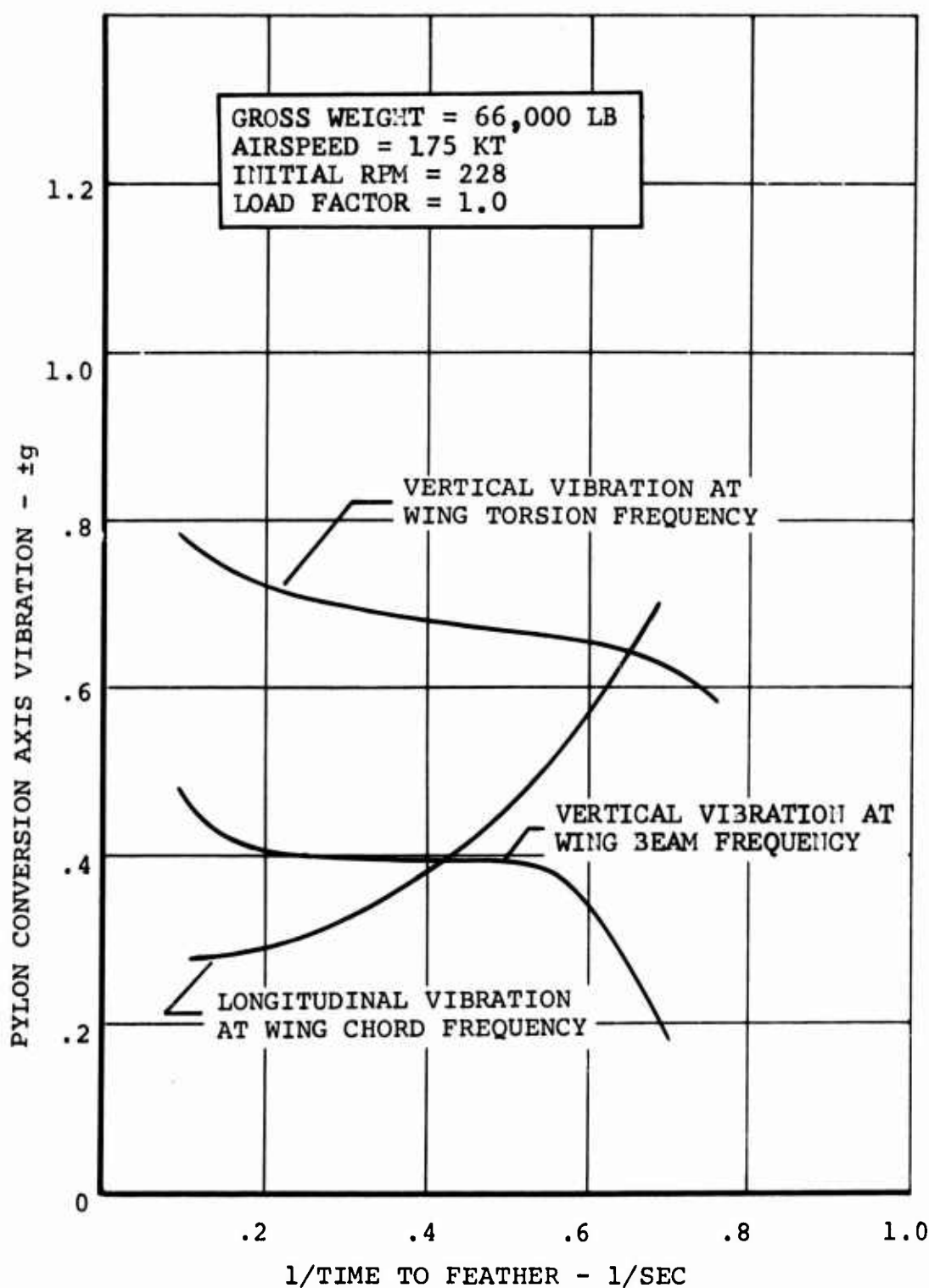
Figure 82. Peak Vibration at Pylon Conversion Axis
During Blade Feathering.
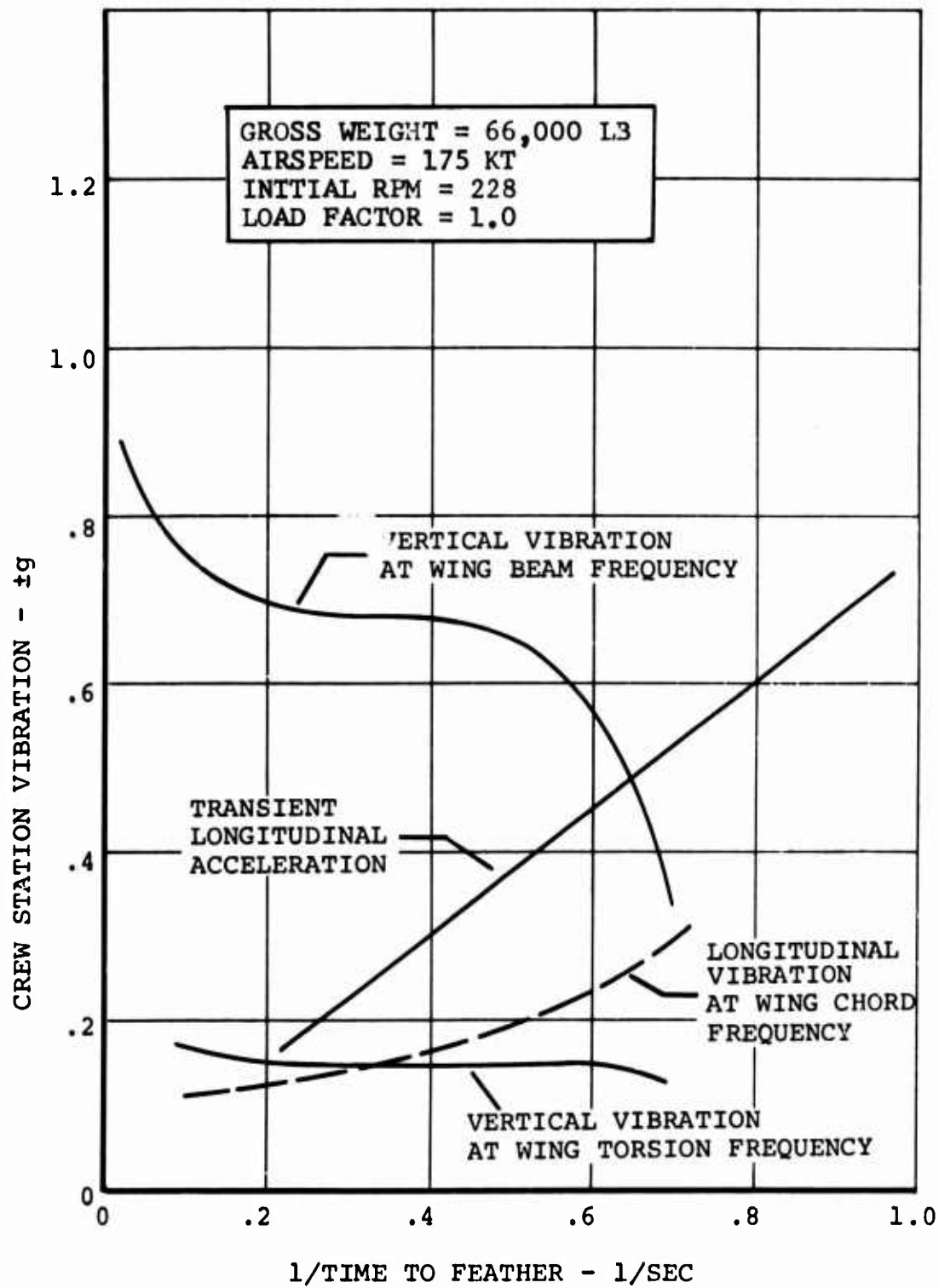
Figure 83.   Peak Vibration at Crew Station During Blade
Feathering.

181
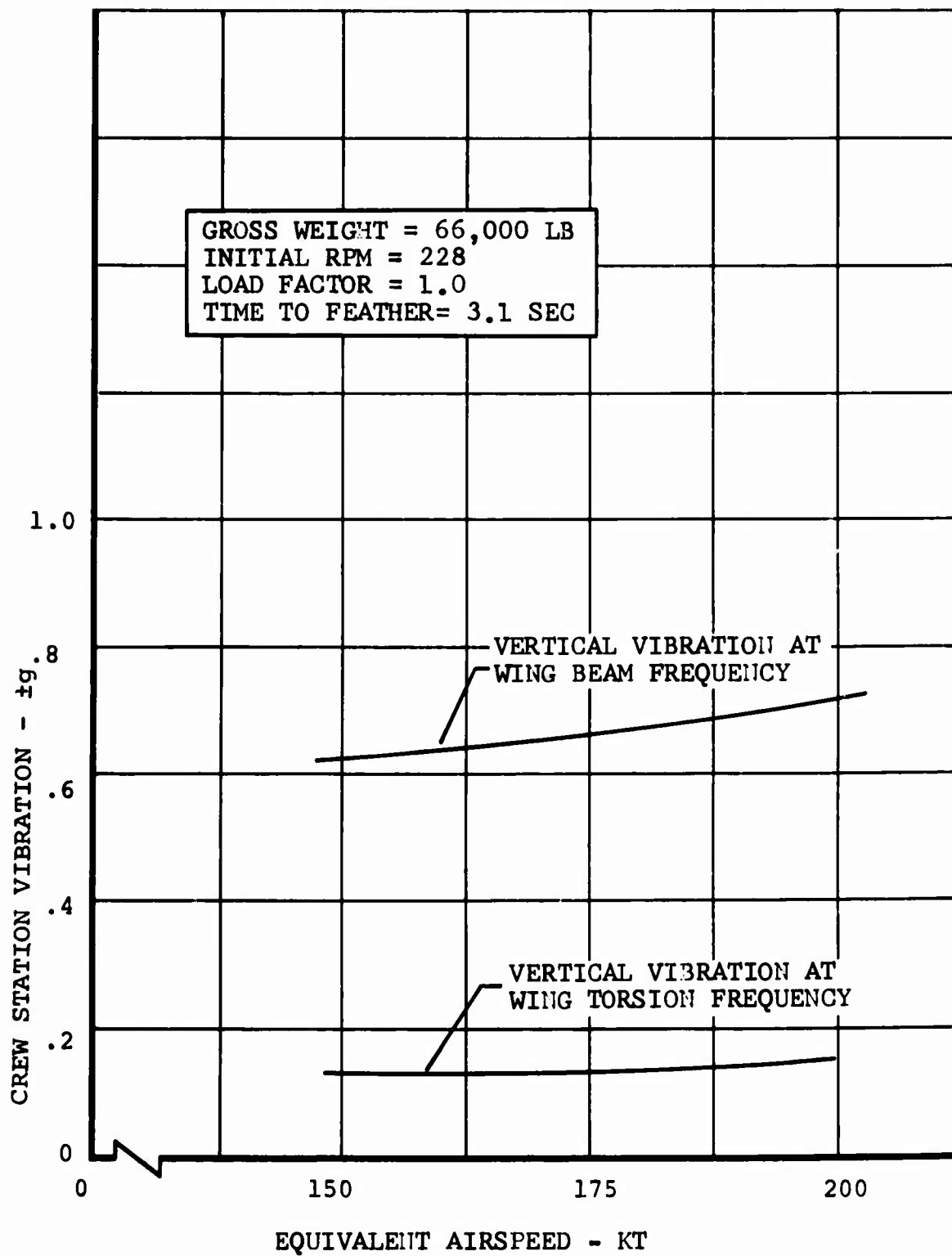
Figure 84.   Influence of Airspeed on Crew Station
Vibration.

182
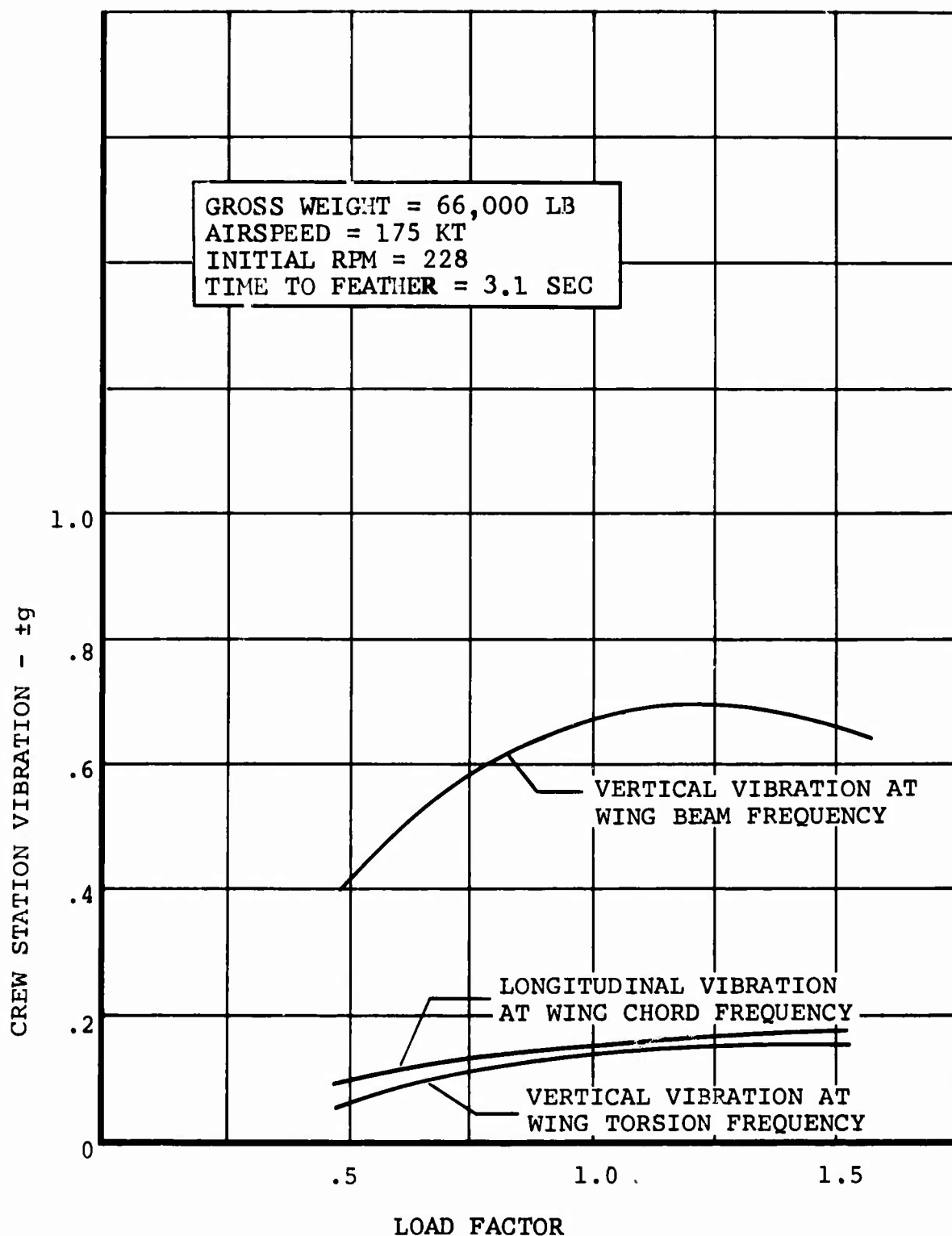
Figure 85.   Influence of Load Factor on Crew Station
            Vibration.

183
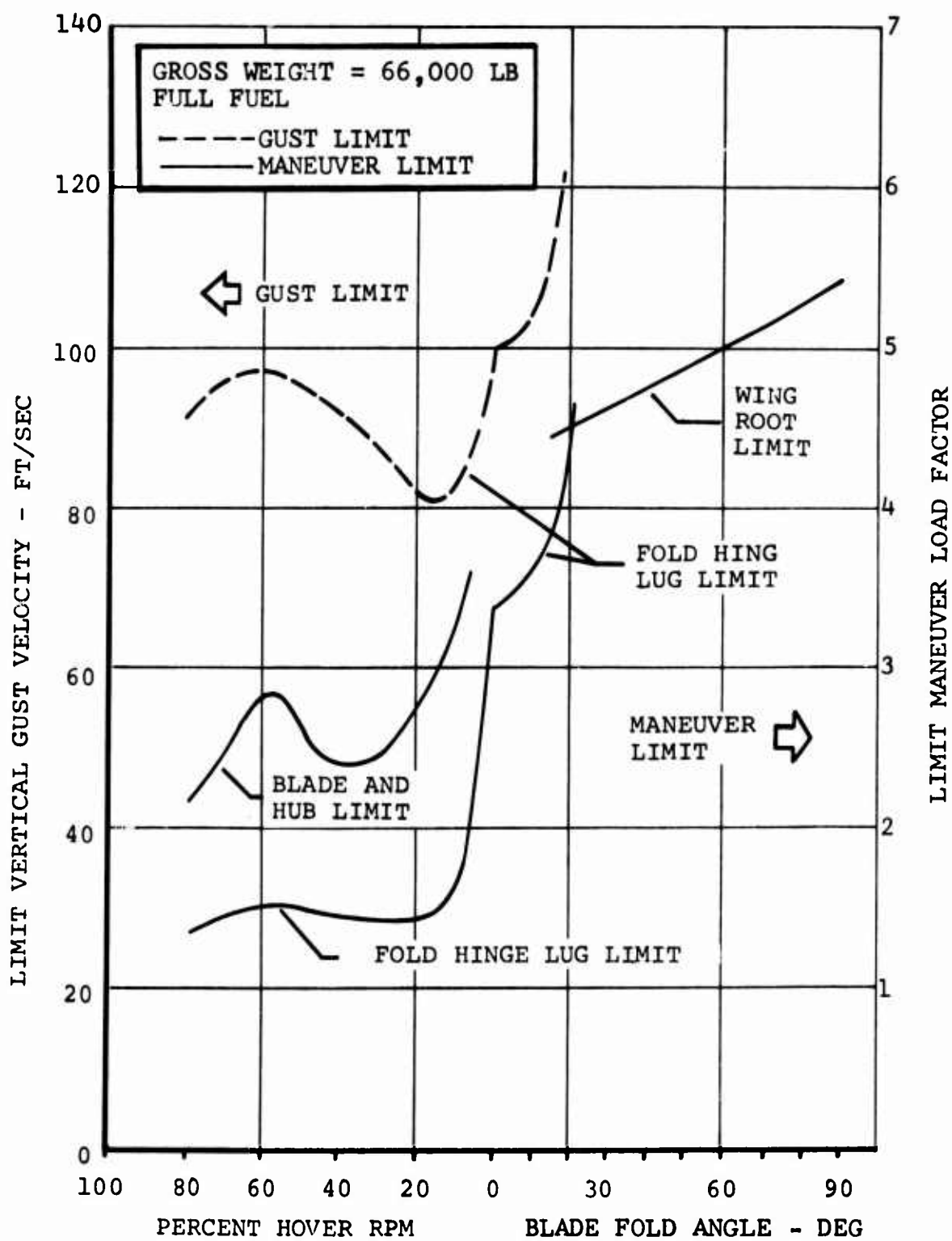
Figure 86. Gust and Maneuver Limits During Feathering and Folding at 175 Knots Airspeed.

184
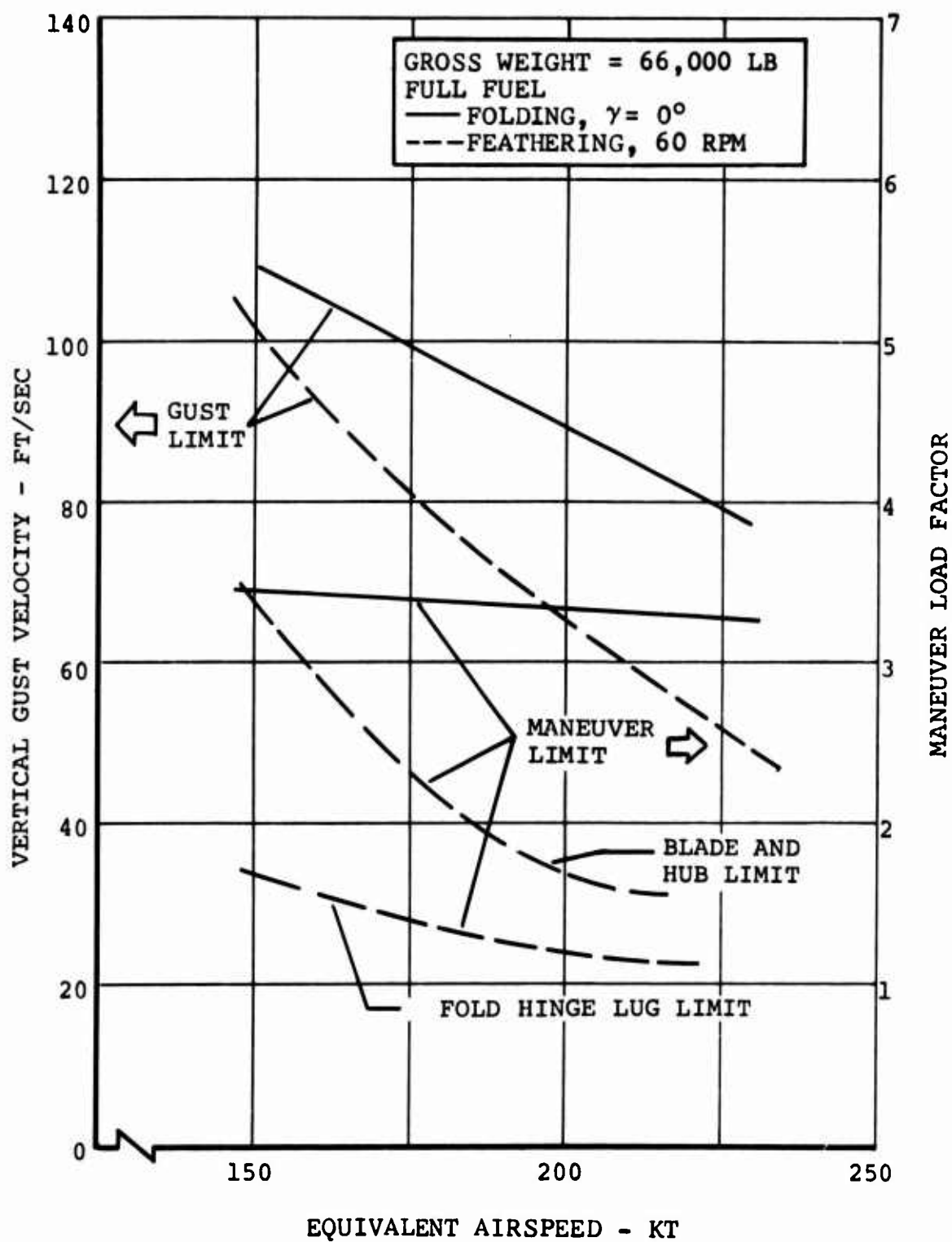
Figure 87. Influence of Airspeed on Gust and Maneuver
Limits During Feathering and Folding.

185
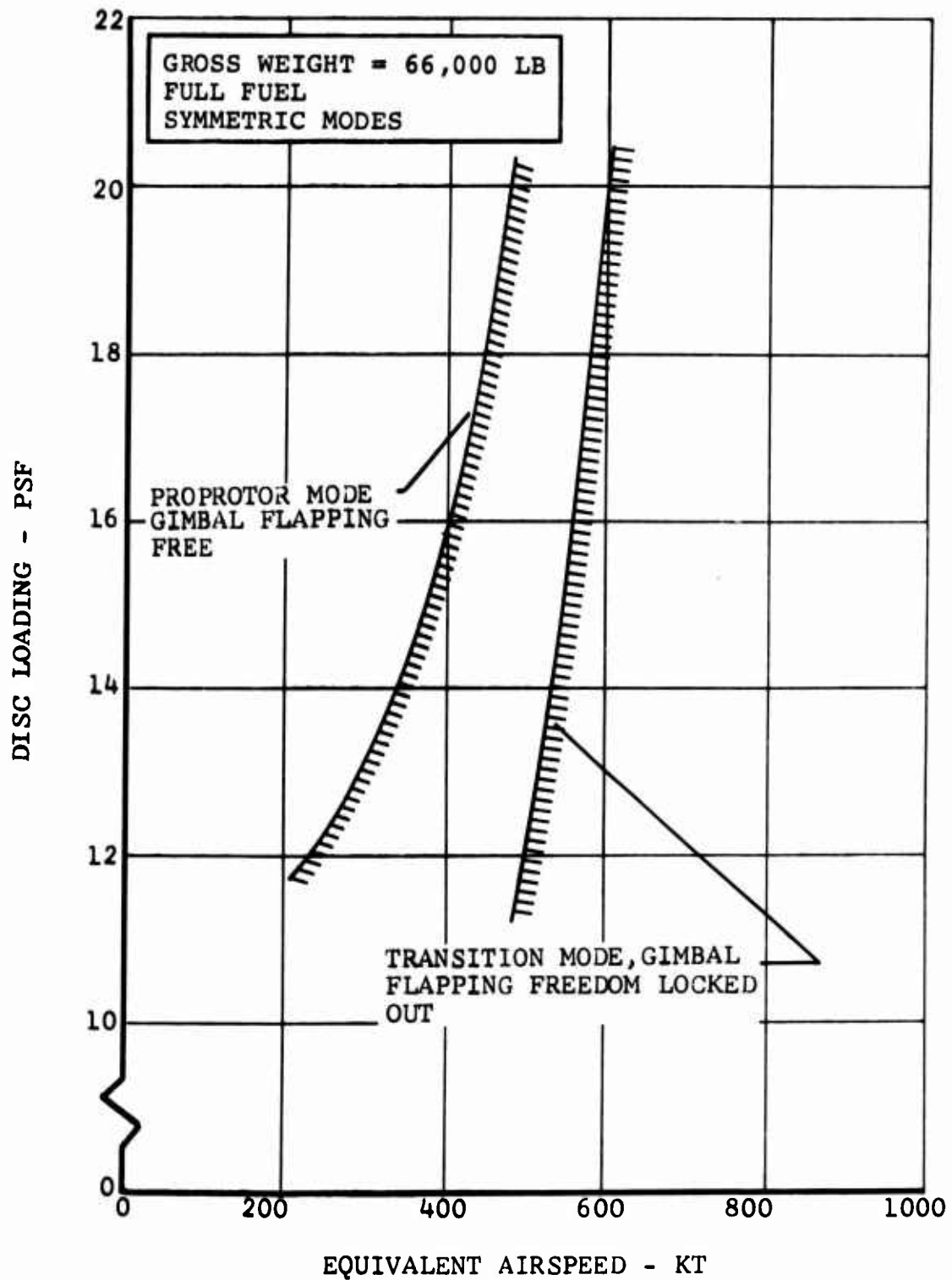
Figure 88. Influence of Disc Loading on Proprotor Stability.

186
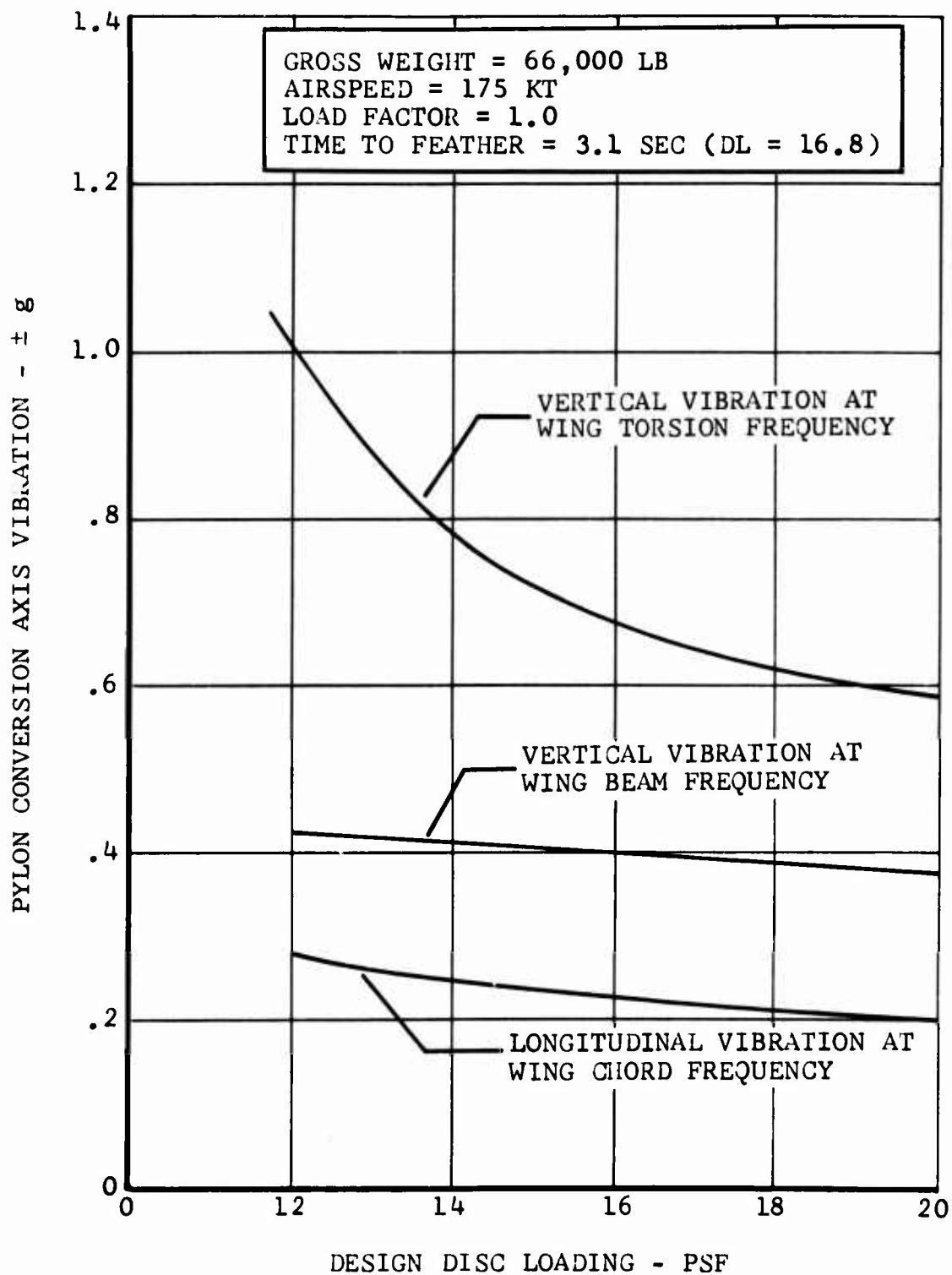
Figure 89.   Influence of Disc Loading on
Pylon Vibration During Feathering.
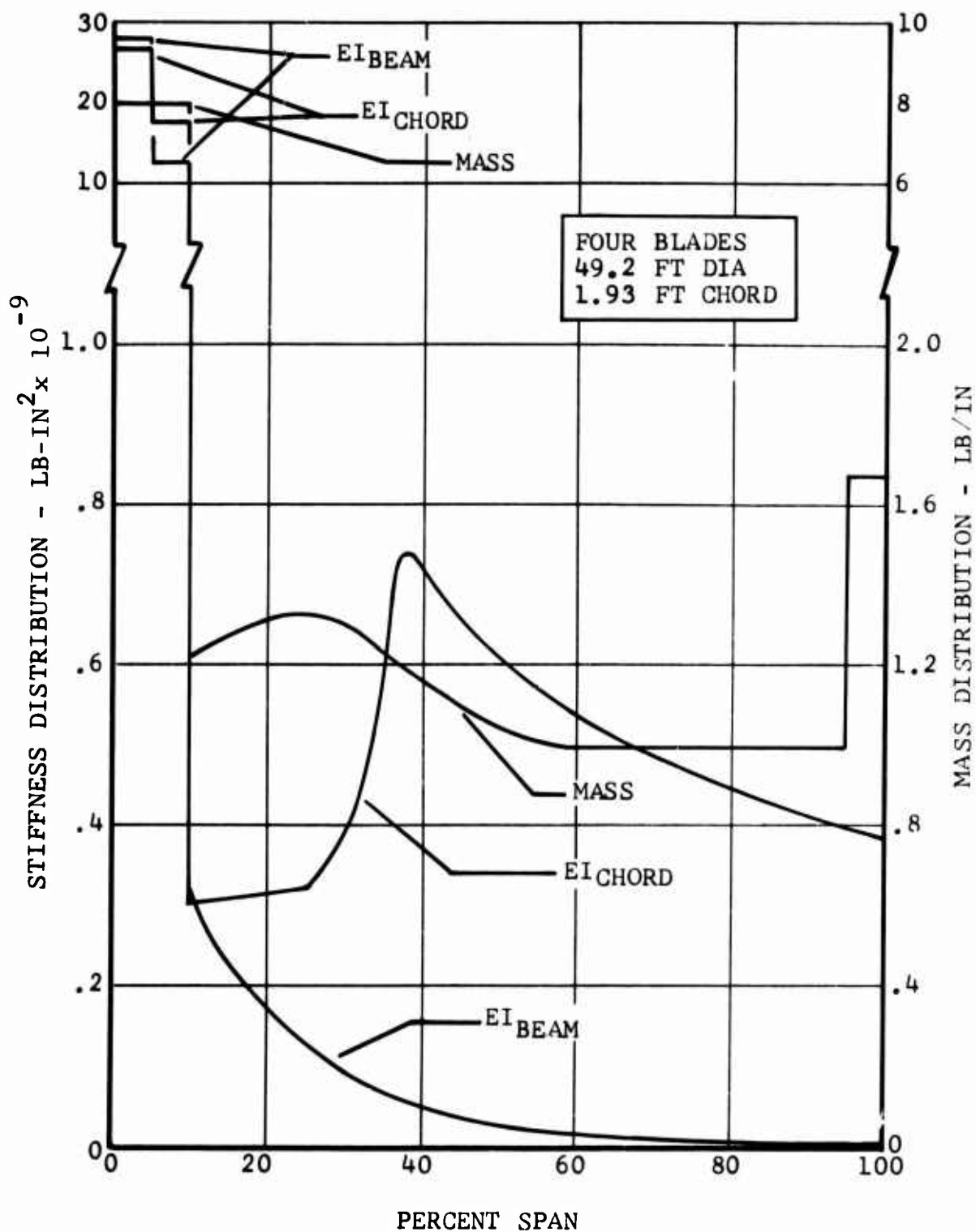
Figure 90.   Mass and Stiffness Parameters
for Hingeless, Soft-Inplane
Folding Proprotor.

188
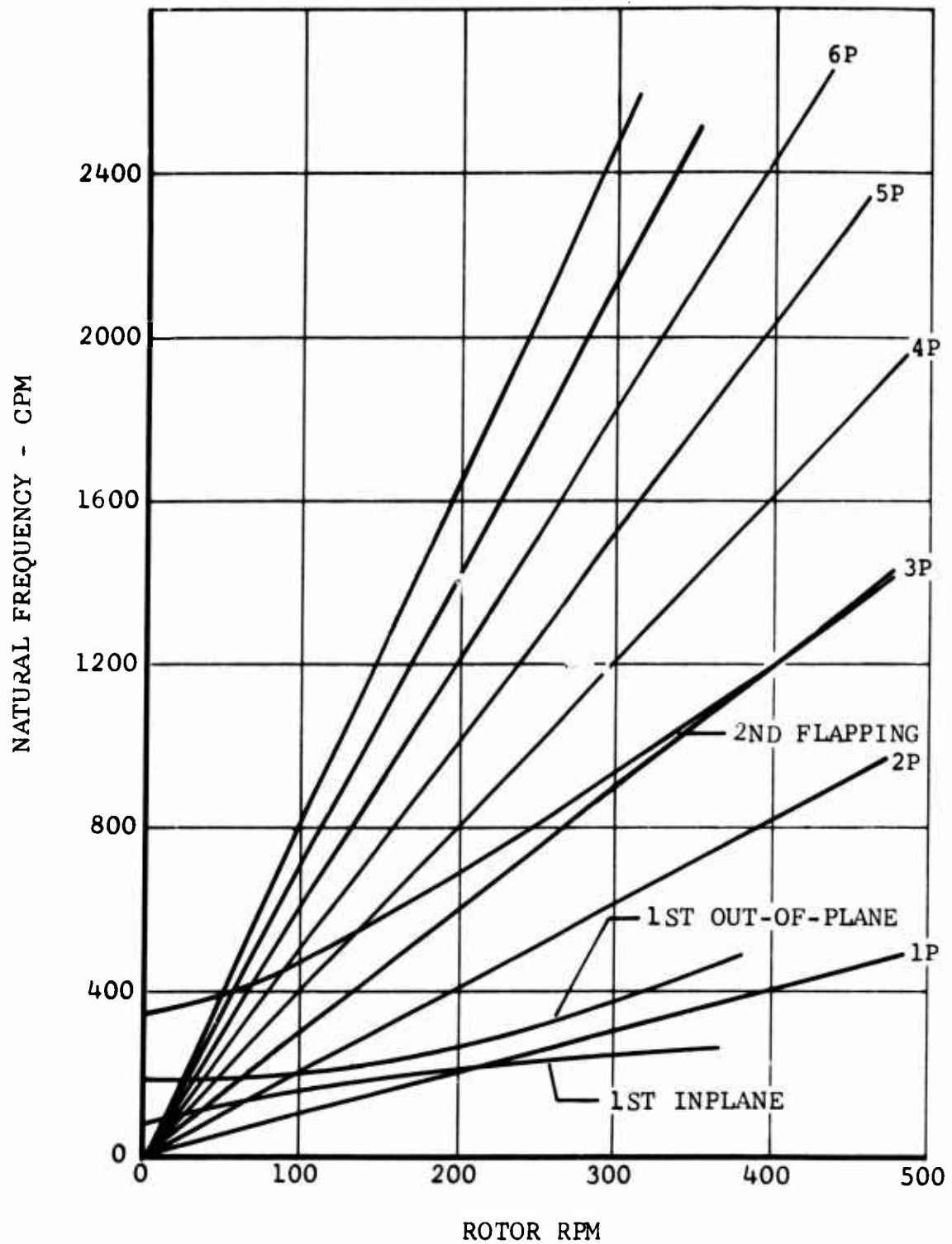
Figure 91. Hingeless Proprotor Natural
          Frequency Spectrum During
          Blade Feathering.

189
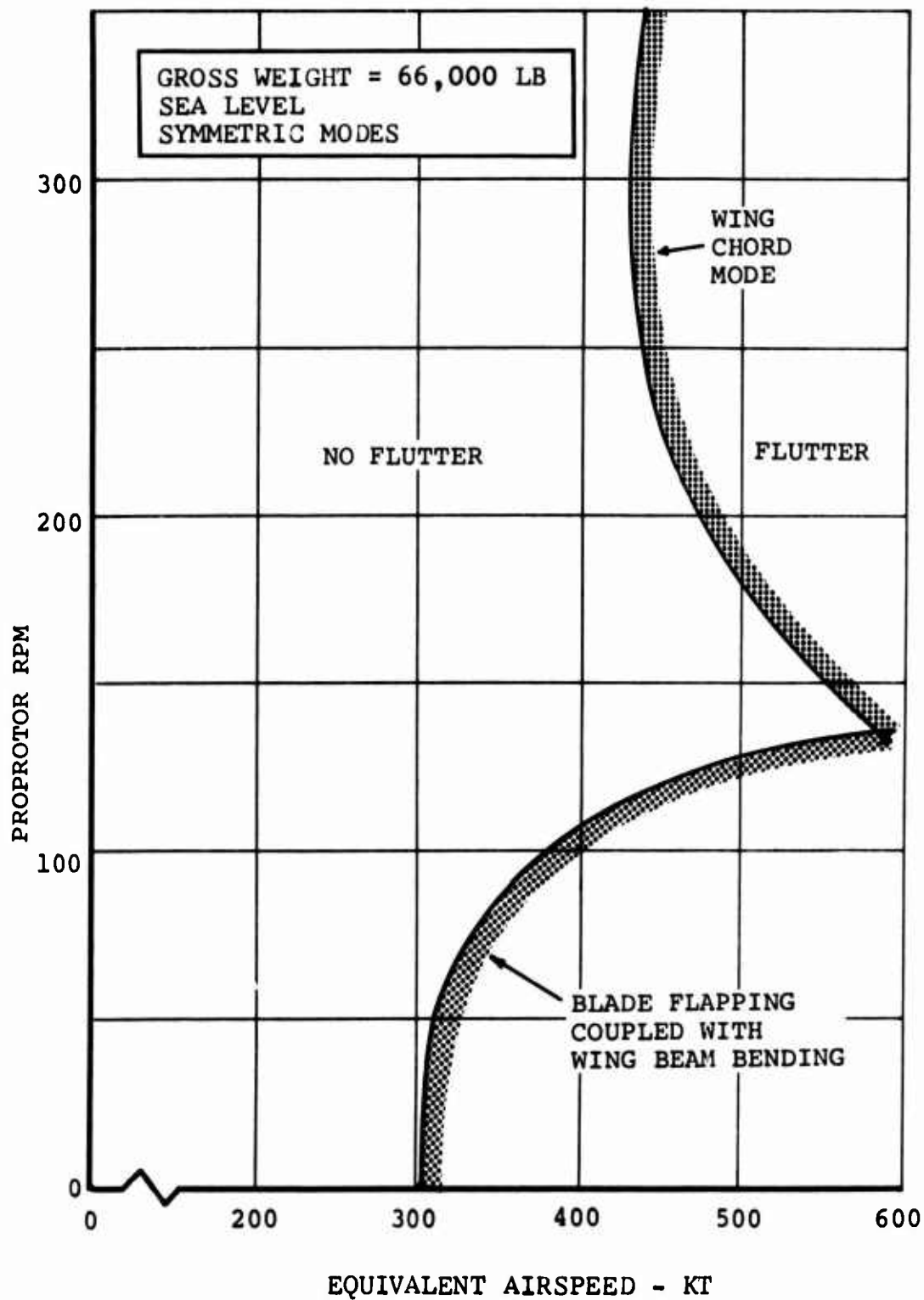
Figure 92. Proprotor Stability Boundary, Hingeless Soft-Inplane Proprotor.

190
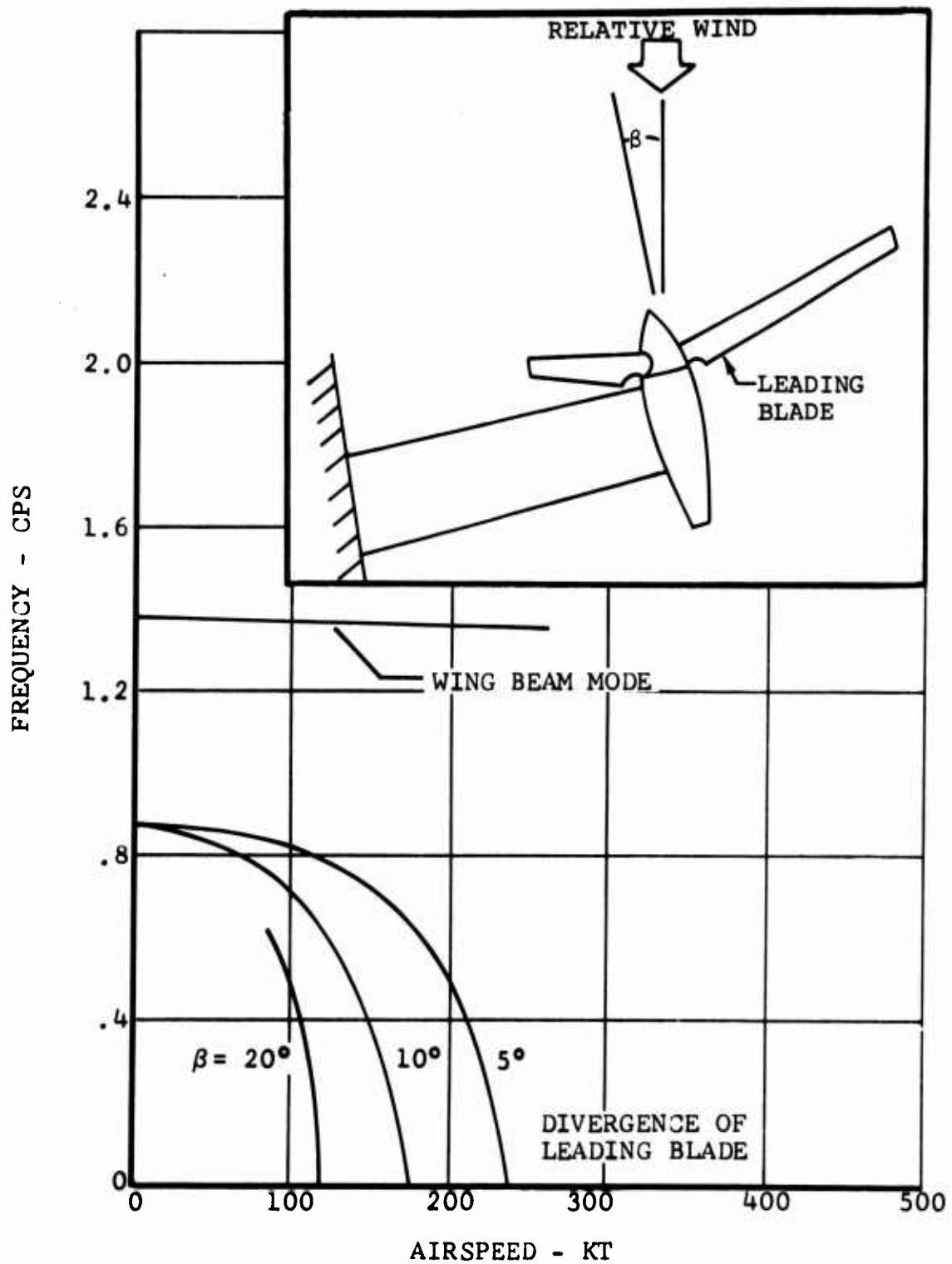
Figure 93. Blade Divergence Airspeed Versus Sideslip
Angle, Hingeless Soft-Inplane Proprotor,
Zero Degrees Fold.

191
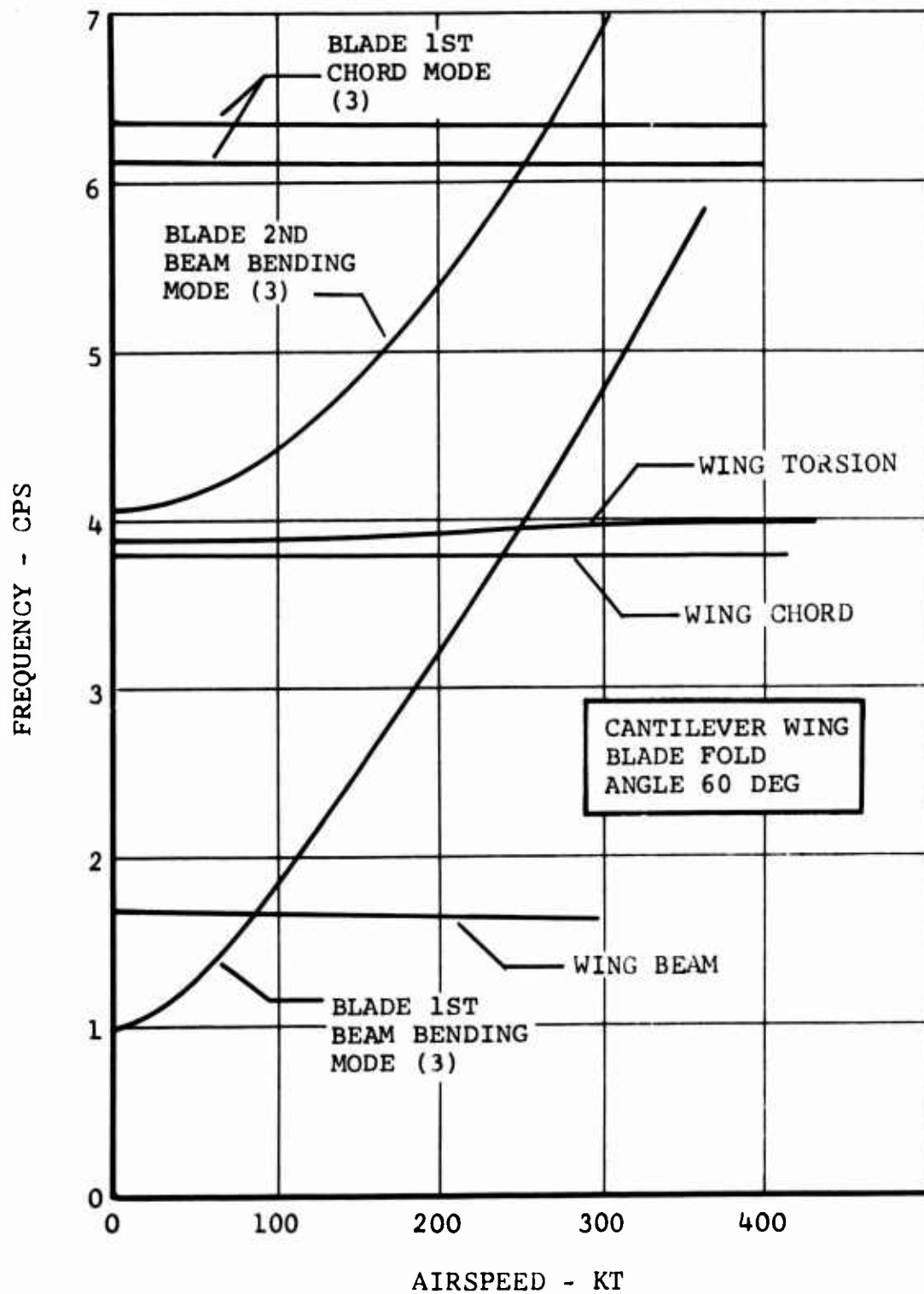
Figure 94. Natural Frequency Variation With Airspeed During Blade Folding, Hingeless Soft-Inplane Proprotor, 60 Degrees Fold.

192
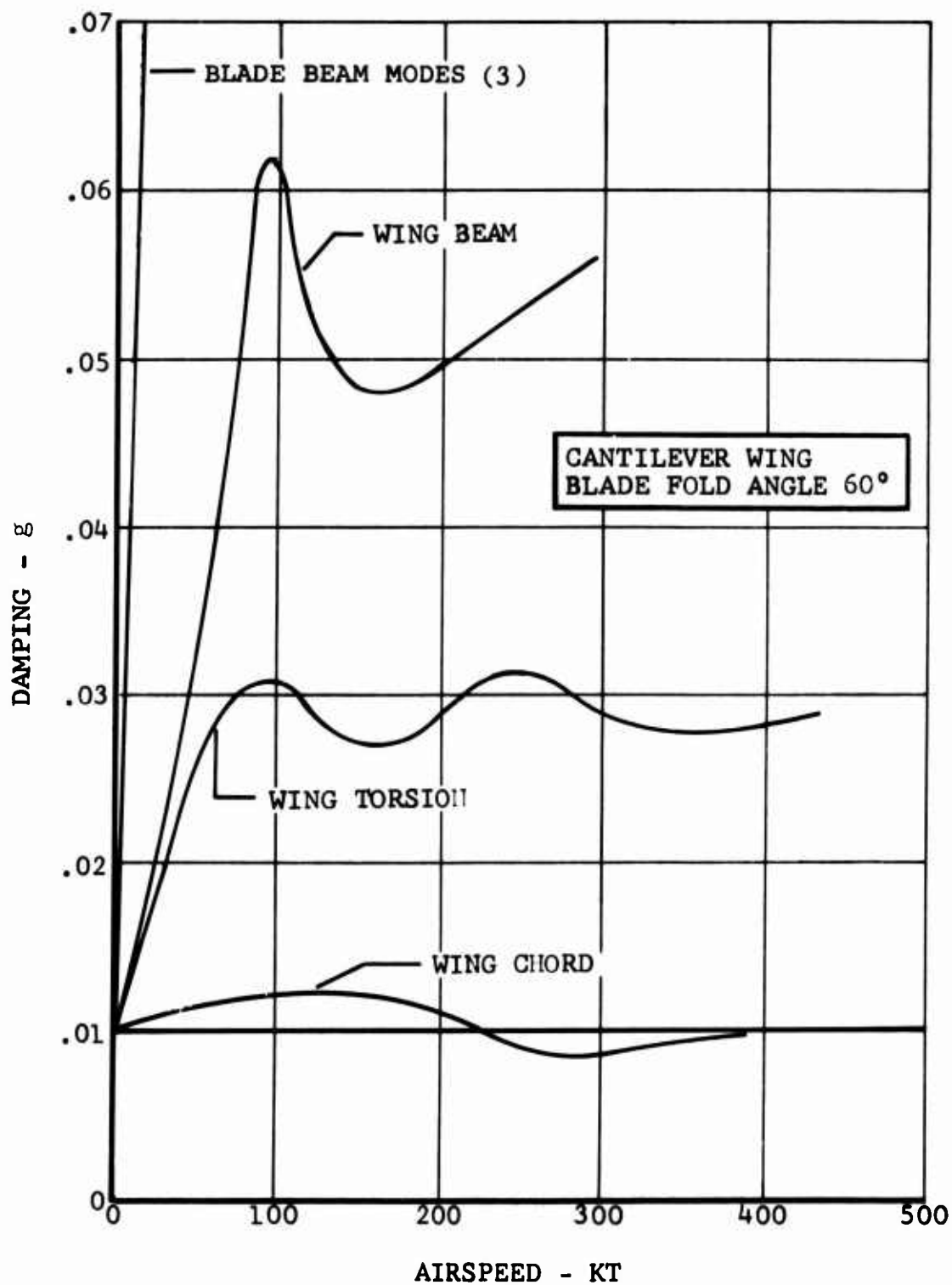
Figure 95. Damping Variation with Airspeed During
Blade Folding, Hingeless Soft Airplane
Proprotor, 60 Degrees Fold.

193
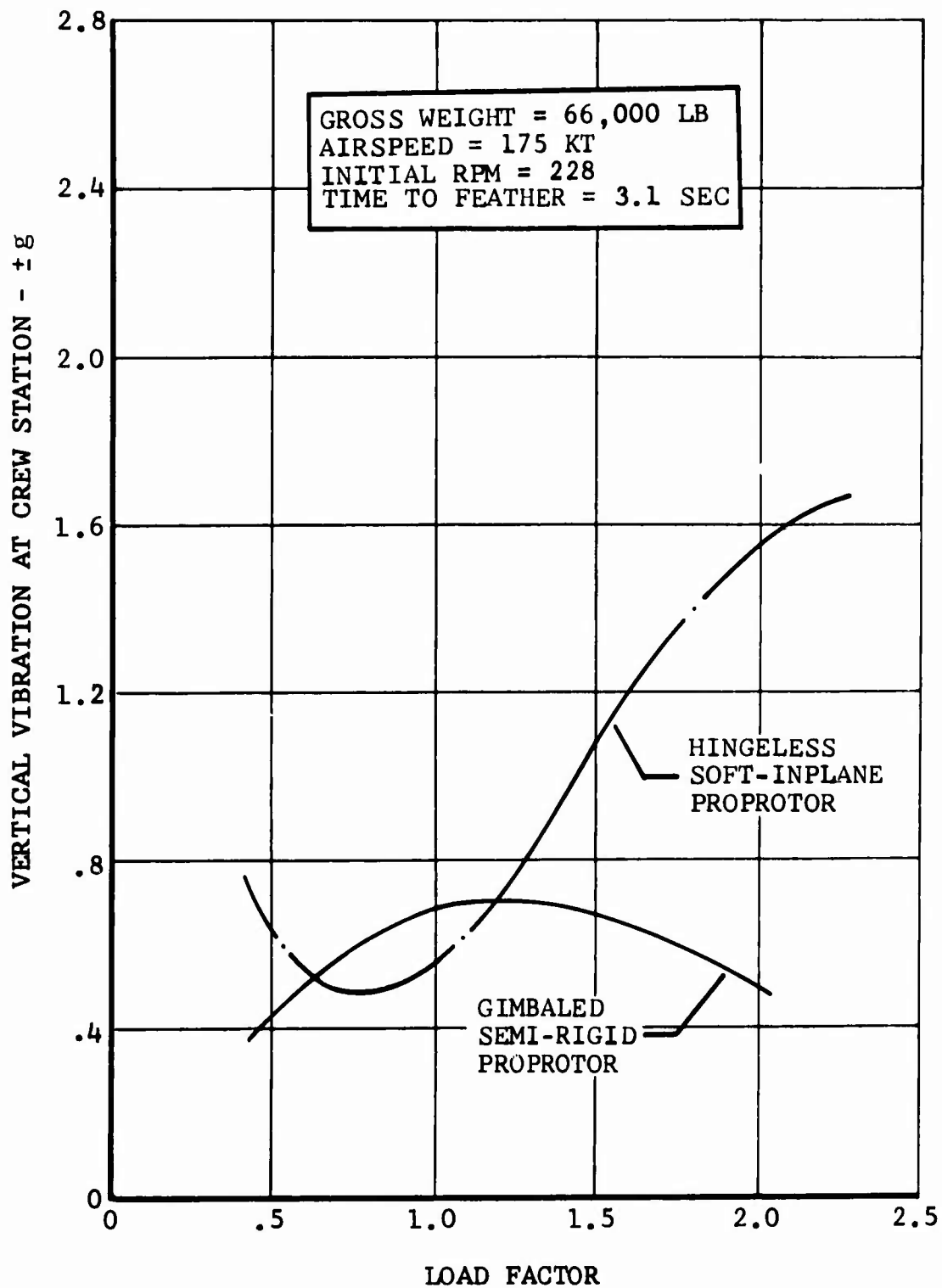
Figure 96. Comparison of Crew Station Vibration
During Blade Feathering.

194
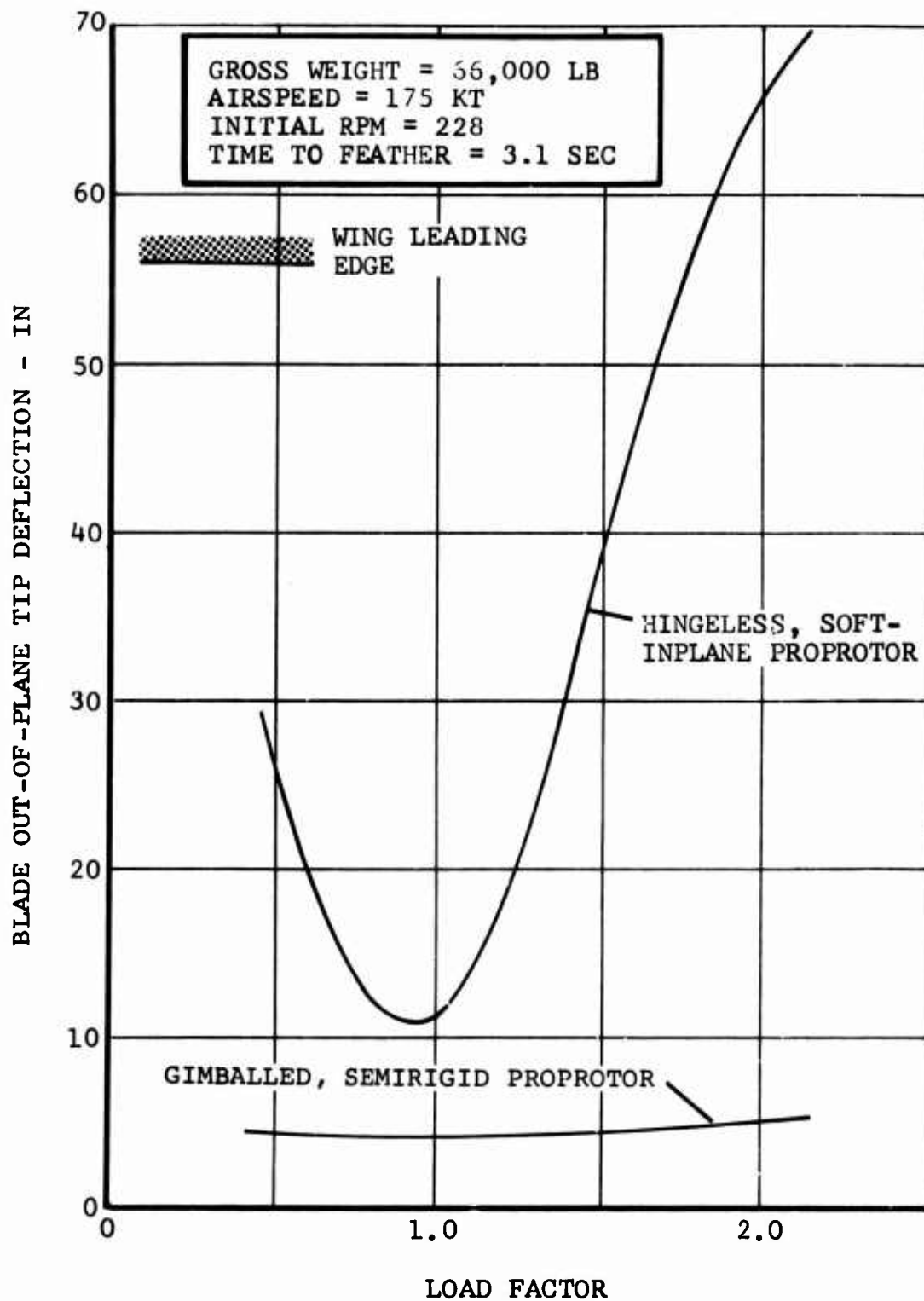
Figure 97.   Comparison of Out-of-Plane Tip Deflections,
Hingeless Soft-Inplane and Gimbaled, Semi-
Rigid, Proprotors.

195
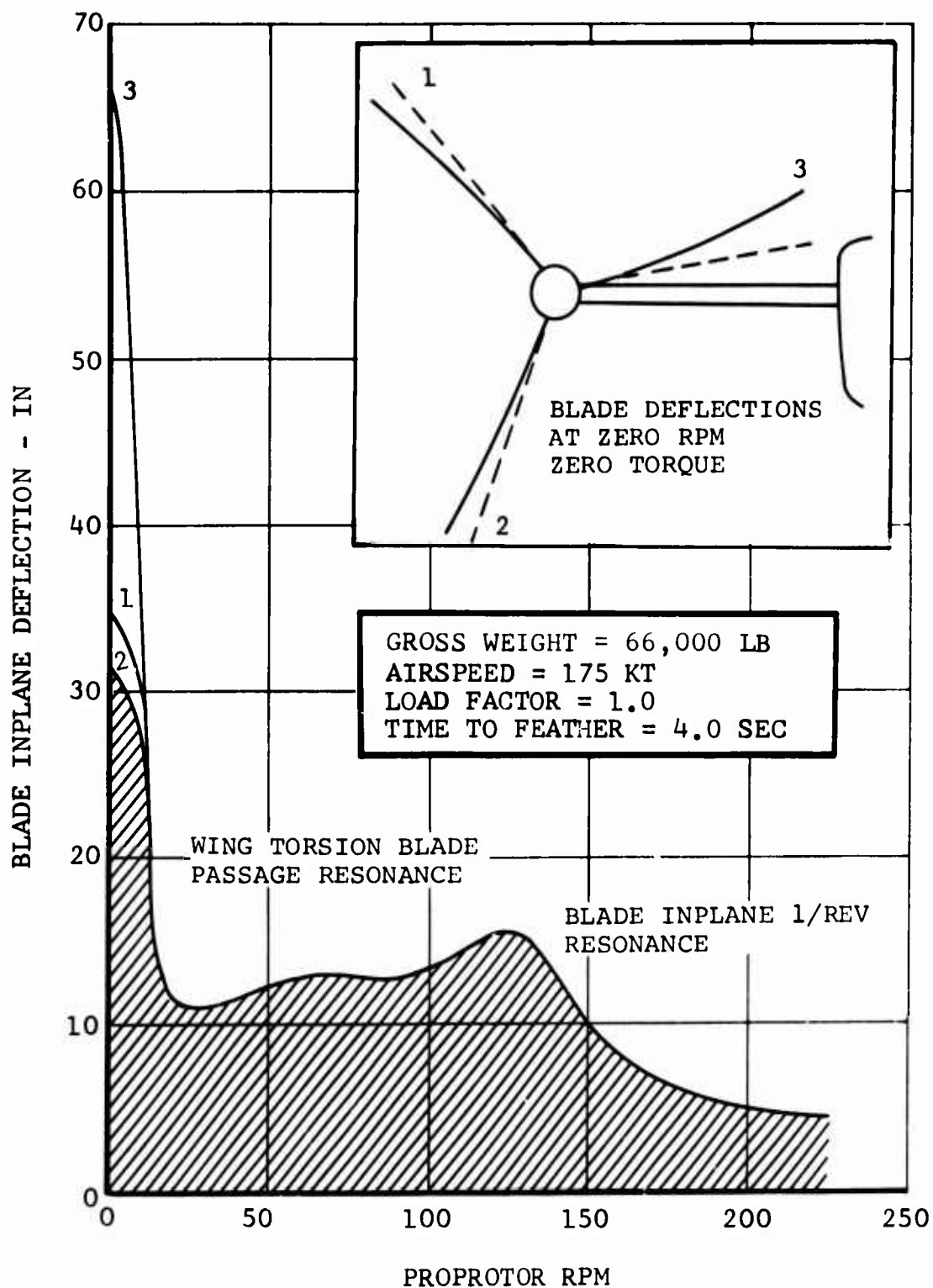
Figure 98.   Envelope of Blade Inplane Deflections During
             Blade Feathering, Hingeless Soft-In-Plane
             Proprotor.

196
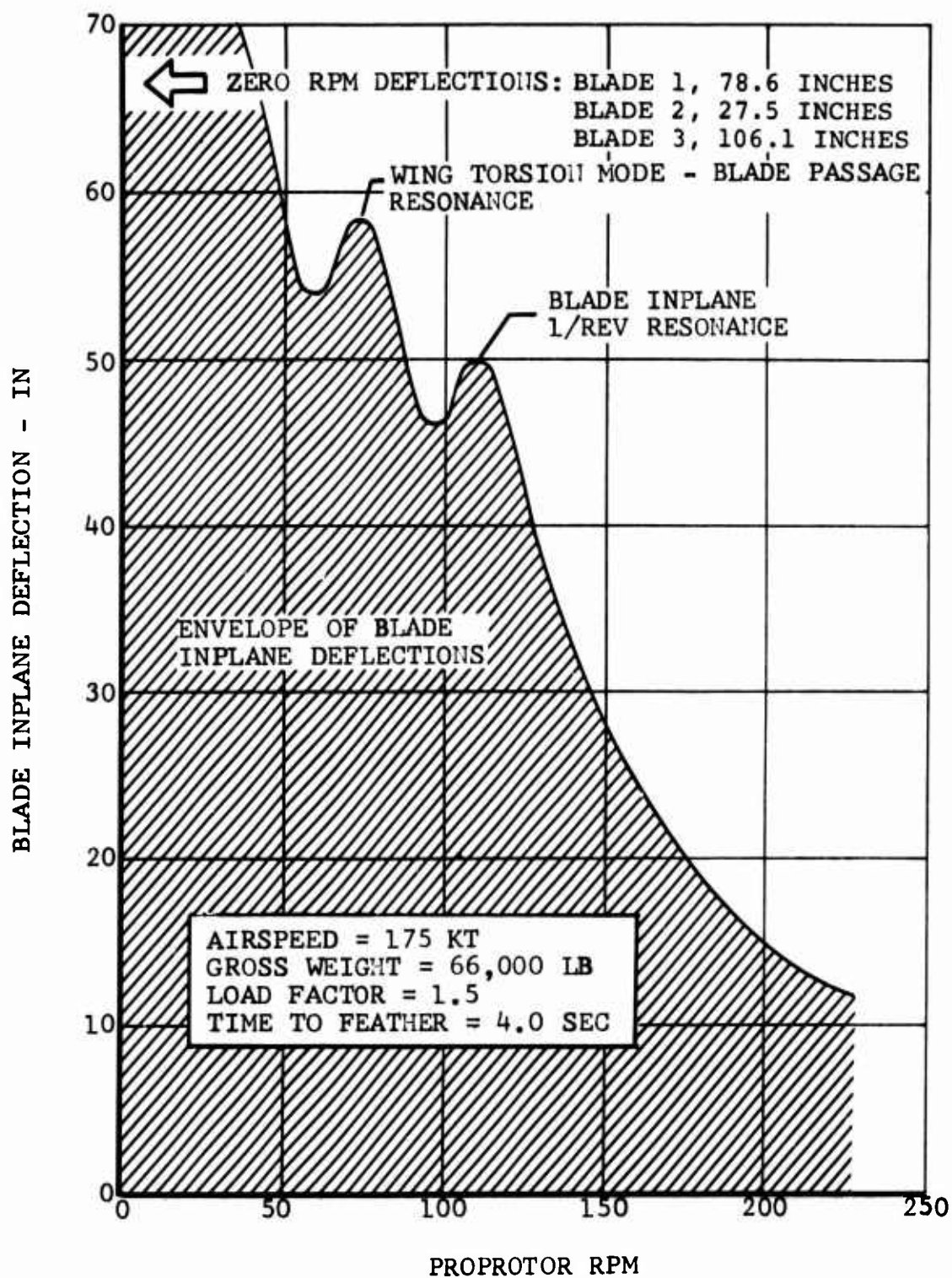
Figure 99. Influence of Load Factor on Blade Inplane
Deflections, Hingeless, Soft-Inplane,
Proprotor.

197
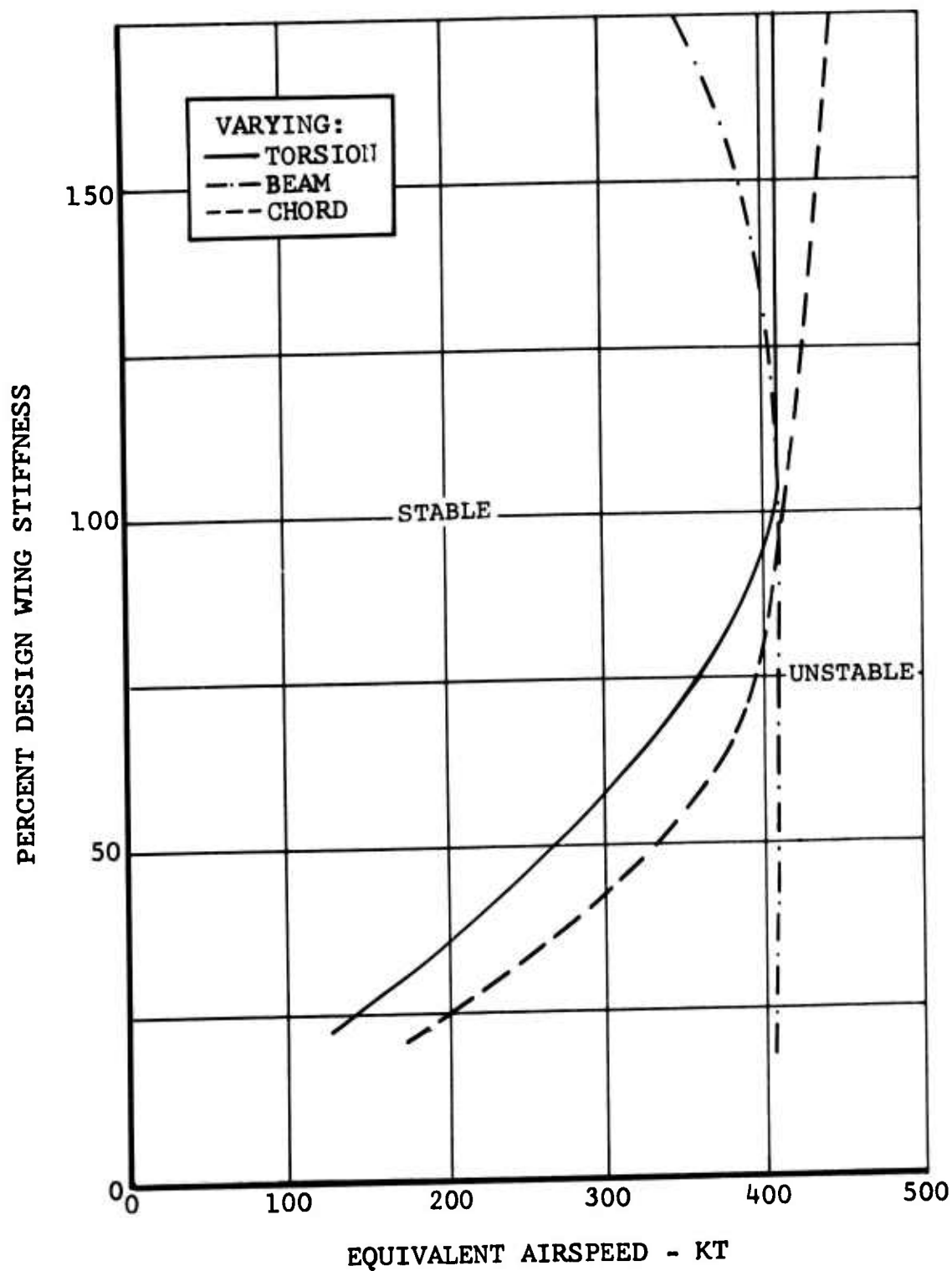
Figure 100.   Influence of Wing Stiffness on
               Proprotor Stability, Gimbal
               Free to Flap.

198
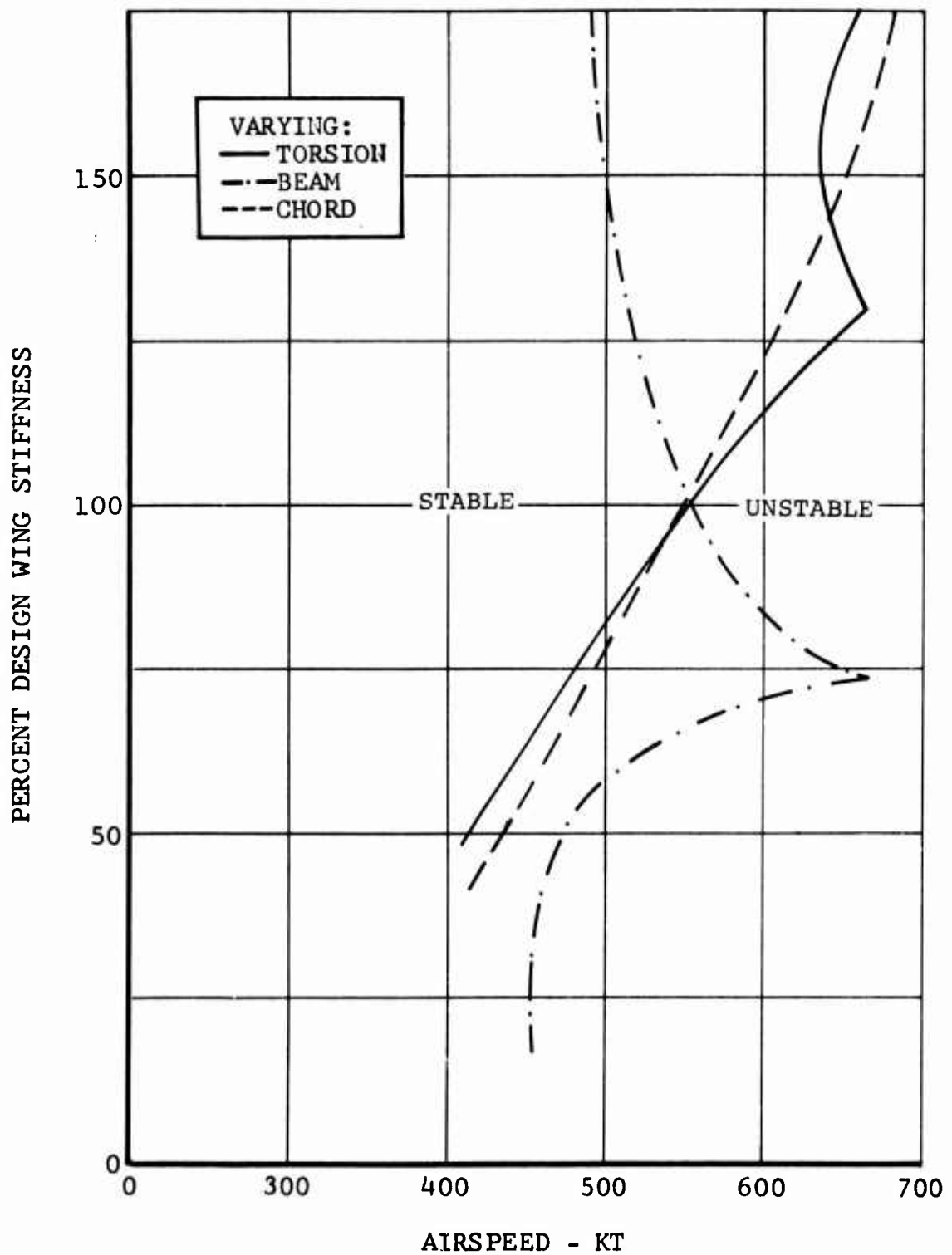
Figure 101.   Influence of Wing Stiffness on Proprotor
             Stability, Gimbal Flapping Freedom
             Locked Out.

199
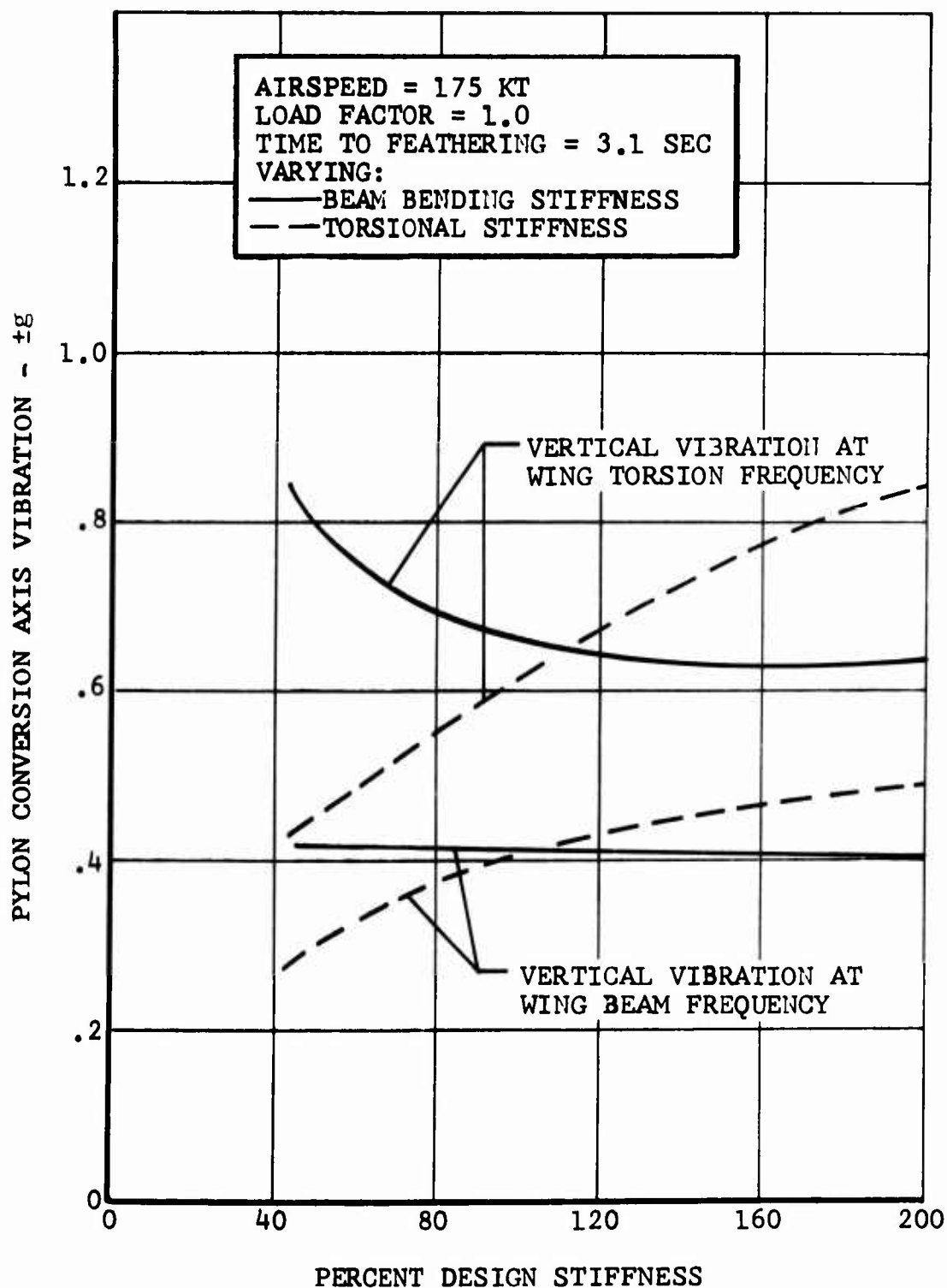
Figure 102.   Influence of Wing Stiffness on
Vibration During Feathering.

200
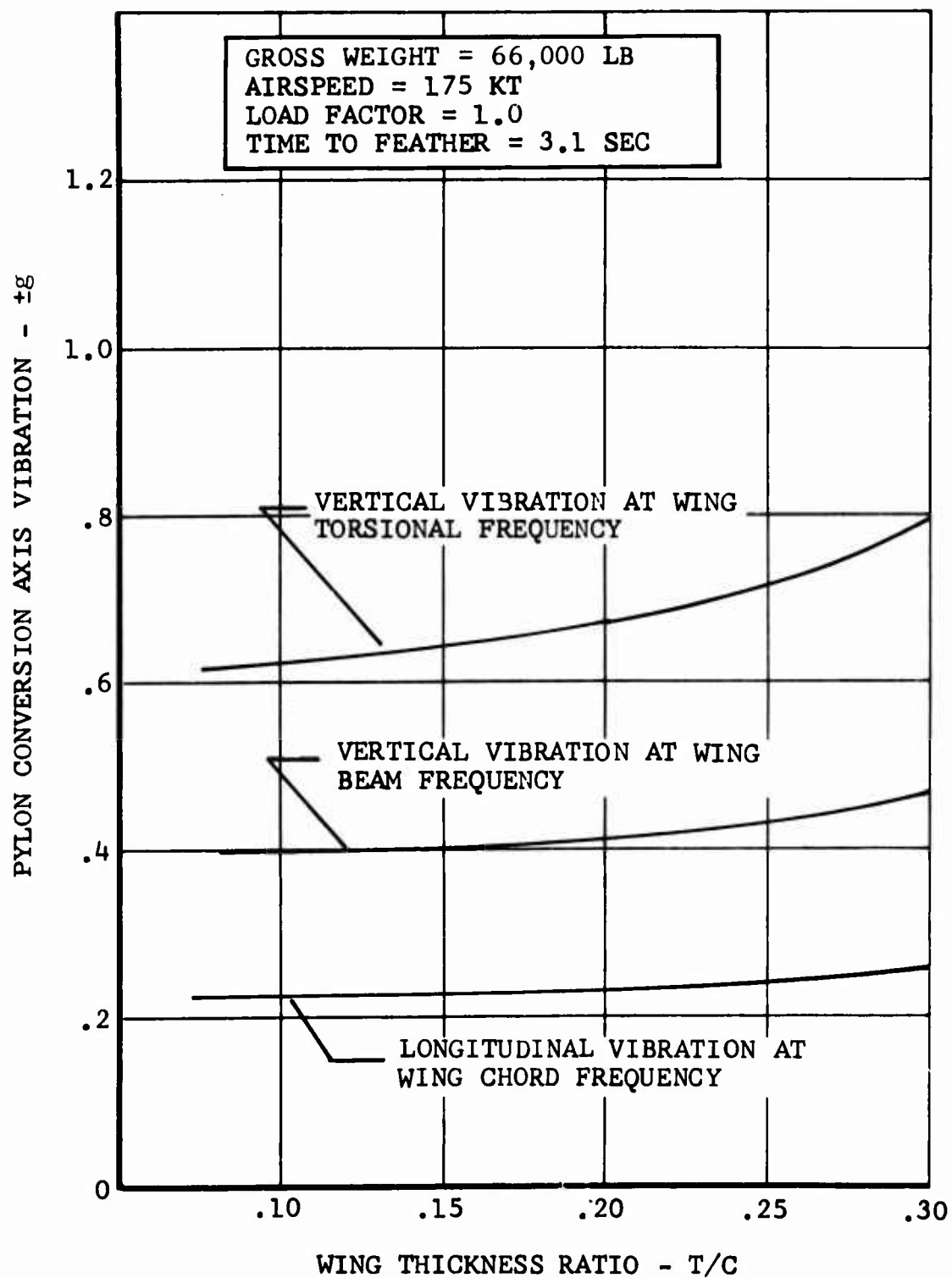
Figure 103. Influence of Wing Thickness on
Vibration During Feathering.

201
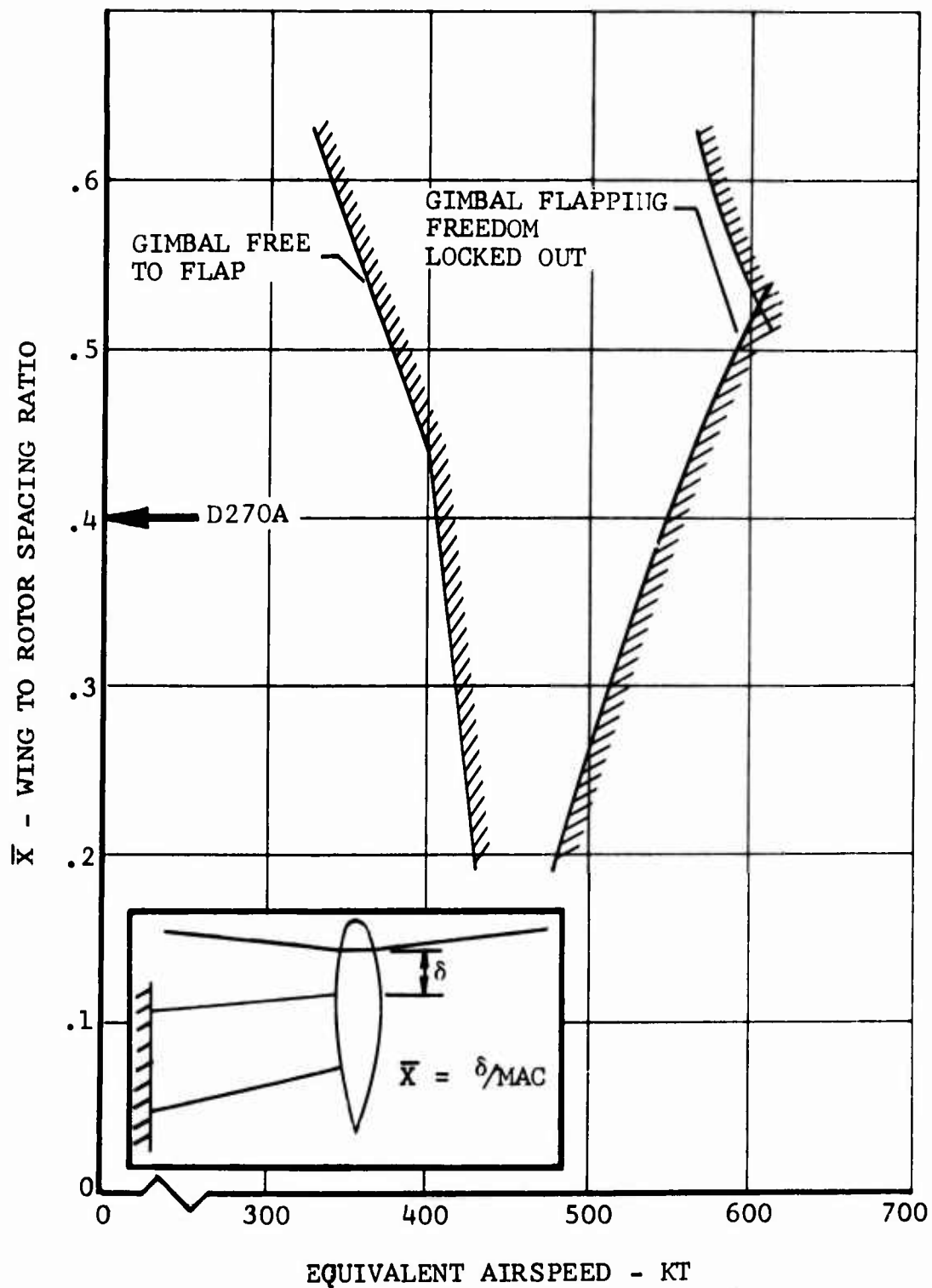
Figure 104. Influence of Wing to Proprotor
Spacing on Proprotor Stability.

202
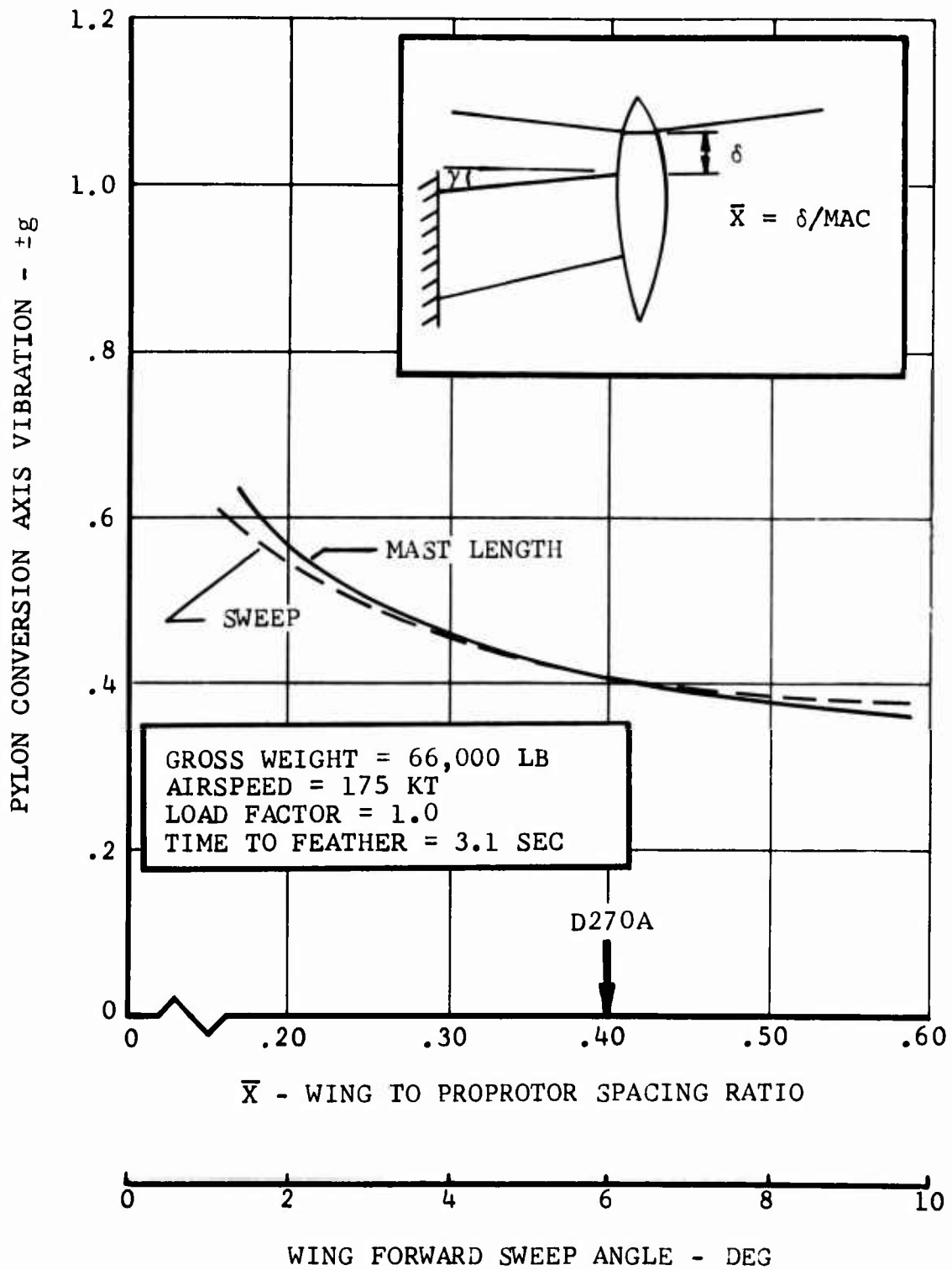
Figure 105.   Influence of Wing to Proprotor Spacing and
Wing Forward Sweep on Vibration During
Blade Feathering.
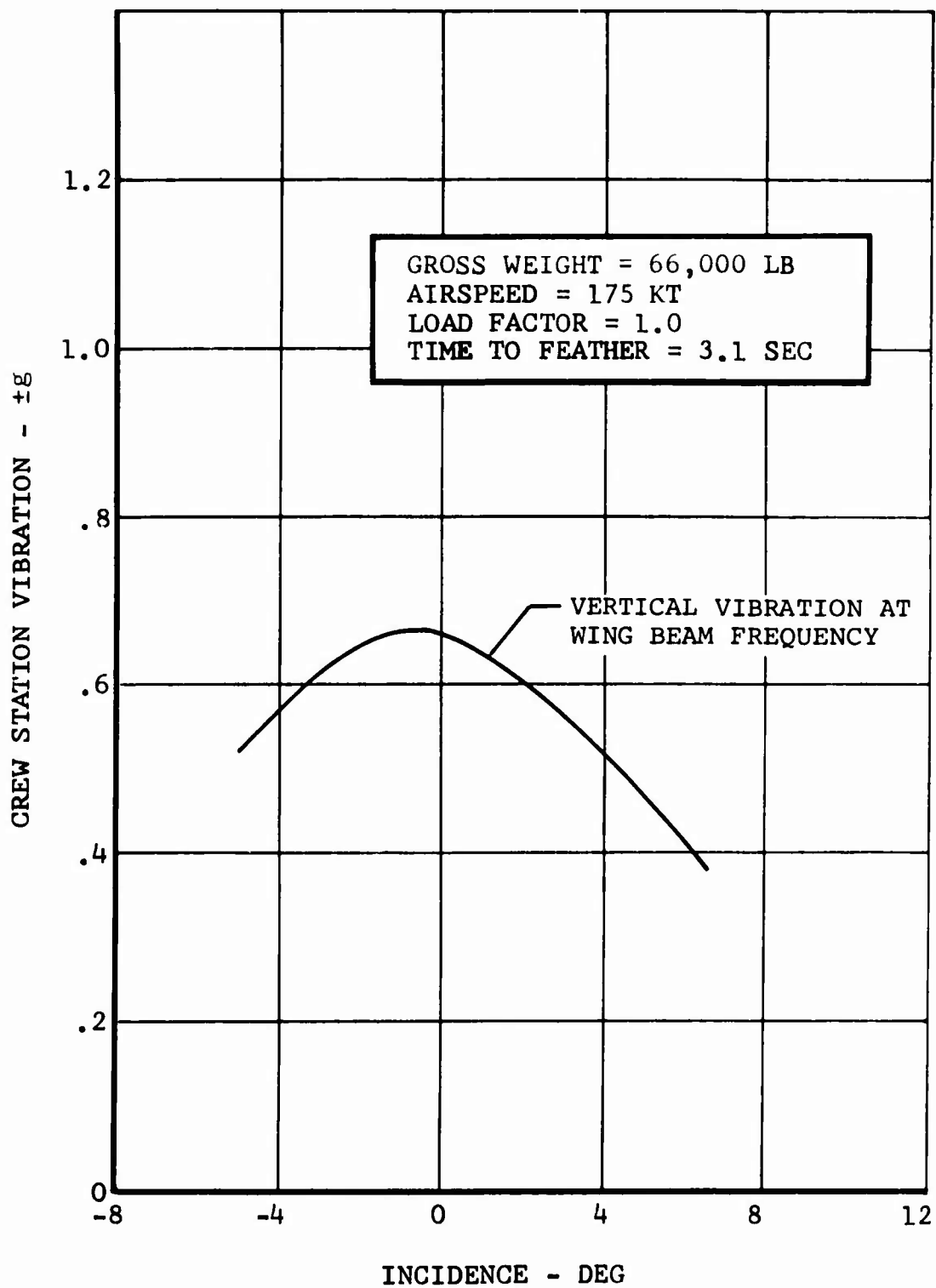
Figure 106. Influence of Pylon Incidence on
Vibration During Feathering.

204
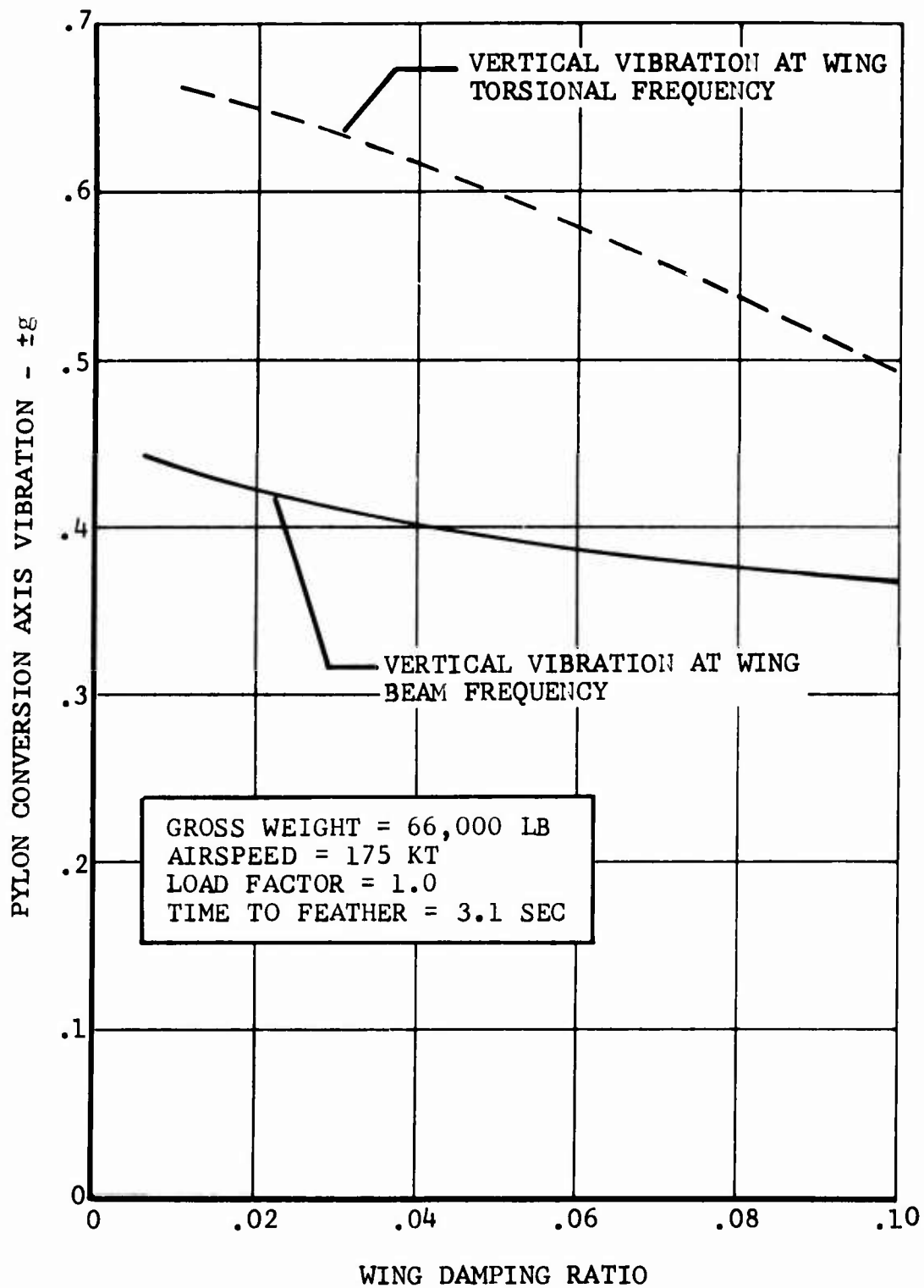
Figure 107. Influence of Wing Structural Damping
on Vibration During Feathering.

205
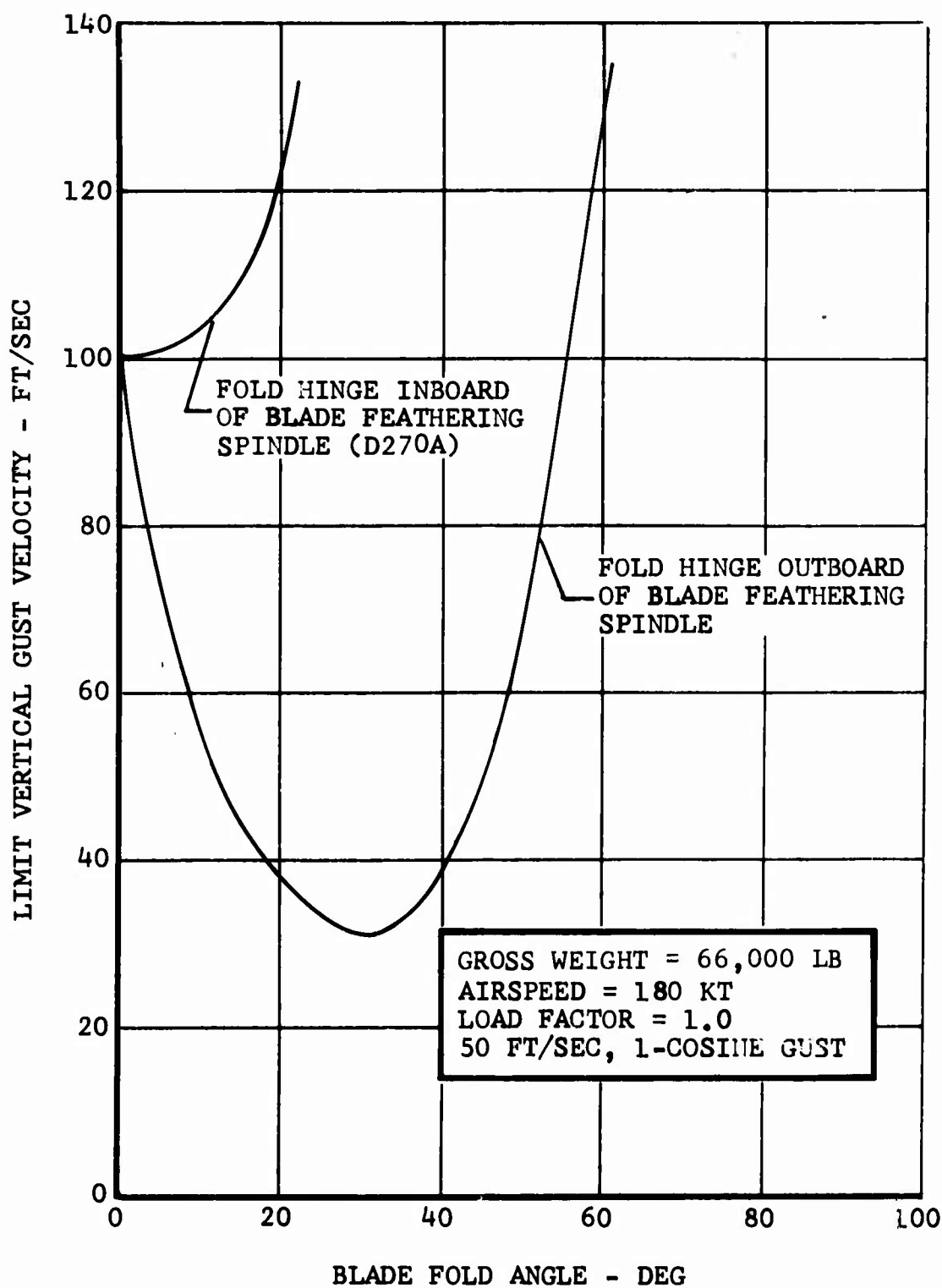
Figure 108.   Influence of Fold Hinge Location on
Gust Limit During Blade Folding.

206

SECTION V

CONCLUSIONS AND RECOMMENDATIONS

A. THEORY AND COMPUTER PROGRAMS

A theory has been developed to predict the stability and response during feathering and folding the blades of a folding proprotor VTOL. The theory, manifested as digital computer programs, is in good agreement with measured stability and response characteristics.

The computer programs are presently restricted to some extent in the configurations they are capable of simulating. For example, the proprotor simulation is restricted to three blades. These restrictions arose from computer storage limitations and may be relaxed if more storage is available. Information is provided in this volume and in Volume II to assist a user in modifying and extending the programs.

It should be noted that the Feathering-Dynamics Analysis Program ARAP06, is also applicable to tilt-proprotor dynamic analysis. Capability in this regard includes prediction of proprotor stability, blade loads, and vibration characteristics. The program may also be used to investigate the dynamic characteristics in helicopter and conversion mode for both proprotor VTOL types.

B. CONCLUSIONS FROM THE DYNAMIC MODEL TEST

Several conclusions regarding the folding proprotor configuration can be made directly from the dynamic model test.

The most significant conclusions is that flapping freedom must be locked out prior to feathering the blades. During tests with the gimbal flapping only lightly restrained, large flapping amplitudes were encountered even near zero shaft angle of attack. As the blade feathering rate was increased, the peak flapping excursion increased. At a shaft angle of attack of 5.6 degrees the blades contacted the mechanical flapping stops of ±12 degrees. Furthermore a flapping instability was encountered at low rpm, in the transition mode airspeed range.

When the gimbal flapping freedom was locked out the blade tip deflections were observed to be small and the flapping instability eliminated.

Locking out the blade flapping freedom appears necessary regardless of how the freedom is attained, i.e., with a gimbal, a true flapping hinge, or using an elastic virtual hinge, as with a hingeless rotor.

C. CONCLUSIONS FROM THE DYNAMIC ANALYSIS AND PARAMETRIC
    STUDY

The dynamic analysis indicates that acceptable dynamic stabil-
ity and response characteristics during blade feathering and
folding can be obtained in a 66,000-pound gross weight FPR
design. The most serious problem area identified in the
course of the analysis, is a low maneuver load factor capa-
bility during blade feathering. This arises from the require-
ment to use fatigue allowable load limits during feathering
rather than static limit loads. For the D270A, another factor
is the strength of the critical component, the fold hinge lug.
When the lug strength is increased to the same level as that
of the hub and blades, the maneuver load limit is considerably
higher.

It is apparent from this study that a criterion for allowable
loads during blade feathering must be established.

A second problem area is the acceptability of the crew station
vibration during blade feathering. The largest response occurs
at a frequency of approximately two cycles per second, the
wing beam bending natural frequency. At this frequency the
peak accelerations reach ±0.65 g, which exceeds an "alarming"
subjective discomfort level.[23] However, the reference
subject discomfort level was established for sinusoidal vibra-
tion whereas the response during feathering is a damped
transient. A requirement for a criteria for an acceptable
level of crew station response is evident.

The results of the parametric study are summarized in terms of
design guidelines, Table IX. A brief discussion of the influ-
ence of major design parameters is given below.

    (1) Disc Loading - A higher disc loading has a favorable
         influence on proprotor stability and on dynamic
         response. The influence of disc loading on other
         dynamic factors is small provided the system
         natural frequency ratios are held constant.

    (2) Proprotor Types - A proprotor type which combines
         stiff blades with the capability to lock out flapping
         freedom, whether real or virtual, is desirable.
         Highly flexible, or freely flapping or lightly
         restrained in flapping blades are susceptible to
         instability at low rotor speeds and can contribute to
         higher response levels during feathering.

    (3) Wing Stiffness - The wing chordwise and torsional
         stiffness have a strong influence on proprotor/
         pylon stability when the blades are free to flap.

Increasing the torsional and chordwise stiffness increases the stability. The wing beamwise stiffness has a small influence. When flapping freedom is locked, the beamwise stiffness is also significant. However, with flapping locked out the important consideration is frequency isotropicity. Consequently a decrease in stiffness can be beneficial if the system frequency anisotropy is increased.

The influence of wing stiffness on the dynamic response is small for a reasonable variation in stiffness. However, a reasonable change in stiffness can have a favorable influence if the system frequencies are shifted toward a more "comfortable" range, from the human factors standpoint.

Wing thickness ratio, the usual means of controlling wing stiffness was found to have a small influence on dynamic response.

(4) Wing-Rotor Spacing - Increased spacing, obtained using a longer mast, has a destabilizing influence when the blades are free to flap, but is stabilizing when flapping is locked out. A longer mast decreases the dynamic response.

Wing forward sweep may be used to increase the effective spacing and thus reduce the response, and does not significantly influence stability.

(5) Feathering Rate - Based on response studies for 25-foot, 38.5-foot, and the D270A 50-foot proprotor, an optimum feathering time may be approximated by

$$\Delta T = 2.75 \sqrt{\frac{D}{38.5}} \quad \text{seconds} \tag{225}$$

where D is the proprotor diameter in feet.

This optimum is not extremely sensitive and may be varied over a considerable range.

D. DESIGN CRITERIA IMPLICATIONS

The flutter-free margin specified in MIL-A-8870 and the 50-foot per second vertical gust encounter at V_{LF}, specified in MIL-A-8860 appear to be within the capability of the folding proprotor concept. However, the 2.0 maneuver load factor at V_{LF}, specified in MIL-A-8860, may be difficult to meet if fatigue allowable load limits are applied during

blade feathering. It is apparent that a criterion for allowable loads during blade feathering is required.

As noted above, design criteria for acceptable crew station acceleration levels, and allowable loads during blade feathering should be developed.

E. RECOMMENDATIONS FOR FURTHER STUDY

Experimental investigations should be extended to include factors such as wing flap and free-flight conditions, which may have a significant impact on the response during feathering. The present theory can be readily extended to include these details.

Full-scale tests are required to identify the hardware dynamic problems associated with feathering and folding. For example, the flapping lockout and blade folding mechanism could induce high dynamic loads depending on their characteristics.

Much of this recommended work is presently being accomplished under Air Force and NASA sponsored research.

TABLE IX

FOLDING-PROPROTOR DYNAMICS DESIGN GUIDELINES

DESIGN PARAMETER	CHARACTERISTICS AFFECTED	PRIMARY CONSIDERATION	DESIGN GUIDELINE(S)
Disc Loading	- Stability - Response	- Proprotor/pylon stability	Higher disc loading is desirable from a dynamics standpoint(1)
Proprotor Blade Stiffness and Hub Type	- Stability - Flapping - Gust, Maneuver Limits - Response	- Blade flapping and stability	Propeller-like blade stiffness characteristics are desirable. This requires (1) Locking out flapping prior to feathering, and (2) Using blades with high root stiffness
Wing Stiffness and Planform	- Stability - Response	- Proprotor/pylon stability	(1) High stiffness in torsion and chord bending desirable (2) Use forward sweep to minimize distance, elastic axis to hub (3) Avoid frequency isotropicity
Wing-Proprotor Spacing	- Stability - Response - Flapping	- Flapping clearance	(1) Use flapping clearance requirements to establish spacing (2) Use forward sweep of wing to increase tip clearance
Feathering Rate	- Response	- Minimum vibration during feathering	Use a time to feather of $2.75 \ (D/38.5)^{\frac{1}{2}}$ seconds (D is the proprotor diameter)

(1) Generally disc loading will be established by a performance and gross weight consideration rather than dynamics.

211

REFERENCES

1. DeTore, J. A., and Gaffey, T. M., "The Stoppable Rotor Variant of the Proprotor VTOL Aircraft," _Journal of The American Helicopter Society_, April 1970

2. Fry, B. L, and Schneider, J. L., _Design Optimization of Stoppable-Rotor V/STOL Aircraft Systems_, Presented at the National Aerospace-Electronics Conference, Dayton, Ohio, May 1969.

3. Deckert, W. H. and Ferry, R. G., "Limited Flight Evaluation of the XV-3 Aircraft," TR-60-4, Air Force Flight Test Center, May 1960.

4. Hall, W. E., "Proprotor Stability at High Advance Ratios," _Journal of the American Helicopter Society_, June 1966.

5. Edenborough, H. K., "Investigation of Tilt-Rotor VTOL Aircraft Rotor-Pylon Stability, AIAA Paper No. 67-16, AIAA 5th Aerospace Sciences Meeting, New York, New York, January 1967.

6. Gaffey, T. M., et al., "Analysis and Model Tests of the Proprotor Dynamics of a Tilt-Proprotor VTOL Aircraft," presented at the Air Force V/STOL Technology and Planning Conference, September 23-25, 1969.

7. Gaffey, T. M., "The Effect of Positive Pitch-Flap Coupling (Negative δ_3) on Blade Motion Stability and Flapping," Journal of the American Helicopter Society, April 1969.

8. Rodden, William P., Frakas, Edith F., and Malcom, Heatner, A., _Flutter and Vibration Analysis by a Collection Method: Analytical Development and Computational Procedure_, Aerospace Corporation, Contract AF04(695)-169, 31 July 1963.

9. Gessow A., and Myers, G. C., Jr., _Aerodynamics of the Helicopter_, MacMilliam, 1952.

10. Fung, Y. C., _An Introduction to the Theory of Aeroelasticity_, Wiley, 1955.

11. Ham, N. D., and Young, M. J., "Torsional Oscillations of Helicopter Blades Due to Stall," _Journal of Aircraft_, Volume 3, No. 3., 1966.

12. Shames, I. H., <u>Mechanics of Fluids</u>, McGraw-Hill, 1962.

13. Przemieniecki, J. S., <u>Theory of Matrix Structural Analysis</u>, McGraw-Hill, 1968.

14. Frueh, F. J., and Miller, J. M., <u>Prediction of Dynamic Response from Flutter Analysis Solutions</u>, AFOSR Report 65-1952, June 1965.

15. Young, M. I. and Lytwyn, R. T., "The Influence of Flapping Restraint on Proprotor Stability at High Advance Ratios," <u>Journal of the American Helicoter Society</u>, September 1967.

16. Reed, W. I., III.,"The Effects of a Time-Varying Test Environment on the Evaluation of Dynamic Stability with Application to Flutter Testing," <u>Journal of the Aero/Space Sciences</u>, July 1958.

17. Contract No. F33615-C-1578, PZ02, <u>Design Studies and Model Tests of the Stoppable Rotor Concept</u>, April 1969.

18. <u>Design Studies of Folding-Proprotor Aircraft</u>, Bell Helicopter Company Report D270-099-001.

19. Contract NAS2-5386, <u>Advancement of Proprotor Technology</u>, September 1969.

20. Reed, W. H., III, <u>Review of Propeller-Rotor Whirl Flutter</u>, NASA Technical Report R-264, July 1967.

21. Anon, <u>Tentative Airworthiness Standards for Verticraft/ Powered Lift Transport Catagory Aircraft</u>, Federal Aviation Agency August 1970.

22. Bisplinghoff, R. L., Ashley, H., and Halfman, R. L., <u>Aeroelasticity</u>, Addison-Wesley, 1955.

23. Parks, D. L., and Synder, F. W., <u>Human Reaction to Low-Frequency Vibration</u>, The Boeing Company, Wichita Division, Document D3-3512-1, July 1961.

24. DeTore, J. A., <u>Lift/Propulsion System Size-Selection Considerations for Stoppable Rotor VTOL Aircraft</u>, Presented at the Air Force V/STOL Technology and Planning Conference, Las Vegas, Nevada, September 1969.

25. Cardinale, S. V. and Donham, R. E., <u>Full-Scale Wind Tunnel Tests and Analysis of a Stopped/Folded Rotor</u>, Lockheed Report LR21016, June 1968.

213

26. Wernicke, K. G., "Tilt-Proprotor Composite Aircraft, Design State of the Art," <u>Journal of the American Helicopter Society</u>, April 1969.

APPENDIX I

MODEL DESCRIPTIVE DATA

Transition Model

The experimental data on wing-blade aerodynamic interference
presented in this report was obtained using the transition
model shown earlier in Figure 24. The scaling of the transition
model is the same as the semispan aeroelastic model discussed
later in this Appendix. The fuselage is free to pitch on the
wind tunnel balance with the pivot located at 35 percent MAC.
The fuselage freedom may be locked out, if desired. The pylon
conversion angle relative to the wing chordline, and the
horizonal stabilizer incidence can be remotely controlled. A
three component strain gage balance is used to measure the
proprotor hub normal forces and sideforce and pitch and yaw
moments. A strain gage at the blade root may be used to measure
the blade beam bending moment.

Figure I-1 shows the transition model layout and dimensions.
The wing thickness ratio is 0.15. Two sets of blades are
available. One set has -20 degrees twist, the other set, -3
degrees twist. (This is the theoretical twist, shaft center-
line to blade tip.) Tests of this model were made in 1968
under the Bell IR&D program.

Semispan Aeroelastic Model

The model used in the wind tunnel test conducted under this
program is a 0.133 scale, dynamic aeroelastic model of a Bell
Helicopter Company 38,000-pound tilt-proprotor VTOL design.
The model was designed, fabricated, and tested by Bell under
the Army Composite Aircraft Program. At the conclusion of
that program the model was transferred by the Army to the
NASA-Langley Aeroelasticity Branch for further research in
proprotor dynamics. For a description of the full-scale design
the reader is referred to Reference 25.

A photograph of the model installed in the 16-foot transonic
dynamics tunnel was shown earlier in Figure 29. The proprotor.
pylon, and wing are Froude and Lock scaled for operation in air
at full-scale density. The model scale factors, based on the
tilt-proprotor design are given in Table I-I.

The fuselage and mounting arrangement may be taken as effectively
rigid with respect to the proprotor/pylon/wing system. While
the mounting is not that normally employed for semispan models,
tests with a conventional reflection plane showed no significant
difference in stability or dynamic response.

215
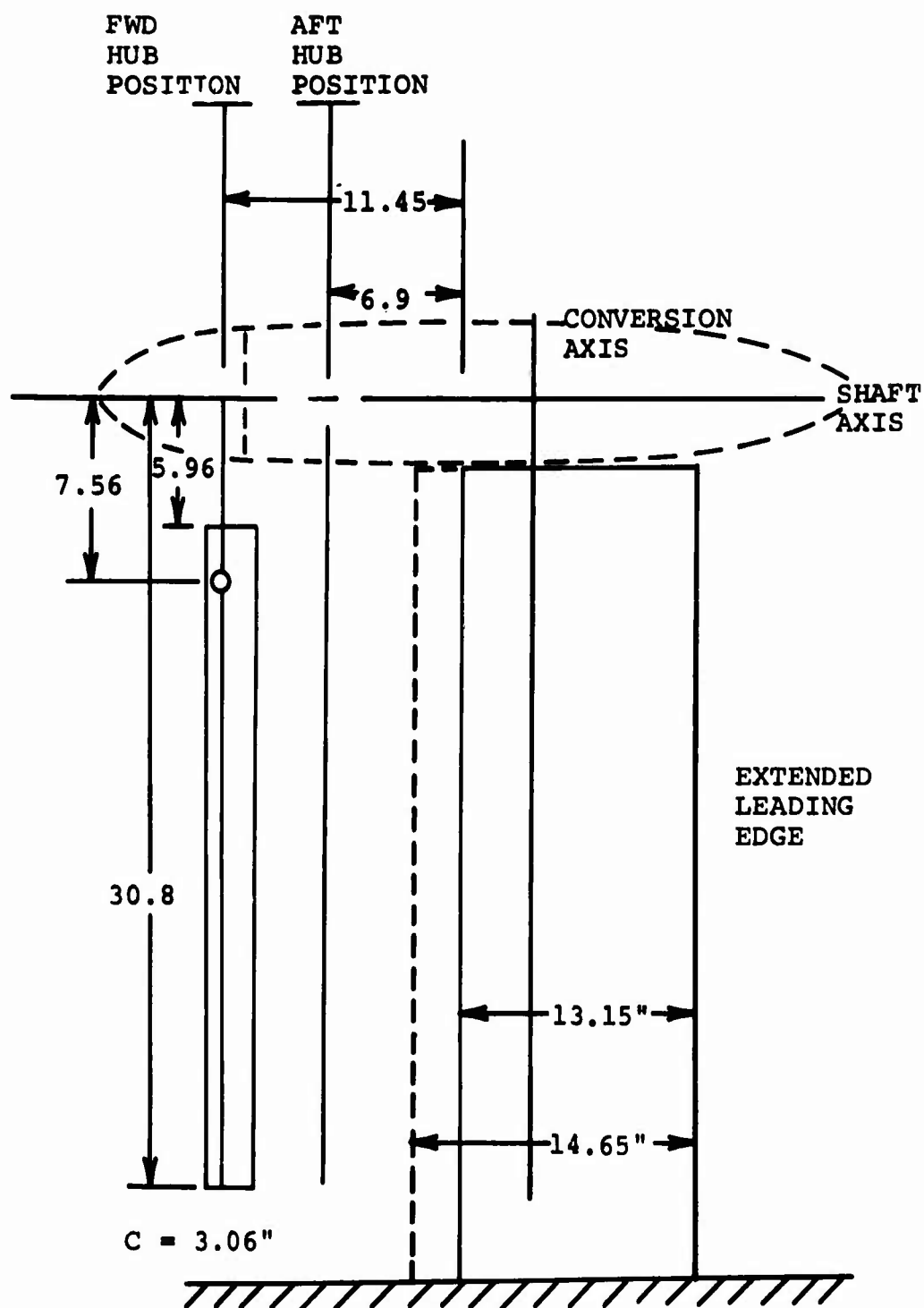
Figure I-1.   Transition Model Layout and Dimensions.

TABLE I-I
MODEL SCALE FACTORS

Parameter	Units	Scale Factor
Length	ft*	0.133
Mass	lb	0.00235
Time	sec	0.365
Froude Number	---	1.0
Lock Number	---	1.0
Mach Number	---	0.365
Reynolds Number	---	0.0487
Velocity	ft/sec	0.365
Frequency	1/sec	2.738
Inertia	lb$\cdot$ft^2	4.21×10^{-5}
Linear Spring Rate	lb/ft	1.78×10^{-2}
Torsional Spring Rate	lb$\cdot$ft/deg	3.16×10^{-4}
Stiffness, EI, GJ	lb$\cdot$in^2	4.21×10^{-5}
*Inch units may be used as long as units are consistant		

For the tests conducted under this program several modifications
were made to the model: The original remote control collective
pitch system was replaced with a system capable of feathering
rates of up to approximately 150 degrees per second. The rate
could be varied (remotely) from 2 degrees per second to the
maximum. This allowed the proprotor feather or unfeather time
to be varied from 30 seconds to 0.4 seconds. The new collective
pitch control system also had twice the range of the original
system, approximately 65 degrees of collective pitch. An auto-
matic flapping lockout was installed in the model to permit
investigation of the effect of locking out flapping freedom as
the blades were feathered. The rpm at which the lockout
occurred could be preset. Flapping could also be locked out
over the entire rpm range. These provisions are shown in
Figure I-2.

217

NOT REPRODUCIBLE
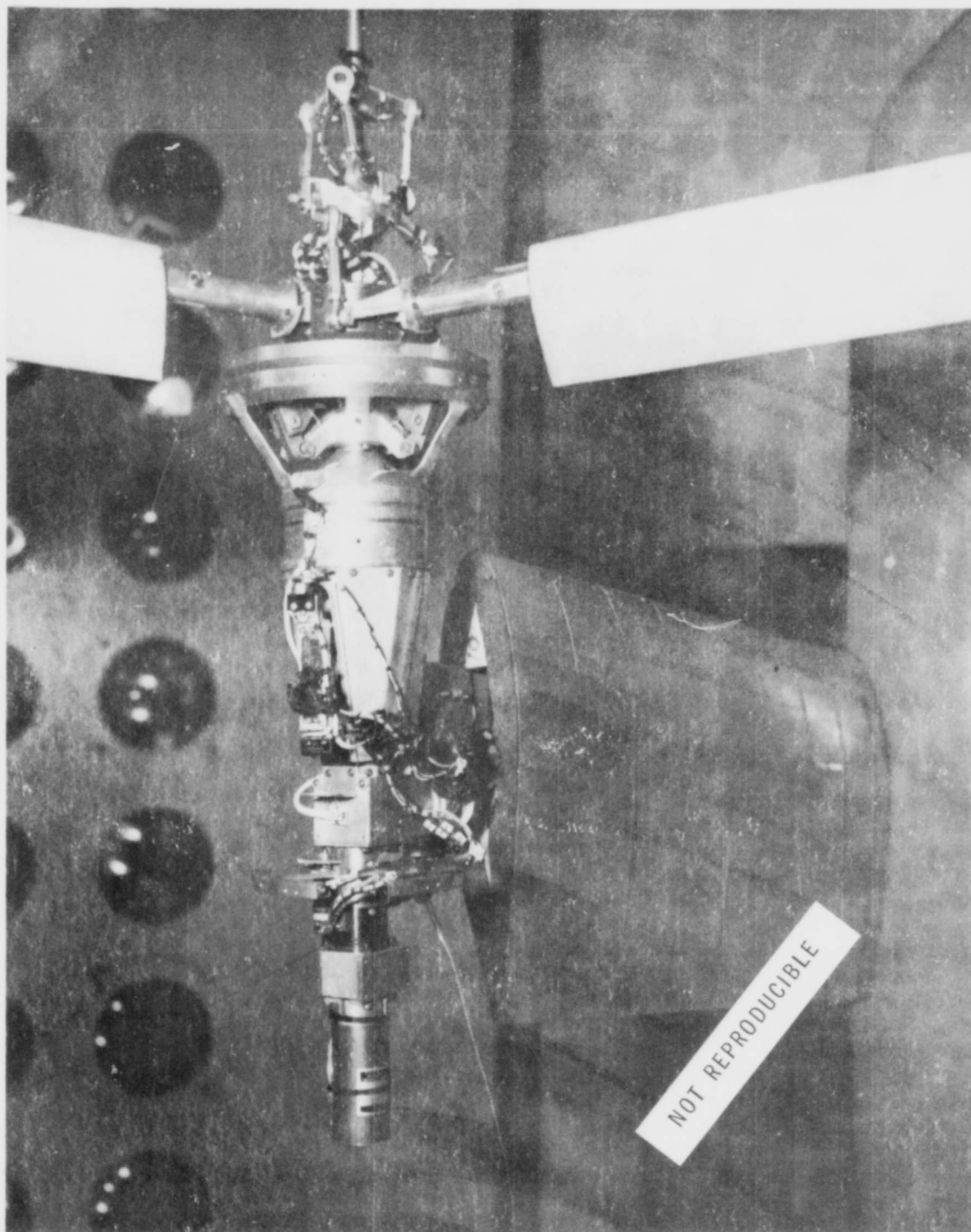
Figure I-2   Pylon Configuration for Feather/Stop Test.

218

For the fold-unfold tests the model was modified as follows:
The hub gimbal freedom and the rotational freedom of the
proprotor were locked out. A new set of grips for the blades
were installed. These contained elements which provided
flexibility about the feathering axis. One cruciform was
located inboard of the fold hinge, the other outboard to
simulate different control arrangements. The fold hinge also
contained a cruciform element to sirulate fold hinge flexi-
bility. Several cruciform spring rates were available. In
the Bell-NASA test a 2000 in-lb/rad cruciform was used at the
fold hinge, and 1000 in-lb/rad cruciforms as the inboard
feathering axis element. Effectively rigid elements were
employed in the outboard feathering element. Figure I-3 shows
this arrangement.

It should be noted that while the model tested is based on a
tilting-proprotor design, the factors which significantly
influence dynamic characteristics (i.e. stiffness and mass
distributions and geometry) approximate Bell Helicopter Company's
folding-proprotor configuration.

Model Dimensions

Figure I-4 is a three-view of the model showing the principal
dimensions.

Proprotor Parameters

The proprotor blades consist of an aluminum spar covered with
fiberglass skin. Expanded foam is used to maintain the blade
contour. Lead weights are bonded to the spar to achieve the
scaled weight distribution and mass balance. The blade pitch-
change axis lies on the quarter-chordline of the blade.

The proprotor blades are attached to a stainless steel yoke
ring which in turn is attached to the mast with a gimbal (Hooke's
joint). The blade centrifugal force is carried by wound wire
straps which allow the blades to feather on the yoke spindles.
This semirigid arrangement allows cyclic flapping (tip-path-
plane tilt) but restrains coning and lead-lag motion. The first
inplane natural frequency of the blade is above the rotor
rotational speed to preclude mechanical instability.

The hub is lightly restrained in the cyclic flapping sense by
a hub restraint of 336 in-lb/radian about the yoke gimbal
center.

The constant chord blades are twisted -27.7 degrees (hub C_L to
tip) and the pitch-change axis is preconed 3 degrees. The
blades have a 14.6 percent root cutout.

219

FOLD HINGE

FEATHERING FLEXIBILITY, INBOARD

FEATHERING FLEXIBILITY, OUTBOARD

NOT REPRODUCIBLE
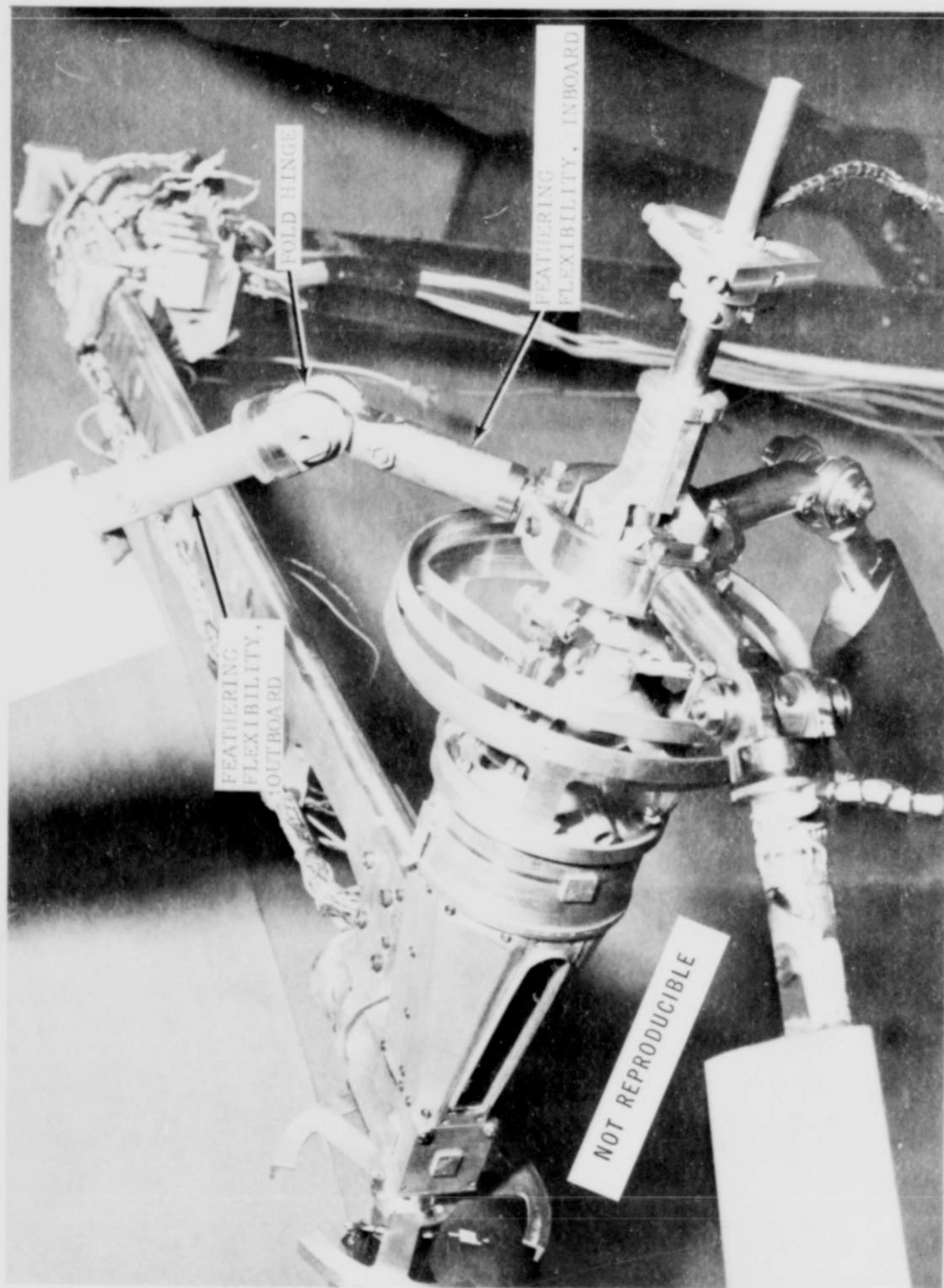
Figure I-3   Hub Configuration for Fold-Unfold Test

3.58

1.11 TO
C_L PYLON

7.34

30.80 RADIUS
STOP/START
CONFIGURATION

34.56 RADIUS
FOLD CONFIGURATION

3.066 CHORD

32.68

CONVERSION AXIS
0.17 BEHIND C_L MOUNT

CONVERSION AXIS

9.55

BL 0.0

11.06

C_L HUB

BL 37.46
(REF)
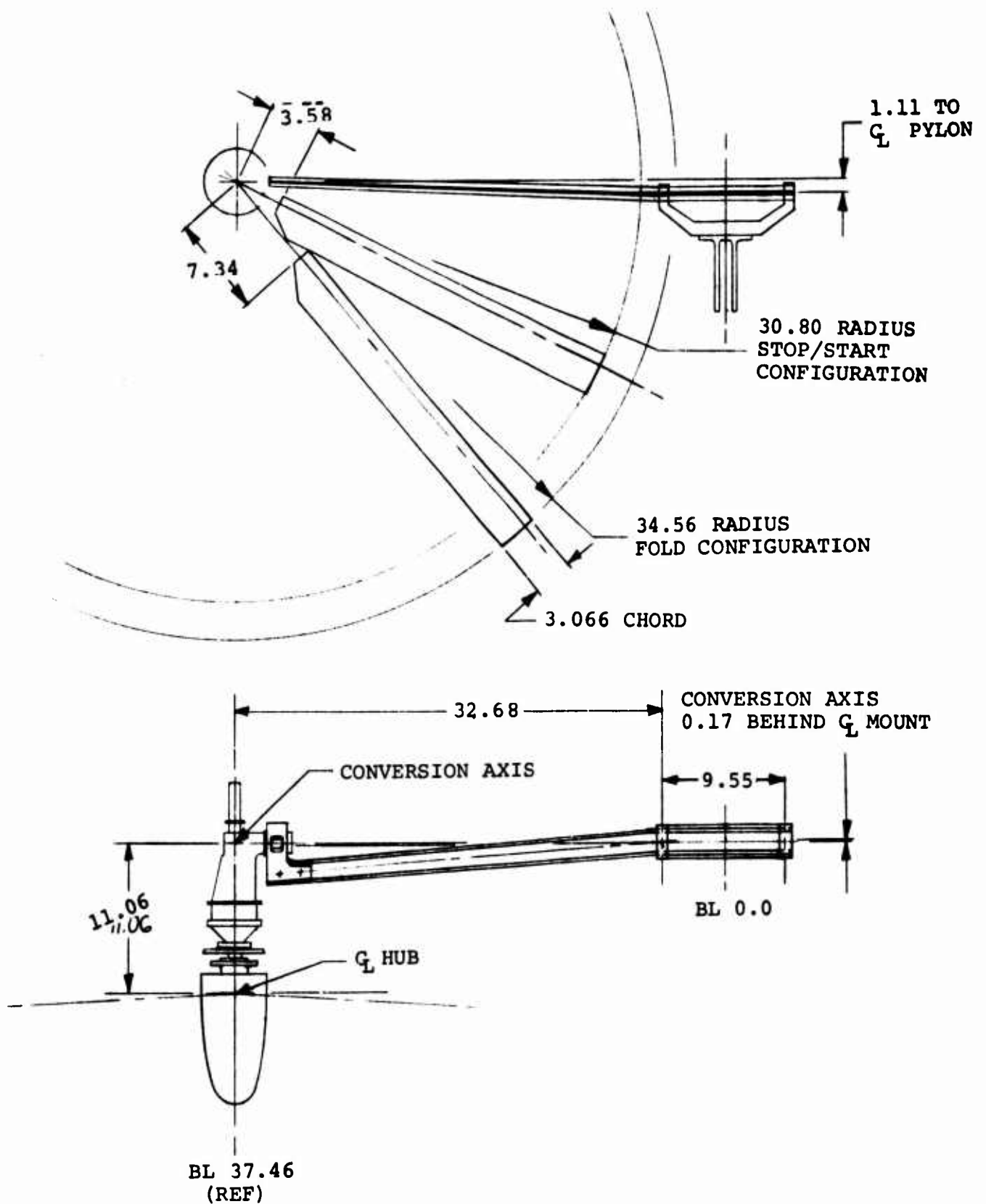
Figure I-4.   Model Layout and Dimensions.

Table I-II gives the proprotor mass and stiffness distributions. The proprotor natural frequencies are shown in Figures I-5 and I-6. These are grouped in terms of collective and cyclic modes; the collective modes are those involving polar symmetric motion about the shaft axis, the cyclic modes are those involving polar asymmetric motion.

Wing Parameters

The wing spar is a hollow aluminum machined spar (bonded top and bottom hat sections) which scales the beamwise, chordwise, and torsional stiffnesses and duplicates the sweep and elastic axis location of the full-scale wing. Segmented balsa fairings of typical flutter model construction are used to obtain the aerodynamic contours. Lead weights are distributed along the spar to obtain the correct weight distribution.

The wing is attached to the mount with a yoke which clamps the spar at each side of the fuselage. The wing stiffnesses and mass distribution is shown in Figures I-7, I-8, and I-9.

Pylon

The pylon is attached to the spar with a tapered conversion spindle at the rear of the spar and a pitch/yaw stop at the front of the spar. The pylon stiffness is not scaled and may be taken as effectively rigid. Fiberglass fairings (not shown) are used to provide the pylon aerodynamic contour. The pylon weight and inertia data are given in Table I-III.

	TABLE I-II			
	MODEL BLADE MASS AND STIFFNESS PROPERTIES			
%R	EI_b $lb \cdot in^2$	EI_c** $lb \cdot in^2$	wt/in*** lb/in	Chordwise cg % chord
2.5	107,800*	149,000	0.110	---
7.5	35,000	35,000	0.0430	---
12.5	122,000***	163,000	0.0454	22.00
17.5	75,000	175,000	0.04031	27.00
22.5	39,500	132,000	0.03093	27.25
27.5	23,000	120,000	0.02009	28.25
32.5	13,500	112,000	0.01763	28.50
37.5	12,300	106,400	0.01645	28.50
42.5	10,450	101,300	0.01558	28.50
47.5	8,700	97,000	0.01820	24.50
52.5	7,200	93,500	0.01445	28.00
57.5	6,000	89,400	0.01712	27.75
62.5	5,000	85,000	0.01756	26.00
67.5	4,050	81,400	0.01784	24.75
72.5	3,200	78,000	0.02153	23.75
77.5	2,400	74,000	0.02061	23.25
82.5	1,700	70,000	0.01963	22.75
87.5	1,200	66,000	0.01916	21.50
92.5	850	63,000	0.01911	20.50
97.5	600	58,000	0.02233	23.05

*Estimated

**Computed, except Station 22.5 through 52.5 percent radius test data used in this area

***Calculated

TABLE I-III
PYLON WEIGHT AND INERTIA PROPERTIES

Feather/Stop Configuration

Pylon Weight	8.8 pounds
Pylon Center of Gravity	7.1 inches ahead of conversion axis
Pylon Inertia about cg Center of Gravity	0.0646 slug-ft^2

Fold/Unfold Configuration

Pylon Weight	9.25 pounds
Pylon Center of Gravity	7.5 inches ahead of conversion axis
Pylon Inertia about Center of Gravity	0.0755 slug-ft^2
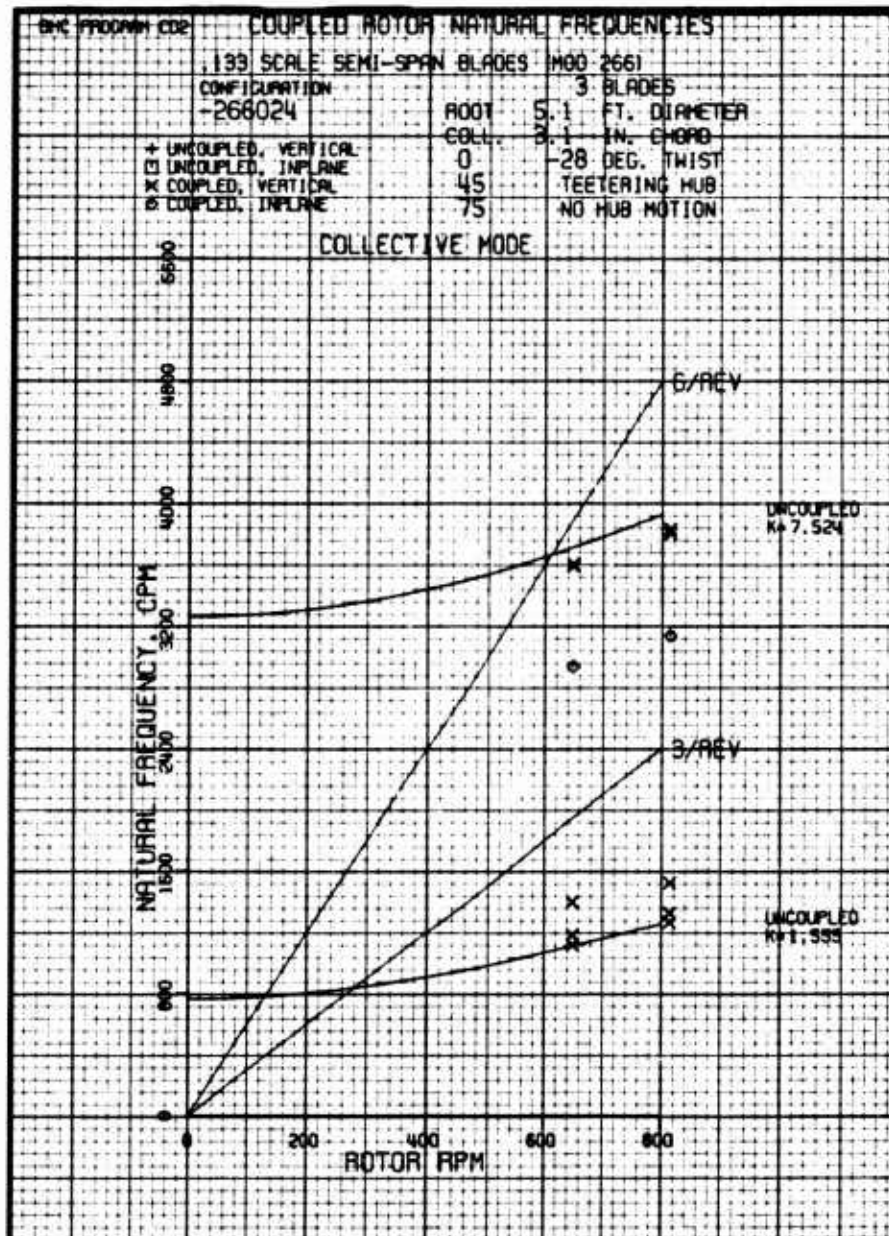
Figure I-5.   Model Proprotor Collective Modes.

225
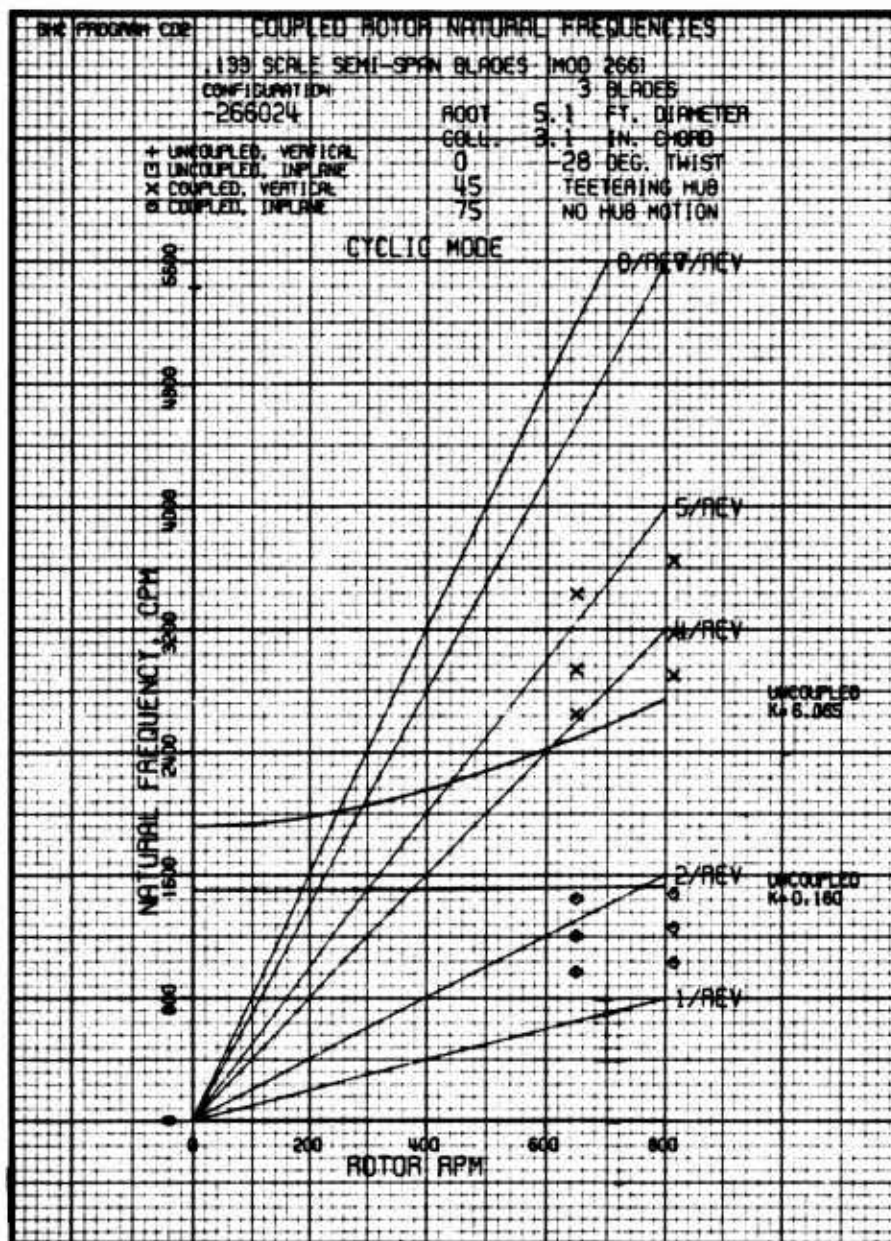
Figure I-6. Model Proprotor Cyclic Modes.

226
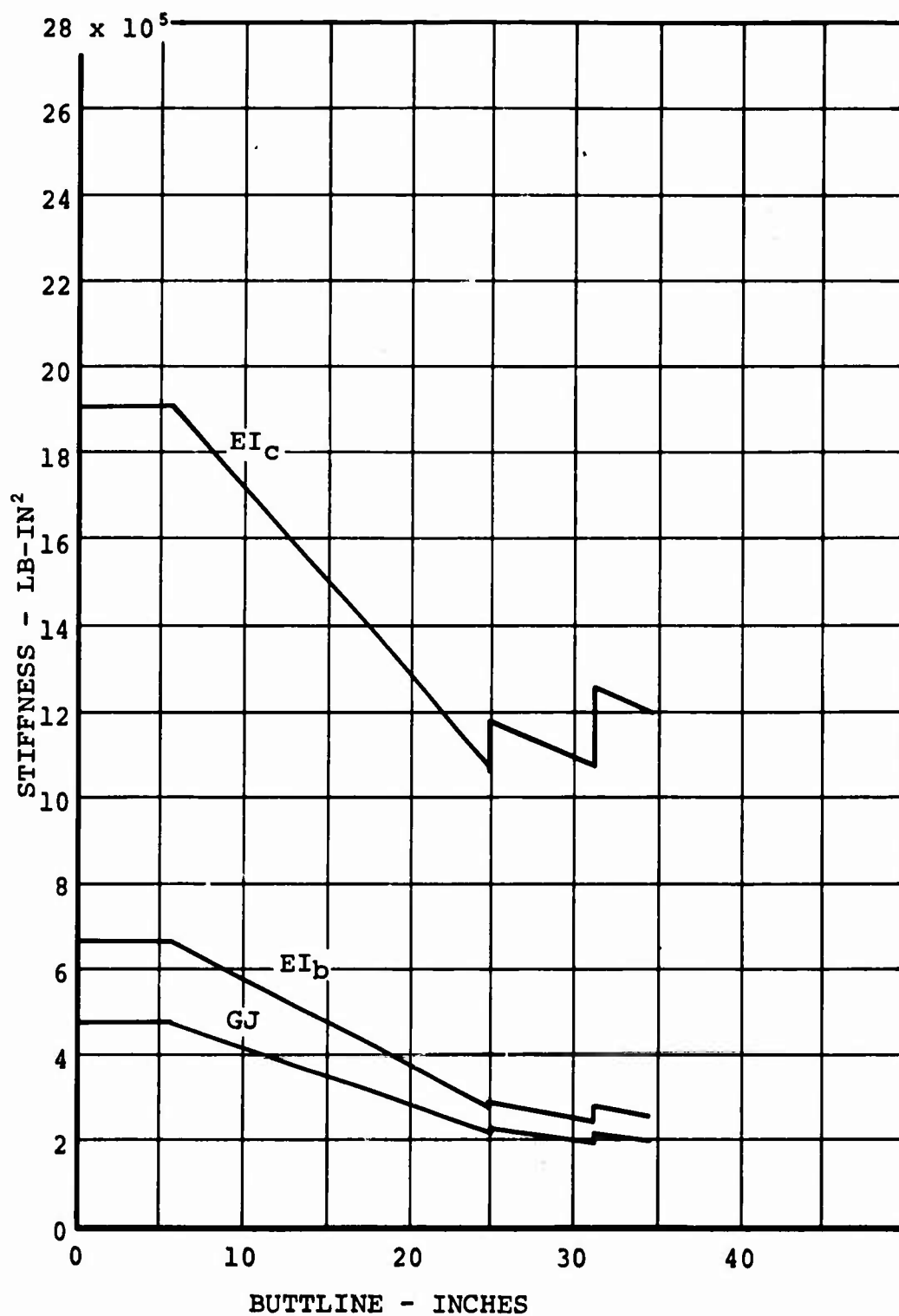
Figure I-7. Model Wing Stiffness Distribution.

227
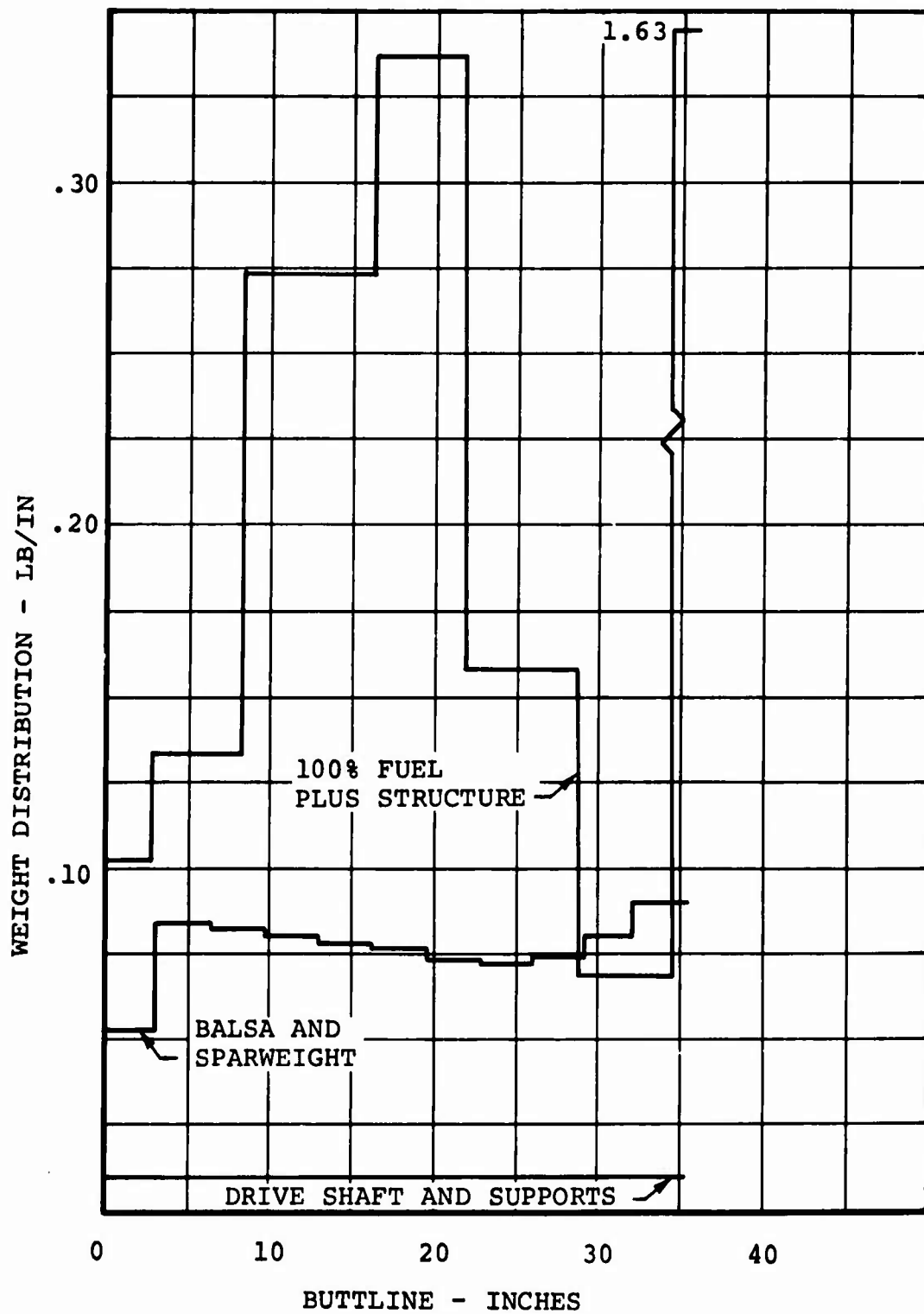
Figure I-8. Model Wing Mass Distribution.

228
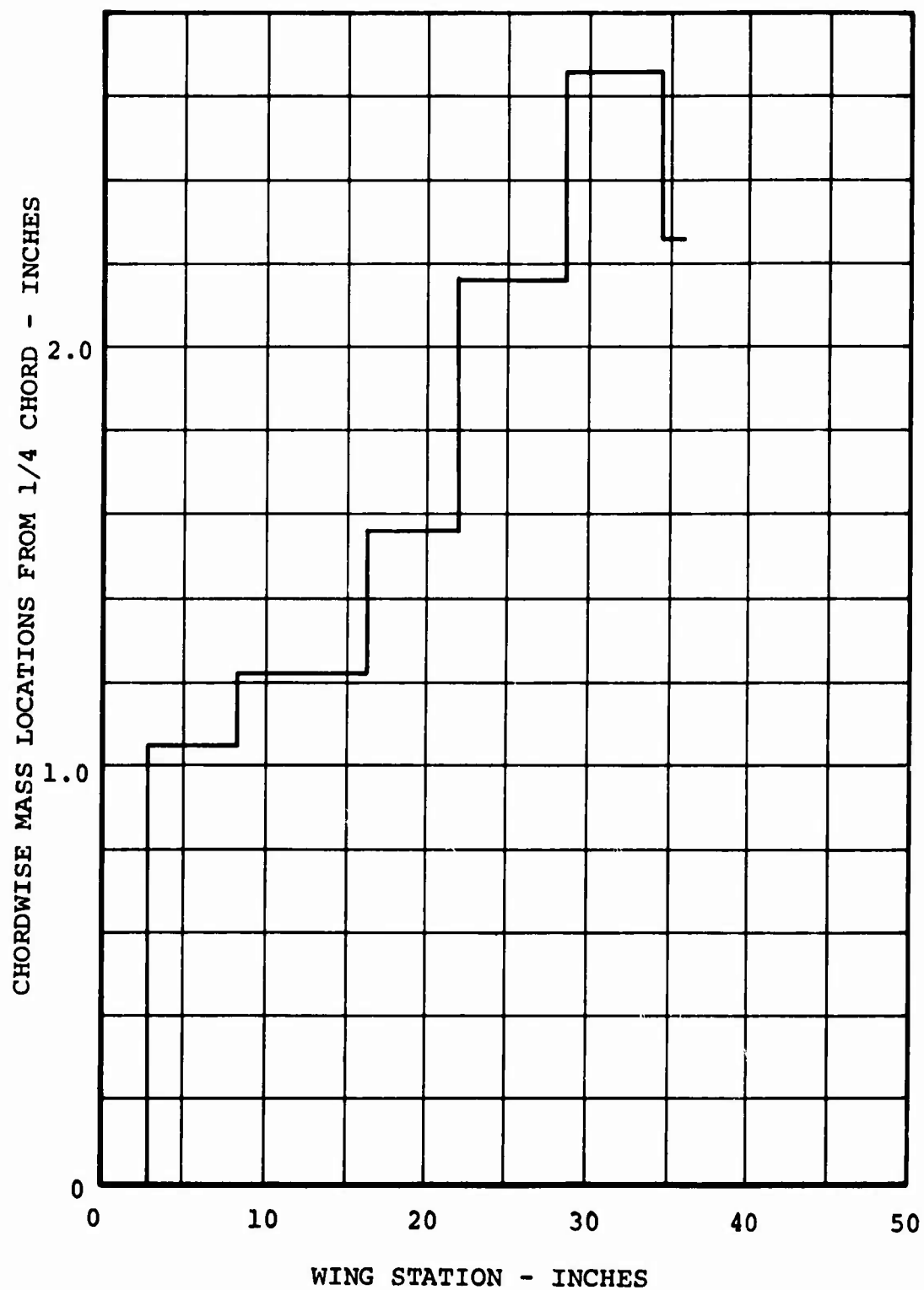
Figure I-9. Model Wing Chordwise Mass
Distribution.

229

Instrumentation

The model was instrumented to provide the data required for the correlation study and to monitor critical loads. Table I-IV lists the instrumentation.

The test data were recorded on CEC Model 124 direct write oscillographs and on magnetic tape. These data are stored at the NASA-Langley Aeroelasticity Branch.

Model Data Summary

Model Natural Frequencies in Stop/Start Configuration

Prior to the wind tunnel test the model natural frequencies and mode shapes were determined at the contractor's facility. The wing-tip spring rates and pylon inertial properties were also measured. Table I-V gives these data.

The natural frequencies were also determined with the model mounted in the wind tunnel. Table I-VI gives the frequencies and mode shapes. The variance with those given in Table I-V is attributed to the differences in the model mounting arrangement. This is caused by a significant difference in the wing root constraint.

The proprotor natural frequencies were determined during the first tests of the model during the Army Composite Aircraft Program. Since the blades were not modified for this test, the natural frequencies from that test are still applicable. Table I-VII lists the zero rpm blade natural frequencies. The target frequencies from Figures I-5 and I-6 are given for reference.

Model Natural Frequencies in Fold/Unfold Configuration

The measured natural frequencies and mode shapes with the blades removed and replaced by equivalent lead weights are given in Table I-VIII.

With the blades installed the natural frequencies are dependent upon the blade fold angle. Figure 40, in Section III, shows the variation in frequency with fold angle for a fold hinge stiffness of 2000 inch-pound/radian and an inboard feathering axis spring rate of 1000 inch-pound/radian. These spring rates were chosen to be tested since they result in the blade natural frequencies crossing wing natural frequencies at some point in the folding cycle. Consequently, they were expected to have the greatest effect on stability.

TABLE I-IV
MODEL INSTRUMENTATION

Parameter Measured	Location of Pickup	Transducer Description
Wing		
Beam Bending	15% and 50% Span	
Chord Bending	28% Span	350Ω, 4Arm Strain Gage
Torsion	15% Span	
Pylon		
Forward Vertical Acceleration	Top of Transmission Case	
Aft Vertical Acceleration	C_L Conversion Axis (Vertical)	Endevco Model #2264
Longitudinal Acceleration	C_L Mast Axis	Accelerometers Range 150g
Forward Lateral Acceleration	Side of Transmission Case	Sensitivity 1.97mv/g
Aft Lateral Acceleration	C_L Conversion Axis (Lateral)	
Rotor		
Blade Beam Bending	35%, 49%, and 65% Radius, Master Blade	350Ω, 4Arm Strain Gage
Blade Chord Bending		350Ω, 4Arm Strain Gage
Pitch Link (Cruciform)	Master Blade	125Ω, 4Arm Strain Gage
Blade Flapping	Master Blade	125Ω, 4Arm Strain Gage
Collective Pitch	---	1KΩ Potentiometer
Rotor RPM	---	Magnetic Pick-Up

All data recorded on direct readout oscillographs.

Collective pitch and rpm displayed at the model control console.

High speed movie cameras mounted in the rotor plane and upstream for photographic record.

TABLE I-V

MODEL PROPERTIES AND FREQUENCIES MEASURED
PRIOR TO WIND TUNNEL TEST

Property	Measured Value
Wing Tip Beamwise Spring Rate[1]	33.3 lb/in
Wing Tip Chordwise Spring Rate[1]	94.5 lb/in
Wing Tip Torsional Spring Rate[1]	9610 in-lb/rad
Pylon Weight[2]	8.8 lb
Pylon Center of Gravity (distance forward of conversion axis)[2]	7.1 inches
Pylon Inertia about Center of Gravity[3]	0.0646 slug-ft^2

[1] References to C_L proprotor shaft

[2] Includes all items outboard of wing tip, including proprotor

[3] Does not include blade flapping inertia

Natural Mode[4]	Frequency	Mode Shape[5]
Wing Beam	5.48 cps	$\theta_p/Z_{CA} = 0.0196$ rad/in
Wing Chord	9.17 cps	$\psi_p/X_{CA} = 0.054$ rad/in
Wing Torsion	18.6 cps	$\theta_p/Z_{CA} = -0.117$ rad/in
Pylon Yaw	40 cps	$\psi_p/X_{CA} = -0.30$ rad/in

[4] With blades removed and replaced by equivalent concentrated weights

[5] Mode shape is expressed in terms of pylon pitch per inch of vertical deflection at the conversion axis and pylon yaw per inch of chordwise deflection at the conversion axis

232

TABLE I-VI			
MODEL NATURAL FREQUENCIES AND MODE SHAPES IN WIND TUNNEL			
Natural Mode	Frequency	Damping	Mode Shape
Wing Beam	5.8 cps	0.005	$\theta_p/Z_{CA} = 0.0168$ rad/in
Wing Chord	9.0 cps	<0.01	$\psi_p/X_{CA} = 0.040$ rad/in
Wing Torsion	17.8 cps	<0.01	$\theta_p/Z_{CA} = -0.130$ rad/in
Pylon Yaw	36.5 cps	---	$\psi_p/X_{CA} = -0.16$ rad/in
Second Beam	74.0 cps	---	---

TABLE I-VII		
PROPROTOR NATURAL FREQUENCIES		
$\theta_C = 0$ RPM		
	Frequency (cps)	
Mode	Measured	Target
First Collective	14.2	15.2
Second Collective	43.0	46.8
First Cyclic	13.5	14.6
Second Cyclic	39.2	42.7
Third Cyclic	88.6	99.4

TABLE I-VIII		
MEASURED NATURAL FREQUENCIES OF FOLD/UNFOLD CONFIGURATION		
Mode	Frequency	Mode Shape
Wing Beam	5.7 cps	$\theta_p/Z_{CA} = 0.0625$
Wing Chord	8.8 cps	$\psi_p/X_{CA} = 0.0785$
Wing Torsion	18.0 cps	$\theta_p/Z_{CA} = 0.0358$
Pylon Yaw	36.5 cps	---

Model Configurations

For the rotating tests a "basic" configuration was defined as follows:

- Wing aerodynamic panels installed with weights simulating 15 percent fuel

- Pylon fairing and spinner removed

- Pylon rigidly attached to wing tip in pitch and yaw senses

- Pitch-flap coupling of 0.414 ($\delta_3 = -22\frac{1}{2}$ degrees)

- Isotropic hub restraint of 338 inch-pound/radian, zero degrees angle-of-attack

Other configurations tested involved the following changes to the basic configuration:

- Flapping locked out

- Variation in hub restraint from 0 to 1200 inch-pound/radian

- Pitch-flap coupling varied from $\delta_3 = 0$ degrees to $\delta_3 = -39$ degrees

For the blade folding tests the model was tested with an effectively rigid pitch change axis element and an element with a spring rate of 1200 inch-pound/radian. The model was also tested with a pylon fairing with faired blade fold slots, to study buffet at large fold angles.

APPENDIX II

D270A DESCRIPTIVE DATA

The D270A is a folding-proprotor V/STOL configuration with a design gross weight of 66,00 pounds. A three view is shown in Drawing D270A-900-110. Three modes of operation are possible: helicopter, proprotor, and airplane. Four Lycoming LTC4V-1 convertible fan/shaft provide power in rotary wing and fixed wing modes. Two fifty-foot diameter proprotors provide a design disc loading of 16.8 psf which is optimum from a productivity standpoint. The design wing loading is 85 psf, near optimum for a cruise condition of 400 knots at 30,000 feet.

The primary dynamic system, consisting of the proprotors, wing, and engines and transmissions, has been designed to be suitable for fuselages up to 13-foot diameter. The primary mission for the D270A is a rescue and a 10-foot diameter fuselage has been selected, primarily to reduce drag.

Descriptive Data and Dimensions

An inboard profile of the D270A is shown in Drawing D270-470-110. General descriptive data are summarized in Table II-I.

Performance

A performance summary for the D270A is given in Table I-II.

Structural Description

Proprotor and Pylon - The rotors of the D270A are mounted at the wing tips on tiltable pods. In addition to the rotor, each pod contains a rotor planetary transmission, rotating and nonrotating rotor controls, a bevel gearbox, the pod tilt actuator, spinner, cowling and accessories. The spinner and stationary cowling are recessed to contain the trailing edges of the rotor blades when the rotor is folded. The Inboard Profile, D270A-470-110, shows the rotor installation at each wing tip. The orientation of the rotor system on the pod is shown in Drawing D270A-410-002.

The proprotor blades are all metal, bonded honeycomb structure with constant chord, linear twist, and a nonlinear beam thickness taper. Drawing D270A-410-001 shows the blade arrangement. In the primary structure, 17-7PH stainless steel is used. The interior of the blade is filled with an aluminum honeycomb core, including the spar. The honeycomb in the spar prevents buckling, permitting the use of thin gage material in this area. An aluminum housing for the pitch change bearings is

TABLE II-I

D270A CHARACTERISTIC DATA

Item	Units	Data
Proprotor		
Blade Airfoil Sections		
Root (CL Mast to R/R)	---	64X18
Tip	---	64X08
Rotor Tip Rotational Mach No. at 95°F		
Helicopter Mode		
At 100 percent rpm	---	0.71
At 90 percent rpm	---	0.64
Conversion Mode		
At 95 percent rpm	---	0.675
At 85 percent rpm	---	0.603
Design C_T/σ	---	0.10
Design Disc Loading		
At Design Gross Weight of 6600 lb	lb/ft^2	16.8
Design Blade Twist (Linear)	deg	25
Solidity	---	0.1275
Number of Blades per Proprotor	---	3
Diameter	ft	50
Disc Area per Proprotor	sq ft	1963.5
Blade Chord	in	40.0
Blade Area (3 Blades)	sq ft	250
Proprotor Flapping Clearance		
(Helicopter)	deg	9.5
Hub Spring Rate (Helicopter)	ft-lb/deg	1500
Folding Hinge Radius	in	26.75
Hub Precone Angle	deg	2
Fuselage-Proprotor Tip Clearance		
(Airplane)	in	32
Tip Speeds		
100 percent rpm - Helicopter	ft/sec	822
95 percent rpm - Helicopter	ft/sec	780
95 percent rpm - Conversion	ft/sec	740
85 percent rpm - Conversion	ft/sec	698
Drive-System Ratios		
Ratio of Engine to Proprotor rpm	---	31.8:1
Ratio of Engine to Interconnect Shaft rpm	---	1.34:1

TABLE II-I - Continued		
Item	Units	Data
Engine		
Number of Engines	---	4
Designation (Convertible Fan/Shaft Version)	---	LTC4V-1
Fan Pressure Ratic	---	1.4:1
Fan Bypass Ratio	---	8.0:1
Military Rating (30 Minutes)		
Horsepower (SLS)	shp	4420
RPM (Output Shaft)	rpm	10000
Transient Torque	ft-lb	2960
Thrust (30000 ft, Mach 0.7)	lb	1840
Airframe		
General		
Overall Length	ft	81.25
Overall Width (Proprotors Turning)	ft	114.25
Overall Height	ft	30.66
Distance Between Proprotor C_L	ft	64.25
Static Ground Line Reference		
Water Line	in	40
Height of Conversion Pivot		
Above Reference Water Line	ft	13.33
Distance from Conversion Pivot to		
Horizontal Tail 1/4 MAC	ft	39.88
Vertical Tail 1/4 MAC	ft	35.66
Distance from Wing 1/4 MAC to		
Horizontal Tail 1/4 MAC	ft	40.88
Vertical Tail 1/4 MAC	ft	36.66
Fuselage		
Fuselage Station (0.0)		
Reference Ahead of Nose	in	130.0
Length (To Tip of Vertical Fin)	ft	81.25
Maximum Breadth	ft	10.00
Maximum Depth	ft	10.00
Empennage		
Vertical Tail		
Total Area	ft^2	205

TABLE II-I - Continued		
Item	Units	Data
Aspect Ratio	---	1.6
Mean Aerodynamic Chord (MAC)	in	139.18
1/4 MAC Fuselage Station (WL 291)	in	954
Leading Edge Sweep	deg	35
Tip Chord (WL 408)	in	102.5
Root Chord (WL 192)	in	170.0
Tip Airfoil Section	---	64008
Root Airfoil Section	---	64015
Rudder Area	ft^2	43.9
Rudder Chord/Total Chord	percent	25
Horizontal Tail		
Total Area	ft^2	250
Aspect Ratio	---	4.5
Incidence (Trimmable Range)	deg	20
Mean Aerodynamic Chord (BL 93.5)	in	92
1/4 MAC Fuselage Station	in	1004.5
Leading Edge Sweep	deg	17
Tip Chord (BL 200)	in	75
Root Chord (BL 0.0)	in	105
Tip Airfoil Section	---	64008
Root Airfoil Section	---	64012
Elevator Area	sq ft	51.25
Elevator Chord/Total Chord	percent	26.5
Wing		
Geometric (Between Rotor C_L)		
Span	ft	64.25
Area	sq ft	706
Aspect Ratio	---	5.85
Root Chord (BL 0.0)	in	157
Tip Chord (BL 385.0)	in	107
Mean Aerodynamic Chord (BL 188.6)	in	133.4
1/4 MAC Fuselage Station	---	514
Root Airfoil (BL 0.0)	---	64X18
Tip Airfoil (BL 385.0)	---	64X15
Leading Edge Sweep	deg	6
Dihedral	deg	2
Root Incidence	deg	3.7

TABLE II-I - Continued		
Item	Units	Data
Flaperon		
Area/Side	sq ft	23.3
Span	in	103
Chord	in	32.6
Flap		
Area/Side	sq ft	34.94
Span	in	148.0
Chord	in	34.0
Pylon		
Conversion Axis/Rotor Shaft Axis Intersection		
Fuselage Station	---	526.0
Waterline	---	200.0
Buttline	---	385.0
Conversion Axis Wing MAC Location	percent	35.75
Conversion Axis Sweep (Forward)	deg	6
Conversion Axis to Rotor Flap Axis	in	122.0
Detail Strength Requirement		
Design Gross Weight	lb	66000
Alternate Gross Weight	lb	82500
Positive Limit Load Factors at Design Gross Weight		
Helicopter	g	2.5
Conversion	g	3.0
Airplane	g	3.0
Negative Limit Load Factors at Design Gross Weight		
Helicopter	g	-0.5
Conversion	g	-1.0
Airplane	g	-1.0
Design Sinking Speed at Design Gross Weight	ft/sec	12

TABLE II-II

D270A PERFORMANCE SUMMARY

Design Gross Weight	66,000 lb
Hover Ceilings at Design Gross Weight	
Standard Day, OGE	13,900 ft
Standard Day, IGE	14,800 ft
95°F Day, OGE	7,950 ft
95°F Day, IGE	8,900 ft
Rate of Climb, Design Gross Weight, SLS	
Helicopter Mode	4,150 ft/min at 70 kt
Proprotor Mode	5,050 ft/min at 135 kt
Airplane Mode	4,200 ft/min at 240 kt
Speed at Design Gross Weight	
Helicopter Mode, Maximum	140 kt
Proprotor Mode, Maximum	324 kt
Airplane Mode, Maximum	452 kt
Airplane Mode, Maximum Cruise	415 kt per 3000 ft
Airplane Mode, Best Range	340 kt per 3000 ft
Alternate Gross Weight	82,400 lb
Maximum Gross Weight (VTOL, IGE, SLS)	93,500 lb
Ferry Range (30 minute reserve)	2,600 nm

bonded into the blade at the root end. The integral housing eliminates the weight and softness of a bolted joint in this area and provides a clean aerodynamic configuration.

Rotor blade pitch change occurs about a spindle located outboard of the folding hinge. Oil lubricated needle bearings carry bending loads from the blade into the spindle.

The proprotor hub is designed for a three-bladed, hub-restrained, gimbal-mounted semirigid rotor. Centrifugal force is transmitted from the blade to the foldable hub spindle through a wire tension-torsion strap. The strap is pinned to the blade, and has a fitting with an integral shoulder bearing against a counter bore in the spindle for attachment to the hub.

The principal structural element of the hub consists of a titanium ring with lugs which attach the folding pitch change spindles. The yoke is attached to the mast with a gimbal joint. Oil lubricated needle bearings accommodate rotor flapping; as an alternate, laminated elastomeric bearings can be used in this area to eliminate the lubrication.

In the helicopter and proprotor modes of flight, hub restraint is provided by a nonrotating elastomeric spring mounted below the rotor. This is shown in Drawing D270A-410-002. A ball bearing transmits rotor flapping to the spring. The hub spring rate is 3840 foot-pound/degree. Before rotor rpm is decreased, hydraulic cylinders below the hub spring lock out the flapping freedom.

A blade folding hinge is provided between the yoke and the blade. Drawing D270A-410-003 shows the configuration. Folding is accomplished inboard of the pitch change axis to permit tracking adjustment to be made to the blade without affecting the alignment of the blade when folded, and so that aerodynamic and dynamic moments generated during folding are isolated from the control system. Also, folding inboard of the feathering axis facilitates driving of the folding mechanism. The hinge consists of a multiple clevis attachment below the feathering axis, actuated by an overcenter toggle linkage above the feathering axis. A planetary power hinge drives the toggle linkage. Dual hydraulic motors, attached to the rotor hub, power the system. A scissor arrangement between the pitch horn and the blade transmits control motion across the folding hinge. The pitch horn is split for assembly purposes and is supported by split angular contact bearings around the yoke spindle.

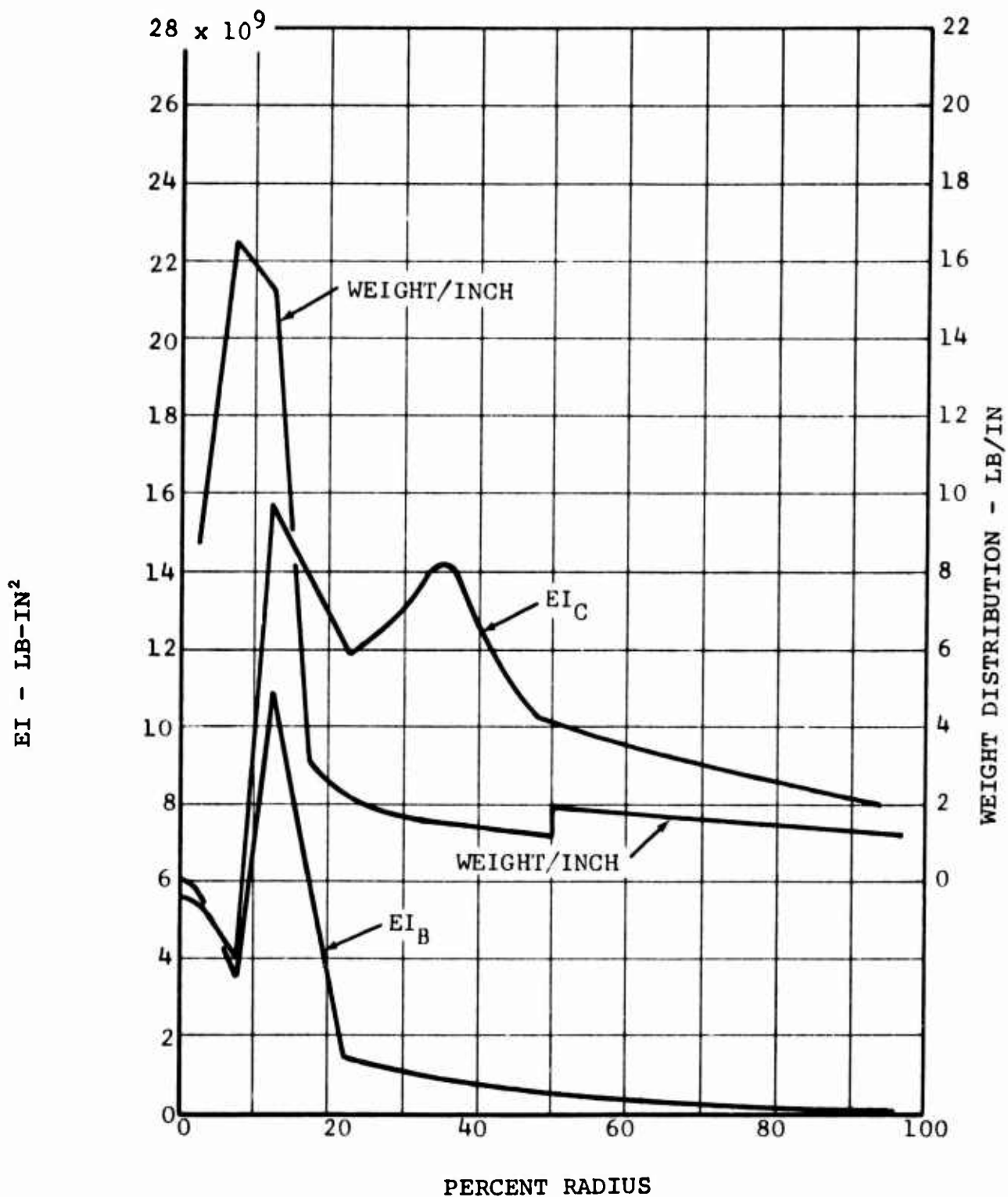Figure II-1 shows the proprotor stiffness and mass distributions.

Figure II-1. D270A Proprotor Stiffness and Mass Distributions.

242

The pylon conversion mechanism consists of a screw jack which attaches the transmission case to the forward part of the wing. By retracting this screw, the pod assembly may be converted from the helicopter to the proprotor mode. Interconnect shafting between the rotors on the conversion actuator assures that the right and left pylons convert simultaneously. The interconnect shaft also drives the range shift actuator in the fuselage which rephases the control system during conversion.

Wing - The wing is a two-spar, single-cell structure using aluminum honeycomb sandwich in the upper and lower surfaces and in the rear spar. The wing sections and structures are indicated in Drawing D270A-470-110. The ailerons and flaps are rib-stiffened aluminum sheet. Concentrated loads from the engine installations and tip-mounted transmission-rotor assemblies are carried entirely by the torque box. All other contour panels and ribs carry airloads only.

The main structural box of the wing consists of a constant section 64X17 airfoil. The front spar is located at 5 percent chord, and the rear spar at 50 percent chord.

Forward of the front spar, the wing contains a shaft extending from wing tip to wing tip to interconnect the pod tilt actuators. Access to the couplings for maintenance of this shafting is through removable panels on the lower surface of the wing. The trailing edge of the wing is made up almost entirely of flap and aileron assemblies which are supported by hinge fittings attached to the torque box, rotor drive interconnect shafting and supports, engine-to-interconnect shaft gearboxes, rotor cyclic and collective control tubing, wing flap and aileron controls and actuators, and hydraulic, electrical, and fuel lines.

The wing strength requirements were dictated by a 2.5g takeoff in helicopter mode. (This is equivalent to 5.0g in airplane mode.) This applies to beam bending and torsional strength. The chordwise strength is in excess of the requirement. The wing stiffness was obtained by using the required bending material so as to achieve a high torsional stiffness. Figures II-2 and II-3 show the wing stiffness and weight distributions.

Empennage - The empennage is of conventional construction. The horizontal tail is located approximately at the midspan of the vertical tail, and the entire stabilizer area is controllable.

The fin is a two-spar structure with all the beam shear and bending carried by the spars. The interspar coverings, together with the spar webs, provide the torsional shear-carrying structure. The fin spars are continuous from the tip
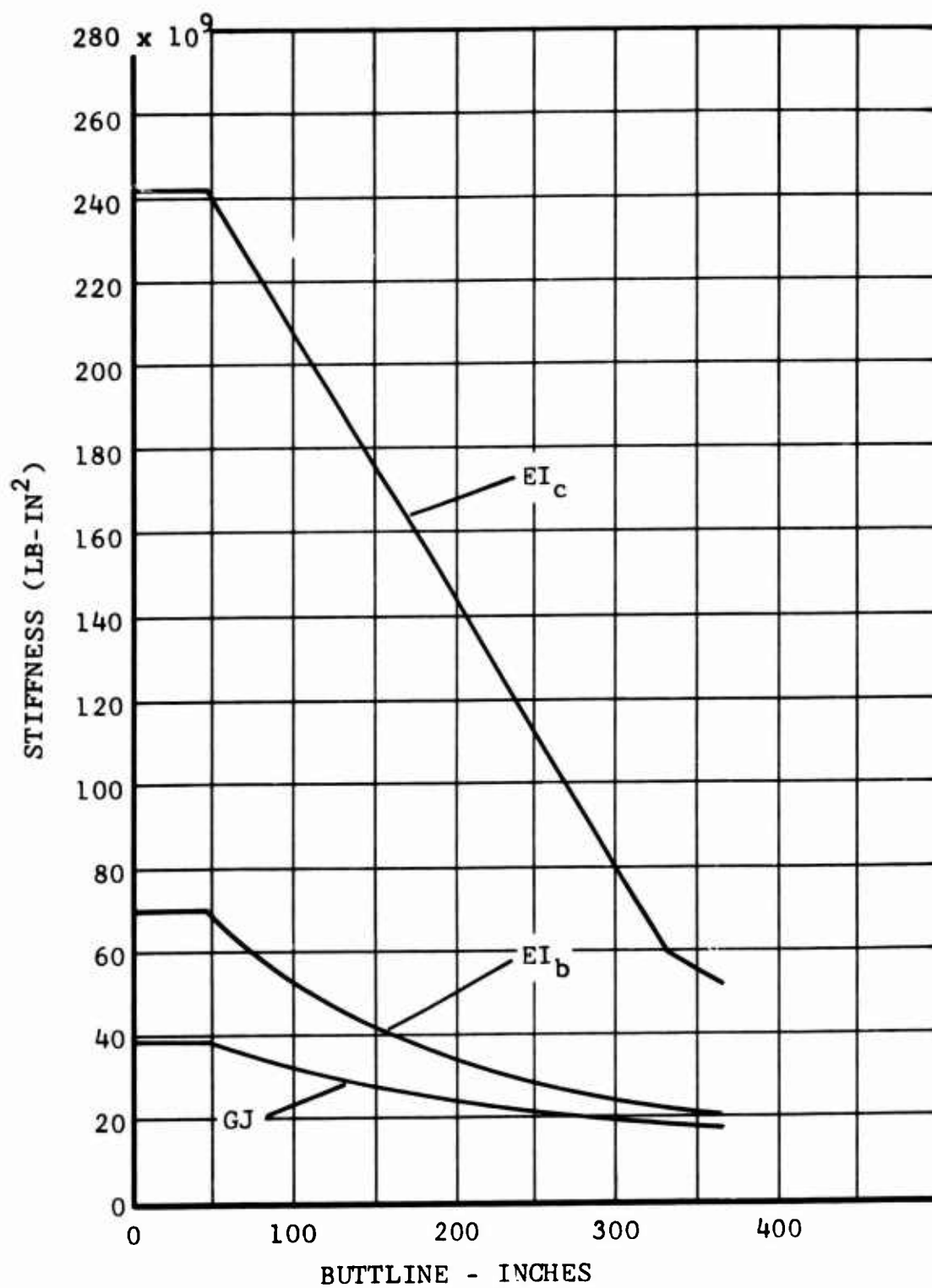
243

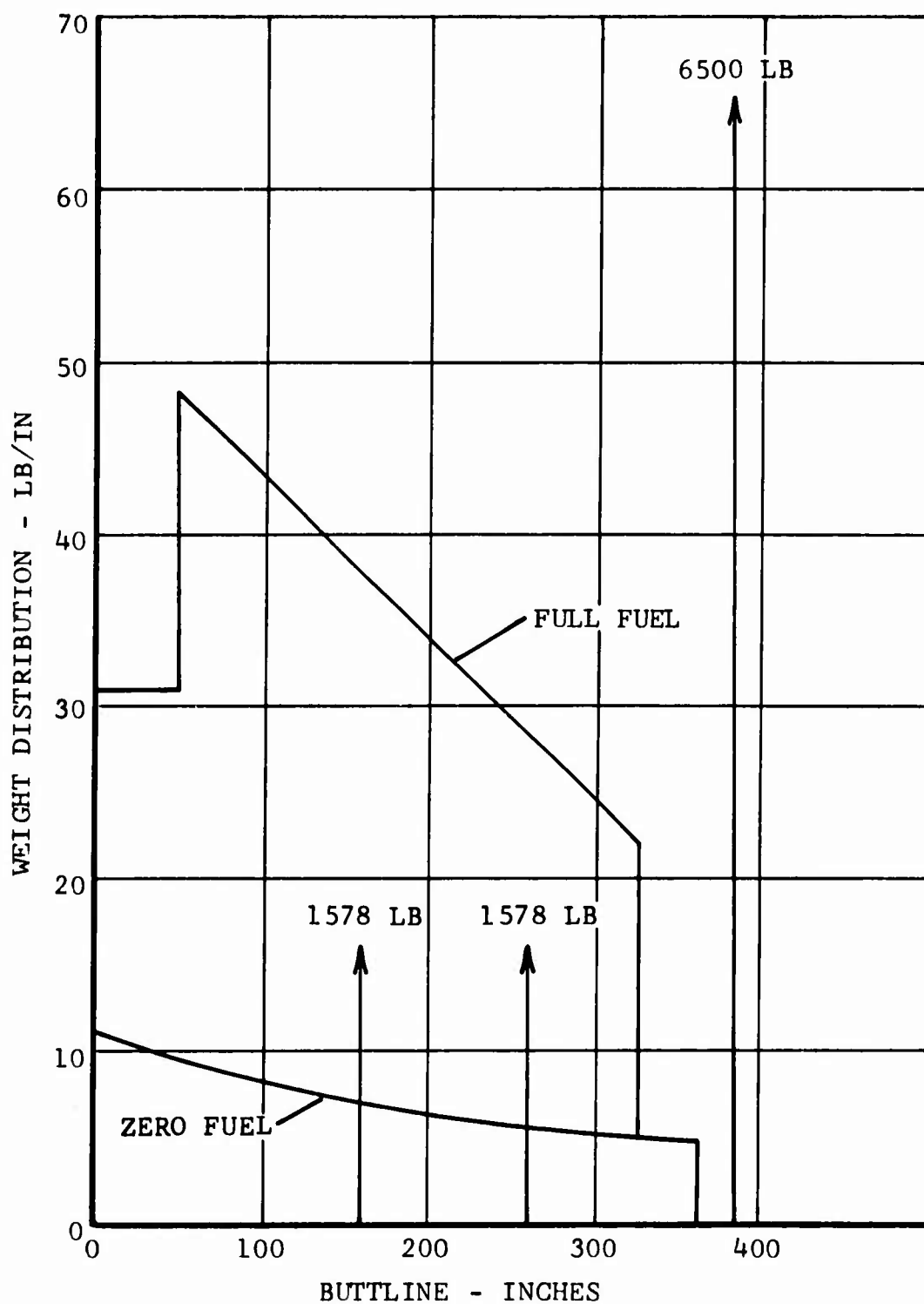Figure II-2. D270 Wing Stiffness Distribution.

244

Figure II-3.   D270A Wing Mass Distribution.

to their attachment to fuselage bulkheads. The entire fin structure is attached to the fuselage by fittings joining the spars and the fuselage bulkheads. The horizontal tail single cell structural box is a typical skin-stringer construction utilizing 7075-T6 skins, stringers and spar caps. Ribs are located at the elevator hinge points and at the horizontal tail-vertical fin intersection.

Both the horizontal and vertical tail sizes are determined by aircraft dynamic stability requirements. The structural requirements are expected to be influenced by aeroelastic considerations in high speed mode. However the aeroelastic aspects have not been considered to date. The empennage aeroelastic characteristics are not expected to impact on the feather/fold sequence.

Fuselage

Description - The fuselage is a conventional structure, semi-monocoque configuration, 72 feet in length, with a circular cross section 10 feet in diameter. The structure design is based on 7075-T6 aluminum alloy materials consisting of formed skins, rolled frames, extruded stringers, and machined forgings. Inboard Profile Drawing D270A-470-110, indicates fuselage layout.

The frames are of three basic types. Splice frames are used to accommodate production and compartment breaks. Forged bulkheads are used on each side of the main landing gear, and one provides a tie between the aft wing spars. Intermediate rolled zee-shaped frames are installed between the main frames on 18-inch centers. The extruded zee-shaped stringers are spliced through the major bulkheads using forged splice fittings which are the same for all locations. The stringers are riveted to the skin and intermediate frames every 9 degrees around the fuselage.

The fuselage strength requirements are determined by in flight gust loads and landing loads. A preliminary estimate of the fuselage stiffness and mass distribution is given in Figure II-4.
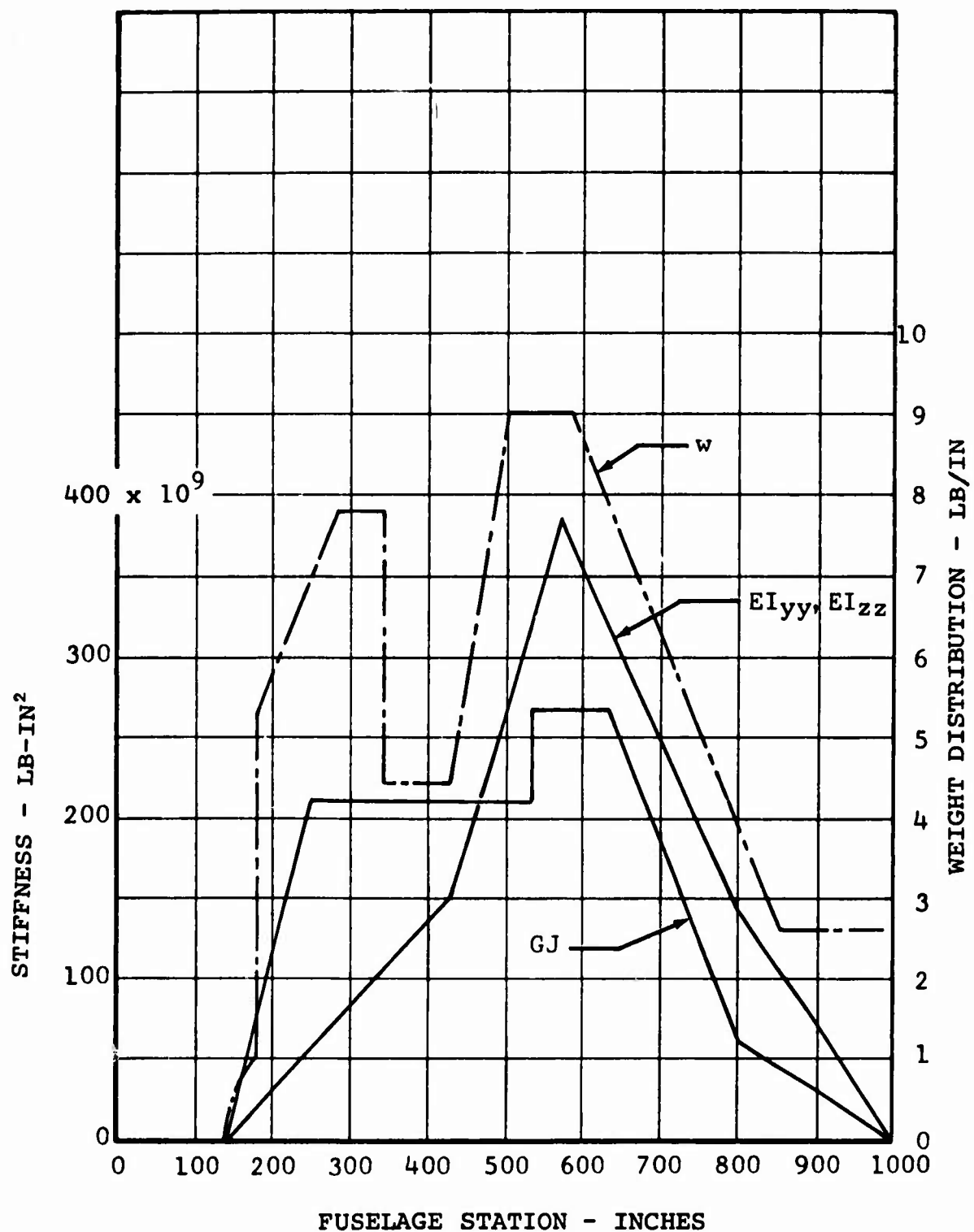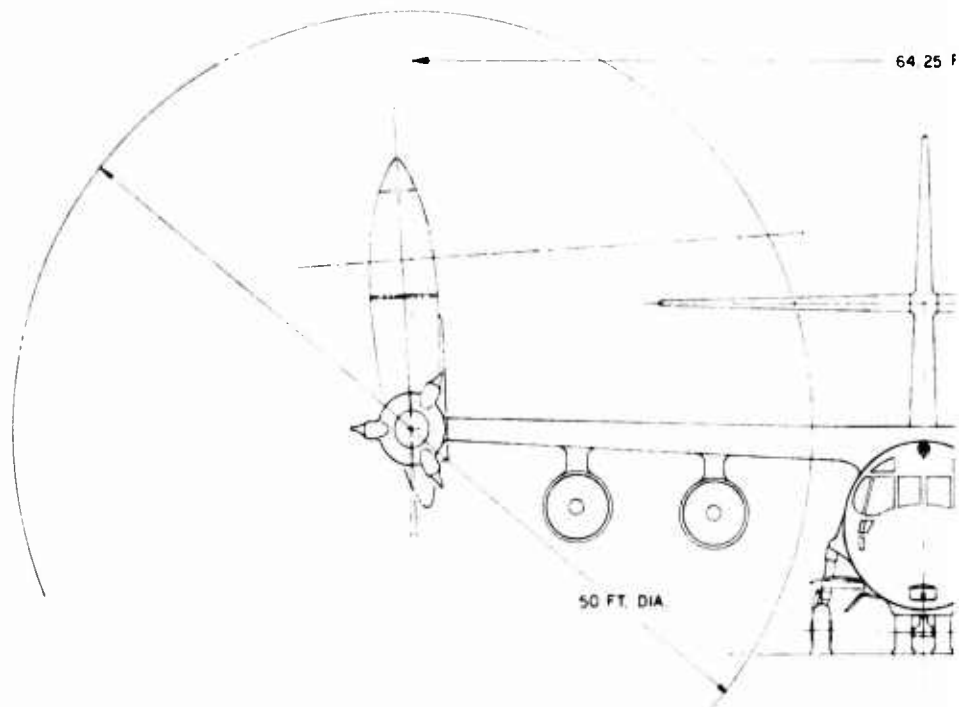
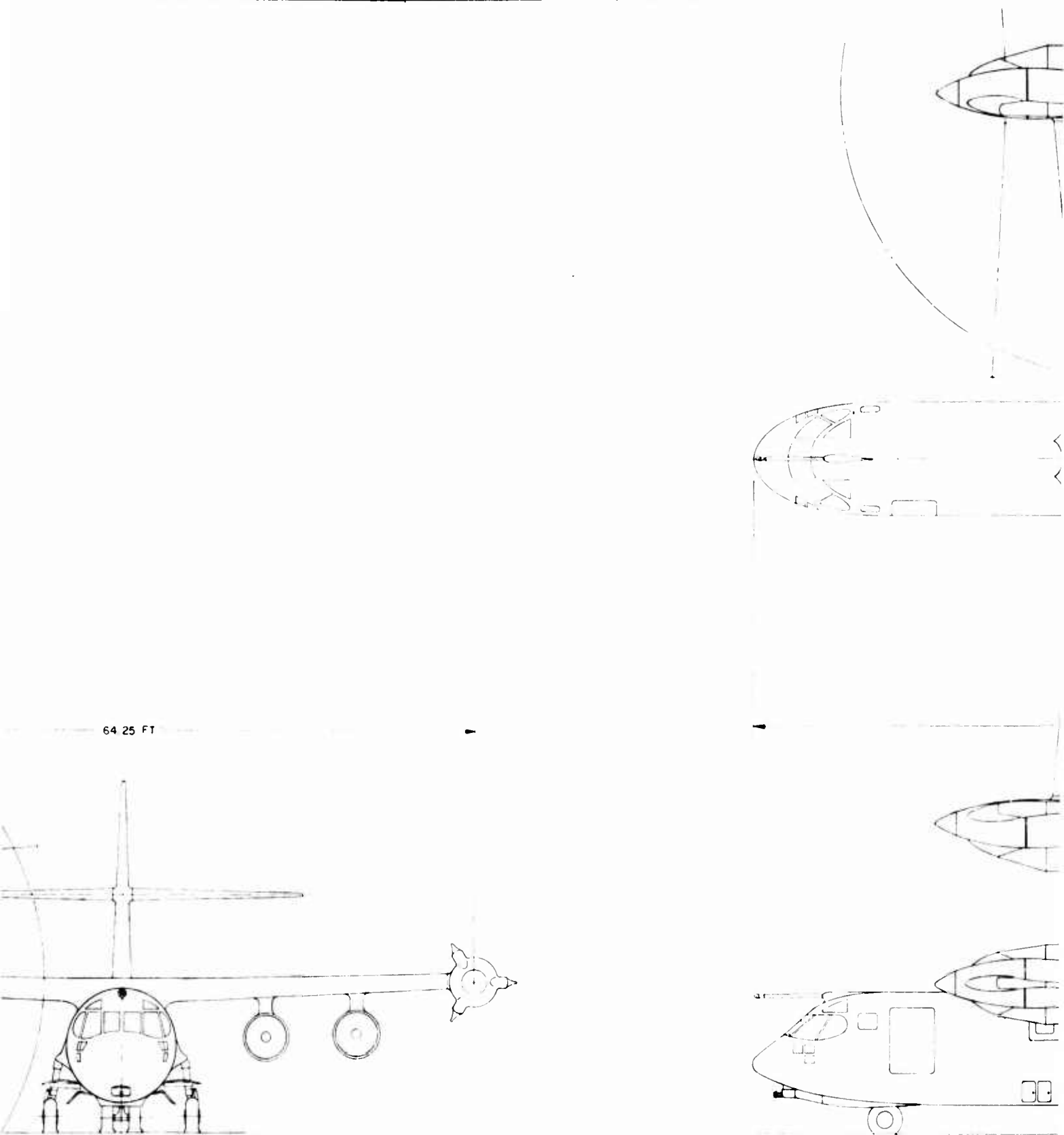Figure II-4.   D270A Fuselage Stiffness
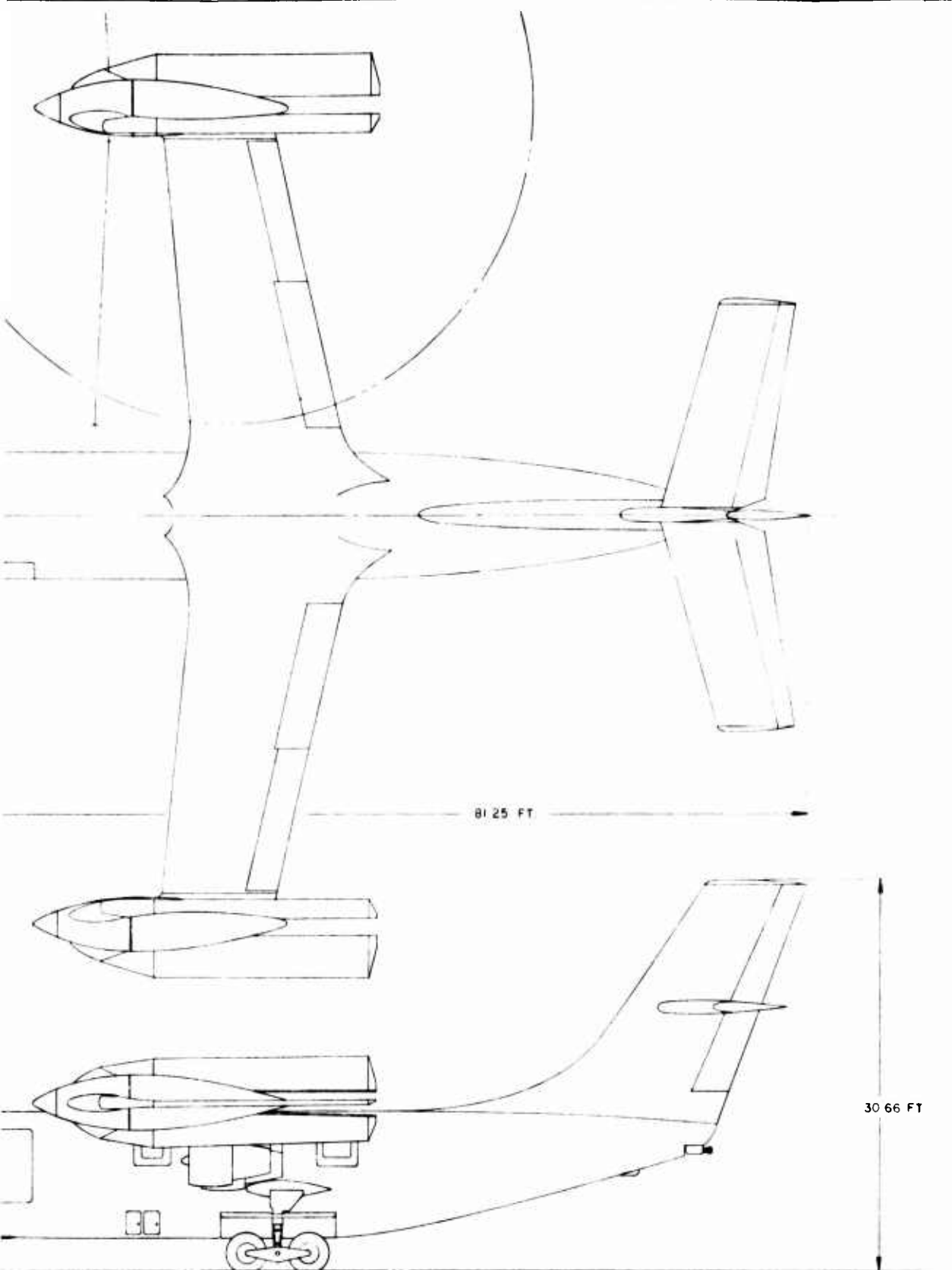Distribution.

247

64 25 F

50 FT. DIA.

64 25 FT

Figure II-5. Three-View of D270A.

...ew of D270A.

81 25 FT

30 66 FT

3

CHARACTERISTICS

WEIGHTS
    DESIGN GROSS WEIGHT   66,000   LB
    WEIGHT EMPTY   43,505   LB
    OIL AND TRAPPED FUEL   624   LB
    CREW   1,200   LB
    STOL GROSS WEIGHT   82,500   LB

POWER PLANT
    MANUFACTURER AND MODEL   LYCOMING   LTC4V-I DERIVATIVE
    MILITARY RATED POWER   4 X 4,420 (SL STD)   17,680   HP
    MILITARY RATED THRUST   4 X 1,854 (400 KTS 30,000 FEET)   7,416   LB
    TRANSMISSION POWER LIMIT   2 [2 X 3,980]   15,920   HP

ROTOR
    DIAMETER   50.0   FT
    NUMBER OF BLADES / ROTOR   3
    DISC AREA / ROTOR   1,963.5   SQ-FT
    BLADE AREA / ROTOR   250.0   SQ-FT
    DISC LOADING   DESIGN GROSS WEIGHT   16.8   LB/SQ-FT
    BLADE AIRFOIL   THEORETICAL ROOT $\frac{t}{c}$ TO $\frac{R}{4}$ 64 X 18
                             TIP   64 X 08
    BLADE CHORD   CONSTANT   40.0   IN
    SOLIDITY   0.1275
    BLADE TWIST   + TO TIP LINEAR   25.0   DEGREES
    TIP SPEED   HELICOPTER MODE (283-314 RPM)   740 - 822   FT/SEC
                             CONVERSION MODE (267-298 RPM)   698 - 780   FT/SEC

WING
    SPAN   64.25   FT
    AREA   706.0   SQ-FT
    WING LOADING   DESIGN GROSS WEIGHT   93.5   LB/SQ-FT
    ASPECT RATIO   5.85
    MEAN AERODYNAMIC CHORD   BL (188.6)   133.4   IN.
    AIRFOIL   BL (0.0)   64 X 18
                             BL (385.5)   64 X 15
    FLAP AREA / SIDE   AFT OF HINGE   34.94   SQ-FT
    FLAPERON AREA / SIDE   AFT OF HINGE   23.3   SQ-FT

EMPENNAGE
    HORIZONTAL TAIL AREA   250.0   SQ-FT
    ASPECT RATIO   4.5
    AIRFOIL   BL (0.0)   NACA 64-012
                             BL (200.0)   NACA 64-008
    ELEVATOR AREA TOTAL   AFT OF HINGE   51.25   SQ-FT
    VERTICAL TAIL AREA   205.0   SQ-FT
    ASPECT RATIO   1.6
    AIRFOIL   WL (192.0) ROOT   NACA 64-015
                             WL (408.0) TIP   NACA 64-008
    RUDDER AREA   AFT OF HINGE   43.9   SQ-FT

30 66 FT

Figure II-5.

DESIGN LAYOUT

TITLE   3 VIEW —
          D270A

DESIGNED C.M.Cox   DATE 10-14-69   SCALE 1/40

APPROVED   D270A-900-110

4

CONVERSION ACTUATOR
INTERCONNECT SHAFT
SUPPORT

FRONT SPAR
5 % CHORD

3°42' INCIDENCE

W L REF

REMOVABLE PANEL

TY

SECTION A-A

2° DI

WL 200

50 FT.

ALUMINUM HONEYCOMB
SKIN PANELS

INTERMEDIATE RIB

ROTOR DRIVE
INTERCONNECT SHAFT
SUPPORT

FRONT SPAR
5% CHORD

REAR SPAR
50% CHORD

FLAP HINGE SUPPORT

FLAP

PILOT'S SEAT

RADAR

CO-PILOT'S SEAT

CREW COMPARTMENT

RESCUE HO

RESC
24

¢ WING CHORD
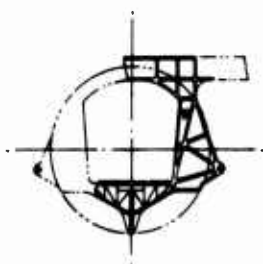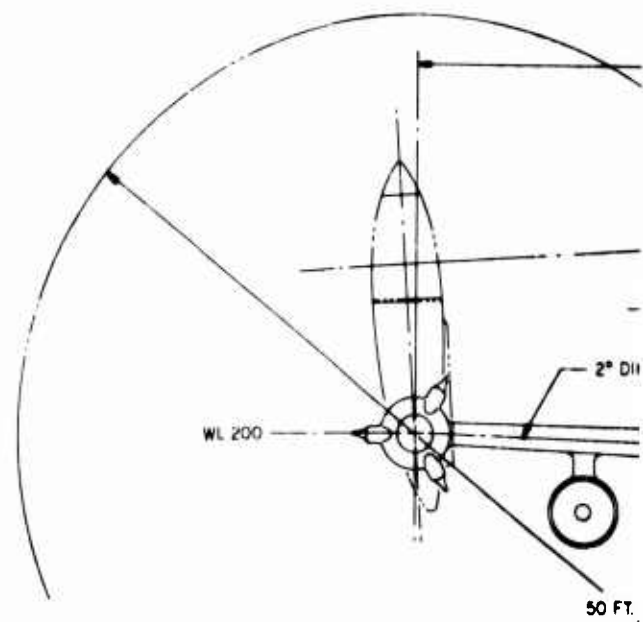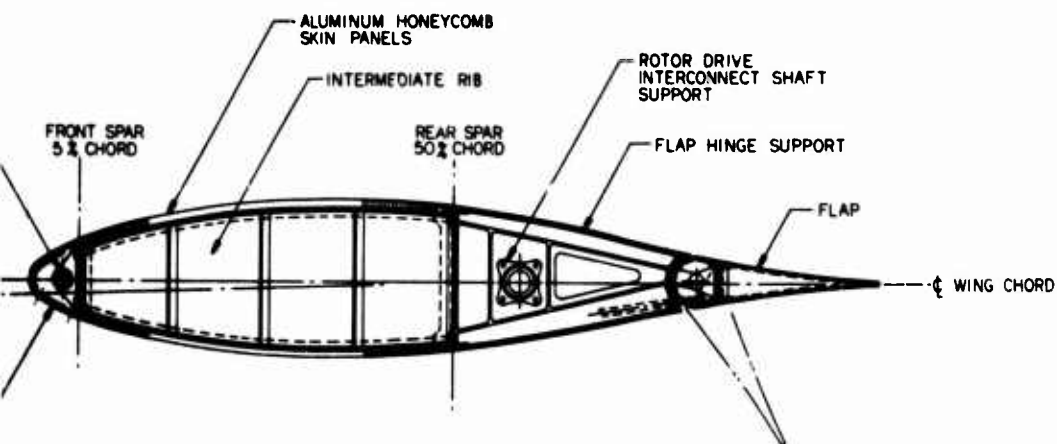
TYPICAL WING SECTION
SCALE : 1/10

64.25 FT

NON-RETI
REFUELIN

2° DIHEDRAL

50 FT. DIA.

12.50-16 TYPE III
CBR, -2.4

4 ADVANCED TECHNOLOGY FAN
SHAFT COMPOUND ENGINES
46 IN. DIA. FANS
(BASED ON LTC 4V-1
GENERATORS)

WL 40 (REF)

15°

90°

STA
130
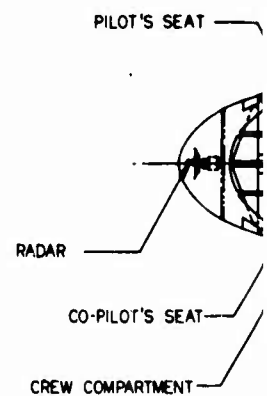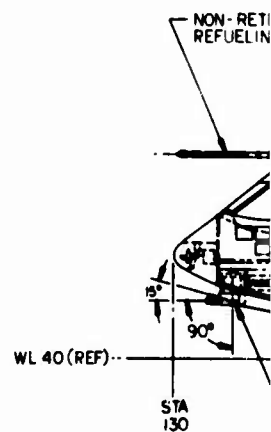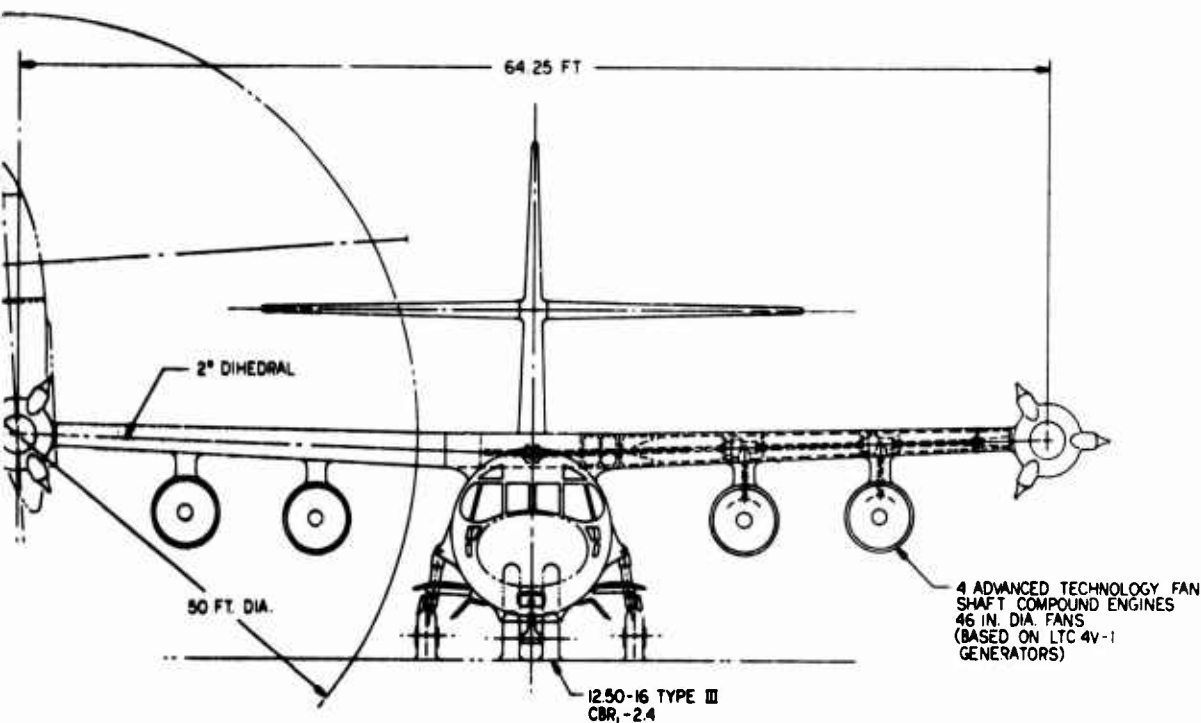
Figure II-6.   D270A Inboard Profile.

Figure II

WING AND CENTER SECTION
FUEL CELL CAPACITY
20,500 LBS
(NO FUEL IN FUSELAGE)

BOTTOM HATCH
48 X 78 INCHES

ELEVATOR

BL 93.5
MAC 92.0

17°

PRESSURE BULKHEAD

PRESSURE DOOR

WINCH LINE AERIAL
RECOVERY SYSTEM

BL 188.6
MAC =133.4

BL 200

IDENTICAL BEVEL
GEAR BOXES

MAC/4
STA 1004.5

STA 954
MAC/4

RUDDER HINGE

STABILIZER ACTUATOR

WL 408

36°

WL 291
MAC 139.18

AUXILIARY POWER
UNIT

WL 192

15°

STA
1105

90°

5.56MM MINIGUN
TURRET

STA
851

STA
895

STA
979

STA
739

RETRIEVAL HOOKS

STA
659

15.00-16 TYPE II
CBR, -2.4

Figure II-6

DESIGN
LAYOUT

INBOARD PROFILE —
D270A

C. LAYMAN

1/40

D270A-470-110

SING[...]

SWASHPLATE

HUB RESTRAINT SPRING

SPINNER SUPPORT DRIVER

COLLECTIVE HEAD

HYDRAULIC SLIP RING

C

D

ROTATING SEAL
(3 PLACES)

HYDRAULIC MOTOR
(FOLDING DRIVE)

SPINNER BULKHEAD

C

D

SWASHPLATE DRIVE
LINKAGE

PILLOW BLOCK
2 PLACES

28.00

SECONDARY PISTON
3 PLACES

PRIMARY PISTON
3 PLACES

YOKE

BEARING HOUSING
2 PLACES

TRUNNION

SECTION D-D
FLAPPING LOCK
HYDRAULICALLY ACTUATED
3000 PSI

CROSS

OIL RESERVOIR

SJ 2720 BEARING
4 PLACES

THRUST BEARING
4 PLACES

SECTION C-C
GIMBAL ASSY

Figure II-7. D2[...]

ANTI-ROTATION SPLINE

SINGLE TILT AXIS

HYDRAULIC PASSAGES

COLLECTIVE BOOST CYLINDER

HYDRAULIC LINE

NUT

INPUT GEAR

13.4
COLLECTIVE
STROKE

TRANSMISSION

SERVO CONTROL VALVE

C CONVERSION AXIS

SCREW SHAFT

SECTION A-A

3400

13.4
COLLECTIVE
STROKE

LOW COLLECTIVE BLADE
ANGLE AT 3/4 R.

PITCH HORN

7.   D270A Pylon Assembly.

VIEW **B-B**

Figure II-7

NUT

INPUT GEAR

SCREW SHAFT

ROTOR

13.4
COLLECTIVE
STROKE

±14° CYCLIC
RANGE

90°
COLLECTIVE
RANGE

LOW COLLECTIVE BLADE
ANGLE AT 3/4 R.

PITCH HORN

PITCH LINK

30°

BLADE AT 3/4 R. FULLY
FEATHERED

DESIGN
LAYOUT

PYLON ASSY, D270A
SHEET 2

S. VAUGHN

D270A-410-C02

250

POWER HINGE
WORM GEAR

D270A-410-001
BLADE ASS'Y

ADJUSTABLE BLADE STOP

℄ FOLD HINGE

STA
33.25

STA
26.75

A

℄ FOLD
HINGE

ROOT FITTING
PITCH HORN ATTACHMENT
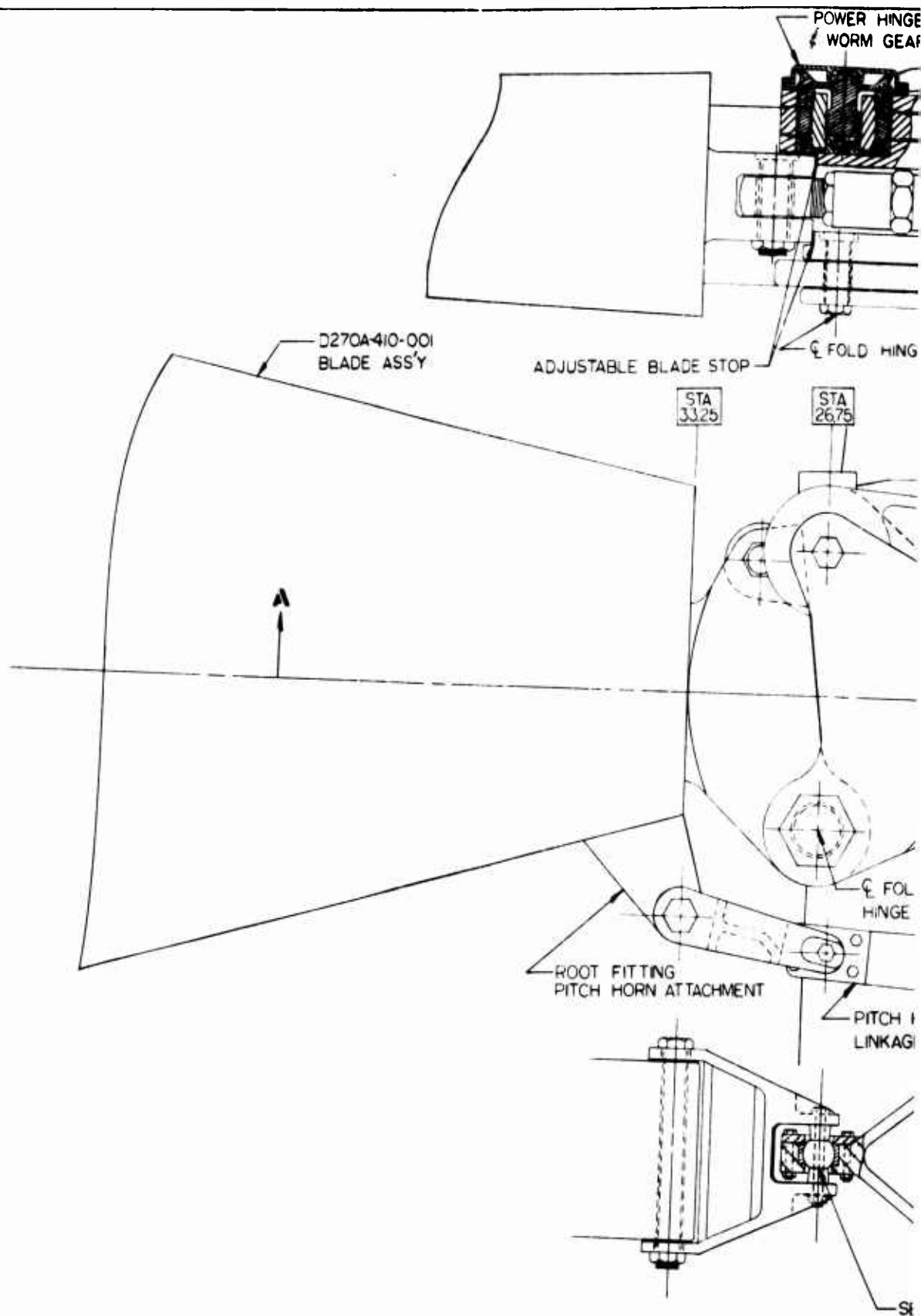
PITCH
LINKAGE

Figure II-8. D270A Folding Mechanism.

POWER HINGE
WORM GEAR

FOLDING TOGGLE LINK

FOLDING DRIVE ARM

BLADE STOP

₵ FOLD HINGE AXIS

STA 33.25

STA 26.75

D270A-410-002

POWER HINGE DRIVESHAFT

ADJUSTABLE TOGGLE STOP

₵ ROTOR SHAFT
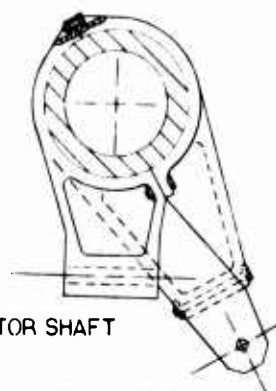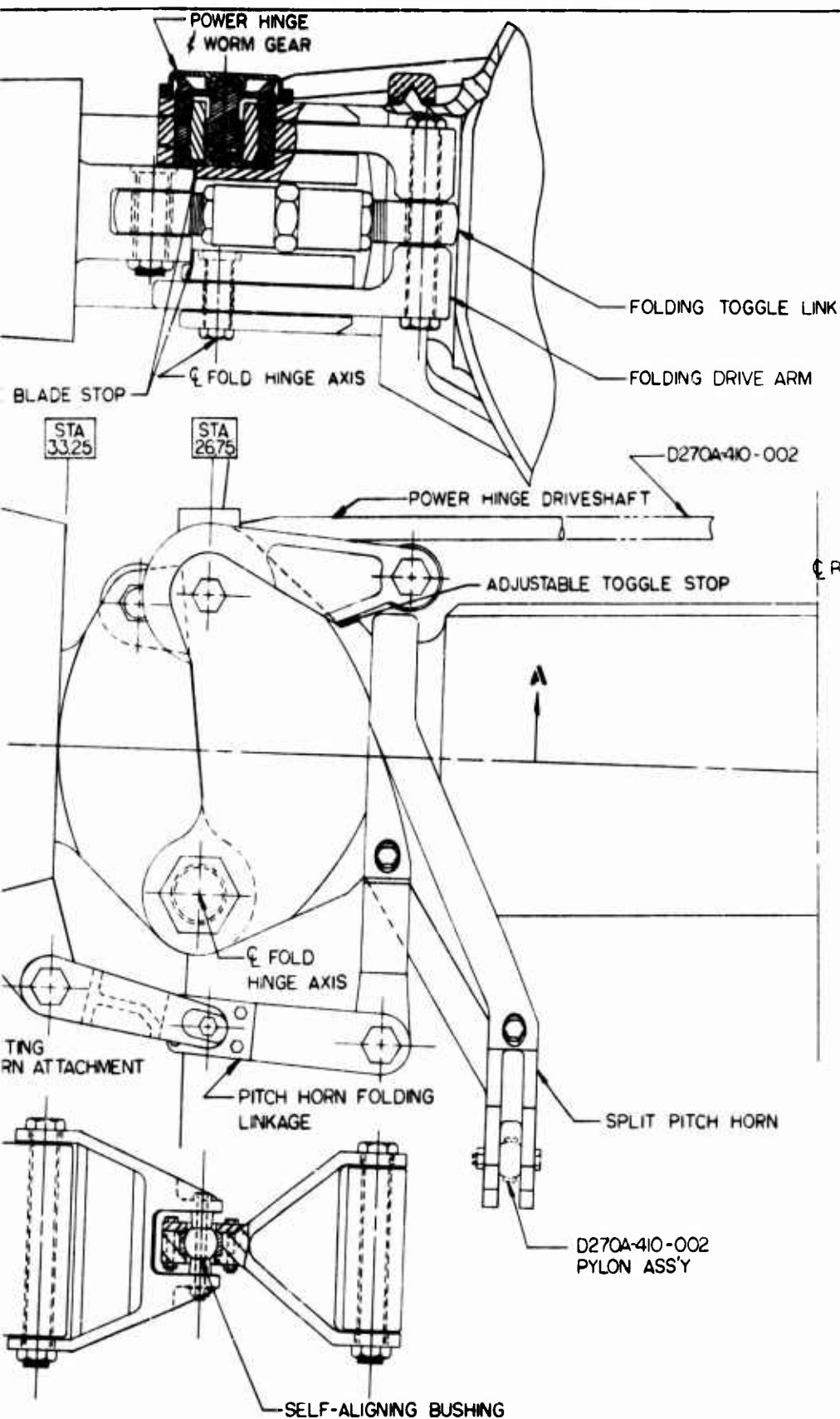
SECTION 13-13
PITCH HORN LINKAGE REMOVED

A

₵ FOLD
HINGE AXIS

BLADE ROOT FITT

TING
RN ATTACHMENT

PITCH HORN FOLDING
LINKAGE

SPLIT PITCH HORN

D270A-410-002
PYLON ASS'Y

RETENTION STRAP
(MULTIPLE WIRE)

STRAP PIN

SELF-ALIGNING BUSHING

'0A Folding Mechanism.

2

FAIRING CUFF

FOLDING DRIVE ARM

FOLDING TOGGLE LINK

$\mathbb{G}$ ROTOR SHAFT

90°
TOTAL FOLD TRAVEL
FOLD TIME-7 SECONDS

'ED

$\mathbb{G}$ PITCH HORN LINKAGE PARALLEL
TO $\mathbb{G}$ FOLD HINGE AT TIME OF
FOLDING

PARTIALLY FOLDED BLADE
¼ SCALE

TEFLON BUSHINGS BONDED
TO YOKE

—BLADE ROOT FITTING REF.

PITCH CHANGE BEARINGS

—RETENTION STRAP
(MULTIPLE WIRE)

SPINDLE

YOKE

SECTION A-A

Figure II-8.

DESIGN
LAYOUT

FOLDING MECHANISM
D270A

JAY CARTER   91669   HALF

D270A-410-003

3
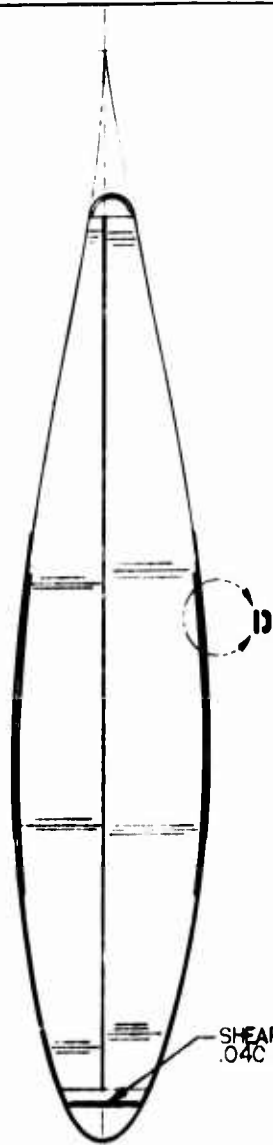
SECTION — B-B
SCALE 1/2

SECTION — A-A
SCALE 1/2

SHEAR WEB
.04C CRES 17-7PH

T.E. ROOT FAIRING
FIBERGLASS REINFORCED
PANEL
PITCH HORN ATTACHMENT

A

A

OIL RESERVOIR

ROOT CLOSURE
PHENOLIC

STA.
34.25   BEAR

SKIN

SPACER DOUBLER

EXTERNAL DOUBLER

ALUMINUM HONEYCOMB
CORE

ABRASIVE STRIP

INTERNAL DOUBLER   SPAR

DETAIL — D
SCALE 10/1

BEARING RETAINER
ALUMINUM

BEARING SPACER
ALUMINUM

BEARING

1

TRAILING EDGE SPAR—
CRES 17-4PH

-T.E. ROOT CLOSURE
.016 CRES 17-7PH

DOUBLER—
.050 CRES 17-7PH

→ B

SPACER DOUBLER—
.020 CRES 17-7PH

OOT FAIRING—
RGLASS REINFORCED
L
IENT—

→ A

EXTERNAL DOUBLER
.016 CRES 17-7PH

SPACER DOUBLER—
.020 CRES 17-7PH

ERVOIR

→ A

CLOSURE
DLIC

L.E. ROOT FAIRING
FIBERGLASS REINFORCED
PANEL

→ B

INTERNAL DOUBLER
.050 CRES 17-7PH

STA.
34.25

—BEARING

STA.
58.25

—ROOT FITTING
ALUMINUM

ER—

BEARING—

ER—

BUSHING
4340 STEEL

—PLUG
ALUMINUM

—SEAL RETAINER
ALUMINUM

2

DGE SPAR
PH

SKIN
.02 CRES 17-7PH

R DOUBER
CRES 17-7PH

SPAR
.032 CRES 17-7PH

RNAL DOUBLER
CRES 17-7PH

ABRASIVE STRIP
.040 CRES 17-7PH

LEAD AL
BLOCK

BLADE ASSEMBLY PLANFORM
SCALE 1/4

Figure II-9.   D270A Blade Assembly.

3

40.00
CHORD
CONSTANT

C

C

E STRIP
RES 17-7PH

LEAD ALLOY NOSE
BLOCK

TIP CAP

BALANCE WEIGHT
SUPPORT
(BONDED & SCREWED IN PLACE)

ADJUSTABLE BALANCE
WEIGHTS TIP CAP
REMOVED

TIP CLOSURE
.020 ALUMINUM

STA
300.00

SECTION — C-C
SCALE 1/2

THICKNESS — INCHES

11.0
10.0
8.0
6.0
4.0
2.0
0

BLA

0   100

THICKNES

TWIST — DEGREES

25°
20°
15°
10°
5°
0°

0   100

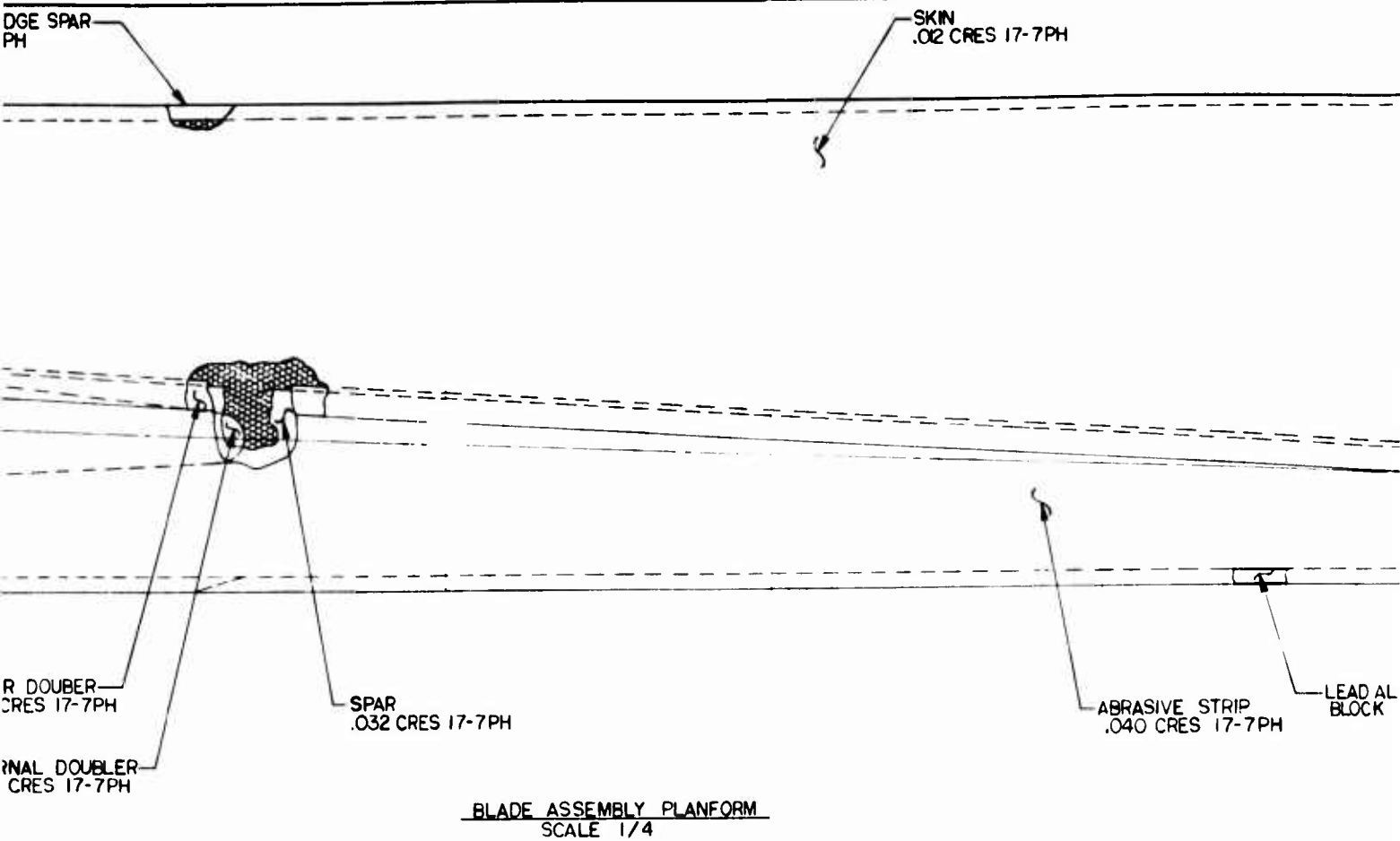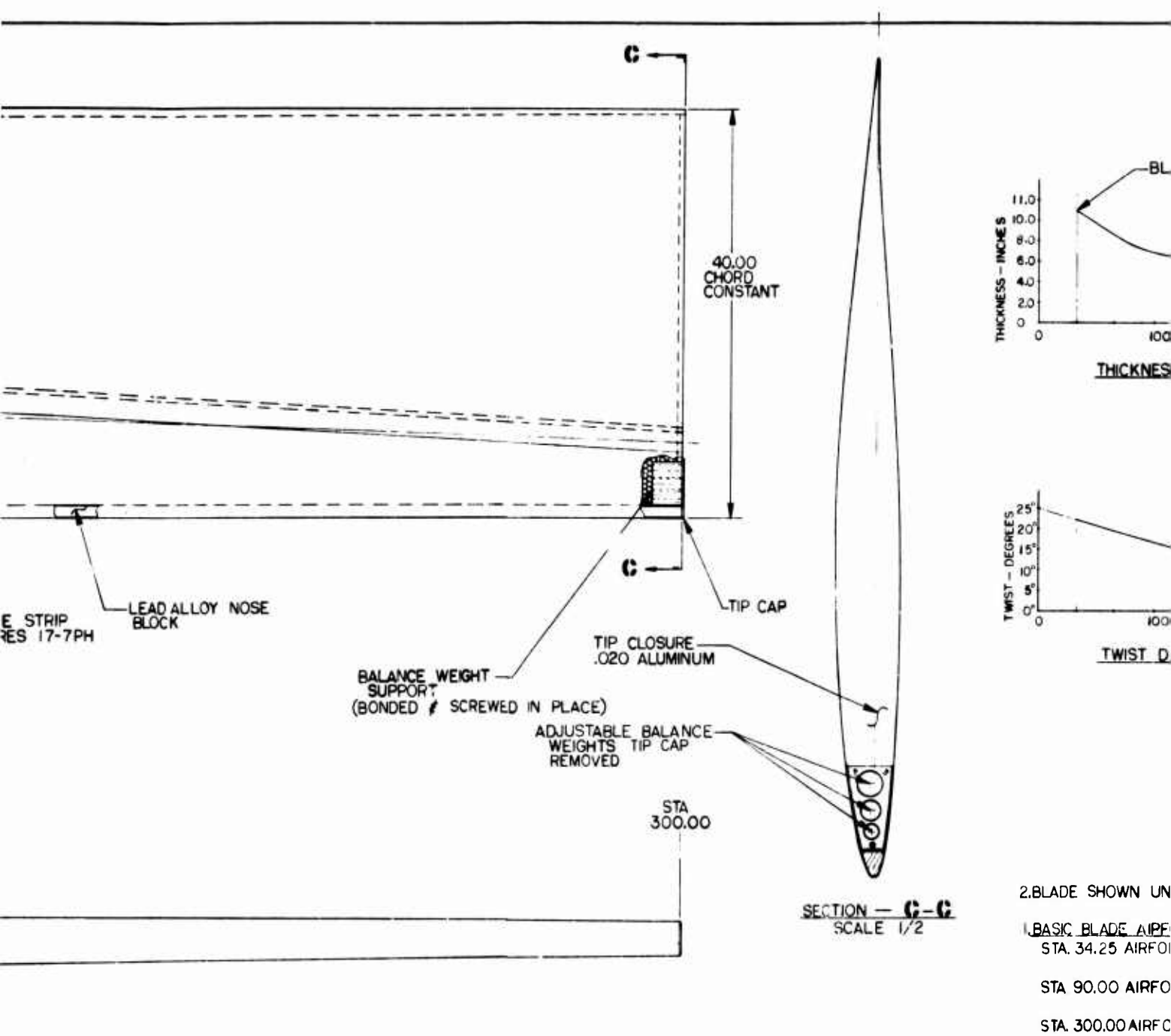TWIST D

2. BLADE SHOWN UN

1. BASIC BLADE AIRFO
STA. 34.25 AIRFOI

STA 90.00 AIRFO

STA. 300.00 AIRFO

GENERAL DATA

Figure II-9.

40.00
CHORD
CONSTANT

TIP CAP

TIP CLOSURE
020 ALUMINUM

BLE BALANCE
TS TIP CAP
ED

STA
300.00

BLADE ROOT

THICKNESS DISTRIBUTION

TWIST DISTRIBUTION

SECTION — C-C
SCALE 1/2

2. BLADE SHOWN UNTWISTED

1. BASIC BLADE AIRFOIL DATA
STA. 34.25 AIRFOIL NACA 64X27.3

STA. 90.00 AIRFOIL NACA 64X17.3

STA. 300.00 AIRFOIL NACA 64X08

GENERAL DATA
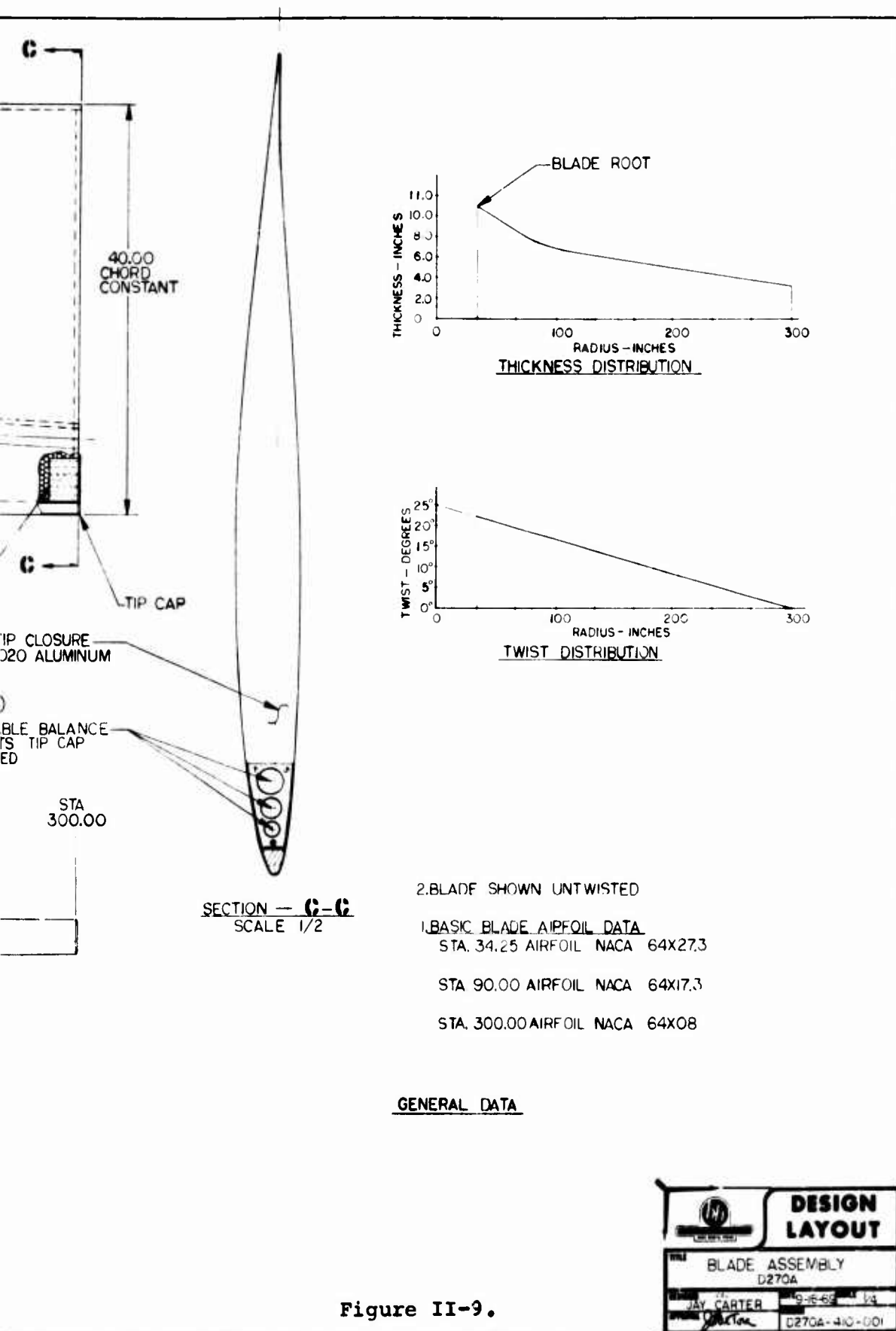
DESIGN LAYOUT

BLADE ASSEMBLY
D270A

JAY CARTER   9-15-69   1/4

D270A-410-001

Figure II-9.

DOCUMENT CONTROL DATA - R & D

(Security classification of title, body of abstract and indexing annotation must be entered when the overall report is classified)

1. ORIGINATING ACTIVITY (Corporate author)	2a. REPORT SECURITY CLASSIFICATION
Bell Helicopter Company Fort Worth, Texas 76101	Unclassified 2b. GROUP

3. REPORT TITLE

A STUDY OF FOLDING PROPROTOR VTOL AIRCRAFT DYNAMICS -- VOLUME I

4. DESCRIPTIVE NOTES *(Type of report and inclusive dates)*

Final Report

5. AUTHOR(S) *(First name, middle initial, last name)*

Jing G. Yen, Ph.D.
Gottfried E. Weber
Troy M. Gaffey

6. REPORT DATE	7a. TOTAL NO. OF PAGES	7b. NO. OF REFS
September 1971	252	26

8a. CONTRACT OR GRANT NO. F33615-69-C-1339 *new* b. PROJECT NO. 1370 c. Task No. 137005 d.	9a. ORIGINATOR'S REPORT NUMBER(S) 9b. OTHER REPORT NO(S) *(Any other numbers that may be assigned this report)* AFFDL-TR-71-7, VOLUME I

10. DISTRIBUTION STATEMENT

Distribution limited to U. S. Government agencies only; test and evaluation; statement applied 12 August 1971. Other requests for this document must be referred to AF Flight Dynamics Laboratory, (FY) Wright-Patterson AFB, Ohio.

11. SUPPLEMENTARY NOTES	12. SPONSORING MILITARY ACTIVITY Air Force Flight Dynamics Laboratory Air Force Systems Command Wright-Patterson Air Force Base, Ohio

13. ABSTRACT

This report describes the results of a study of the dynamic stability and response during the feathering and folding of the blades of a folding-proprotor VTOL. This study involved the development of analytical methods of predicting the dynamic characteristics during feathering and folding, correlation of the theoretical methods with experimental data, a dynamic analysis of a representative folding-proprotor VTOL design, and a parametric study to identify design factors which can be used to control dynamic characteristics during feathering and folding. Correlation of the theory with measured dynamic stability and response characteristics during feathering and folding is good, and indicates the analytical methods can be used with confidence. The results of the dynamic analysis indicate satisfactory stability and response characteristics can be achieved in a 66,000-pound gross-weight class, folding-proprotor VTOL. The results of the parametric study are summarized in terms of design guidelines. This volume contains the development of the theory, correlation of theory with experimental data, and the dynamic analysis and parametric study. Volume II is a guide to the computer programs and contains FORTRAN listings.

DD FORM 1473
1 NOV 65

14. KEY WORDS	LINK A		LINK B		LINK C	
	ROLE	WT	ROLE	WT	ROLE	WT
Folding Proprotor						
Dynamic Stability						
Dynamic Response						
Feathering/Unfeathering						
Propeller Whirl Flutter						
Reduced Frequency						